

Université du Québec
Institut National de la Recherche Scientifique
Centre Énergie, Matériaux et Télécommunications

**SYNTHESIS AND CHARACTERIZATION OF NEAR-INFRARED
COLLOIDAL CORE/SHELL QUANTUM DOTS FOR SOLAR
TECHNOLOGIES**

Par
Xin Tong

Thèse présentée pour l'obtention du grade de
Philosophiae doctor (Ph.D.)
en sciences de l'énergie et des matériaux

Jury d'évaluation

Président du jury et
examineur interne

Fiorenzo Vetrone
INRS-EMT, Université du Québec

Examineur externe

Rafik Naccache
Concordia University

Examineur externe

Sebastien Francoeur
Polytechnique Montréal

Directeur de recherché

Federico Rosei
INRS-EMT, Université du Québec

ABSTRACT

Colloidal quantum dots (QDs) have attracted considerable attention owing to their outstanding optical properties including broad light absorption, size/composition-tunable optical emission, high photoluminescence quantum yield (PLQY) and multiple exciton generation. In this regard, QDs have been extensively used as building blocks in various solar technologies including luminescent solar concentrators (LSCs), solar cells and solar-driven photoelectrochemical (PEC) hydrogen generation. Specifically, QDs with near-infrared (NIR) optical properties exhibit great potential for various applications because their broadband NIR light absorption is favorable to improve the efficiency of photovoltaic devices and their tunable NIR photoluminescence (PL) emission matches well with the wavelength region of biomedical window (~750-1350 nm) and optical communication (~1350-1600 nm). As a result, NIR QDs have been employed to fabricate high performance optoelectronic devices such as solar cells, light-emitting diodes (LEDs) and photodetectors, and are used for biological imaging/detection and optical fibers as well.

However, to date, a majority of NIR QDs contain highly toxic chemical elements (e.g. Pb and Hg), which are harmful to human health and the natural environment and are not favorable for their future commercialization towards real-life applications. NIR, environmentally friendly QDs (e.g. CuInS/Se QDs) have been developed in recent years, while their multicomponent nature leads to the easily formation of surface trap states and defects. These surface traps/defects can deteriorate the PLQY and photo/chemical-stability of QDs, which leads to the non-radiative recombination of QDs, thus hindering the development of high-efficiency and long-term stable QDs-based optoelectronic devices. To address these problems, one approach is to develop heavy metal-free and NIR core/shell structured QDs with optimized optical properties and enhanced photo/chemical-stability, focusing on the comprehensively investigation of their growth mechanism, band structure engineering, photoexcited electron-hole dynamic to realize high performance solar energy conversion applications (e.g. solar-drive PEC cells).

In the first part, we synthesized NIR, environmentally friendly CuInSe_xS_{2-x} (CISeS, C represents Copper instead of Carbon)/ZnS core/shell QDs by employing cation exchange

method. Morphological investigation of these QDs suggests that such cation exchange approach leads to the formation of a thin ZnS shell on the surface of CISES core QDs. Optical characterizations show the NIR optical absorption (up to 1000 nm) and PL spectrum (emission center at ~960 nm). By comparing the PL intensity and PL lifetime of bare CISES QDs and CISES/ZnS core/shell QDs, it is demonstrated that the ZnS shell enables the effective passivation of the surface defects/traps on the CISES QDs. These NIR, heavy metal-free QDs were then used as photosensitizers to fabricate QDs-sensitized photoanode by using electrophoretic deposition (EPD) technique. As-fabricated CISES/ZnS core/shell QDs-sensitized photoanode was applied as a working electrode in a PEC cell for solar-driven hydrogen generation. Under standard one sun illumination (AM 1.5G, 100 mW/cm²), the QDs-based PEC cell exhibits a saturated photocurrent density of ~5.3 mA/cm², which is higher than the saturated photocurrent density (~2.57 mA/cm²) of bare CISES QDs-based PEC cell, indicating the effective surface passivation of CISES QDs by the ZnS thin shell for suppressed non-radiative recombination, thus enhancing the device performance. Moreover, CISES/ZnS core-shell QDs-based PEC cell exhibited improved device stability as compared to bare CISES QDs-based devices.

In the second part, we synthesized NIR, heavy metal-free CuInSe₂/CuInS₂ (CISE/CIS) “giant” core/shell QDs (g-QDs) via sequential cation exchange technique. Morphological investigation demonstrates the formation of a CuInS₂ thick shell with wurtzite (WZ) phase. Optical characterization of these NIR, heavy metal-free g-QDs exhibit tunable NIR absorption and PL spectra (up to 1100 nm). These NIR, environment-friendly g-QDs show a red-shift of PL peaks and prolonged lifetime with increasing shell thickness, demonstrating their “quasi-type II” band structure, wherein the electrons can delocalize into the shell region while the holes are well confined in the core region. By choosing appropriate physical parameters and solving the Schrödinger equation of these g-QDs, the electron-hole wavefunction distribution as a function of shell thickness is presented. The simulation results further verify the “quasi-type II” band structure of as-synthesized g-QDs, which is in accordance with their optical characterization. As a proof of concept, a PEC cell based on such NIR and “green” g-QDs was fabricated, showing a saturated photocurrent density of ~3 mA/cm² under standard one sun illumination

(AM 1.5G, 100 mW/cm²). By comparing the stability of PEC device based on g-QDs with various shell thickness, it is demonstrated that g-QDs with thicker shell exhibit higher photo/chemical stability in solar-driven PEC hydrogen production.

Apart from the heavy metal-free NIR core/shell QDs, heterostructured semiconductor nanocrystals with non-spherical shapes such as dot-in-rod, tetrapod and pyramid have emerged as potential candidates in solar technologies, which exhibit particularly small spatial electron-hole wavefunction overlap for ultralong PL lifetime that are beneficial to the photogenerated charge carrier separation/transfer in boosting the efficiency of QDs-based photovoltaic applications. In the third part, we developed a new type of NIR-emitting, pyramid-shaped CISeS/CdSeS/CdS g-QDs, which were synthesized by using a facile two-step method. As-synthesized g-QDs exhibit a pyramidal shape and the CdSeS/CdS shell was demonstrated to possess a zinc blende (ZB) phase. Optical properties of g-QDs exhibit NIR PL emission (~830 nm) with considerable PLQY of 17%. This type of pyramidal-shaped g-QDs show unprecedentedly prolonged PL lifetime up to ~2 μs with increasing shell thickness, indicating that the pyramidal shape of these g-QDs can induce efficient electron-hole separation and form a “quasi-type II” band structure. Theoretical simulation was used to calculate the spatial electron-hole wave function distribution of as-synthesized g-QDs with various shell thickness, demonstrating the direction-dependent electron-hole wave function distribution and "quasi type-II" band structure of such pyramidal g-QDs. We subsequently used these g-QDs to fabricate PEC cells, showing a high saturated photocurrent of ~5.5 mA/cm² and outstanding device stability under one sun illumination (AM 1.5 G, 100 mW/cm²). These results indicate that this type of pyramid-shaped g-QDs show efficient electron-hole separation and are promising to achieve high performance photovoltaic devices.

ACKNOWLEDGEMENTS

First of all, I would like to thank my supervisors Prof. Federico Rosei and Prof. Zhiming Wang for their patient and invaluable suggestions, as well as great support and encouragement throughout my PhD path. I want to acknowledge the Chinese Scholarship Council for providing the financial support to my PhD study in Canada.

In particular, I would like to express my gratitude and appreciation to my group leader Dr. Haiguang Zhao for his constant support and discussion of my research projects. I am grateful to Prof. Jiang Wu, Prof. Xiaobin Niu and Prof. Haining Ji at UESTC for their support. Moreover, I would like to thank our collaborators Prof. Alexander O. Govorov, Prof. Shuhui Sun, Prof. Dongling Ma, Prof. Alberto Vomiero and Dr. Xiang-Tian Kong for their kind help for my research projects.

I would like to thank my group member, Dr. Yufeng Zhou for providing me useful suggestions, huge support and great help. I want to thank my other group members for their help throughout my work, these people include: Dr. Gurpreet Singh Selopal, Dr. Fabiola Navarro-Pardo, Dr. Adhikari Rajesh, Dr. Lei Jin, Dr. Kaustubh Basu, Hui Zhang, Chao Wang, Jiabin Liu, Kanghong Wang, Daniele Benetti, Rusoma Akilimali and other NFL colleagues.

I would like to express my appreciation to my good friends at INRS-EMT, Dr. Qiliang Wei, Yanqing Fu, Dr. Fan Yang, Xiaohua Yang, Dr. Jun Ge and Dr. Wei Huang for all the fun we had during my stay at INRS-EMT.

In addition, I want to thank the staff and technician at INRS-EMT. All of them are very nice. I would like to acknowledge Jean-Philippe Masse at Polytechnique Montréal for TEM characterization.

I would like to thank my dearest parents and my wife Fan Jia, they love me deeply and unconditionally give their full love to me.

CONTENTS

CHAPTER 1 INTRODUCTION.....	1
1.1 Colloidal semiconductor quantum dots	1
1.2 Synthesis, toxicity and optoelectronic properties of quantum dots.....	3
1.2.1 Synthesis of bare quantum dots.....	3
1.2.2 Synthesis of core/shell quantum dots	4
1.2.3 “Giant” core/shell quantum dots	6
1.3 Toxicity of heavy metal-based quantum dots	9
1.4 Near-infrared, heavy metal-free core/shell quantum dots.....	11
1.5 Quantum dots-based photoelectrochemical cells for solar-driven hydrogen generation	13
1.6 Characterization	17
1.7 Thesis objectives and organization	19
1.7.1 Research objectives	19
1.7.2 Thesis organization.....	21
CHAPTER 2 SYNTHESIS AND CHARACTERIZATION OF HEAVY METAL-FREE, NEAR-IR INFRARED COLLOIDAL CORE/SHELL QUANTUM DOTS FOR EFFICIENT PHOTOELECTROCHEMICAL HYDROGEN GENERATION	23
2.1 Synthesis of heavy metal-free, near-infrared quantum dots and fabrication of quantum dots-based photoelectrochemical cells.....	23
2.1.1 Synthesis of heavy metal-free, near-infrared $\text{CuInSe}_x\text{S}_{2-x}$ core and core/shell quantum dots	24
2.1.2 Fabrication of quantum dots-based photoelectrochemical cells.....	25
2.1.3 Structure and optical properties of quantum dots and quantum dots-sensitized photoanodes.....	26
2.2 Measurement and performance of quantum dots-based photoelectrochemical cells.	36
2.2.1 Measurement of quantum dots-sensitized photoanodes	36
2.2.2 Photoelectrochemical performance of quantum dots-based photoanodes.....	36

2.3 Summary.....	41
CHAPTER 3 SYNTHESIS AND CHARACTERIZATION OF NEAR-INFRARED, HEAVY METAL-FREE COLLOIDAL “GIANT” CORE/SHELL QUANTUM DOTS FOR SOLAR-DRIVEN PHOTOELECTROCHEMICAL CELLS.....	43
3.1 Synthesis and characterization of near-infrared, heavy metal-free colloidal “giant” core/shell quantum dots	43
3.1.1 Synthesis of near-infrared, heavy metal-free CuInSe ₂ /CuInS ₂ “giant” core/shell quantum dots	44
3.1.2 Structure and optical properties.....	45
3.2 Theoretical investigation of near-infrared, heavy metal-free colloidal “giant” core/shell quantum dots.....	55
3.2.1 Theoretical calculation method	55
3.2.2 Wave function in CuInSe ₂ /CuInS ₂ “giant” core/shell quantum dots	57
3.3 Fabrication and measurement of CuInSe ₂ /CuInS ₂ “giant” core/shell quantum dots-based photoanode for solar-driven photoelectrochemical hydrogen production	59
3.3.1 Fabrication of CuInSe ₂ /CuInS ₂ “giant” core/shell quantum dots-sensitized photoanode.....	59
3.3.2 Incident photo to current efficiency measurement and theoretical calculation of hydrogen generation rate	60
3.3.3 Photoelectrochemical performance of CuInSe ₂ /CuInS ₂ “giant” core/shell quantum dots-sensitized photoanode	61
3.3 Summary.....	69
CHAPTER 4 SYNTHESIS AND CHARACTERIZATION OF NEAR-INFRARED COLLOIDAL HETEROSTRUCTURED PYRAMIDAL “GIANT” CORE/SHELL QUANTUM DOTS FOR HIGH PERFORMANCE PHOTOELECTROCHEMICAL CELLS	70
4.1 Synthesis and characterization of near-infrared colloidal heterostructured pyramidal “giant” core/shell quantum dots.....	70
4.1.1 Synthesis of near-infrared colloidal heterostructured pyramidal CuInSe _x S _{2-x} /CdSeS/CdS “giant” core/shell quantum dots.....	71

4.1.2 Structure and optical properties.....	72
4.2 Theoretical study of near-infrared colloidal heterostructured pyramidal “giant” core/shell quantum dots	85
4.2.1 Theoretical calculation method	85
4.2.2 Wave function in pyramidal $\text{CuInSe}_x\text{S}_{2-x}/\text{CdSeS}/\text{CdS}$ “giant” core/shell quantum dots	86
4.3 Fabrication and measurement of pyramidal $\text{CuInSe}_x\text{S}_{2-x}/\text{CdSeS}/\text{CdS}$ “giant” core/shell quantum dots-based optoelectronic devices.....	91
4.3.1 Fabrication of pyramidal $\text{CuInSe}_x\text{S}_{2-x}/\text{CdSeS}/\text{CdS}$ “giant” core/shell quantum dots-sensitized photoanode and solar cells.....	91
4.3.2 Device performance of pyramidal $\text{CuInSe}_x\text{S}_{2-x}/\text{CdSeS}/\text{CdS}$ “giant” core/shell quantum dots-sensitized photoanode and solar cells.....	92
4.4 Summary.....	97
CHAPTER 5 CONCLUSIONS AND PERSPECTIVES	98
5.1 Conclusions.....	98
5.2 Perspectives	100
BIBLIOGRAPHY	102
RÉSUMÉ.....	110

LIST OF FIGURES

Figure 1.1 Schematic diagram of electronic energy levels in molecule, QDs and bulk semiconductor ¹⁰.

Figure 1.2 Absorption spectra of PbSe QDs with various sizes (from 2.5 to 4.8 nm) ¹¹.

Figure 1.3 PL spectra of QDs with various chemical compositions ¹³.

Figure 1.4 Schematic diagrams of (a) hot-injection and (b) heat-up techniques ^{27, 33}.

Figure 1.5 Various band alignment of core/shell QDs ⁴³.

Figure 1.6 Theoretical calculation of electron-hole wave functions in CdSe/CdS g-QDs and PbSe/CdSe g-QDs. (a) Band alignment of CdSe and CdS in bulk (left). Spatial probability distribution, $\rho(r)$, of the hole and electron. Here the $\rho(r)$ is proportional to the $r^2|\psi_{e,h}|^2$, wherein the $|\psi_{e,h}|$ are the electron and the hole wave functions. (b) Electron-hole overlap integral and optical bandgap energy of PbSe/CdSe g-QDs. (c) Band alignment of PbSe/CdSe QDs representing two core/shell structure with different core and shell sizes, which all exhibit a quasi-type II band structure ^{60, 61}.

Figure 1.7 Working principle of NIR, heavy metal-free CuInS₂/ZnS core/shell QDs based-QDSCs (left) and their $J-V$ curves (right) ⁸¹.

Figure 1.8 Schematic diagram of QDs-based PEC cell for hydrogen generation ¹⁰⁵.

Figure 2.1 TEM images of (a) CISES QDs; (b) Cd-CISES and (c) Zn-CISES QDs showing analogous pyramidal structure and nearly same sizes. Inset images of (a), (b) and (c) display schematic diagrams of QDs structures of CISES, Cd-CISES and Zn-CISES, respectively. (d) HRTEM image of an individual Zn-CISES QD with lattice spacing of 0.327 nm. (e) TEM image of TiO₂/Zn-CISES heterostructure with uniform dispersion of Zn-CISES QDs (white dashed circle presents a single QD on the surface of TiO₂). (f) HRTEM of TiO₂/single Zn-CISES QD heterostructure (higher magnification image of the white line circle in (e)).

Figure 2.2 Size distribution of CISES QDs. Sizes are measured as the height of projected triangles (distance from a vertex to the middle of the opposite) in TEM image for 100 QDs. The average sizes were 5.64 ± 0.77 nm.

Figure 2.3 (a) XRD pattern of CISeS QDs films formed by drying of dropped CISeS QDs solution on the top of FTO glass substrate, diffraction peaks at 26.9, 45.1 and 53.1° matching well between diffraction peaks of (112), (204/220) and (312) facets in pure CuInS₂ (★, JCPDS card no. 03-065-1572) and CuInSe₂ (▲, JCPDS card no. 00-040-1487) with tetragonal phase. (b) EDS spectra of TiO₂/Zn-CISeS heterostructure (in Figure 1e), confirming the presence of the elements including Ti, O, Zn, Cu, In, Se and S.

Figure 2.4 (a) Cross-sectional SEM image of Zn-CISeS QDs-sensitized photoanode. EDS mapping analysis of all the elements in relevant TiO₂/Zn-CISeS/ZnS electrode including (b) Ti, (c) O, (d) Zn, (e) Cu, (f) In, (g) Se and (h) S.

Figure 2.5 (a) Cross-sectional SEM image of TiO₂/Zn-CISeS/ZnS and corresponding (b) EDS spectra of specified region (white solid line) in (a).

Figure 2.6. XPS spectra of Zn and Cd-CISeS QDs-TiO₂ photoanodes. (a) Full spectrum of Zn-CISeS QDs-TiO₂ photoanode; (b) High resolution Zn 2p core-level spectra; (c) Full spectrum of Cd-CISeS QDs-TiO₂ photoanode; (d) High resolution Cd 3d core-level spectra.

Figure 2.7 (a) Absorption spectra of CISeS in toluene before and after Zn (Cd) treatment. The inset image exhibits the extrapolation of Tauc plots [$(\alpha h\nu)^2$ versus photon energy ($h\nu$)]. (b) Band alignment and schematic diagram of Zn-CISeS QDs-sensitized photoanode. Absorption and PL spectra (c) and lifetime (d) of CISeS QDs with Zn treatment at different temperatures.

Figure 2.8 (a) UPS full spectrum of the Zn-CISeS QDs deposited on mesoporous TiO₂. Corresponding high resolution UPS spectrum of (b) high binding energy cut-off (determining Fermi level) and (c) low binding energy cut-off (determining VB maximum).

Figure 2.9 UV-visible-NIR absorption (blue line) and PL (red line) spectra of as-synthesized CISeS QDs dispersed in toluene.

Figure 2.10 EDS spectra of Zn-CISeS QDs treated at 50 and 150 degree, showing molar ratio of [Zn/(Cu+In)] of 7.5% and 31.8%, respectively.

Figure 2.11 UPS spectra of (a) CISeS QDs, (c) Cd-CISeS QDs deposited on TiO₂ and corresponding band alignment as well as schematic diagram of (b) CISeS QDs and (d) Cd-CISeS QDs-sensitized photoanodes.

Figure 2.12 Photocurrent density versus bias potential (versus RHE) for (a) the TiO₂/CISeS/ZnS, (b) TiO₂/Zn-CISeS/ZnS and (c) TiO₂/Cd-CISeS/ZnS photoanodes in the dark

(black curve), under continuous (red curve) and chopped (blue curve) illumination (AM 1.5G, 100 mW/cm²) (d) Stability measurements (photocurrent density as a function of time) of TiO₂/CISeS/ZnS and TiO₂/Zn-CISeS/ZnS photoanodes at 0.6 V versus RHE under AM 1.5G illumination (100 mW/cm²) and optical images of TiO₂/Zn-CISeS/ZnS photoanode before (left) and after (right) stability measurement (9h, AM 1.5G, 100 mW/cm²).

Figure 2.13 J-V curves of the TiO₂/CISeS/ZnS photoanode formed by 15min EPD and various cycles of ZnS via SILAR. One (a), two (b), four (c), and six (d) ZnS cycles are studied, presenting that the 2-cycle ZnS is the most favorable for achieving higher photocurrent density due to the more efficient photocorrosion inhibition compared to other cycles of ZnS coating.

Figure 2.14 J-V curves of the TiO₂/Zn-CISeS/ZnS photoanode with Zn-CISeS QDs treated at different temperature of (a) 50 °C and (b) 100 °C, showing saturated photocurrent density of ~3.03 and 1.75 mA/cm².

Figure 2.15 Photocurrent density versus bias potential (vs RHE) for optimized TiO₂/Zn-CISeS/ZnS photoanode with champion photocurrent density of ~5.3 mA/cm² under illumination of one sun (AM 1.5G 100 mW/cm²).

Figure 3.1 (a) Schematic diagram of sequential cation exchange procedures for synthesis and structure of Zn-CISe/CIS g-QDs. TEM images of (b) CdSe/13CdS and (c) CdSe/6CdS g-QDs with inset HR-TEM images showing (002) plane of WZ CdS. (d) SAED pattern of CdSe/13CdSg-QDs. (e) EDS spectra of Zn-CISe/13CIS g-QDs (e) and Zn-CISe/6CIS g-QDs (i). (f) TEM images of Zn-CISe/13CIS and (g) Zn-CISe/6CIS g-QDs with inset HR-TEM images exhibiting (100) plane of WZ CuInS₂. (h) SAED pattern of Zn-CISe/13CIS g-QDs.

Figure 3.2 EDS spectra of (a) CdSe/6CdS and (b) CdSe/13CdS g-QDs before sequential cation exchange. And the spectra of CdSe/6CdS g-QDs confirms all the elements including Cd, S and Se. The element of Se is absent in (b) due to the thicker CdS shell of CdSe/13CdS g-QDs.

Figure 3.3 EDS spectra of (a) CdSe/13CdS and (b) CISe/13CIS g-QDs. The spectra confirm the presence of all the elements in CdSe/13CdS (Cd, S and Se) and CISe/13CIS (Cu, In, S and Se) g-QDs. The atomic concentration of Se is 1.2% and 1.23% in CdSe/13CdS and CISe/13CIS g-QDs, respectively, indicating very small volume of core QDs in such core/shell g-QDs.

Figure 3.4 TEM images of (a) CISe/13CIS and (b) Zn-CISe/13CIS g-QDs, exhibiting no significant change of QD's sizes and shapes before and after Zn treatment. (c) SAED pattern of

CISe/13CIS g-QDs, which is well indexed to (100), (002), (101), (110), (103) and (112) plane of wurtzite (WZ) phase CuInS_2 . (d) EDS spectra CISe/13CIS g-QDs, confirming the presence of all the elements including Cu, In, Se and S.

Figure 3.5 Size distribution of (a) CISe/13CIS and (b) Zn-CISe/13CIS g-QDs. Sizes are measured as the diameter of the spheres in TEM image for 100 QDs. The average sizes were 9.2 ± 0.6 nm and 9.2 ± 0.7 nm for CISe/13CIS and Zn-CISe/13CIS g-QDs, respectively. The results indicates the Zn surface treatment has negligible effect for the size of QDs and only forms an ultrathin ZnS layer on the g-QDs.

Figure 3.6 XRD pattern of CISe/13CIS g-QDs films formed by drying of dropped CISe/13CIS g-QDs solution on the top of silicon substrate. The diffraction peaks match well with the (100), (002), (101), (102), (110), (103), (112) and (201) planes of WZ phase CuInS_2 (JCPDS card no. 01-077-9459).

Figure 3.7 SAED pattern of (a) CdSe/6CdS and (b) Zn-CISe/6CIS g-QDs that are indexed to (100), (002), (101), (110), (103) and (112) plane of WZ phase of CdS (JCPS No. 00-041-1049) and CuInS_2 (JCPS No. 01-077-9459), respectively.

Figure 3.8 Absorption and PL spectra of (a) CISe, (b) Zn-CISe/6CIS and (c) Zn-CISe/13CIS g-QDs in toluene before and after sequential cation exchange. (d) Transient PL spectra of Zn-CISe/CIS g-QDs in toluene.

Figure 3.9 (a) PL and (b) absorption spectra of intermediate $\text{Cu}_2\text{Se}/13\text{Cu}_2\text{S}$ g-QDs dispersed in toluene. No PL peak of CdSe/13CdS g-QDs is observed in (a), indicating full conversion of Cd^{2+} to Cu^+ by cation exchange.

Figure 3.10 Transient PL spectra of CdSe, CdSe/6CdS and CdSe/13CdSg-QDs, showing fitted lifetime of ~ 19 ns, 29 ns and 43 ns, respectively.

Figure 3.11 Band diagram of a $\text{CuInSe}_2/\text{CuInS}_2$ core/shell QD surrounded by air.

Figure 3.12 (a) Band structure of a CISe/CIS core/shell QD (3.3 nm-diameter core, 2 nm-thick shell) with energy levels and wave functions of 1S electron, 1S hole and impurity hole. (b) Normalized radial distribution functions for 1S electron and 1S hole of CISe/CIS core/shell QDs. The core diameter is 3.3 nm. The shell thickness varies from 0 (bare CISe QD) to 6 nm. Dashed vertical lines show the core/shell boundaries; dotted vertical lines show the shell/vacuum boundaries for each value of shell thickness. (c) Squared OI of the 1S electron

state and hole states (1S hole and impurity hole) in CISE/CIS core/shell QDs as a function of shell layer thickness.

Figure 3.13 (a) TEM image of TiO₂/Zn-CISE/6CIS g-QDs heterostructure with uniform distribution of QDs (white dash circle represents QDs on the surface of TiO₂). (b) EDS spectra of TiO₂/Zn-CISE/6CIS g-QDs heterostructure. Elements of Zn and Se are not detected, due to their relatively small amount in the QDs.

Figure 3.14 (a) Cross-sectional SEM image of Zn-CISE/6CIS g-QDs-sensitized photoelectrode and relevant (b) EDS spectra of all chemical composition with relative mass concentration, (c) EDS 2D mapping of all the elements including (c) Ti, (d) O, (e) Zn, (f) Cu, (g) In, (h) S and (i) Se, and (j) EDS line scan illustrating the semi-quantified variation of elements along the yellow line (highlighted in the SEM image).

Figure 3.15 (a) Cross-sectional SEM image of Zn-CISE/13CIS g-QDs-sensitized photoanode and corresponding (b) EDS spectra. EDS mapping analysis of (c) Ti, (d) O, (e) Zn (f) Cu (g) In (h) S (i) Se and (j) EDS line scan illustrating the semi-quantified variation of elements along the yellow line (highlighted in SEM image).

Figure 3.16 (a) Approximate band alignment and schematic diagram of Zn-CISE/CIS g-QDs-sensitized photoanodes. Photocurrent density-bias potential dependence (versus RHE) of (b) Zn-CISE/13CIS g-QDs and (c) Zn-CISE/6CIS g-QDs-sensitized photoanodes in the dark (black curve), under continuous (red curve) and chopped (blue curve) illumination (AM 1.5G, 100 mW/cm²). (d) Photocurrent density as a function of time (stability measurements) of TiO₂/CISE/ZnS (black curve), TiO₂/Zn-CISE/6CIS/ZnS (red curve) and TiO₂/Zn-CISE/13CIS/ZnS (blue curve) photoelectrodes at 0.8 V versus RHE under AM 1.5G irradiation (100 mW/cm²).

Figure 3.17 Photocurrent density versus bias potential (versus RHE) for TiO₂/CISE/ZnS photoanode in the dark (black curve), under continuous (red curve) and chopped (blue curve) illumination (AM 1.5 G, 100 mW/cm²).

Figure 3.18 Current density versus bias potential (vs RHE) for FTO/TiO₂ photoanode with photocurrent density of ~0.25 mA/cm² under illumination of one sun (AM 1.5G, 100 mW/cm²).

Figure 3.19 IPCE spectra of TiO₂/CISE/ZnS, TiO₂/Zn-CISE/6CIS and TiO₂/Zn-CISE/13CIS QDs-sensitized photoelectrodes at 0.8 V versus RHE.

Figure 3.20 Photocurrent density versus bias potential (versus RHE) for (a) the TiO₂/Cu₂Se/ZnS, (b) TiO₂/Cu₂Se/6Cu₂S/ZnS and (c) TiO₂/Cu₂Se/13Cu₂S/ZnS photoanodes in the dark (black curve), under continuous (red curve) and chopped (blue curve) illumination (AM 1.5 G, 100 mW/cm²).

Figure 3.21 Photocurrent density versus bias potential (vs RHE) for (a) the TiO₂/CdSe/ZnS, (b) TiO₂/CdSe/6CdS/ZnS and (c) TiO₂/CdSe/13CdS/ZnS photoanodes in the dark (black curve), under continuous (red curve) and chopped (blue curve) under illumination of one sun (AM 1.5G, 100 mW/cm²).

Figure 3.22 H₂ evolution of CdSe/CdS g-QDs, as a function of time under 100 mW/cm² illumination with AM 1.5 G filter. The evolution of H₂ exhibits a nearly linear increase over time⁶⁷.

Figure 4.1 TEM images of (a) CISES with inset HRTEM images displaying (112) plane of chalcopyrite phase. TEM images of (b) CdS#3 and (c) CdS#6 QDs with inset HRTEM images exhibiting (111) plane of ZB phase CdSeS. (d) TEM images of CdS#9 QDs with inset HRTEM images showing (111) plane of ZB phase CdS. (e) XRD patterns of CdS#3, CdS#6 and CdS#9 QDs. (f) Schematic diagram of growth processes and structure of heterostructured CISES/CdSeS/CdS g-QDs.

Figure 4.2 Size distribution of (a) CISES, (b) CdS#3, (c) CdS#6 and (d) CdS#9 QDs, showing sizes of 5.5±0.7 nm, 4.0±0.3 nm, 7.4±0.6 nm and 12.7±0.9 nm, respectively. Sizes are measured as the height of projected triangles (distance from a vertex to the middle of the opposite side) in TEM images for at least 100 QDs.

Figure 4.3 (a) XRD pattern of CISES QDs films prepared by drying the dropped CISES QDs solution on the top of silicon substrate. (b) SAED pattern of CISES QDs. All of the diffraction peaks lie between (112), (204/220) and (312) facets of pure chalcopyrite CuInS₂ (JCPDS card no. 03-065-1572) and pure chalcopyrite CuInSe₂ (JCPDS card no. 00-040-1487), indicating the chalcopyrite phase and alloyed nature of as-prepared CISES core QDs.

Figure 4.4 TEM of CdS#3 QDs, showing possible quasi-octahedral shape.

Figure 4.5 SAED patterns of (a) CdS#3, (b) CdS#6 and (c) CdS#9 QDs, which are consistent with the XRD patterns in Figure 4.1e.

Figure 4.6 Representative TEM images of (a) CdS#1, (b) CdS#2, (c) CdS#4, (d) CdS#5, (e)

CdS#7 and (f) CdS#8 QDs.

Figure 4.7 HRTEM image of CdS#9 g-QDs, showing two (111) facets and the angle of 70.5 degree observed from [110] direction, which is consistent with the three-dimensional pyramids geometry.

Figure 4.8 Size distribution of (a) CdS#1, (b) CdS#2, (c) CdS#4, (d) CdS#5, (e) CdS#7 and (f) CdS#8 QDs. Sizes were measured as the height of projected triangles (distance from a vertex to the middle of the opposite side) in TEM images for at least 100 QDs.

Figure 4.9 (a) UV-Vis absorption and (b) PL spectra of heterostructured CISES/CdSeS/CdS g-QDs at different growth stages in toluene. (c) PL lifetime of CdS#3, CdS#6 and CdS#9 g-QDs in toluene.

Figure 4.10 Tauc plot derived from absorption spectra of all QDs.

Figure 4.11 (a) PLQY of CISES QDs (sample No. 0) and corresponding core/shell QDs (CdS#1 to CdS#9 QDs). (b) Transient PL spectrum of CISES QDs with fitted average lifetime of $\sim 165 \pm 4$ ns.

Figure 4.12 PL decay curves of (a) CdS#2, (b) CdS#4, (c) CdS#5 and (d) CdS#8 QDs, displaying fitted average lifetime of $\sim 1.01 \mu\text{s}$, $1.46 \mu\text{s}$, $1.53 \mu\text{s}$ and $1.91 \mu\text{s}$, respectively.

Figure 4.13 Theoretical modeling of the CISES/CdSeS/CdS g-QDs. (a) Geometrical models of the series of g-QDs (CdS#0-9). Each edge of each component of the QDs is rounded by a radius of 0.3 nm. (b) Electronic band structure with energy levels and wave functions of 1S electrons, impurity holes and 1S holes in a g-QD (CdS#9). (c)-(e) Normalized radial distribution function of 1S electrons in the series of g-QDs along Line 1, Line 2 and Line 3, respectively. The Lines 1-3 are vectors pointing from the origin to the vertex, face center and edge center of the tetrahedron QD, respectively, as demonstrated in (b). The vertical lines show the positions of the surfaces of CISES (dashed), CdSeS (dotted) and CdS (dash-dotted) of each g-QD. (f) Inverse squared OI of the 1S electrons and impurity holes in the series of g-QDs with two different crystal structures, ZB and WZ, for the CdSeS shell and CdS shell. The inverse squared overlap of pyramidal QDs is much higher than that of the spherical QDs (ZB). The experimental lifetime is plotted for comparison (right axis).

Figure 4.14 Band structure for the CISES/CdSeS/CdS heterostructure. (a) The crystal structure of the shells (CdSeS and CdS) is ZB phase, which applies to the samples in the experiments.

(b) The crystal structure of the shells (CdSeS and CdS) is WZ phase, which are used for comparison purpose in theoretical models.

Figure 4.15 (a) Radial distributions of 1S electrons in the g-QDs (CdS#3, CdS#6, CdS#9) along three different directions. The Lines 1-3 are vectors pointing from the origin to the vertex, face center and edge center of the tetrahedron QD, respectively, as demonstrated in Figure 1b of the main text. (b) Maps of wave functions, $\log_{10}(|\psi|^2)$, at the QD surfaces for the g-QDs with two shells, CdS#6-9. The optical tunneling path of 1S electrons in the QDs is shown by the red arrow, which is along Line 2.

Figure 4.16 Normalized radial distribution function of holes in the series of g-QDs along Line 1, Line 2 and Line 3, respectively. The Lines 1-3 are vectors pointing from the origin to the vertex, face center and edge center of the tetrahedron QD, respectively.

Figure 4.17 UV-visible absorption and PL spectra of optimized CdS#6 g-QDs for fabrication of PEC and solar cells.

Figure 4.18 (a) TEM image of CdS#6 g-QDs-sensitized photoelectrode with homogeneous distribution of QDs (white dashed circle indicates the QDs on the surface of TiO₂ nanoparticles). (b) EDS spectra of CdS#6 g-QDs-sensitized photoelectrode.

Figure 4.19 (a) Cross-sectional SEM image of CdS#6 g-QDs-sensitized photoanode and corresponding (b) EDS spectra. EDS mapping analysis of (c) Cd, (d) S, (e) Se, (f) Ti, (g) O and (h) Si.

Figure 4.20 (a) Scheme and predictable band alignment and of heterostructured CISES/CdSeS/CdS g-QDs-based photoelectrodes. Linear sweep voltammetry of (b) TiO₂/CdS#6 g-QDs/ZnS and (c) TiO₂/CdS#9 g-QDs/ZnS systems in the dark and under AM 1.5 G irradiation at 100 mW/cm². (d) Normalized steady state current density-time (J-t) curves of CISES QDs (black curve), CdS#6 g-QDs and CdS#9 g-QDs-decorated photoanodes at 0.6 V versus RHE under standard one sun illumination.

Figure 4.21 Linear sweep voltammetry of TiO₂/CISES/ZnS photoanode in the dark (black curve), under continuous (red curve) and chopped (blue curve) under standard one sun illumination (AM 1.5 G, 100 mW/cm²).

Figure 4.22 (a) Current density versus voltage curve of CdS#6 g-QDs based solar cells under one sun irradiation (AM 1.5 G, 100 mW cm⁻²). (b) Open circuit voltage (V_{oc}) decay as the

function of time. (c) Electron lifetime (τ) as a function of V_{oc} calculated from V_{oc} decay measurements. (d) Photovoltaic parameters calculated from I–V measurements of QDSCs based on CdS#6 g-QDs as light harvesters.

LIST OF TABLES

Table 2.1 EDS analysis of composition (Mass concentration) of TiO₂/Zn-CiSeS /ZnS photoanode. Ratio of elements/Ti (defined as 1) is listed, and Zn and S are much higher owing to the ZnS SILAR coating.

Table 2.2. XPS analysis of cationic composition (atomic concentration) of Zn-CiSeS (treated at 100 °C) and Cd-CiSeS QDs deposited on TiO₂ films. S and Se components are excluded due to their complex peak overlaps.

Table 2.3 CiSeS QDs with Zn treatment under various temperatures and corresponding molar ratio of [Zn/(Cu+In)], QDs core radius, shell thickness, PL peak position and lifetime.

Table 2.4 Composition and size information of CiSeS QDs and Zn-CiSeS QDs (treated at 50, 100 and 150 °C) and relevant PEC performance of QDs-sensitized photoanodes.

Table 3.1 ICP-OES analysis results of CdSe/13CdS g-QDs, showing Cu and Se solution concentration of 23.43 and 0.16 ppm and molar ratio of ~1:0.01.

Table 3.2 ICP-OES analysis results of Cu₂Se/13Cu₂S nanocrystals.

Table 3.3 ICP-OES analysis results of CiSe/13CIS g-QDs, showing Cu and In solution concentration of 2.86 and 6.04 ppm and molar ratio of ~1:1.17.

Table 3.4 Optical parameters of CiSe, Zn-CiSe/6CdS and Zn-CiSe/13CdS g-QDs including parameters of fitted lifetime and the measured QY.

Table 3.5. Physical parameters of bulk CiSe and CIS.

Table 4.1 Detailed information for injection volumes of mixed Cd and S precursors and corresponding sample labels during shell growth of heterostructured CiSeS/CdSeS/CdS g-QDs.

Table 4.2 Absorption peak positions of heterostructured CiSeS/CdSeS/CdS QDs (CdS#2 to CdS#7).

Table 4.3 PL peak positions of CiSeS core QDs and corresponding core/shell QDs (CdS#1 to CdS#9).

Table 4.4 Stokes shift of CiSeS QDs to CdS#9 g-QDs.

Table 4.5 PLQY of bare CiSeS QDs and relevant core/shell QDs (CdS#1 to CdS#9).

Table 4.6. Average lifetime of the CISES core QDs and corresponding core/shell QDs (CdS#2 to CdS#6, CdS#8 and CdS#9).

Table 4.7 PL lifetime of spherical g-QDs with respect to as-synthesized pyramidal-shaped g-QDs.

Table 4.8 Geometrical parameters used in modeling.

Table 4.9 Physical parameters used in modeling.

Table 4.10 Geometry parameters of spherical QDs calculated in Figure 4.13f.

LIST OF CHEMICAL COMPOUNDS, ABBREVIATIONS AND SYMBOLS

Chemical Compounds

OA	oleic acid
ODE	1-octadecene
OLA	oleylamine
DDT	1-dodecanethiol
CdS	cadmium sulfide
CdO	cadmium oxide
S	sulfur
Se	selenium
InP	indium phosphide
ZnS	zinc sulfide
Cd	cadmium
Pb	lead
PbSe	lead selenide
PbTe	lead telluride
CdSe	cadmium selenide
CdSeS	alloyed cadmium sulfide selenide
CdTe	cadmium telluride
Ag ₂ S	silver sulfide
Ag ₂ Se	silver selenide
AgInS ₂	silver indium disulfide
AgInTe ₂	silver indium ditelluride
CuInS ₂	copper indium disulfide
CuInSe ₂	copper indium diselenide
CuFeS ₂	copper iron disulfide
CuFeSe ₂	copper iron diselenide

Na ₂ S	sodium sulfide
Na ₂ SO ₃	sodium sulfite
TiO ₂	titanium dioxide
ZnO	zinc oxide
NiO	nickel oxide
CuI	copper(I) iodide
Cu ₂ S	copper sulfide
Cu ₂ Se	copper selenide
[(CH ₃ CN) ₄ Cu]PF ₆	tetrakis(acetonitrile)copper(I)hexafluorophosphate
InCl ₃	indium chloride
In(Ac) ₃	indium(III) acetate
CTAB	hexadecyltrimethylammonium bromide
TOPO	trioctylphosphine oxide
TOP	trioctylphosphine
Zn(Ac) ₂ ×2H ₂ O	zinc acetate dehydrate
HCl	hydrochloric acid
NaOH	sodium hydroxide
KCl	potassium chloride
AgCl	silver chloride
Na ₂ S×9H ₂ O	sodium sulfide nonahydrate

Abbreviations

PL	photoluminescence
UV	ultraviolet
CB	conduction band
VB	valence band
N ₂	nitrogen gas
QD(s)	quantum dot(s)
LED(s)	light-emitting diode(s)
LSC(s)	luminescent solar concentrator(s)
PLQY	photoluminescence quantum yield

NIR	near-infrared
PEC	photoelectrochemical
CISeS	$\text{CuInSe}_x\text{S}_{2-x}$
CISe/CIS	$\text{CuInSe}_2/\text{CuInS}_2$
EPD	electrophoretic deposition
g-QD(s)	“giant” core/shell quantum dot(s)
FTO	fluorine doped tin oxide
WZ	wurtzite
ZB	zinc blende
DI	deionized
J-V	current-voltage
RHE	reversible hydrogen electrode
PCE	power conversion efficiency
QDSC(s)	quantum dot-sensitized solar cell(s)
SILAR	successive ion layer adsorption reaction
c-ALD	colloidal atomic layer deposition
IPCE	incident photon to current efficiency
XPS	X-ray photoelectron spectroscopy
XRD	X-ray diffraction
TEM	transmission electron microscopy
HRTEM	high resolution transmission electron microscopy
UPS	ultraviolet photoelectron spectroscopy
EDS	Energy-dispersive X-ray spectroscopy
SEM	scanning electron microscope
SAED	selected area electron diffraction
AM	air mass
ICP-OES	inductively coupled plasma optical emission spectrometry
GC	gas chromatography

Symbols

μ micro

J_{sc}	short circuit current
V_{oc}	open circuit voltage
E_g	band gap energy
R_B	Bohr radius
m_e	effective masses of electrons
m_h	effective masses of holes
m_0	electron mass at rest in vacuum
$\mathbf{r}_{\text{impurity}}$	position of impurity
L_h	scale of hole
N_{Cu}	numbers of Cu atoms
N_{In}	numbers of In atoms

CHAPTER 1 INTRODUCTION

1.1 Colloidal semiconductor quantum dots

Colloidal semiconductor nanocrystals, often referred to colloidal quantum dots (QDs), have attracted numerous research interests over the past decades¹⁻⁶. Colloidal QDs are nanometer-scale semiconductor crystals (with diameter less than ~ 20 nm) capped with surfactant molecules (ligands) and dispersed in solution, showing discrete energy levels between those of molecule and bulk semiconductor (**Figure 1.1**)^{6, 7}. Generally, the bulk semiconductor has a band gap energy (E_g), when the semiconductor absorbs a photon with energy more than E_g , the electrons in the valence band (VB) are excited to the conduction band (CB) and leave a hole in the VB, producing an electron-hole pair (i.e. exciton). The size of exciton is defined by the exciton Bohr radius (R_B) of semiconductor materials. Once the size of a semiconductor QD is comparable or less than the size of R_B , the charge carriers turn into spatially confined, resulting in quantum confinement effect that gives rise to the size-dependent optical properties of QDs⁸⁻

10.

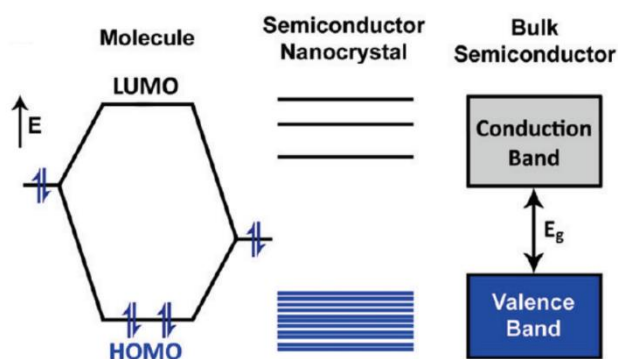


Figure 1.1 Schematic diagram of electronic energy levels in molecule, QDs and bulk semiconductor¹⁰.

For example, as shown in **Figure 1.2**, the PbSe QDs with various sizes exhibit different optical absorption spectra, as expressed by the red-shift of excitonic peaks with increasing QD size (from 2.5 to 4.8 nm), in which the broadening of the excitonic peaks is attributed to the loss of quantum confinement^{11, 12}. In addition, the optical properties of QDs can be tuned by their structure and composition. **Figure 1.3** displays the photoluminescence (PL) spectra of QDs with diverse chemical compositions, covering range of wavelengths from ultraviolet (UV)-

visible to near-infrared (NIR) region ¹³. This unique quantum confinement effect of QDs allows for the design and synthesis of QDs with well-controlled size/shape/composition to achieve fine-control of the optoelectronic properties ^{1, 13, 14}. In the last few decades, a variety of high-quality colloidal QDs with broad light absorption, size-dependent PL emission, high PL quantum yield (PLQY), and decent chemical-/photo-stability have been realized via using various types of synthetic techniques ¹⁵⁻¹⁷. Due to these excellent optoelectronic properties, QDs have been widely employed as building blocks in solar technologies including light-emitting diodes (LEDs), luminescent solar concentrators (LSCs), QDs-sensitized solar cells (QDSCs), as well as solar-driven photoelectrochemical (PEC) hydrogen evolution etc., providing a powerful platform for the development of numerous classes of optoelectronic devices ^{7, 18-21}.

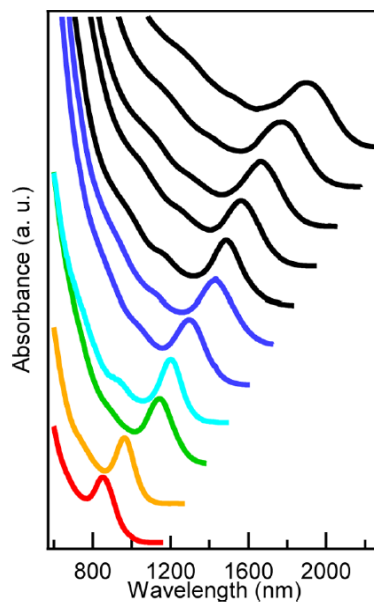


Figure 1.2 Absorption spectra of PbSe QDs with various sizes (from 2.5 to 4.8 nm) ¹¹.

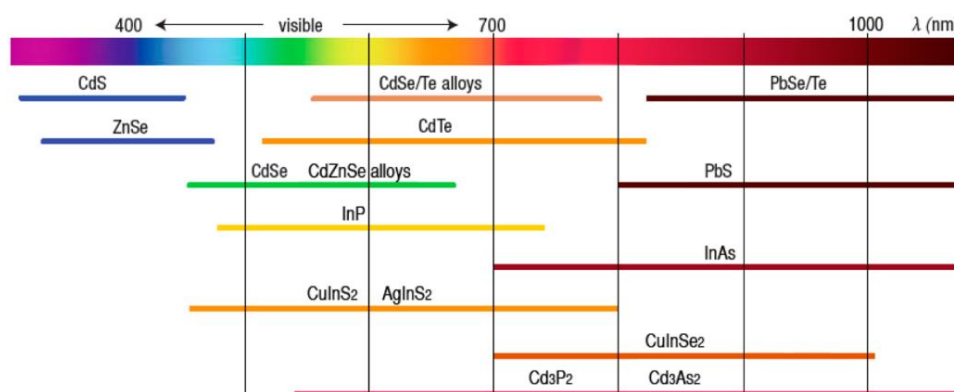


Figure 1.3 PL spectra of QDs with various chemical compositions ¹³.

1.2 Synthesis, toxicity and optoelectronic properties of quantum dots

1.2.1 Synthesis of bare quantum dots

To achieve high performance colloidal QDs-based optoelectronic and/or biomedical devices, a crucial aspect is to synthesize highly monodisperse QDs with uniform size distribution. In 1993, Bawendi *et al.* used a high temperature, solution-based technique to prepare CdS, CdSe and CdTe QDs with very good monodispersity, opening the investigations of Cd-based QDs and their various applications²². Monodispersity is significant for understanding the fundamental optoelectronic properties of QDs as it allows for the exhibition of uniform optical and electrical properties²³⁻²⁸. Therefore, it is very important to study the synthesis and growth mechanism of QDs to achieve highly monodispersed QDs with narrow size distribution.

Cost-effective and high-quality thermal decomposition methods are commonly used to synthesize colloidal QDs with controllable size and shape^{23, 29-31}. In these methods, the hot-injection or heat-up technique can be utilized to separate the nucleation and growth stages of QDs. As shown in **Figure 1.4a**, the hot-injection method refers to the approach which rapidly injects the precursors into a high-temperature flask with reaction solvents. The temperature to inject the precursor is a key factor that determines the decomposition of precursors. Once the precursors are injected, the supersaturation of the precursors leads to the nucleation of QDs. Due to that the precursors are injected at low temperature, the overall temperature of the reaction is lowered and the nucleation stage is terminated. With the consumption of the precursor monomers in the nucleation process, the decreased supersaturation then induces the subsequent growth of QDs^{26, 32}. While in the heat-up method (**Figure 1.4b**), these two stages are realized by steadily heating the mixture of the precursors and the organic solvents. With continuous supply of external thermal energy, the precursors can reach the necessary supersaturation and initiate uniform nucleation and growth of QDs³³.

The purification process after the synthesis of the QDs is also a very critical step which enables the elimination of unreacted precursors and excess ligands. These long organic ligands can limit the charge transport of the QDs, thereby lowering the performance of QDs-based optoelectronic devices (e.g. QDSCs)^{4, 34}. A typical purification process is based on the centrifugation

technique of colloidal QDs dispersed in organic solvent. In this purification process, by adding excess polar nonsolvent (e.g. methanol, ethanol, etc.) and using the centrifugation technique, the QDs are precipitated at the bottom of the centrifuge tube and leave the unreacted precursors and ligands in the supernatant. The purification process of QDs is completed by re-dissolving the QDs in organic solvent such as toluene.

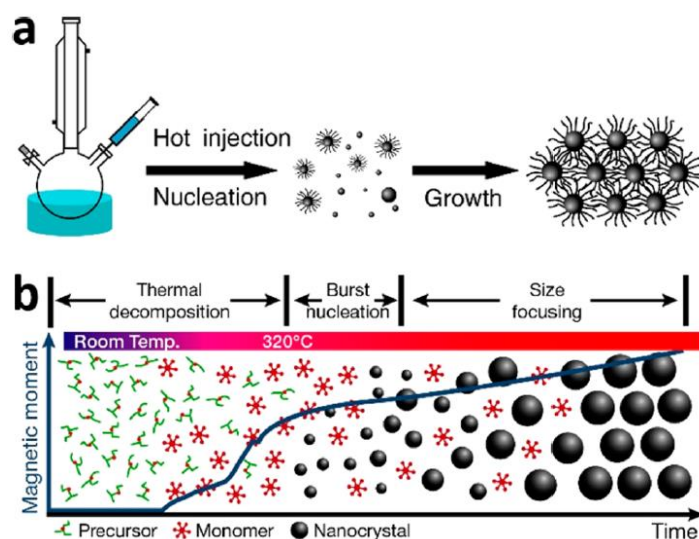


Figure 1.4 Schematic diagrams of (a) hot-injection and (b) heat-up techniques ^{27, 33}.

1.2.2 Synthesis of core/shell quantum dots

With merely capping of organic ligands, bare QDs exhibit high surface sensitivity to their surrounding chemical environment. This surface sensitivity typically induces surface-related defects/trap states, which serve as nonradiative recombination centers of photoexcited charge carriers to reduce the QD's PLQY and long-term stability ³⁵⁻³⁷. The formation of core/shell structure has demonstrated an efficient approach to passivate the surface of QDs. In these core/shell systems, the formed robust inorganic shell leads to the effective protection of the core QDs that results in suppressed surface defects/traps, enhanced PLQY and stability ^{16, 38}. In addition, by appropriately choosing the core and shell materials, it is feasible to modulate the band structure of the core/shell QDs and optimize the separation and transfer of photoexcited charge carriers (electron-hole), which is promising for various photovoltaic applications such as QDSCs and QDs-based PEC cells ^{19, 39-41}.

According to the relative position of CB and VB edges of core and shell materials, the band

structure of core/shell QDs are generally classified as type-I, type-II and quasi-type II^{38, 42, 43}. As shown in **Figure 1.5**, type I core/shell QDs exhibit a band alignment that both band edges of the core material are within that of the shell materials, confining both electrons and holes into the core for improved PLQY and chemical-/photo-stability^{4, 38, 44}. Type-II core/shell QDs possess a staggered CB and VB edge of core and shell materials, giving rise to an efficient spatial charge separation (electrons and holes)^{40, 45, 46}. Quasi-type II core/shell QDs have either small CB and VB offsets, in which one type of the charge carriers are delocalized into shell region while the other type of charge carrier is still confined in the core region^{47, 48}.

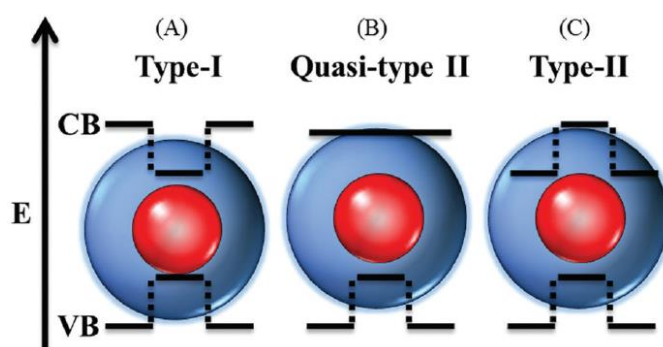


Figure 1.5 Various band alignment of core/shell QDs⁴³.

Core-shell QDs are mostly synthesized via two-step synthetic approaches including a cation exchange method and/or a successive ion layer adsorption reaction (SILAR) technique^{16, 38}. For SILAR technique, the core QDs are first synthesized and then the cationic and anionic precursors are sequentially injected into the pre-synthesized core QDs. The quantity of anion and cation precursors for each monolayer of shell materials can be calculated according to the volume increment of each monolayer shell in core/shell QDs. The reaction temperature of shelling is normally lower than that employed for the core QD synthesis, which effectively prevent the nucleation of the shell material and ripening of the core QDs^{13, 16, 31, 38}. For instance, SILAR method was employed to synthesize CdSe/CdS core/shell QDs, the CdSe core QDs were first prepared through a hot-injection technique and dispersed in 1-octadecene (ODE) and oleylamine (OLA). This reaction mixture containing CdSe cores was subsequently heated to 240 °C in inert gas and then the Cd/S (1:1) precursors were injected into the mixture to grow the CdS shell⁴⁹. Moreover, core-shell QDs including CdSe/ZnS, PbSe/PbS and InP/ZnS QDs have been similarly synthesized as well^{42, 50-52}.

Lower temperature (less than 150 °C) can be used to grow the shell materials by cation exchange technique as compared to the high-temperature shelling through SILAR method. In the shell formation process of cation exchange method, the cationic precursor of the shell material is introduced and the shell growth was achieved with the gradual substitution of cations of core materials through newly incorporated cationic precursors. In particular, the overall sizes of QDs have no significant variation. The core size and structure of the QDs can be controlled via changing the reaction parameters including starting core sizes, the molar ratio of QD/precursors, reaction time and temperature ^{16, 38}. Cation exchange has been generally used to coat a wider-band gap shell material onto lead chalcogenide core QDs to form, for example, the PbS/CdS, PbSe/CdSe and PbTe/CdTe core/shell QDs ^{34, 42, 53}. In addition, CuInS₂/ZnS and CISeS/Zn(Cd)S core/shell QDs can be also synthesized by a cation exchange technique ^{54, 55}.

Moreover, room-temperature colloidal atomic layer deposition (c-ALD) has been recently proposed to synthesize PbS/CdS core/shell QDs ⁵⁶. The c-ALD technique is able to achieve accurate control (one CdS monolayer) of the shell thickness and prepare PbS/CdS core-shell QDs with considerable optoelectronic properties ⁵⁶.

1.2.3 “Giant” core/shell quantum dots

A special case in diverse kinds of core/shell QDs is “giant” core/shell QDs (g-QDs), which possess a very thick shell (typically, from 1.5 nm up to tens of nm) and a core with quantum confinement behavior ⁵⁷. The g-QDs exhibit outstanding chemical- and photo-stability with respect to bare and core/thin shell QDs. This is attributed to the thick shell that efficiently insulates the core QDs from their surface chemistry and ambient chemical circumstance ^{49, 58, 59}. In g-QDs systems, by appropriately tailoring the electronic band structures and chemical compositions, the electrons can be delocalized into the shell region, leaving the confined holes within the core region. The efficient delocalization of electrons into the shell region results in a significantly prolonged lifetime of excitons and the formation of a quasi or full-type II band alignment in g-QDs, which are favorable for the photovoltaic applications requiring efficient separation/transfer of photogenerated charge carriers and reduced charge recombination ^{57, 60}.

For instance, as shown in **Figure 1.6a**, with increasing shell thickness of CdS in the CdSe/CdS g-

QDs, electrons are delocalized into the shell region and holes are still confined within the core, forming a quasi-type II band structure ⁶⁰. **Figure 1.6b** and **c** exhibit the electron-hole wave functions in PbSe/CdSe g-QDs with various sizes of PbSe core and thickness of the CdSe shell, indicating the tunable “quasi-type II” and “Type I” band structure ⁶¹.

The g-QDs were generally synthesized via the SILAR and/or cation exchange techniques ^{57, 62, 63}. For example, Chen *et al.* synthesized CdSe/CdS g-QDs by using SILAR method: CdSe core QDs with specified size were first prepared and then used for CdS shell growth, in which the elemental S dissolved in ODE and Cd-oleate in ODE were used as precursors. The CdS shell was grown monolayer-by-monolayer via sequentially adding monolayer equivalents of cation (Cd) and anion (S) precursors to CdSe core QDs. The amount of S and Cd precursors for each monolayer of CdS shell was determined according to the volume increment of each CdS monolayer shell in CdSe/CdS g-QDs.

It was found that the thick CdS shell could isolate the wavefunction of core QDs from g-QDs surface, leading to enhanced photo-stability and suppressed PL blinking ⁴⁹. Notably, in CdSe/CdS g-QDs, the CdSe and CdS normally form a Type I band alignment (**Figure 1.6a**). However, compared to the large band offset of VB and heavy effective mass of holes between CdSe and CdS, with increasing CdS shell thickness, the smaller band offset of CB and the lighter effective mass of electrons could still result in the electron delocalization into the shell region to form the quasi-type II band structure in CdSe/CdS g-QDs ^{60, 61}.

The optical properties of ensemble and individual CdSe/(CdSeS)/CdS g-QDs were investigated by Klimov’s group and these g-QDs with alloyed shell were found to possess very long biexciton lifetimes, showing efficient suppression of nonradiative Auger recombination. This suppression is attributed to spatial separation of electron-hole wave functions for reduced electron-hole overlap and/or the interfacial potential smoothing originated from the gradient alloyed layer at the core/shell interface in CdSe/CdS g-QDs ⁶⁴.

The g-QDs have large Stokes shift (defined as the difference between peaks of absorption and emission spectra), in which the overlap of QDs’ absorption spectra and PL spectra is very small. For example, in CdSe/CdS g-QDs, the light absorption is dominated by the thick CdS shell, while the PL emission is originated from the CdSe core, which result in large Stokes shift with negligible

re-absorption for application of large-scale, high efficiency and stable LSCs^{65,66}.

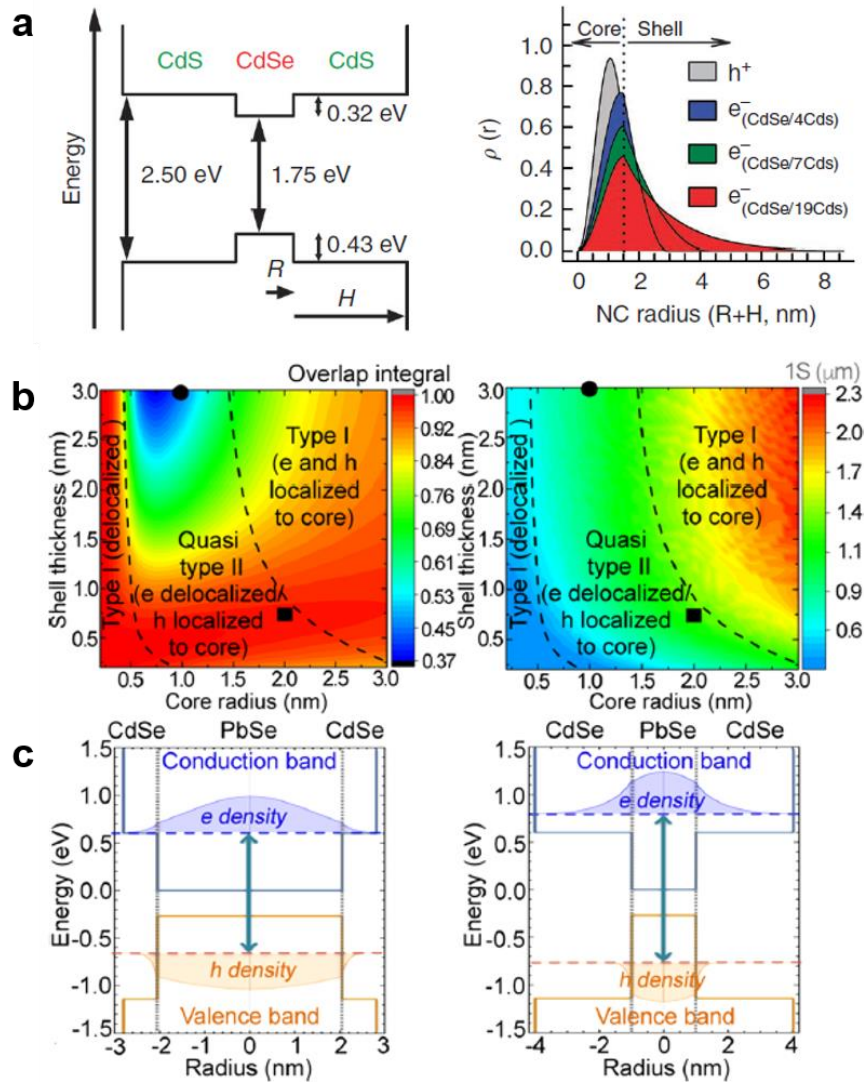


Figure 1.6 Theoretical calculation of electron-hole wave functions in CdSe/CdS g-QDs and PbSe/CdSe g-QDs. (a) Band alignment of CdSe and CdS in bulk (left). Spatial probability distribution, $\rho(r)$, of the hole and electron. Here the $\rho(r)$ is proportional to the $r^2|\psi_{e,h}|^2$, wherein the $|\psi_{e,h}|$ are the electron and the hole wave functions. (b) Electron-hole overlap integral and optical bandgap energy of PbSe/CdSe g-QDs. (c) Band alignment of PbSe/CdSe QDs representing two core/shell structure with different core and shell sizes, which all exhibit a quasi-type II band structure^{60,61}.

The g-QDs have shown excellent photo-and chemical-stability as compared to core and core/thin-shell QDs. Their tunable optoelectronic properties result in large Stokes-shift, efficient light absorption and charge separation/transfer, which are favorable for solar techniques such as LSCs, QDSCs and solar-driven PEC hydrogen generation^{63, 66-68}.

Although numerous g-QDs are developed, the current hurdles in this field are:

i). Most of the g-QDs contain highly toxic heavy metals of Cd and Pb. For example, the widely synthesized and studied CdSe/CdS, PbS/CdS, CdSe/ZnSe and InP/CdS g-QDs all suffer from the heavy metal issues that are harmful to environmental and human health (See section 1.3 for more details), further hindering their future commercialized applications.

ii) The light absorption of g-QDs is mainly limited in the UV-visible region. With relatively large volume of thick shell (in comparison to the core) in g-QDs, the absorption spectrum of g-QDs is almost determined by the shell materials. However, the available shell materials in g-QDs including CdS, ZnS and ZnSe all possess relatively large bandgap (normally larger than 2.5 eV), leading to the dominant UV-visible light absorption of g-QDs, which is not favorable for most of the solar technologies requiring the broad light absorption extended to NIR region for maximum incident photons and photogenerated charge carriers.

iii) The lack of NIR-emitted g-QDs. Most of the g-QDs synthesized to date exhibit optical emission less than the NIR wavelength range (typically, 700 nm), which restrict the NIR applications of the g-QDs including NIR LEDs and deep-issue bioimaging etc.

iv) Most of the g-QDs show a typical spherical shape which indeed can exhibit efficient electron/hole separation in the case of quasi-type II band structure, but still shows considerable wave functions overlap for fast exciton recombination. The non-spherical shape of g-QDs could lead to smaller electron-hole wave function overlap and is beneficial to the improved charge separation/transfer of g-QDs in photovoltaic applications (e.g. QDSCs and QD-based PEC cells).

In this perspective, future developments should focus on the synthesis of environment-friendly, NIR g-QDs with non-spherical morphologies (such as pyramids) and investigation of their optical properties and electron-hole dynamic for applications in various optoelectronic and biomedical devices.

1.3 Toxicity of heavy metal-based quantum dots

Although various core and core/shell QDs have been developed and shown outstanding and tunable optoelectronic properties that are favorable for their practical applications, it is noted that most of these QDs contain the heavy metals of Cadmium and Lead. In this case, one of the most crucial aspects should be considered for real-life usage of these heavy metals-based QDs: Toxicity

⁶⁹. The toxicity of heavy metals has been demonstrated to be a main threat to the environment and cause serious human health problems. While these metals have no biological role, their toxicity still does harm to the human body as well as its characteristic functioning. They may disturb the metabolic processes by playing the role as a pseudo element in the human body and exhibit a chronic feature that are accumulated in the food chain ⁷⁰.

The toxicity of these heavy metals is determined by several factors such as the dosage of elements and route of exposure, and the biological status (e.g. age and genetics etc.) of exposed individuals. Specifically, Cadmium, Lead, Mercury and Arsenic possess high degree of toxicity and rank among the metals that are significant to the public health ⁷¹. Such toxicity can result in numerous disorders and other excessive damages and these above-mentioned heavy metals are classified as certain or possible human carcinogens, as certified by the US Environmental Protection Agency and the International Agency for Research on Cancer ⁷². Here, we will briefly introduce the commonly used heavy metals in the synthesis of colloidal QDs: Cadmium and Lead.

Cadmium is one of the most toxic heavy metals that are deteriorated to the environment and our health. It is widely employed in lots of industrial activities, for instance, the production of pigments ⁷³. However, with increasing usage of cadmium in batteries, their commercialization is blocked in developed countries due to considerable environmental concerns. Once this metal is absorbed, it can get accumulated in our body during the whole life, as a result, Cd has been classified as human carcinogens ⁷⁴. It is proposed by the US National Toxicology Program that there is enough evidence to define cadmium as a human carcinogen, on account of the reproducible findings of the lung cancer associated with cadmium exposure ⁷⁵. In addition, the environmental cadmium exposure has demonstrated the cancers related to the liver and stomach etc. ⁷⁶

Lead is another highly toxic and widely-used metal which has resulted in extensive and world-wide environmental/health issues ⁷⁷. Lead exposure comes from various aspects including industrial activities, mining and vehicle exhausts etc., it can be absorbed by plants with fixation to soil and water systems. Therefore, the contamination of food or drinking water could result in the human exposure of lead ⁷⁸. Lead could interfere the physiological processes of plants without any biological functions, such as causing highly instability of ion uptake by plants for further metabolic changes. Human exposure to lead is still a very serious health concern as it can influences various

organs in the body such as the kidneys and liver, as well as the human body systems including central nervous and reproductive system ^{79,80}. It is indicated by various experimental studies that lead is a probable human carcinogen as it could induce renal tumors in animals and gene diseases/chromatid exchanges in living cells ^{81,82}.

Overall, the highly toxicity of heavy metals (i.e. Cd and Pb) remains challenging for the real-life applications of QDs. It is significant to develop more QDs without highly toxic heavy metals so as to alleviate their environmental and human health concerns and facilitate the practical applications of QDs-based optoelectronic and biomedical devices.

1.4 Near-infrared, heavy metal-free core/shell quantum dots

Over the past few decades, the investigations of colloidal QDs are mainly focused on the improvement of their optical properties such as the PLQY and stability ^{4,6,13,38}. For example, the synthesis of II-VI group Cd-based QDs (CdS, CdSe, CdTe, etc.) with high PLQY and their various high performance QDs-based optoelectronic devices have been reported ^{22,83}. These Cd-based QDs mainly possess absorption and PL spectra in the visible range, since the band gap of these materials lies between 1.7 eV and 3.5 eV ⁸⁴. In addition, there are some other QDs such as InP, PbSe, PbS, Ag₂S, Ag₂Se, CuInS₂ and CuInSe₂ QDs showing PL emission in the NIR region over ~700 nm. As compared with the visible QDs, these NIR QDs exhibit following advantages: (1) Despite the NIR PL emission, these QDs show potential absorption of NIR photons (more than 40% of the solar spectrum), which is favorable to improve the efficiency of photovoltaic devices (e.g. solar cells); (2) The NIR emission of QDs can be tuned to the wavelength range (~1500 to 1600 nm) for optical communication; (3) These NIR QDs with NIR emission over 700 nm show potential biomedical applications such as biomedical imaging; (4) With high PLQY, these NIR QDs can be used for NIR LEDs ⁸⁵⁻⁸⁹;

Holding these advantages, NIR QDs have been widely applied to achieve high performance optoelectronic devices including QDSCs, photodetectors, LEDs and PEC cells etc. ^{19,39,90}. However, there are still several limitations in these NIR QDs. For example, as illustrated in section 1.3, NIR QDs such as PbSe, PbS and PbTe have highly toxic heavy metal of Pb, which may cause very serious environmental pollution and is harmful to human health. These heavy

metals in QDs further hinder the future commercialization of QDs in optoelectronic devices. Therefore, it is significant to investigate the synthesis of environmentally friendly NIR QDs and their applications in optoelectronic and biomedical devices.

In the last few years, eco-friendly NIR QDs such as AgInS₂, CuInS₂, CuInSe₂, and CuInSe_xS_{2-x} QDs have drawn considerable attention and are extensively investigated for optoelectronic and biomedical devices^{13, 91}. Nevertheless, these NIR, “green” QDs are very sensitive to the ambient environment due to their multicomponent nature, which are prone to induce the surface defects/traps states that act as non-radiative recombination centers for reduced PLQY and chemical/photo-stability⁹²⁻⁹⁴. In this perspective, building a core/shell architecture is an effective approach to improve the optoelectronic properties and stability of these QDs.

For instance, Li *et al.* have synthesized NIR, environmentally friendly CuInS₂/ZnS core/shell QDs for fabrication of QD-LED. Since the ZnS shell efficiently suppress the surface defects/traps of CuInS₂ QDs, the CuInS₂/ZnS core/shell QDs exhibit a PLQY as high as 60%. As-fabricated QD-LED exhibits a maximum external quantum efficiency of 3.36% at 2.8V and highest luminance of 113.83 cd/m² at 7.6V⁹⁵. Meinardi and co-workers synthesized NIR, heavy metal-free CuInSe_xS_{2-x} (CISeS)/ZnS core/shell QDs and used them to fabricate LSCs. The optical properties of such core/shell QDs exhibit large Stoke shift for reduced re-absorption. The stability of this type of NIR environment-friendly core/shell QDs is improved by the growth of the ZnS shell. The optical properties of the QDs are well maintained in the subsequent device fabrication processes. The resulting QDs-based LSCs showed an optical efficiency of 3.27%²¹.

NIR, eco-friendly core/shell QDs show optical absorption in the NIR region that matches the solar spectrum well, which is favorable for QDs-based photovoltaic devices. Therefore, these QDs have also been employed to achieve high performance QDSCs. For example, Pan *et al.* prepared NIR CuInS₂/ZnS core/shell QDs and used them to fabricate QDSCs⁹⁶. As shown in the left figure of **Figure 1.7**, the growth of a ZnS layer on the surface of CuInS₂ QDs leads to the suppression of their surface defect/trap states and formation of a Type-I band structure, thus enhancing the PLQY and stability of QDs. The core/shell QDs/TiO₂ heterostructure can largely reduce the carrier recombination at the interface of the electrolyte due to the presence of the

ZnS shell, thereby improving the power conversion efficiency (PCE) of the QDSCs. **Figure 1.7** (right figure) displays the current-voltage ($J-V$) curve of as-fabricated NIR, heavy metal-free QDSCs, showing a maximum PCE up to 7.04% ⁹⁶.

McDaniel *et al.* also employed NIR, environmentally friendly CISes/ZnS core/shell QDs for fabrication of QDSCs. Similarly, the ZnS shell can largely reduce the surface defects/traps on CISes core QDs for suppressed non-radiative recombination, thereby improving the PCE of QDSCs. These QDSCs using NIR and heavy metal-free core/shell QDs are very stable even after exposure in the air for several months, indicating that the core/shell QDs are capable to enhance the stability of QDs-based optoelectronic devices ⁹⁷. These results demonstrate that NIR environment-friendly core/shell QDs are promising building blocks in optoelectronic devices.

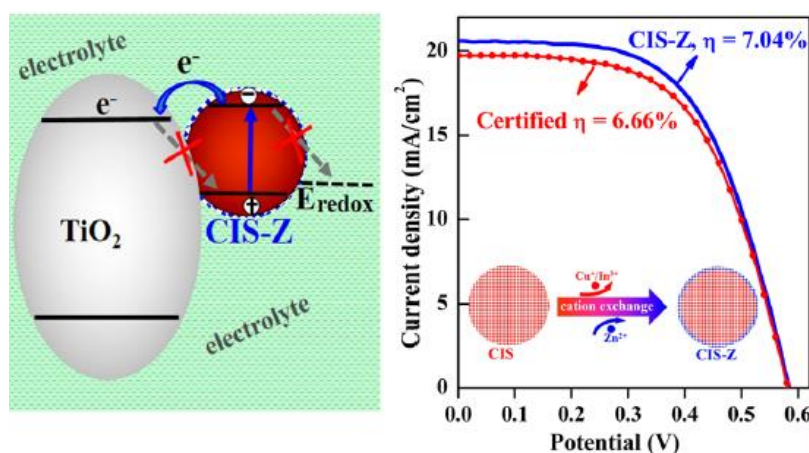


Figure 1.7 Working principle of NIR, heavy metal-free CuInS₂/ZnS core/shell QDs based-QDSCs (left) and their $J-V$ curves (right) ⁹⁶.

1.5 Quantum dots-based photoelectrochemical cells for solar-driven hydrogen generation

The efficient conversion of solar energy to sustainable and clean fuels is an attractive technique to address future global energy needs. Solar-driven PEC cell is a solar-to-fuel conversion system that can harvest the solar energy to split water and produce hydrogen energy, which represents a major opportunity to resolve the energy crisis ⁹⁸. A typical three-electrode PEC cell are composed of a semiconductor working electrode, a counter electrode, a reference electrode and the electrolyte ⁹⁹. The water splitting processes in PEC cells are generally divided into three steps: (1) The semiconductor working electrode (photoanode) absorbs solar energy and generates electron-hole

pairs at the interface of semiconductor/electrolyte; (2) Effective separation and transport of photogenerated electron-hole pairs: electrons migrate from the photoanode to the counter electrode, while the holes are generally consumed by the sacrificial agent (e.g. $\text{Na}_2\text{S}/\text{Na}_2\text{SO}_3$) in the electrolyte. (3) The electrons on counter electrode reduce water to generate hydrogen ^{98,99}.

In order to achieve efficient solar-driven hydrogen generation, the semiconductor working electrode used in the PEC cell should have the following properties: (1) The band gap of semiconductor materials is suitable to provide required solar energy for water splitting; (2) The band alignment of semiconductor material and the water redox energy level is appropriate to facilitate the separation and transport of photogenerated charge carriers; (3) The lifetime and mobility of photogenerated carriers are supposed to be large enough to suppress the charge recombination; (4) The electrical resistance of the semiconductor materials should be low enough for efficient transport of carriers in the system ¹⁰⁰⁻¹⁰²; In addition, in order to achieve a robust PEC system, the semiconductor material used as photoanode should be stable under light illumination. However, to date, there is no semiconductor photoelectrode that satisfy all the above-mentioned properties in all investigations of PEC cells. Currently, most of the research groups are focused on developing various approaches to optimize the optoelectronic properties of the semiconductor materials, thus improving the performance of PEC cells ^{103, 104}.

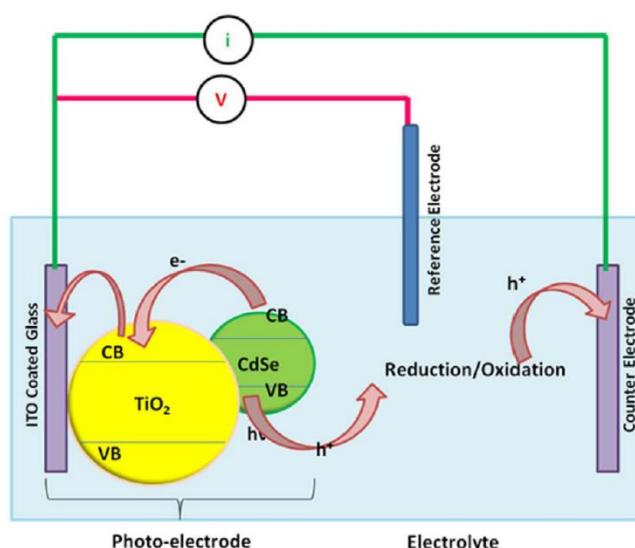


Figure 1.8 Schematic diagram of QDs-based PEC cell for hydrogen generation ¹⁰⁵.

In the last few years, using colloidal QDs to sensitize the semiconductor materials has been

demonstrated as an efficient method to boost the performance of PEC cells^{105, 106}. Specifically, Cd-based (e.g. CdS, CdSe, CdTe etc.) QDs have been used to sensitize wide-bandgap semiconductors (TiO₂, ZnO, etc.) with various morphologies (e.g. nanotubes, nanowires, etc.) for improved PEC performance^{19, 67, 107, 108}. This enhancement is attributed to special properties of QDs such as size-dependent tunable band gaps, large optical absorption coefficient, large intrinsic dipole moment for effective separation of photoexcited charge carriers and multiple exciton generation effect for large number of photogenerated carriers^{109, 110}. Therefore, the QDs-modified semiconductor materials are able to facilitate the separation, transport and generation of charge carriers, thus enhancing the performance of PEC cell.

To further understand the basic principle of QDs-based PEC cells, **Figure 1.8** shows the schematic diagram of a PEC cell using a CdSe QDs-sensitized TiO₂ photoelectrode as a working electrode. Upon exposure to light illumination, the CdSe QDs absorb UV-visible light and generate electron-hole pairs, which are separated at the interface of QDs/TiO₂. Due to a suitable band alignment of CdSe QDs and TiO₂, the photogenerated electrons from the CdSe QDs spontaneously transfer to the CB of the TiO₂, which are subsequently collected by the conductive substrate and migrate to the counter electrode to reduce water and produce hydrogen. Meanwhile, the photogenerated holes are consumed by the sacrificial agent in the electrolyte¹⁰⁵. It can be seen that the band alignment of QDs/semiconductor and the water redox energy level is crucial for the performance of the QDs-based PEC cells.

CdS, CdSe and CdTe QDs have been used to sensitize the metal oxide semiconductor working electrode in PEC cells to enhance the solar-to-hydrogen conversion efficiency. For example, Fan's group used the CdS QDs to modify the TiO₂ photoelectrode and obtained a photocurrent density of 4.84 mA/cm² under simulated solar irradiation¹¹¹. Sun et al. also fabricated a TiO₂ nanotube-array photoelectrode sensitized by CdS QDs, showing a significantly increased photocurrent from 0.22 to 7.82 mA/cm²¹¹². Xie et al. designed a TiO₂ nanorod arrays/CdS QDs/ALD-TiO₂ structure, in which the CdS QDs largely enhance the visible light absorption and leads to an improved solar energy conversion efficiency¹¹³. Similarly, the CdSe and CdTe QDs-sensitized photoelectrodes are fabricated, showing saturated photocurrent density of ~3 mA/cm² and ~6 mA/cm² under illumination (AM 1.5G, 100 mW/cm²), respectively^{114, 115}. Moreover, the CdS and CdSe QDs are

both employed to co-sensitize the ZnO nanowire arrays and as-sensitized photoelectrode showed nearly entire visible absorption (up to 650 nm) with a high incident photon to current efficiency (IPCE) of ~45%. This structure acted as a tandem cell and a photocurrent density as high as ~12 mA/cm² is achieved at 0.4 V (Ag/AgCl) ¹⁰¹. These studies indicate that Cd-based QDs with outstanding visible absorption are promising building blocks for high efficiency solar-driven PEC hydrogen generation.

Despite the widely used QDs with visible absorption, the development of QDs with NIR absorption, such as PbS(Se), AgInS(Se), CuInS(Se) etc., is promising to maximum the light absorption of QDs and may leads to further improved performance of QDs-based PEC cells. For instance, a PbS/TiO₂ photoanode-based PEC cell is achieved to exhibit a hydrogen generation rate of 5.2 mL·h⁻¹ with overall conversion efficiency of 1.15 %, indicating that the NIR PbS QDs are promising for solar-to-hydrogen conversion ¹¹⁶. PbS QDs/CdS/TiO₂ heterostructure has been fabricated and shows a photocurrent density of ~6 mA/cm² with hydrogen generation rate of 60 mL·cm⁻²·day, wherein the IPCE spectra confirmed the infrared contribution from the NIR PbS QDs ¹¹⁷.

More importantly, the heavy metal-free NIR QDs are favorable photosensitizers in PEC cells in view of environmental and human health concerns and their future commercialization. Yu's group developed the Cu-based ternary chalcogenides QDs including CuInS₂, CuInSe₂ and CuInSeS alloyed QDs and used them to fabricate PEC cells, showing photocurrent density of 0.29 mA/cm², 0.21 mA/cm² and 0.19 mA/cm², respectively. It is found the Se decomposition in the QDs leads to the drop of photocurrent ¹¹⁸. Li et al. synthesized CuInS₂ QDs with different sizes as photosensitizers to prepare the QDs/TiO₂ photoelectrode, the maximum photocurrent of ~2 mA/cm² is obtained in these QDs-based PEC cells ¹¹⁹. CuInSe₂ QDs with hollow structures were also employed to fabricate the PEC cell for hydrogen production, while the attained photocurrent is as low as ~1 mA/cm² ¹²⁰. It can be concluded that the heavy metal-free NIR QDs (typically, I-III-VI₂ QDs) do not perform very well in the QDs-based PEC systems, which is mainly attributed to their multicomponent feature for easily induced surface defects/traps, leading to non-radiative recombination which lower the charge separation/transfer in PEC cells ⁸⁷.

Using core/shell structured QDs is an efficient approach to suppress the surface defects/traps of QDs and enhance their photostability, thus achieving efficient and stable QDs-based PEC system

for hydrogen production. By appropriately tuning the core/shell structure of QDs, it is possible to facilitate the separation and transport of photogenerated carriers in the QDs. For example, the “quasi-type II” band alignment is conducive to efficient transfer/separation of photogenerated charge carriers, thereby improving the performance of QDs-based PEC devices.

Recently, g-QDs have also attracted significant attention for solar-driven PEC H₂ generation due to their excellent photo/chemical stability and tunable band structure as compared to bare QDs⁵⁷. For instance, CdSe/CdS g-QDs have been applied to sensitize mesoporous TiO₂ film for solar-driven PEC H₂ production, showing a saturated photocurrent density reaching up to 10 mA/cm² under standard one sun illumination. The “quasi-type II” band structure allows the efficient electron-hole separation in g-QDs, resulting in the enhanced PEC performance and device stability (thick CdS shell) with respect to the bare CdSe QDs⁶⁷. Wang et al. further optimized the CdSe/CdS g-QDs by introducing the CdSeS interfacial layer, which effectively enabled the gradient band alignment for optimized charge carriers transfer and extended absorption spectra, leading to a record photocurrent density of ~17.5 mA/cm² among all the colloidal QDs-based PEC cells¹²¹. However, these g-QDs are still composed of heavy metal (Cd), limiting the real-life usage of these high efficiency QDs-based PEC cells. The heavy metal-free, NIR g-QDs are thus desirable to develop to realize high performance “green” QDs-based PEC H₂ production.

1.6 Characterization

Here we briefly introduce various characterization techniques used for all the objectives in this thesis including the characterization of nanostructure, optical properties and device performance:

Transmission electron microscopy (TEM) images and selected area electron diffraction (SAED) patterns of QDs and TiO₂/QDs were acquired by using a JEOL 2100F TEM. The X-ray diffraction (XRD) pattern was obtained by utilizing a Panalytical X-Pert PRO MRD with Cu K α radiation. The morphology of cross-sectional FTO/TiO₂/QDs was observed by using a JSM-7401F scanning electron microscope and the chemical composition mapping was obtained by Energy-dispersive X-ray spectroscopy (EDS) analysis. Inductively coupled plasma atomic emission spectroscopy (ICP-OES) was measured via an Agilent 5100 ICP-OES system. X-ray photoelectron spectroscopy (XPS) data were obtained using a VG Escalab 220i XL equipped with a twin Al source and

subsequently analyzed by Casa XPS software.

UV–visible–NIR absorption spectra were measured by using a Cary 5000 UV–visible–NIR spectrophotometer (Varian) with a scan speed of $600 \text{ nm}\cdot\text{min}^{-1}$. PL spectra and PL lifetime of the QDs in solution were acquired via a Fluorolog-3 system (Horiba JobinYvon). The PLQY of QDs with emission peaks ranging from 800 to 1000 nm and 1100 to 1200 nm was measured via using IR 125 dye (dissolved in dimethyl sulfoxide) and IR 26 dye (dissolved in 1,2-dichloroethane) as references, respectively. Ultraviolet photoelectron spectroscopy (UPS) measurements were performed on a VG ESCALAB 3 Mark II high vacuum system.

A three-electrode system consisting of an Ag/AgCl reference electrode (saturated with KCl), a Pt counter electrode, and an as-fabricated working electrode was used to evaluate the PEC performance of the QD-sensitized photoanode. Subsequently, the photoanode was fully dipped into the electrolyte containing 0.25 m Na₂S and 0.35 m Na₂SO₃ (pH = 12.5), which served as sacrificial hole scavenger to prevent QD photocorrosion. Electrochemical measurements were acquired using a CHI-760D electrochemical workstation (with sweep rate of $20 \text{ mV}\cdot\text{s}^{-1}$) and the following formula $V_{\text{RHE}} = V_{\text{Ag/AgCl}} + 0.1976 + \text{pH} \times (0.059)$ was used to convert the measured potentials (vs Ag/AgCl) to the potentials with respect to the reversible hydrogen electrode (RHE). Photocurrent density–voltage (J – V) curves were measured under simulated sunlight (1 Sun = AM 1.5G, $100 \text{ mW}\cdot\text{cm}^{-2}$) using a (Sciencetech SLB-300A) Compact Solar Simulator Class AAA. To verify the standard 1 Sun illumination ($100 \text{ mW}\cdot\text{cm}^{-2}$) on the as-fabricated photoanode (working electrode) in the three-electrode system, a Si reference diode (Sciencetech) was used to adjust the distance between photoanode and solar simulator before each measurement. The distance from sun simulator to PEC cell was 30 cm.

The IPCE was derived from current–voltage measurements using different band-pass optical filters¹⁹. H₂ evolution was measured during the PEC experiment. The produced H₂ gas was detected using a gas chromatography (GC) device equipped with a thermal conductivity detector. Argon was used as the carrier gas for GC analysis. An airtight syringe was used for sampling from the vacuum sealed chamber⁶⁷.

1.7 Thesis objectives and organization

1.7.1 Research objectives

This thesis consists of three parts with three relevant objectives:

Part I: Heavy metal-free, NIR colloidal QDs for PEC hydrogen production

NIR QDs such as PbS, PbSe and their core/shell structures have become attractive nanomaterials for optoelectronic devices mainly due to their NIR light absorption. However, most of the NIR QDs contain toxic elements such as Pb and Cd. Although these NIR QDs-based optoelectronic devices have shown excellent performance, the toxic elements in processes of QD's synthesis and device fabrication are harmful to human health and the environment, thus hindering the future commercialization and practical application of QDs-based optoelectronic devices. I-III-VI₂ QDs such as CuInS₂, CuInSe₂ and CISES etc. are emerging as promising alternatives to heavy metals-based QDs due to their less toxicity, size-tunable PL emission and broad NIR light absorption etc. However, the easily induced surface defects/traps could lead to non-radiative recombination to lower the efficiency of photovoltaic devices. The growth of core/shell QDs can effectively passivate the QDs' surface for optimized optical properties and enhanced stability.

Therefore, the objectives for part I are:

1. Investigating the synthesis, morphologies and optical properties of NIR, heavy-metal-free CISES/ZnS core/shell QDs.
2. Studying the morphology, elements distribution and band alignment of NIR, eco-friendly CISES/ZnS core/shell QDs-based photoanode.
3. Comparing the PEC performance and stability of bare CISES and CISES/ZnS core/shell QDs-based PEC devices and analyzing the function of ZnS shell on CISES QDs.

Part II: Synthesis and application of NIR, environment-friendly g-QDs

In recent years, g-QDs have been widely studied and shown outstanding optoelectronic properties and stability, which are ideal candidates for nanodevices. The optical properties (e.g. Stokes-shift) and band structure of g-QDs are feasible to tune and meet the requirement of

various optoelectronic devices such as LSCs, LEDs, QDSCs and PEC cells. However, most of the current g-QDs contain heavy metals such as Cd that are harmful to human's health and natural environment. The highly toxic feature of these g-QDs is not favorable for their future commercialization and real-life applications. In addition, the majority of g-QDs possess visible optical absorption and PL emission, hampering their optoelectronic and biomedical applications in the NIR region.

Therefore, the objectives for Part II are:

1. Synthesizing NIR, heavy-metal-free $\text{CuInSe}_2/\text{CuInS}_2$ (CISe/CIS) g-QDs with various shell thickness and studying their morphology and crystal structure.
2. Investigating the optical properties of as-synthesized NIR, heavy metal-free CISe/CIS g-QDs including absorption and PL spectra, as well as PL lifetime.
3. Choosing appropriate physical parameters and theoretical models to calculate the electron-hole wave functions in these NIR, eco-friendly CISe/CIS g-QDs.
4. Measuring the PEC performance and stability of these g-QDs-based PEC cells and probing the influence of shell thickness on device performance.

Part III: Optoelectronic properties in NIR-emitting g-QDs with pyramidal shape

Heterostructured non-spherical QDs have been demonstrated to exhibit excellent optoelectronic properties such as ultralong lifetime, which is favorable for photovoltaic devices. Nevertheless, these heterostructured non-spherical QDs still have several limitations including stability. The g-QDs with thick shell have presented superior photo/chemical stability and are regarded as promising building blocks for solar technologies. Since most of the g-QDs are spherical, it is interesting to synthesize non-spherical g-QDs and investigate their optoelectronic properties. In addition, as most of the g-QDs are optically active in UV-visible region, extending the optical emission of g-QDs in NIR region should be a promising research direction in this field.

Therefore, the objectives for Part III are:

1. Preparing heterostructured CISeS/CdSeS/CdS g-QDs with pyramidal shape.
2. Studying the optoelectronic properties of as-prepared pyramidal-shaped g-QDs.
3. Using suitable theoretical models to simulate the spatial electron-hole wave functions in such

pyramidal-shaped g-QDs.

4. Fabricating and measuring the pyramidal-shaped g-QDs-based PEC cells and QDSCs.

1.7.2 Thesis organization

This thesis consists of six chapters which are organized as follows:

Chapter 1 briefly introduces the background and basic concepts of colloidal semiconductor QDs, core/shell QDs and QDs-based PEC cells, as well as the motivation and research objectives of this thesis.

Chapter 2 presents the synthesis and characterization of heavy metal-free, NIR colloidal core/shell QDs for high-efficiency and stable PEC hydrogen generation. The relevant publication is:

Xin Tong, Yufeng Zhou, Lei Jin, Kaustubh Basu, Rajesh Adhikari, Gurpreet Singh Selopal, Xin Tong, Haiguang Zhao, Shuhui Sun, Alberto Vomiero, Zhiming M. Wang, and Federico Rosei. *Nano Energy*, 2017, 31, 441-449.

Chapter 3 presents the synthesis and characterization of a new type of NIR, eco-friendly g-QDs with tunable NIR optical properties for application in solar-driven PEC hydrogen production. The relevant publication is:

Xin Tong, Xiang-Tian Kong, Yufeng Zhou, Fabiola Navarro-Pardo, Gurpreet Singh Selopal, Shuhui Sun, Alexander O. Govorov, Haiguang Zhao, Zhiming M. Wang, and Federico Rosei. *Advanced Energy Materials*, 2018, 8, 2, 1701432.

Chapter 4 presents the synthesis, optoelectronic properties and PEC application of a NIR-emitting g-QDs with unique pyramidal shape. The relevant publication is:

Xin Tong, Xiang-Tian Kong, Chao Wang, Yufeng Zhou, Fabiola Navarro-Pardo, David Barba, Dongling Ma, Shuhui Sun, Alexander O. Govorov, Haiguang Zhao, Zhiming M. Wang, and Federico Rosei. *Advanced Science*, 2018, 5, 8, 1800656.

Chapter 5 provides a conclusion of all the research objectives in this thesis and the discussion of prospective research direction in future work.

According to the policy of INRS, an appendix providing a summary of this thesis is included after the end of the main body.

CHAPTER 2 SYNTHESIS AND CHARACTERIZATION OF HEAVY METAL-FREE, NEAR-INFRARED COLLOIDAL CORE/SHELL QUANTUM DOTS FOR EFFICIENT PHOTOELECTROCHEMICAL HYDROGEN GENERATION

In this section, the fabrication of a PEC device by using NIR, environmentally friendly colloidal CISES/ZnS (Zn-CISES) core/shell QDs is presented. The morphology and optical properties of CISES/ZnS core/shell QDs and relevant QDs-decorated photoanode are studied as well. The PEC performance of NIR, heavy metal-free QDs-based PEC system is measured under standard AM 1.5G solar irradiation (100 mW/cm^2). It was demonstrated that the CISES QDs with ZnS thin shell effectively suppress the surface defects/traps for optimized optical properties including enhanced PL intensity and elongated lifetime. The resulting optimized PEC cell based on core/shell Zn-CISES QDs exhibited largely improved saturated photocurrent density up to $\sim 5.3 \text{ mA/cm}^2$ with respect to bare CISES QDs. Moreover, the Zn-CISES QDs-based PEC device exhibits very good stability.

Most of the experimental work were completed by me and I also wrote the draft of this manuscript. Dr. Haiguang Zhao helped me for optical characterizations. Dr. Yufeng Zhou and Dr. Lei Jin gave assistance for the fabrication of the QDs-based photoanode.

2.1 Synthesis of heavy metal-free, near-infrared quantum dots and fabrication of quantum dots-based photoelectrochemical cells

QDs-based PEC cells are very promising because of their high solar energy to fuel conversion efficiency and low fabrication costs^{105, 108, 111, 122-124}. However, its commercial development is hindered by various challenges, including the widespread use of toxic heavy metal-based QDs as sensitizers^{19, 67, 101, 114, 117}. Eco-friendly QDs such as CuInS/Se QDs have been explored for energy applications due to their facile synthesis, high absorption coefficients and size/composition-dependent optoelectronic properties, presenting a promising candidate for efficient PEC cells¹²⁵⁻¹²⁹.

2.1.1 Synthesis of heavy metal-free, near-infrared CuInSe_xS_{2-x} core and core/shell quantum dots

Before the synthesis of CISES core and core/shell QDs, we first consider the suitable sizes of QDs for mesoporous film sensitization to be ~4-5 nm and we followed the synthetic parameters of CISES QDs from the literature by Hunter McDaniel *et al.* with slight modifications⁵⁴. We also consider the synthetic parameters of Zn and Cd-treatment for growth of core/shell QDs to suppress the non-radiative recombination of CISES core QDs and enhance the photovoltaic performance of QD-sensitized photoanode. As a reference, we followed the certain parameters of CISES/ZnS and CISES/CdS core/shell QDs for high performance QDSCs developed by Klimov group⁹⁷.

Synthesis of CISES core QDs⁵⁴: Typically, CuI (1 mmol) and In(Ac)₃ (1 mmol) were mixed with 5 mL of 1-dodecanethiol (DDT) and 1 mL of OLA in a 50 mL flask and degassed under vacuum at 90 °C for 30 min. The temperature was then raised to 140 °C and maintained for 15 min to fully dissolve the precursors. Meanwhile, OLA /DDT-Se solution (2 M) was prepared by mixing Se (2 mmol) powder with OLA (1.5 mL) and DDT (0.5 mL) at room temperature under N₂ flow. Subsequently, the reaction mixture was heated to 210 °C and OLA /DDT-Se solution (2 M) was injected dropwise via syringe. The temperature was maintained at 210 °C for 10 min to conduct QD nucleation, and then the flask was heated quickly to a growth temperature of 235 °C, maintained for 20 min. The reaction was then quenched with cold water. The as-synthesized QDs were precipitated with ethanol, centrifuged to eliminate unreacted precursors, and re-dispersed in toluene.

Zn-CISES and CISES/CdS (Cd-CISES) core/shell QDs were synthesized following a modified cation exchange procedure⁹⁷. Typically, for CISES QDs treated with Zn²⁺, 0.25 M Zn-oleate solution was first prepared by dissolving 3 mmol of oleic acid (OA) and 1 mmol of Zn(Ac)₂ in 4 mL of ODE. Five milliliters of the QDs re-dispersed in ODE were then added to 4 mL of 0.25 M Zn-oleate solution and the reaction mixture was heated to 50 (100 or 150 °C) and maintained for 10 min. For cation exchange with Cd²⁺, 0.25 M Cd-oleate was prepared by dissolving 3 mmol of OA and 1 mmol of CdO in 4 mL of ODE. Five milliliters of the QDs in ODE were then added to 4 mL of 0.25 M Cd-oleate solution and the reaction mixture was heated to 65 °C

for 5 min. The reaction was then quenched with cold water and the as-synthesized QDs were precipitated with ethanol, centrifuged to eliminate unreacted precursors, and re-dispersed in toluene.

2.1.2 Fabrication of quantum dots-based photoelectrochemical cells

Mesoporous TiO₂ films were first prepared with following procedures: Using ultrasonication to clean Fluorine doped tin oxide (FTO) glass substrates (Pilkington TEC 8, sheet resistance 6-9 Ω/square) for 15 min in Triton™ X-100, acetone and ethanol, respectively, followed by deionized (DI) water rinse and dried in N₂ gaseous flow. The cleaned FTO glass substrates were then treated in a UV-ozone cleaner for 10 min to further eliminate surface organic contaminations. Subsequently, a blocking layer of TiO₂ was deposited on FTO substrates by spin coating at 6000 r.p.m. for 30 s utilizing the commercial solution Ti-Nanoxide BL/SC. After the drying process was completed, the as-deposited TiO₂ films were annealed at 500 °C on a hot plate for 30 min and cooled down to room temperature. Titania paste containing ~20 nm nanoparticles in diameter (18 NR-T, paste 1) was then tape-casted on FTO substrates and kept in air for 12 min to completely spread out. The electrodes were subsequently dried at 120 °C for 6 min. A mixture of active anatase particles (~20 nm) and larger anatase scatter particles (~450 nm) paste (18 NR-AO, paste 2) was then deposited on the top of paste 1 by using identical tape-casting technique and following procedures of spreading and drying. The photoanodes were later sintered at 500 °C for 30 min in a furnace and cooled down to obtain the TiO₂ films. Electrophoretic deposition (EPD) was employed to deposit CISeS or Zn(Cd)-CISeS QDs on TiO₂ film. A blank FTO (negative electrode) and TiO₂ FTO (positive electrode) glasses were vertically immersed in QDs solution. An applied voltage of 200 V was added between these two electrodes with a distance of ~1 cm, and the deposition time varied with concentration and species of CISeS QDs, typically, 60 min, 20 min and 15 min for pure CISeS QDs, Zn-CISeS QDs (treated by ZnS with different temperatures of 50, 100 and 150 °C) and Cd-CISeS QDs, respectively. To remove the absorbed QDs on the surface of the TiO₂ film, the as-deposited TiO₂/FTO slides were rinsed with toluene at half the deposition time and in the end of the EPD procedure. Subsequently, the SILAR method was used to deposit a ZnS layer on the as-

deposited TiO₂/QDs electrode. For typical ZnS deposition, the TiO₂/QDs electrode was immersed into a 0.1 M solution of Zn(Ac)₂ for 1 min and then into 0.1 M solution of Na₂S for 1 min. During each immersion, the electrode was rinsed with corresponding solvents of methanol and methanol/DI water (1:1 V/V), respectively, and then dried in N₂ flow. After SILAR procedure, silver paste was painted on the photoanode for enhanced conductivity regarding PEC measurement, and the photoanode's surface (excluding the active area) was covered with epoxy resin to complete device fabrication.

2.1.3 Structure and optical properties of quantum dots and quantum dots-sensitized photoanodes

TEM was used to characterize sizes and morphologies of as-synthesized QDs (**Figure 2.1**). As shown in **Figure 2.1a**, with specific reaction parameters (solvent, temperature and time etc.), as-synthesized CISES QDs exhibit a triangular projected shape in TEM images, suggesting a pyramidal shape with average size of 5.64 nm (\pm 0.77 nm) (**Figure 2.2**), where the size is defined as the height of the projected triangles, consistent with the reported structure in similar reaction conditions ⁵⁴.

As Zn surface treatments are effective to passivate the bare CISES QDs to reduce surface defects ⁹⁷, we used a cation exchange approach to form a thin inorganic ZnS protecting shell on CISES QDs. In parallel, for comparison, we also synthesized CdS capped CISES QDs via a cation exchange approach. The core/shell Zn-CISES (with Zn treatment at 100 °C) and Cd-CISES core /shell QDs displayed similar pyramidal structure and size distribution, indicating that the Zn and Cd surface treatment does not change the overall size/structure ⁹⁷. A high-resolution TEM (HRTEM) image of a single Zn-CISES QD is shown in **Figure 2.1d**. The measured lattice spacing of 0.327 nm lies between 0.319 nm (indexed to the (112) plane of pure CuInS₂) and 0.335 nm (indexed to the (112) plane of pure CuInSe₂) that is consistent with the (112) plane of alloyed CISES QDs, demonstrating the alloy nature of CISES. This conclusion is also consistent with X-ray diffraction (XRD) patterns (**Figure 2.3a**). HRTEM investigations do not allow to identify a clear interface between the CISES core and ZnS shell, possibly due to the ultra-thin layer of ZnS (<0.1 nm) ⁹⁷.

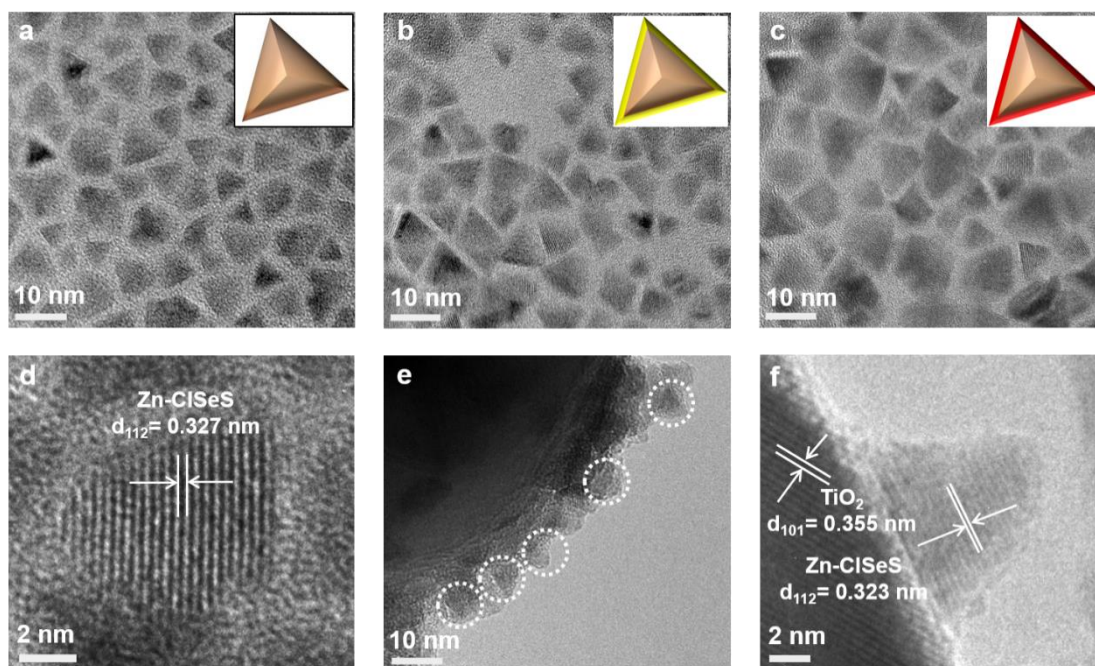


Figure 2.1 TEM images of (a) CISES QDs; (b) Cd-CISES and (c) Zn-CISES QDs showing analogous pyramidal structure and nearly same sizes. Inset images of (a), (b) and (c) display schematic diagrams of QDs structures of CISES, Cd-CISES and Zn-CISES, respectively. (d) HRTEM image of an individual Zn-CISES QD with lattice spacing of 0.327 nm. (e) TEM image of TiO₂/Zn-CISES heterostructure with uniform dispersion of Zn-CISES QDs (white dashed circle presents a single QD on the surface of TiO₂). (f) HRTEM of TiO₂/single Zn-CISES QD heterostructure (higher magnification image of the white line circle in (e)).

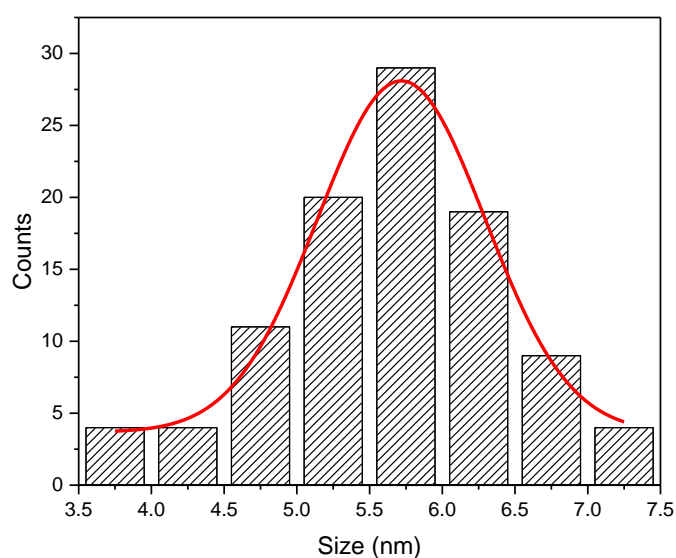


Figure 2.2 Size distribution of CISES QDs. Sizes are measured as the height of projected triangles (distance from a vertex to the middle of the opposite) in TEM image for 100 QDs. The average sizes were 5.64 ± 0.77 nm.

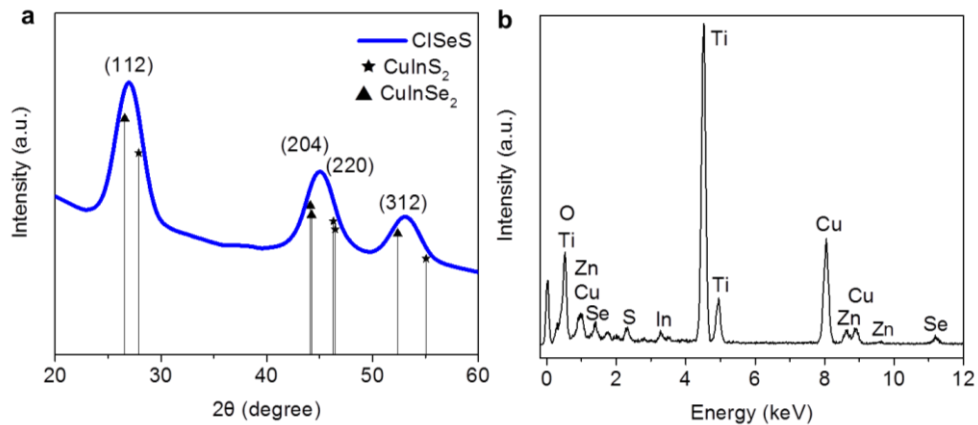


Figure 2.3 (a) XRD pattern of CISeS QDs films formed by drying of dropped CISeS QDs solution on the top of FTO glass substrate, diffraction peaks at 26.9, 45.1 and 53.1° matching well between diffraction peaks of (112), (204/220) and (312) facets in pure CuInS₂ (★, JCPDS card no. 03-065-1572) and CuInSe₂ (▲, JCPDS card no. 00-040-1487) with tetragonal phase. (b) EDS spectra of TiO₂/Zn-CISeS heterostructure (in Figure 1e), confirming the presence of the elements including Ti, O, Zn, Cu, In, Se and S.

Generally, to effectively connect QDs and TiO₂, the QDs are deposited into the TiO₂ film by various techniques, such as bi-linker technique or EPD approach¹³⁰. For bi-linker technique, various types of bifunctional molecule can efficiently link the QD to the surface of TiO₂, and the electron transfer rate at the QD/TiO₂ interface has been demonstrated to be mainly associated with the linker length, showing an exponential decay of electron transfer rate as a function of increasing length due to tunneling of electrons through the linker molecule^{34, 131}. In this work, the surface capping ligands of QDs are DDT and OLA or OA with length of ~2 nm¹³². Compared to linker approach, EPD is an efficient method that leads to shrink or removal of the surface capping ligands, which results in close contact of QDs and TiO₂ for enhanced electron transfer rate, enhancing the performance of relevant QDs-based PEC devices^{19, 130}. Therefore, to realize high performance PEC devices, we further deposited the as-synthesized CISeS or Zn(Cd)-CISeS QDs into the mesoporous TiO₂ film by EPD.

The heterostructure of TiO₂/Zn-CISeS is displayed in **Figure 2.1e**, which shows that the QDs are uniformly attached onto the surface of TiO₂ nanoparticles without any noticeable agglomeration. The HRTEM image of QDs/TiO₂ (**Figure 2.1f**) demonstrates the highly intimate connection between QDs and TiO₂ nanoparticles, suggesting the possibility of a fast electron transfer rate from QDs to TiO₂, thereby improving the performance of QDs-sensitized PEC device due to the decrease of exciton recombination. In addition, there is no visible structural

and/or lattice change during EPD (**Figure 2.1f**, **Figure 2.3b**) with respect to the colloidal Zn-CISeS QDs before EPD (**Figure 2.1d**). Similar hybrid structures were also found for the QDs of CISeS and Cd-CISeS in the TiO₂ film. These results indicate that EPD is an efficient approach to directly deposit QDs onto the TiO₂ film with good connection ¹³⁰.

The presence and distribution of QDs inside the film were further confirmed by energy-dispersive X-ray spectroscopy (EDS). Cross-section scanning electron microscope (SEM) imaging and relevant EDS mapping of the Zn-CISeS QDs-sensitized photoanode are reported in **Figure 2.4**. The thickness of the mesoporous TiO₂ film with transparent and scattering layer is estimated to be ~13.2 μm. The Zn-CISeS QDs were found to be uniformly dispersed in the TiO₂ film. The relative mass concentration of Zn-CISeS QDs with respect to TiO₂ is reported in **Figure 2.5** and **Table 2.1**.

X-ray photoelectron spectroscopy (XPS) analysis (**Figure 2.6** and **Table 2.2**) was used to study the surface chemical bonding in the TiO₂/Zn(Cd)-CISeS anode. A high resolution XPS (HRXPS) spectrum of Zn 2p and Cd 3d confirms the presence of Zn and Cd elements with proportion of 23% and 14% (atomic concentration) when calculated with cationic Cu and In components. Using this Zn (or Cd) concentration and the diameter of core/shell QD from TEM images, the thickness of the shell was calculated by assuming a homogeneous shell/core coverage. The estimated shell thickness is around 0.12 nm, consistent with HRTEM results and the designed thickness of ~0.1 nm ¹³³.

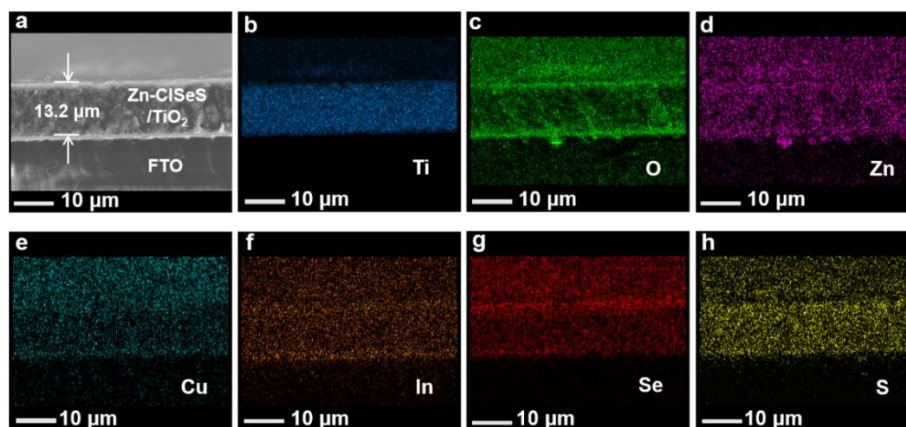


Figure 2.4 (a) Cross-sectional SEM image of Zn-CISeS QDs-sensitized photoanode. EDS mapping analysis of all the elements in relevant TiO₂/Zn-CISeS/ZnS electrode including (b) Ti, (c) O, (d) Zn, (e) Cu, (f) In, (g) Se and (h) S.

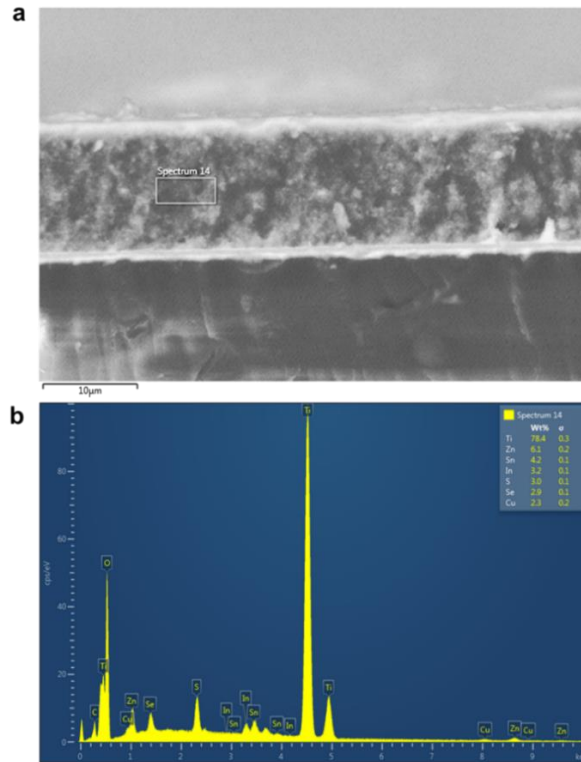


Figure 2.5 (a) Cross-sectional SEM image of TiO₂/Zn-CISES/ZnS and corresponding (b) EDS spectra of specified region (white solid line) in (a).

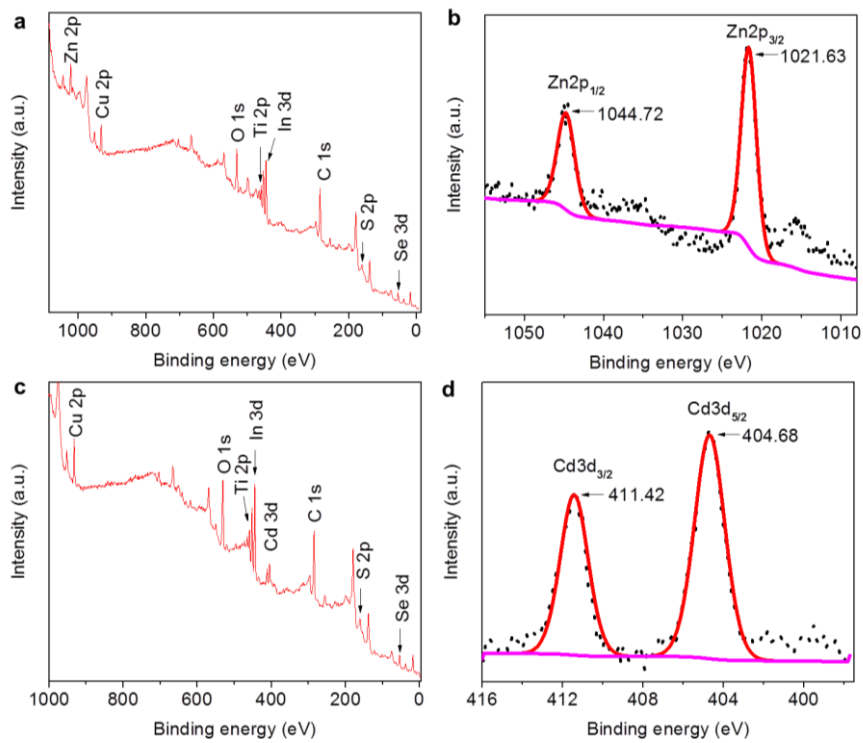


Figure 2.6. XPS spectra of Zn and Cd-CISES QDs-TiO₂ photoanodes. (a) Full spectrum of Zn-CISES QDs-TiO₂ photoanode; (b) High resolution Zn 2p core-level spectra; (c) Full spectrum of Cd-CISES QDs-TiO₂ photoanode; (d) High resolution Cd 3d core-level spectra.

Table 2.1 EDS analysis of composition (Mass concentration) of TiO₂/Zn-CISeS /ZnS photoanode. Ratio of elements/Ti (defined as 1) is listed, and Zn and S are much higher owing to the ZnS SILAR coating.

Ti (Wt%)	In/Ti (Wt%)	Zn/Ti (Wt%)
100	4.1	7.8
Cu/Ti (Wt%)	Se/Ti (Wt%)	S/Ti (Wt%)
2.9	3.7	3.8

In addition, in the HRXPS spectra (**Figure 2.6b and d**), there is no obvious peak (Zn or Cd dangling bonds) located at low binding energies, which is usually an indication of surface defects/traps during the anode preparation, indicating that the EPD process does not introduce significant traps/defects¹³⁰.

The as-prepared QDs show the typical absorption spectrum of the CISeS material, covering the broad wavelength range from ~400 nm up to 1000 nm (**Figure 2.7a**)⁵⁴. No significant change in the absorption spectra was recorded after cation exchange (**Figure 2.7a**), consistent with the thin shell thickness. The bandgap of Zn-CISeS, Cd-CISeS and CISeS QDs was calculated to be ~1.49, 1.48 and 1.51 eV, according to Tauc plots (inset in **Figure 2.7a**), respectively. These values are in good agreement with the bandgap derived from the PL peak, taking into account the Stokes shift between the first excitonic absorption peak and the emission peak (**Figure 2.9**)¹³³.

Table 2.2. XPS analysis of cationic composition (atomic concentration) of Zn-CISeS (treated at 100 °C) and Cd-CISeS QDs deposited on TiO₂ films. S and Se components are excluded due to their complex peak overlaps.

Elements	Cu (mol%)	In (mol%)	Zn (mol%)
TiO ₂ /Zn-CISeS	27	50	23
TiO ₂ /Cd-CISeS	34	52	14

As the heavy metal of Cd in Cd-CISeS QDs could lead to possible health and environment issues, we further investigated and highlighted the environment-friendly Zn-CISeS QDs. The thickness of ZnS shell on core CISeS QDs was tuned by controlling the Zn-treatment temperatures (i.e. 50, 100 and 150 °C) based on identical reaction time (10 min). The ZnS shell thickness was estimated based on the overall size of QDs measured by TEM and the molar ratio of Zn/(Cu+In) calculated by EDS (**Figure 2.10**) or XPS analysis (**Figure 2.6**), by assuming a

uniform coverage of the shell on the QD core. Shell thicknesses of ~ 0.04 , 0.12 and 0.2 nm were obtained at 50 , 100 and 150 $^{\circ}\text{C}$, respectively. As shown in **Figure 2.7c**, the CISeS QDs before and after Zn treatment (with increasing temperatures) exhibit similar absorption spectra with slight blue-shift, consistent with the QD's growth mechanism of cation exchange: increasing thickness of ZnS and decreasing core radius of CISeS QDs ⁹².

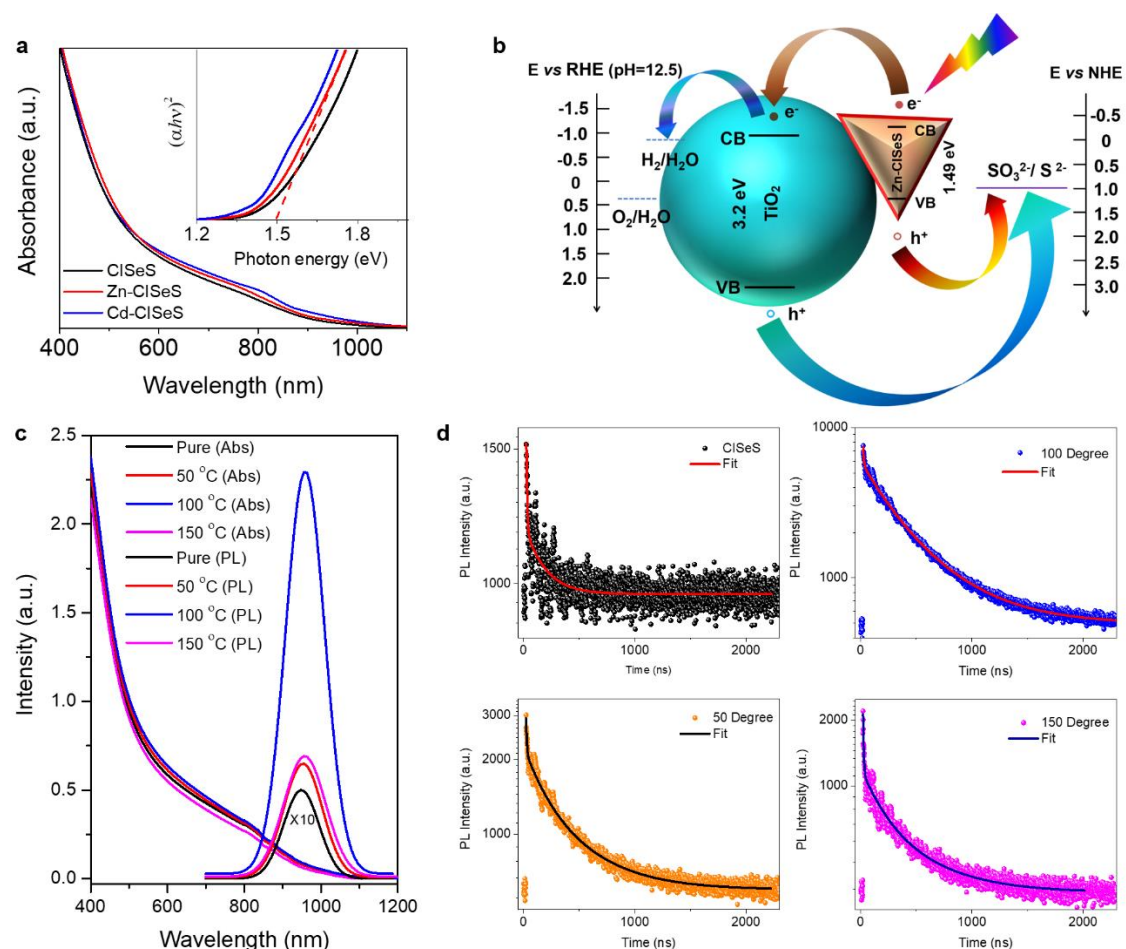


Figure 2.7 (a) Absorption spectra of CISeS in toluene before and after Zn (Cd) treatment. The inset image exhibits the extrapolation of Tauc plots $[(\alpha h\nu)^2$ versus photon energy $(h\nu)]$. (b) Band alignment and schematic diagram of Zn-CISeS QDs-sensitized photoanode. Absorption and PL spectra (c) and lifetime (d) of CISeS QDs with Zn treatment at different temperatures.

The PL spectra of CISeS QDs after Zn surface treatment at various temperatures show no significant change of PL peak positions, but largely improved PL intensity as compared to bare CISeS QDs due to improved surface passivation. Consistently, CISeS QDs with Zn treatment exhibit prolonged lifetime compared to bare QDs (**Figure 2.7d**). The detailed information of PL spectra and lifetime of these CISeS QDs with different Zn treatment temperatures were summarized in **Table 2.3**, confirming that the Zn-CISeS treated at 100 $^{\circ}\text{C}$ show the highest PL

intensity and the longest PL lifetime. This demonstrates that surface traps/defects on CISEs QDs were successfully suppressed by growing a very thin ZnS shell at 100 °C⁹⁷.

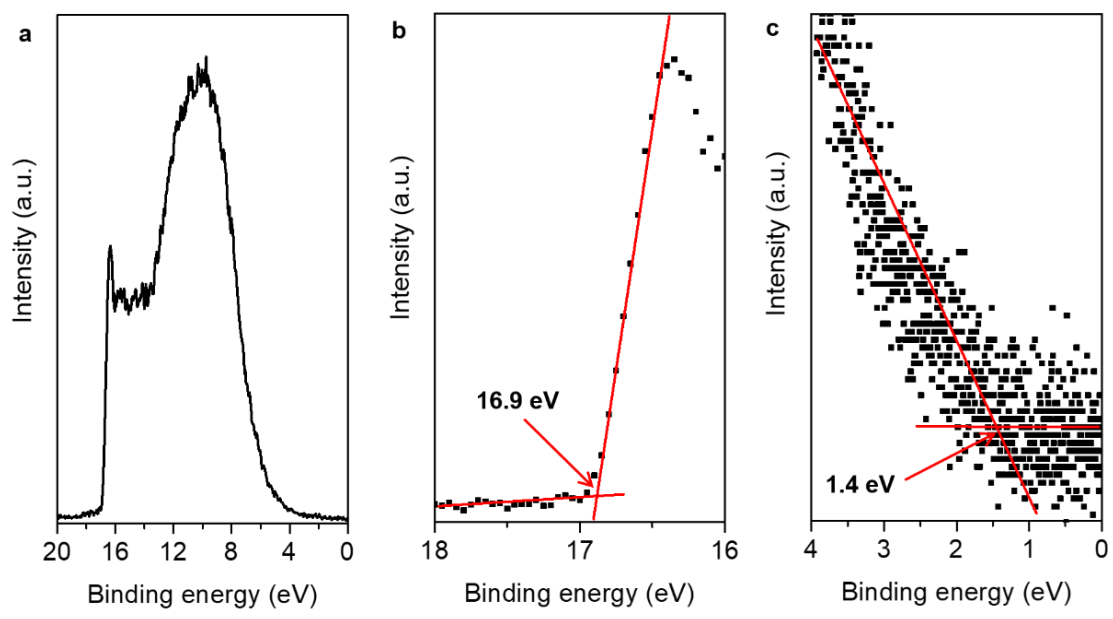


Figure 2.8 (a) UPS full spectrum of the Zn-CISEs QDs deposited on mesoporous TiO₂. Corresponding high-resolution UPS spectrum of (b) high binding energy cut-off (determining Fermi level) and (c) low binding energy cut-off (determining VB maximum).

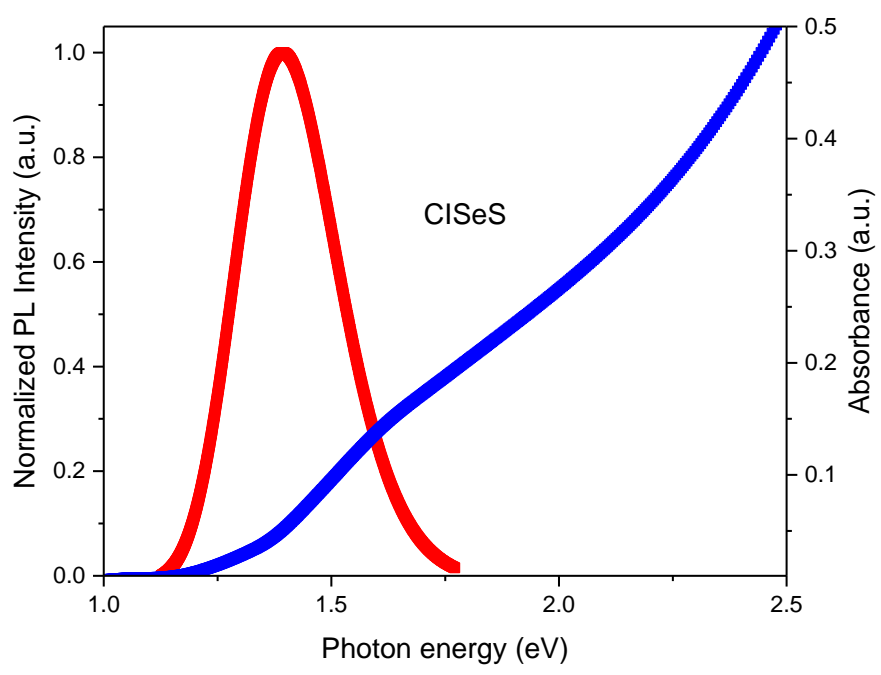


Figure 2.9 UV-visible-NIR absorption (blue line) and PL (red line) spectra of as-synthesized CISEs QDs dispersed in toluene.

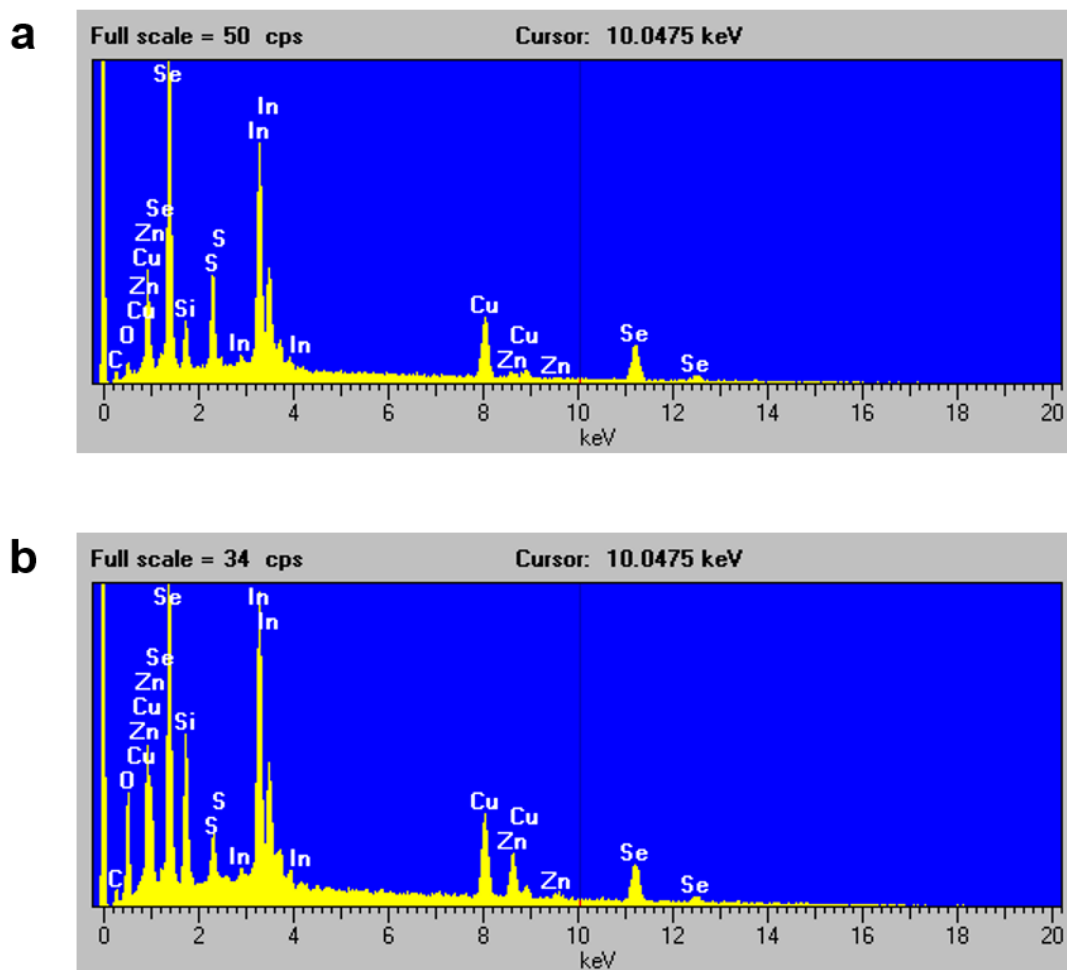


Figure 2.10 EDS spectra of Zn-CISeS QDs treated at 50 and 150 degree, showing molar ratio of $[Zn/(Cu+In)]$ of 7.5% and 31.8%, respectively.

Table 2.3 CISeS QDs with Zn treatment under various temperatures and corresponding molar ratio of $[Zn/(Cu+In)]$, QDs core radius, shell thickness, PL peak position and lifetime.

Sample	Molar ratio $[Zn/(Cu+In)]$	Core Radius (nm)	Shell thickness (nm)	PL peak position (nm)	Lifetime (ns)
Pure CISeS	0	5.64	0	949	165±4
Zn-50 °C	8.12%	5.56	0.04	952	425±7
Zn-100 °C	29.79%	5.4	0.12	956	480±20
Zn-150 °C	46.54%	5.24	0.2	959	405±10

Ultraviolet photoelectron spectroscopy (UPS) with He I radiation (21.21 eV) was further used to estimate the Fermi level and maximum valance band energy level of various QDs and TiO₂^{134, 135}. The UPS analysis of the Zn-CISeS QDs/TiO₂ sample is illustrated in **Figure 2.8**. **Figure 2.8a** reports the UPS full spectrum of TiO₂/Zn-CISeS and **Figure 2.8b** shows a high binding

energy cut-off of 16.9 eV, which determines the Fermi level of Zn-CISeS QDs on TiO₂ located at -4.31 eV with respect to the vacuum level. The high resolution UPS spectrum of low binding energy cut-off from 0 to 4 eV is displayed in **Figure 2.8c**, suggesting that the VB maximum is at -5.71 eV with respect to vacuum. According to the optical band gap of Zn-CISeS QDs derived from their absorption spectra (**Figure 2.7a**), the calculated CB minimum is -4.22 eV. The band alignment and schematic diagram of Zn-CISeS QDs-sensitized photoanode for PEC cell is illustrated in **Figure 2.7b**. The Zn-CISeS QDs is able to form a type II band alignment with TiO₂ that is favorable for the dissociation of photoexcited carriers at the QDs/TiO₂ interface, where photogenerated holes oxidize the sacrificial agent (Na₂S and Na₂SO₃) in the electrolyte and electrons are injected into TiO₂ and are subsequently collected by the FTO electrode. Finally, they migrate to the Pt counter electrode for water reduction¹⁸. The band alignment and schematic investigations of CISeS and Cd-CISeS QDs-modified TiO₂ are shown in **Figure 2.11**, both presenting favorable band energy levels for water reduction.

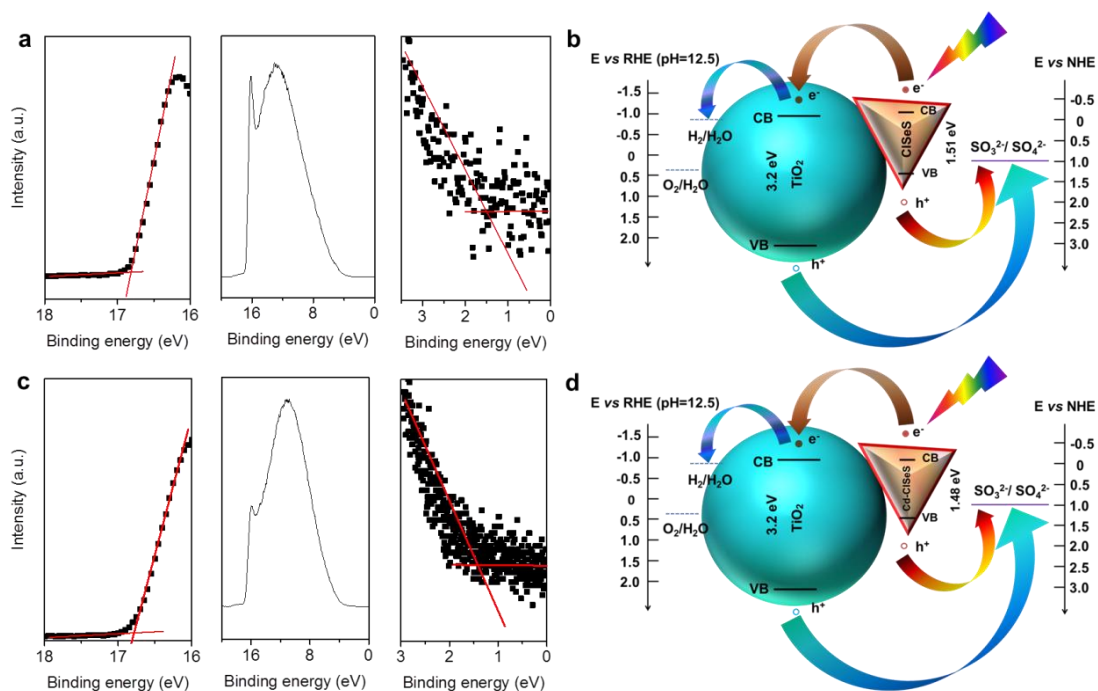


Figure 2.11 UPS spectra of (a) CISeS QDs, (c) Cd-CISeS QDs deposited on TiO₂ and corresponding band alignment as well as schematic diagram of (b) CISeS QDs and (d) Cd-CISeS QDs-sensitized photoanodes.

2.2 Measurement and performance of quantum dots-based photoelectrochemical cells

2.2.1 Measurement of quantum dots-sensitized photoanodes

A three-electrode system consisting of a Pt counter electrode, an Ag/AgCl reference electrode (saturated with KCl) and an as-fabricated working electrode was used to assess the PEC performance of the QDs-sensitized photoanode. The photoanode was then fully dipped into the electrolyte containing 0.25 M Na₂S and 0.35 M Na₂SO₃ (pH=12.5), which served as sacrificial hole scavenger to prevent QDs photocorrosion. The following formula $V_{\text{RHE}} = V_{\text{Ag/AgCl}} + 0.1976 + \text{pH} \times (0.059)$ was used to convert the measured potentials (versus Ag/AgCl) to the potentials versus the reversible hydrogen electrode (RHE) in electrochemical measurements by an electrochemical workstation (CHI-760D with 20 mV/s sweep rate). Photocurrent density-voltage (*J-V*) curves were measured under simulated sunlight (1 sun = AM 1.5 G, 100 mW/cm²) employing a Compact Solar Simulator Class AAA (Sciencetech SLB-300A). To guarantee the standard 1 Sun illumination (100 mW/cm²) on the photoanode in our three-electrode system, before each measurement, a Si reference diode (Sciencetech) was used to adjust the distance (typically, the distance between the reactor and the lamp is around 20 cm) between photoanode and solar simulator before each measurement. The distance from sun simulator to PEC cell is around 30 cm.

2.2.2 Photoelectrochemical performance of quantum dots-based photoanodes

Figure 2.12 displays the PEC performance of CISeS, Zn-CISeS and Cd-CISeS QDs-sensitized photoanodes in dark, under continuous and chopped illumination using a typical three electrode configuration with working electrode (as-fabricated photoanodes), Ag/AgCl (saturated with KCl) reference electrode and Pt counter electrode. Prior to PEC measurements, an additional inorganic ZnS layer is deposited on the TiO₂/QDs by SILAR following the EPD process, to prevent photocorrosion of the electrodes¹⁹. As shown in **Figure 2.12a**, under dark conditions (without any illumination), no significant current density is produced (> 0.4 V); while a saturated photocurrent density of ~2.57 mA/cm² is obtained at a potential of 0.6 V versus the RHE under standard AM 1.5G illumination (100 mW/cm², ~30 cm from the sun simulator to

PEC cell) for the TiO₂/CISES/ZnS system.

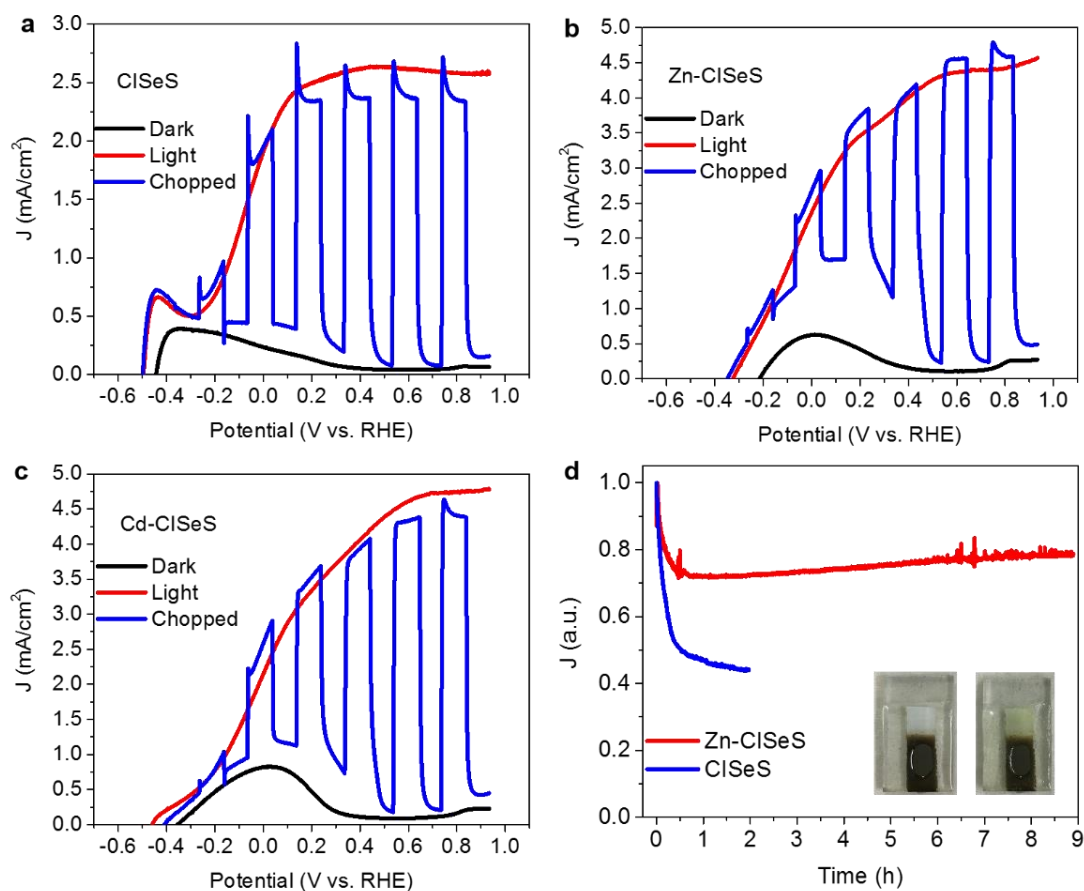


Figure 2.12 Photocurrent density versus bias potential (versus RHE) for (a) the TiO₂/CISES/ZnS, (b) TiO₂/Zn-CISES/ZnS and (c) TiO₂/Cd-CISES/ZnS photoanodes in the dark (black curve), under continuous (red curve) and chopped (blue curve) illumination (AM 1.5G, 100 mW/cm²) (d) Stability measurements (photocurrent density as a function of time) of TiO₂/CISES/ZnS and TiO₂/Zn-CISES/ZnS photoanodes at 0.6 V versus RHE under AM 1.5G illumination (100 mW/cm²) and optical images of TiO₂/Zn-CISES/ZnS photoanode before (left) and after (right) stability measurement (9h, AM 1.5G, 100 mW/cm²).

This value is comparable with a NIR PbS QDs/TiO₂ based anode and 8-fold higher than the similar CISES QDs based cathode for hydrogen generation^{19, 118}. To choose the proper number of SILAR cycles, various ZnS layer cycles (1, 2, 4 and 6) were performed on the same TiO₂/CISES anode prepared with identical QDs solution and EPD time (15 min). The relevant *J-V* curves are shown in **Figure 2.13**, indicating that the 2-cycle ZnS SILAR deposition is prone to inhibit photocorrosion and maximize PEC performance.

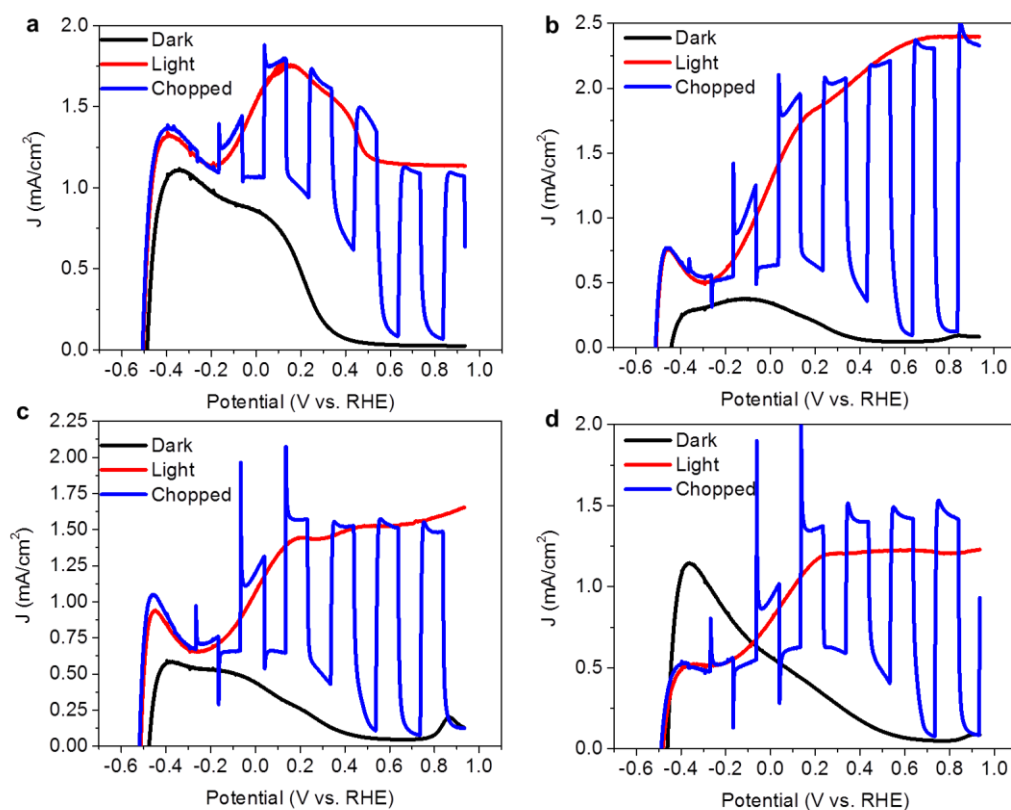


Figure 2.13 J-V curves of the $\text{TiO}_2/\text{CISeS}/\text{ZnS}$ photoanode formed by 15min EPD and various cycles of ZnS via SILAR. One (a), two (b), four (c), and six (d) ZnS cycles are studied, presenting that the 2-cycle ZnS is the most favorable for achieving higher photocurrent density due to the more efficient photocorrosion inhibition compared to other cycles of ZnS coating.

However, the stability of this bare QDs based PEC cell is still limited. After 2 h of continuous illumination under standard one sun, the photocurrent density dropped to 38% of its initial value. Generally, QDs are sensitive to the surface defects created during device operation that act as charge traps, leading to a low photoconversion efficiency and limited long-term stability^{136, 137}. A promising solution to address this challenge consists in using core/shell structured QDs, which have shown significantly enhanced photocurrent and stability in a QDs based PEC system, such as CdTe/CdS or PbS/CdS core/shell QDs based PEC system^{19, 138}. Recently, core-shell CISeS/ZnS(CdS) QDs have been explored as potential light absorbers in QDs based solar cells, due to their excellent properties such as reduced surface traps, suppressed charge recombination and enhanced photo- and chemical- stability^{97, 133}. The efficiency of a solar cell is largely improved by using core/shell QDs even with a very thin shell layer (in general, less than 0.1 nm) of ZnS or CdS^{97, 133}. Herein, we further use the core/shell structured CISeS/Zn(Cd)S QDs as photosensitizers to fabricate the PEC cell (detailed information for

fabrication of core/shell QDs is shown in section 2.1.2). In the following, all the anodes were fabricated using the TiO₂ film containing one transparent layer and one scattering layer and the anodes after QDs deposition were further capped with 2 cycles of ZnS. The as-prepared TiO₂/Zn-CiSeS/ZnS (**Figure 2.12b**) and TiO₂/Cd-CiSeS/ZnS (**Figure 2.12c**) photoanodes exhibit a large enhancement of saturated photocurrent density of ~4.27 mA/cm² and ~4.62 mA/cm² respectively compared to bare QDs, elucidating the effective passivation of surface traps on CiSeS QDs and suppression of charge recombination in Zn-CiSeS and Cd-CiSeS QDs-sensitized photoelectrodes.

In the following, we focus on using Zn-CiSeS QDs because they are green NIR QDs with a comparable photocurrent density to that of toxic Cd-CiSeS QDs. In addition to the TiO₂/Zn-CiSeS (100 °C Zn treatment)/ZnS photoanode with photocurrent density of ~4.27 mA/cm², the TiO₂/Zn-CiSeS (50 °C)/ZnS photoelectrode shows a saturated photocurrent of ~3.03 mA/cm² (**Figure 2.14a**), which is higher than pure CiSeS QDs (~2.57 mA/cm²). This indicates that the ZnS thin shell of CiSeS QDs with Zn treatment at 50 °C suppresses the surface defects/traps on CiSeS QDs. In contrast, the TiO₂/Zn-CiSeS (150 °C)/ZnS photoanode has a very low saturated photocurrent density of ~1.75 mA/cm² (**Figure 2.14b**), suggesting that the CiSeS QDs with Zn treatment at 150 °C created a relatively thick ZnS shell on CiSeS QDs that hinders electron/hole transfer due to the wide band gap of ZnS¹²⁸. Detailed information on the PEC performance of core CiSeS QDs with different ZnS shell thicknesses are summarized in **Table 2.4**. It is concluded that the optimal ZnS shell on CiSeS QDs can efficiently suppress the surface defects/traps and leads to improved device performance, while relatively thick ZnS shell results in a large tunneling barrier due to its wide band gap and electronic band positioning, inhibiting electron/hole transfer¹²⁸.

Further optimization of Zn-CiSeS (100 °C) based PEC cell including the improved TiO₂ film uniformity and QDs concentration in film lead to a maximum photocurrent density of ~5.3 mA/cm² (**Figure 2.15**). In previous work using heavy metal free, NIR colloidal QDs-sensitized photoelectrodes for hydrogen generation, photocurrent densities of ~0.3 mA/cm², ~0.6 mA/cm² and ~2 mA/cm² were achieved, based on CiSeS QDs, Ag₂S QDs and CuInS₂ QDs^{118, 119, 139}, respectively. Other work using CuInS₂ and CuInSe₂ QDs based anodes (before the toxic CdS

treatment) reported photocurrent densities of ~ 3.7 mA/cm² or 0.6 mA/cm²^{107, 120}. Our optimized core/shell structure presents a promising approach for further using CISES green QDs for water reduction as we obtained an unprecedented value of the photocurrent density (~ 5.3 mA/cm²), which is much higher than previously reported values for NIR colloidal green QDs based PEC devices^{107, 118-120, 139}.

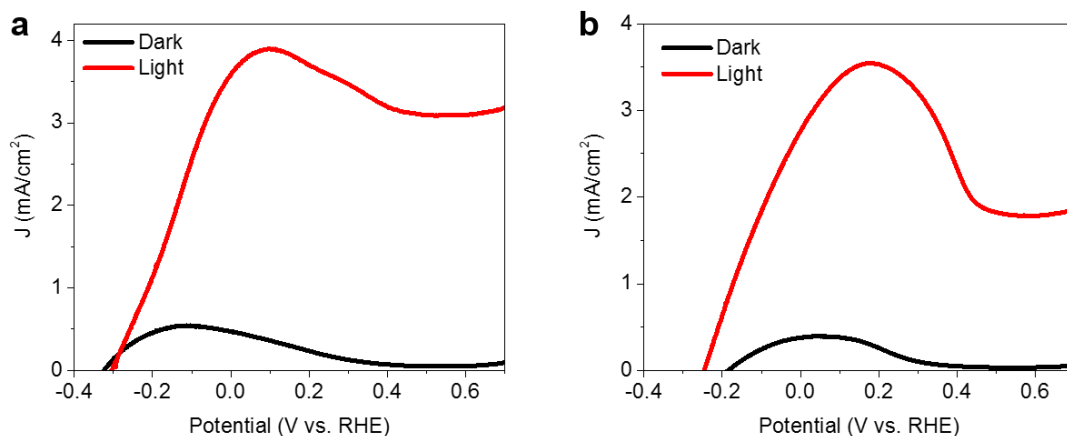


Figure 2.14 J-V curves of the TiO₂/Zn-CISES/ZnS photoanode with Zn-CISES QDs treated at different temperature of (a) 50 °C and (b) 100 °C, showing saturated photocurrent density of ~ 3.03 and 1.75 mA/cm².

Figure 2.12d displays the photocurrent density as a function of time for TiO₂/CISES/ZnS (blue curve) and TiO₂/Zn-CISES/ZnS (red curve) photoanodes measured at 0.6 V versus RHE under AM 1.5G solar illumination (100 mW/cm²). To better compare the decay trend, we divide the maximum photocurrent density of the photoanodes with or without Zn treatment, which makes the two curves decay from the same value (i.e. 1). Compared to the untreated anode, after 9h illumination, the Zn-CISES QDs photoanode based PEC cell shows only a $\sim 23\%$ drop of initial photocurrent density, which is ~ 3 -fold lower than that of CISES QDs-sensitized photoanode ($\sim 62\%$ drop of original performance only after 2h) due to the presence of a thin shell of ZnS. There is no noticeable color change of active area for the Zn-CISES based anode before and after a 9h PEC test (inset of **Figure 2.12d**), showing no significant morphology change of Zn-CISES QDs-based photoanode and demonstrating a good stability of the anode during the measurement that is consistent with lower current density loss. The stability of this system is comparable with the best reported anode based on QDs (30% drop after 20 min for TiO₂ nanorod/CdS/NiO/CdSe structures and 28% drop after 2h for TiO₂ nanowire/CdS/Co-Pi structures)^{140, 141}. After 45-min illumination, there is no significant change (up to 9h) for the

current density, suggesting the long-term stability in the PEC system using $\text{TiO}_2/\text{Zn-CISeS}/\text{ZnS}$ as anode.

Table 2.4 Composition and size information of CISeS QDs and Zn-CISeS QDs (treated at 50, 100 and 150 °C) and relevant PEC performance of QDs-sensitized photoanodes.

Sample	Molar ratio [Zn/(Cu+In)]	Core Radius (nm)	Shell thickness (nm)	Photocurrent density (mA/cm^2)
Pure CISeS	0	5.64	0	2.57
Zn-50 °C	8.12%	5.56	0.04	3.03
Zn-100 °C	29.79%	5.4	0.12	5.31
Zn-150 °C	46.54%	5.24	0.2	1.75

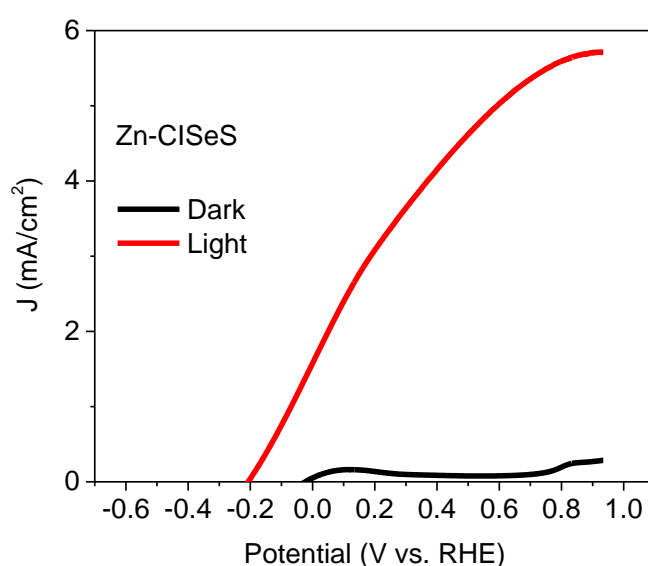


Figure 2.15 Photocurrent density versus bias potential (vs RHE) for optimized $\text{TiO}_2/\text{Zn-CISeS}/\text{ZnS}$ photoanode with champion photocurrent density of $\sim 5.3 \text{ mA}/\text{cm}^2$ under illumination of one sun (AM 1.5G $100 \text{ mW}/\text{cm}^2$).

2.3 Summary

In summary, we fabricated and characterized photoanodes which use heavy metal-free, NIR colloidal bare CISeS and core/shell Zn-CISeS QDs as sensitizers. The CISeS QDs-sensitized photoanode led to a saturated photocurrent density of $\sim 2.57 \text{ mA}/\text{cm}^2$ upon exposure to standard AM 1.5G solar illumination ($100 \text{ mW}/\text{cm}^2$, $\sim 30 \text{ cm}$ from sun simulator to PEC cell). To reduce surface traps of core CISeS QDs, we added an inorganic ZnS surface passivation by cation exchange. The QDs were effectively deposited into the mesoporous TiO_2 film by EPD, showing intimate connection between QDs and TiO_2 nanoparticles. UPS spectra show appropriate band

alignment of the QDs and TiO₂ and the as-fabricated core/shell Zn-CISeS QDs-sensitized photoanode demonstrates efficient charge separation and transport, leading to a saturated photocurrent density of ~5.3 mA/cm² (the highest value to date for environment-friendly, NIR colloidal QDs for hydrogen generation). The stability of the TiO₂/Zn-CISeS/ZnS system is comparable to the best reported anode based on QDs^{140, 141}. Overall the Zn-CISeS QDs are a promising system for environment-friendly, cost-effective, robust and highly efficient solar driven hydrogen production, paving the way for broader and deeper investigations of green QDs for high performance PEC systems.

CHAPTER 3 SYNTHESIS AND CHARACTERIZATION OF NEAR- INFRARED, HEAVY METAL-FREE COLLOIDAL “GIANT” CORE/SHELL QUANTUM DOTS FOR SOLAR-DRIVEN PHOTOELECTROCHEMICAL CELLS

In this section, a new type of NIR and heavy metal-free g-QDs, i.e. CISE/CIS g-QDs, is synthesized by using a sequential cation exchange. The morphology and crystal structure of as-prepared CISE/CIS g-QDs demonstrate the formation of a thick CuInS₂ shell with wurtzite (WZ) phase. The optical properties of these g-QDs exhibit tunable NIR absorption and PL spectra (up to ~1100 nm). The PL lifetime of these heavy metal-free, NIR g-QDs is prolonged with increasing shell thickness, indicating the formation of quasi-type II band structure, which is consistent with the theoretical simulation. Finally, these NIR, heavy metal-free g-QDs are used as light harvesters for fabrication of QDs-based PEC cells, showing a saturated photocurrent density up to ~3 mA/cm² as well as excellent stability.

I did most of the experimental work and wrote the draft of this manuscript. Dr. Xiang-Tian Kong helped me with the theoretical simulation. Dr. Haiguang Zhao and Dr. Yufeng Zhou helped me to measure the optical properties of QDs.

3.1 Synthesis and characterization of near-infrared, heavy metal-free colloidal “giant” core/shell quantum dots

QDs-based optoelectronic devices has developed dramatically in recent years^{7,96,142}. However, the performance of QDs-based optoelectronic devices is still hindered by several aspects including stability^{4,38}. The g-QDs with a robust and inorganic thick shell present an alternative strategy to enhance the stability of QDs and tune the optical properties^{49,57,143}. Although g-QDs have been widely used in both biomedical and optoelectronic devices, there are still several significant limitations including limited optical absorption and emission in visible region as well as their toxic compositions (e.g. Cd and Pb), hindering their NIR applications and future commercial purpose^{61,62,65,68,144,145}. NIR and heavy metal-free g-QDs are therefore significant

for further developments of QDs-based optoelectronic devices and biomedical applications.

3.1.1 Synthesis of near-infrared, heavy metal-free CuInSe₂/CuInS₂ “giant” core/shell quantum dots

In this work, we employed a self-limited cation exchange approach via using CdSe/CdS g-QDs as templates. To balance the introduction of In³⁺ and the extraction of Cu⁺, the TOP-InCl₃ complex and relatively mild condition (temperature of 100 °C for 4 hours) is used, acting as both the In source and Cu-extracting precursor. In this case, the Cu⁺ is extracted by the TOP ligands while the more stable In³⁺ can directly replace the extracted Cu⁺ at identical surface site, leading to the nearly unchanged morphology and crystal structure in the as-synthesized CISE/CIS g-QDs¹⁴⁶.

“Giant” CdSe/CdS QDs were first synthesized following the method reported by Dabbousi *et al.*⁵⁰: Typically, 1g of TOPO (trioctylphosphine oxide) was mixed with Cd-oleate (0.38 mmol, 1 mL) and ODE (8 mL) in a flask and purged by N₂ at room temperature for 30 min. The reaction system was degassed for 30 min at 100 °C, then heated to 300 °C. The mixture of trioctylphosphine (TOP)-Se (4 mmol, 4 mL), OLA (3 mL), and ODE (1 mL) at room temperature was quickly injected into the flask under vigorous stirring. The reaction was then quenched with cold water after injection. The as-synthesized QDs were precipitated with ethanol, centrifuged to eliminate unreacted precursors and re-dispersed in toluene.

CdS layers were deposited on CdSe QDs via SILAR approach reported by Ghosh *et al.*¹⁴⁷ “Giant” CdSe/CdS QDs were synthesized by growing CdS monolayers over the CdSe cores. Typically, OLA (5 mL), ODE (5 mL) and CdSe QDs (~2×10⁻⁷ mol in toluene) were mixed in a 100 mL flask and degassed for 30 min at 110 °C. The reaction flask was then heated to 240 °C under N₂. Subsequently, the Cd-oleate dispersed in ODE (0.25 mL, 0.2 M) was injected dropwise via syringe and the reaction proceeded for 2.5 h, followed by dropwise injection of 0.2 M sulfur in ODE with same volume. The shell was then annealed for 10 min. All subsequent shells were annealed at 240 °C for 10 min following the injection of sulfur and ~2.5 h following dropwise injection of the Cd-oleate in ODE. Sulfur/Cd-oleate injection volumes for shell deposition cycles 1–13 were as follows: 0.25, 0.36, 0.49, 0.63, 0.8, 0.98, 1.18, 1.41, 1.66, 1.92,

2.2, 2.51 and 2.8 mL, respectively. The reaction was then quenched with cold water and the as-synthesized QDs were precipitated with ethanol, centrifuged to eliminate unreacted precursors, and re-dispersed in toluene.

Zn-CISE/CIS g-QDs were then synthesized by sequential cation exchange, similar to the procedure described by Stam *et al.*¹⁴⁶ Typically, for Cu⁺ cation exchange, [Cu(CH₃CN)₄]PF₆ (0.4 mmol) mixed with methanol (4 mL) and toluene (4 mL) were added to 3 mL of CdSe/CdS g-QDs in a flask and 0.5 mL OA was then added to the mixture. The reaction proceeded for 10 min at room temperature with vigorous stirring. Subsequently, 3 mL of DDT was added and the as-synthesized Cu₂Se/Cu₂S g-QDs were centrifuged and re-dispersed in 5 mL of toluene. For In³⁺ cation exchange, 2 M TOP-InCl₃ solution was first prepared by dissolving 1 mmol of InCl₃ in 0.5 mL of TOP and diluted with 3 mL of ODE. 3.5 mL of 2 M TOP- InCl₃ solution in ODE was then added to 5 mL of Cu₂Se/Cu₂S g-QDs in toluene at 100 °C and the mixture was allowed to react for 4 h with stirring. Finally, 5 mL DDT was added and the as-synthesized CISE/CIS g-QDs were precipitated with ethanol, centrifuged to eliminate unreacted precursors, and re-dispersed in toluene.

For CISE/CIS g-QDs treated with Zn²⁺, 5 mL of CISE/CIS g-QDs re-dispersed in ODE were added to 0.2 M Zn-oleate solution (3 mmol of OA and 1 mmol of Zn(Ac)₂ dissolved in 4 mL of ODE), and the reaction mixture was heated to 100 °C and maintained for 2 min.

3.1.2 Structure and optical properties

In this work, CdSe/CdS g-QDs were served as template to synthesize Zn-CISE/CIS g-QDs by sequential cation exchange procedures¹⁴⁶. As shown in **Figure 3.1a**, Cd²⁺ in CdSe/CdS g-QDs was exchanged by Cu⁺ and as-synthesized Cu₂Se/Cu₂S g-QDs were partially exchanged by In³⁺ to form CuInSe₂/CuInS₂ g-QDs. We further grew a very thin ZnS protective shell by cation exchange to suppress the surface defects on the QDs and enhance the colloidal stability of as-synthesized g-QDs⁹⁷.

Figure 3.1b and c display the TEM images of CdSe/CdS g-QDs with 13 and 6 monolayers of CdS shell (CdSe/13CdS and CdSe/6CdS). The CdSe/CdS g-QDs exhibit a spherical shape with radius of ~1.65 nm for CdSe and shell thickness of ~4.2 nm and ~2 nm for CdSe/13CdS and

CdSe/6CdS g-QDs, respectively. The corresponding EDS spectrum of CdSe/6CdS g-QDs (**Figure 3.2a**) confirms the presence of elemental Cd, S and Se, while Se is absent in the EDS spectrum of CdSe/13CdS g-QDs (**Figure 3.2b**). This is attributed to a less concentrated sample in the grid during EDS measurements by TEM. Further characterization of the EDS spectrum (**Figure 3.3a**) in a SEM and the Inductively coupled plasma optical emission spectrometry (ICP-OES) analysis (**Table 3.1**) both confirm the presence of elemental Se in CdSe/13CdS g-QDs.

HRTEM images (Inset images in **Figure 3.1b and c**) of these two kinds of QDs both display a lattice spacing of ~ 0.335 nm that is well indexed to the (002) plane of WZ phase CdS, demonstrating the dominance of the WZ crystal structure of CdS in the CdSe/CdS g-QDs due to the larger volume of the CdS shell with respect to the CdSe core, consistently with previous reports^{49, 143, 148}.

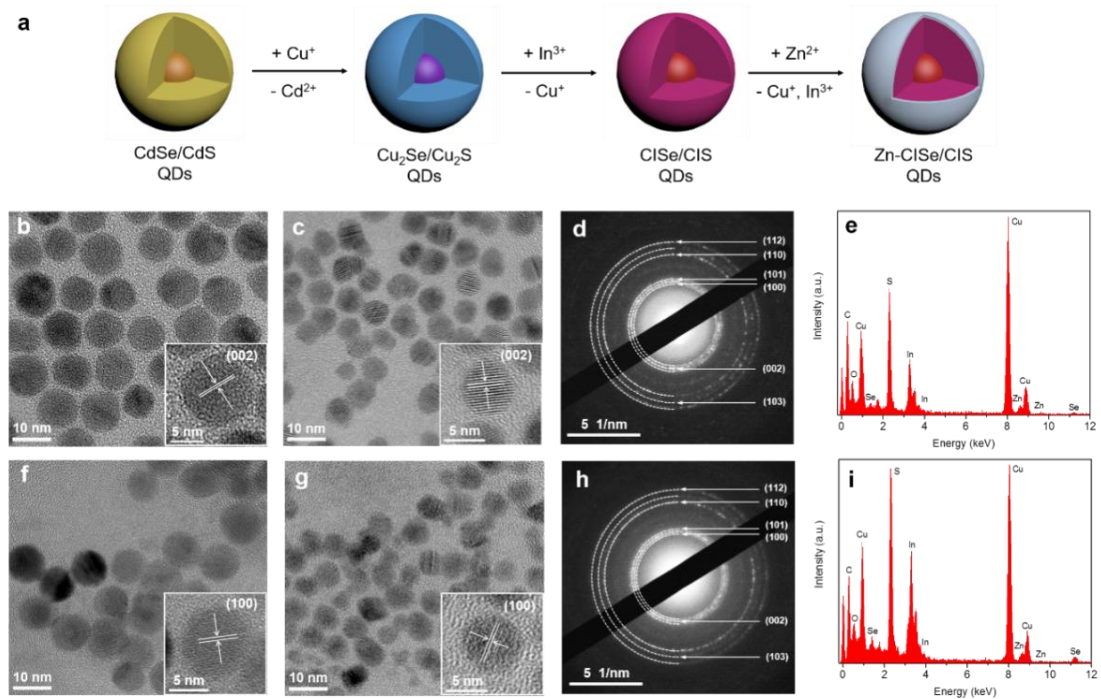


Figure 3.1 (a) Schematic diagram of sequential cation exchange procedures for synthesis and structure of Zn-CISe/CIS g-QDs. TEM images of (b) CdSe/13CdS and (c) CdSe/6CdS g-QDs with inset HR-TEM images showing (002) plane of WZ CdS. (d) SAED pattern of CdSe/13CdSg-QDs. (e) EDS spectra of Zn-CISe/13CIS g-QDs (e) and Zn-CISe/6CIS g-QDs (i). (f) TEM images of Zn-CISe/13CIS and (g) Zn-CISe/6CIS g-QDs with inset HR-TEM images exhibiting (100) plane of WZ CuInS₂. (h) SAED pattern of Zn-CISe/13CIS g-QDs.

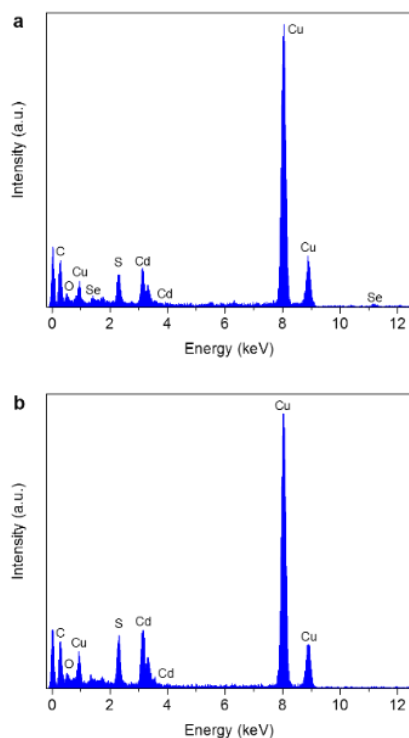


Figure 3.2 EDS spectra of (a) CdSe/6CdS and (b) CdSe/13CdS g-QDs before sequential cation exchange. And the spectra of CdSe/6CdS g-QDs confirms all the elements including Cd, S and Se. The element of Se is absent in (b) due to the thicker CdS shell of CdSe/13CdS g-QDs.

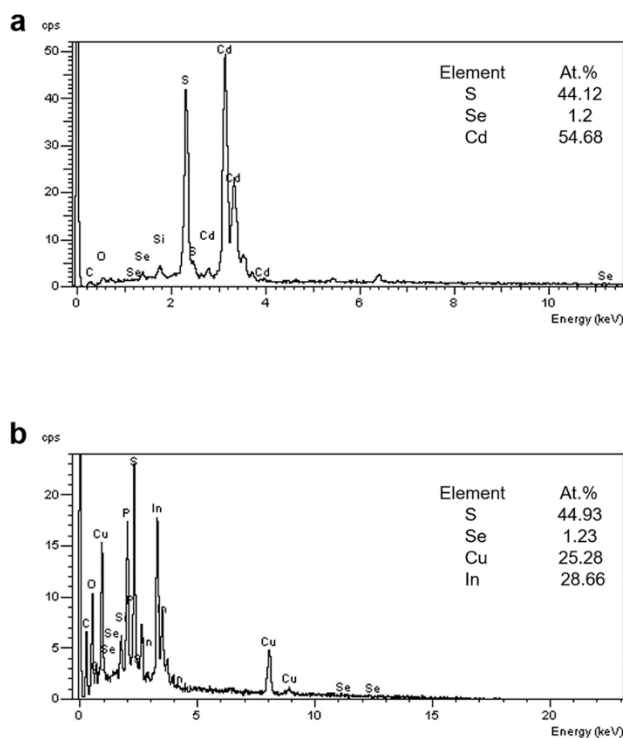


Figure 3.3 EDS spectra of (a) CdSe/13CdS and (b) CISE/13CIS g-QDs. The spectra confirm the presence of all the elements in CdSe/13CdS (Cd, S and Se) and CISE/13CIS (Cu, In, S and Se) g-QDs. The atomic concentration of Se is 1.2% and 1.23% in CdSe/13CdS and CISE/13CIS g-QDs, respectively, indicating very small volume of core QDs in such core/shell g-QDs.

Table 3.1 ICP-OES analysis results of CdSe/13CdS g-QDs, showing Cu and Se solution concentration of 23.43 and 0.16 ppm and molar ratio of ~1:0.01.

Element (Wavelength)	Correlation coefficient	Concentration (ppm)	Molar ratio (Cd: Se)
Cd (214.439 nm)	0.99985	23.43	1:0.01
Se (203.985 nm)	0.99990	0.16	

After sequential cation exchange, the TEM images of as-synthesized Zn-CISe/13CIS (**Figure 3.1f**) and Zn-CISe/6CIS (**Figure 3.1g**) g-QDs show no noticeable change of shapes and sizes compared to the CdSe/13CdS and CdSe/6CdS g-QDs, indicating an effective preservation of QD morphology using the cation exchange method, consistently with the literature ¹⁴⁶. The latter approach is effective to control the morphologies of QDs by varying the shape/size of the initial QD templates. Unlike the directly synthesized irregular shaped CuInSe(S) QDs, the spherical shape of CISe/CIS g-QDs can be obtained by using the cation exchange approach. The TEM images of CISe/13CIS (**Figure 3.4a**) and Zn-CISe/13CIS g-QDs (**Figure 3.4b**) also possess similar shape and size because the Zn surface treatment only forms a very thin ZnS protective shell (<0.1 nm) and has already been demonstrated to have a negligible effect on QD morphology in previous work ^{97, 149}.

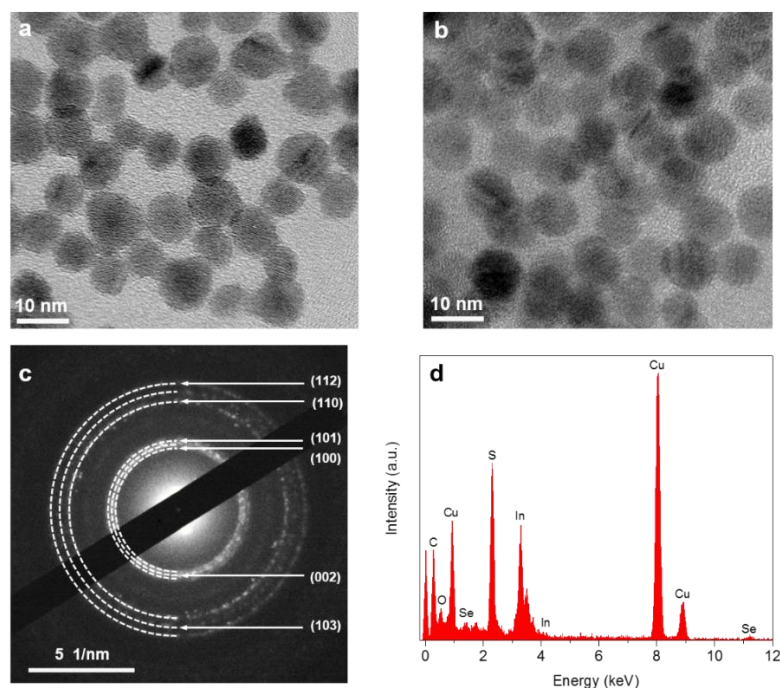


Figure 3.4 TEM images of (a) CISe/13CIS and (b) Zn-CISe/13CIS g-QDs, exhibiting no significant change of QD's sizes and shapes before and after Zn treatment. (c) SAED pattern of CISe/13CIS g-QDs, which is well indexed to (100), (002), (101), (110), (103) and (112) plane of WZ phase CuInS₂. (d) EDS spectra CISe/13CIS g-QDs, confirming the presence of all the elements including Cu, In, Se and S.

To further support this conclusion, size histograms of CISE/13CIS and Zn-CISE/13CIS are displayed in **Figure 3.5**, showing sizes of 9.2 ± 0.6 nm and 9.2 ± 0.7 nm, respectively, indicating no significant size variation before and after Zn surface treatment. The HRTEM images (Inset images in **Figure 3.1f and g**) reveal a lattice distance of ~ 0.338 nm, which is indexed to the (100) plane of WZ phase CuInS_2 . The lattice distances measured in selected area electron diffraction (SAED) patterns of CdSe/13CdS (**Figure 3.1d**) and Zn-CISE/13CIS g-QDs (**Figure 3.1h**) are well indexed to the (002), (100), (101), (110), (103) and (112) planes of WZ phase CdS and CuInS_2 , respectively, which are typical planes with relatively high diffraction intensity in WZ CdS (JCPs No. 00-041-1049) and CuInS_2 (JCPs No. 01-077-9459).

For CISE/13CIS g-QDs, the planes of WZ phase CuInS_2 in the SAED pattern (**Figure 3.4c**) are consistent with the diffraction peaks in the XRD pattern (**Figure 3.6**), indicating the formation of a very thick WZ phase CuInS_2 shell. Similarly, the lattice spacing in SAED patterns of CdSe/6CdS (**Figure 3.7a**) and Zn-CISE/6CIS (**Figure 3.7b**) g-QDs are also well indexed to the (002), (100), (101), (110), (103) and (112) planes of the WZ phase CdS and CuInS_2 , further demonstrating the WZ crystal structure of as-synthesized Zn-CISE/CIS g-QDs.

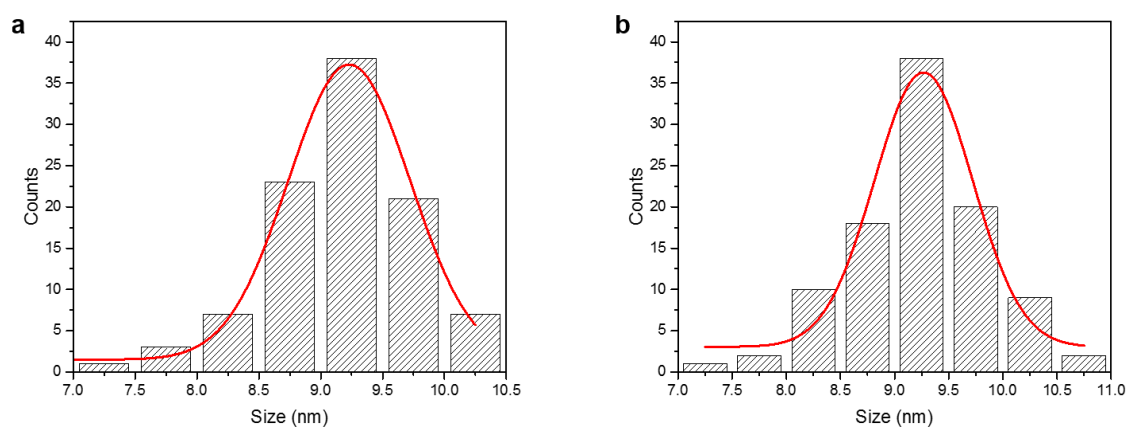


Figure 3.5 Size distribution of (a) CISE/13CIS and (b) Zn-CISE/13CIS g-QDs. Sizes are measured as the diameter of the spheres in TEM image for 100 QDs. The average sizes were 9.2 ± 0.6 nm and 9.2 ± 0.7 nm for CISE/13CIS and Zn-CISE/13CIS g-QDs, respectively. The results indicate the Zn surface treatment has negligible effect for the size of QDs and only forms an ultrathin ZnS layer on the g-QDs.

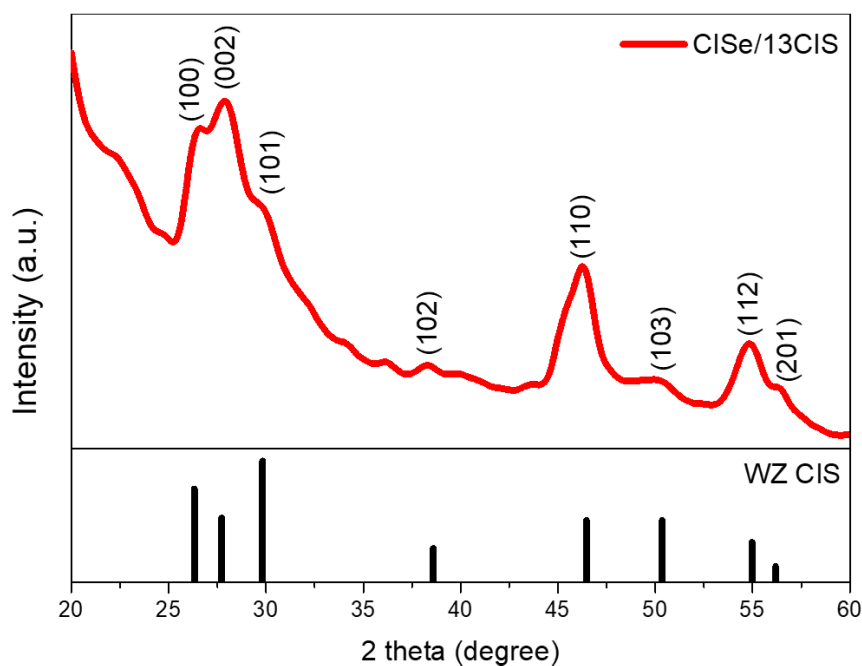


Figure 3.6 XRD pattern of CISe/13CIS g-QDs films formed by drying of dropped CISe/13CIS g-QDs solution on the top of silicon substrate. The diffraction peaks match well with the (100), (002), (101), (102), (110), (103), (112) and (201) planes of WZ phase CuInS_2 (JCPDS card no. 01-077-9459).

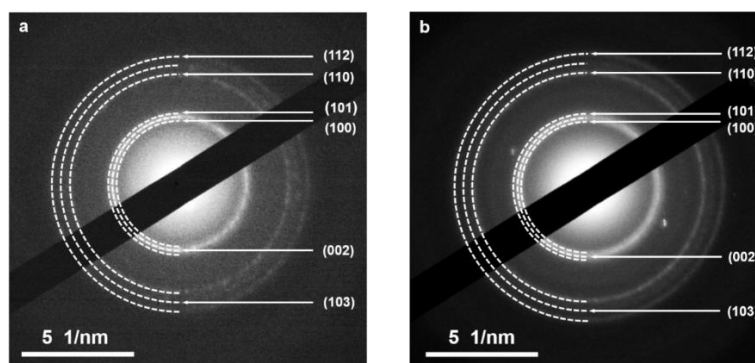


Figure 3.7 SAED pattern of (a) CdSe/6CdS and (b) Zn-CISe/6CIS g-QDs that are indexed to (100), (002), (101), (110), (103) and (112) plane of WZ phase of CdS (JCPDS No. 00-041-1049) and CuInS_2 (JCPDS No. 01-077-9459), respectively.

In addition, the EDS spectra of Zn-CISe/13CIS (**Figure 3.1e**) and Zn-CISe/6CIS (**Figure 3.1i**) g-QDs both confirm the presence of all the elements including Cu, In, Se, S and Zn. The residual Cd after first cation exchange of CdSe/13CdS to $\text{Cu}_2\text{Se}/13\text{Cu}_2\text{S}$ g-QDs is measured by using ICP-OES. As shown in **Table 3.2**, the ICP-OES analysis indicates that 99.7% (molar ratio) of Cd^{2+} has been exchanged by Cu^+ in $\text{Cu}_2\text{Se}/13\text{Cu}_2\text{S}$ core/shell g-QDs even with a thick shell of 13 layers of CIS. This can be considered as full exchange of Cd by Cu cations. In addition, the $\text{Cu}_2\text{Se}/13\text{Cu}_2\text{S}$ g-QDs were used for In^{3+} cation exchange to form CISe/13CIS g-QDs and no

Cd²⁺ was introduced in the this synthesis process, thus the Cd²⁺ in Cu₂Se/13Cu₂S g-QDs was almost identical as confirmed by ICP-OES measurements, demonstrating that the as-synthesized Zn-CISe/CIS g-QDs are free of heavy metals, consistent with the literature ¹⁴⁶. The molar ratio of Cu/In is ~1:1.2 in the CISe/CIS g-QDs as measured by ICP-OES (**Table 3.3**). The morphology of as-prepared CISe/CIS g-QDs shows nearly identical sizes and shapes of CdSe/CdS template, indicating that the CIS shell thickness of CISe/CIS g-QDs can be controlled by tuning the CdS shell thickness of the CdSe/CdS template. Using this sequential cation exchange technique leads to a full exchange of Cd²⁺ by Cu⁺ and In³⁺. The as-synthesized CISe/CIS g-QDs do not contain toxic heavy metals and are environmentally friendly.

Table 3.2 ICP-OES analysis results of Cu₂Se/13Cu₂S nanocrystals.

Element (Wavelength)	Correlation coefficient	Concentration (ppm)	Molar ratio (Cd: Cu)
Cd (214.439 nm)	0.99	0.24	0.3%
Cu (324.754 nm)	0.99	45.87	

Table 3.3 ICP-OES analysis results of CISe/13CIS g-QDs, showing Cu and In solution concentration of 2.86 and 6.04 ppm and molar ratio of ~1:1.17.

Element (Wavelength)	Correlation coefficient	Concentration (ppm)	Molar ratio (Cu: In)
Cu (324.754 nm)	0.99790	2.86	1:1.17
In (303.936 nm)	0.99987	6.04	

The optical properties of CISe, Zn-CISe/6CIS and Zn-CISe/13CIS g-QDs in solution are reported in **Figure 3.8a-c**. Before the sequential cation exchange, CdSe, CdSe/6CdS and CdSe/13CdS g-QDs show absorption spectra covering the UV to visible region with first-excitonic peaks near ~550, 590 and 610 nm, respectively. After sequential cation exchange, the absorption spectra of CISe, Zn-CISe/6CIS and Zn-CISe/13CIS g-QDs have shifted to the NIR region up to 1100 nm without apparent first-excitonic peaks, which is the typical absorption spectra of CuInS(Se) QDs ^{54, 120, 129}. The PL spectra of CISe, Zn-CISe/6CIS and Zn-CISe/13CIS g-QDs before and after sequential cation exchange further demonstrate the red shift of the g-QD's PL peaks from ~565, 605 and 625 nm to ~765, 1075 and 1100 nm, respectively.

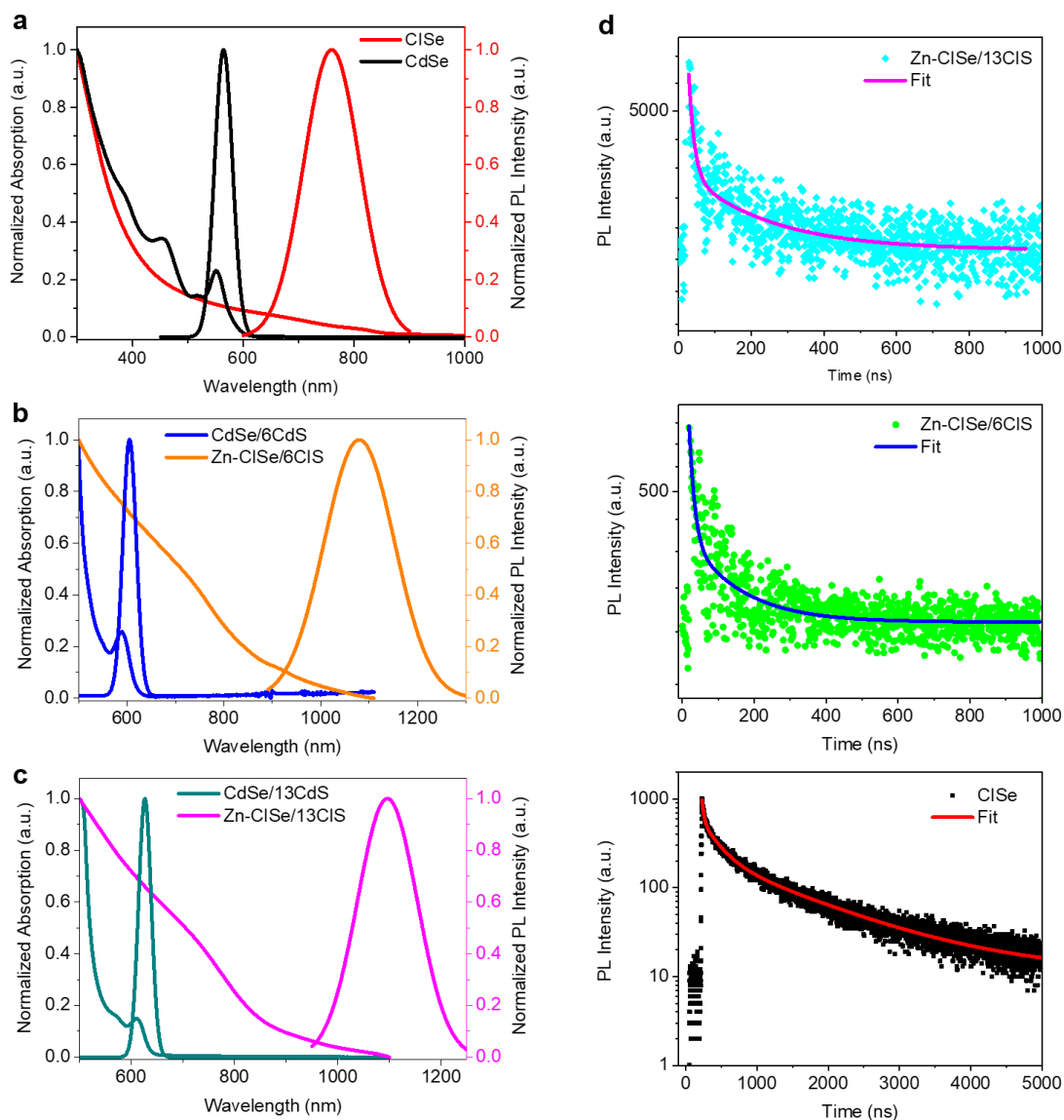


Figure 3.8 Absorption and PL spectra of (a) ClSe, (b) Zn-ClSe/6ClS and (c) Zn-ClSe/13ClS g-QDs in toluene before and after sequential cation exchange. (d) Transient PL spectra of Zn-ClSe/ClS g-QDs in toluene.

In addition, as the ICP-OES measurements already demonstrated the full exchange of Cd by Cu cations, after the first step of Cu^+ for Cd^{2+} cation exchange, the peak originating from CdSe/13CdS g-QDs disappears in the PL spectrum of the as-synthesized $\text{Cu}_2\text{Se}/13\text{Cu}_2\text{S}$ g-QDs (**Figure 3.9a**). With constant CuInSe_2 core radius, by increasing the shell thickness, the PL peak positions of the Zn-ClSe/ClS g-QDs gradually red-shift from ~765 to ~1100 nm.

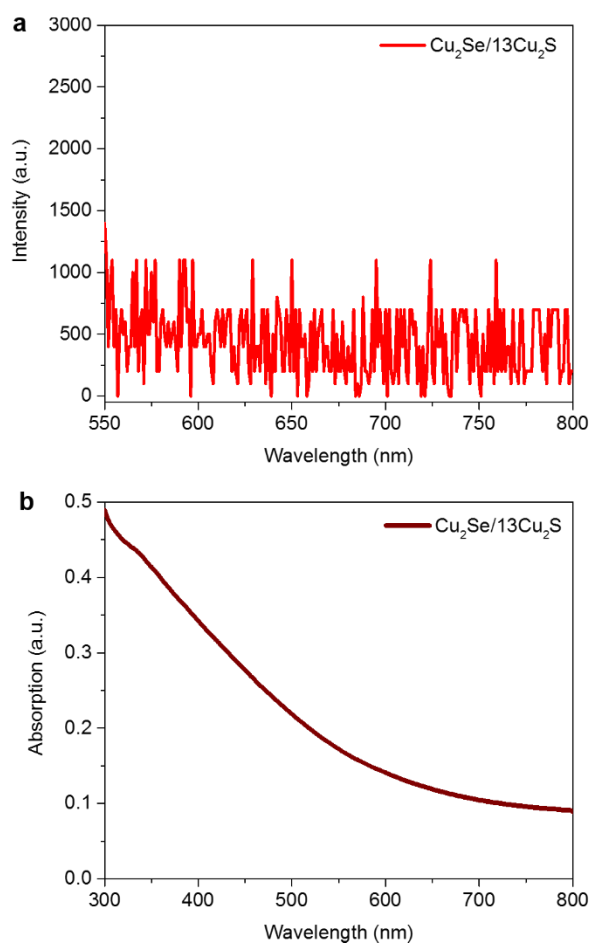


Figure 3.9 (a) PL and (b) absorption spectra of intermediate $\text{Cu}_2\text{Se}/13\text{Cu}_2\text{S}$ g-QDs dispersed in toluene. No PL peak of $\text{CdSe}/13\text{CdS}$ g-QDs is observed in (a), indicating full conversion of Cd^{2+} to Cu^+ by cation exchange.

Compared to CISe QDs, a large red-shift of the PL peak positions was found in CISe/CIS g-QDs. In general, in a core/shell system, the electron leakage from the core into the shell region leads to a red-shift of the PL peak. Such phenomenon has been observed and verified in many core/shell structured g-QDs (such as quasi-type II CdSe/CdS or type II InP/CdS)^{46,60}. To further understand the exciton dynamics of as-synthesized CISe/CIS g-QDs with different shell thickness, transient fluorescence spectroscopy was used to measure the lifetime of QDs in solution before and after sequential cation exchange, as shown in **Figure 3.10** and **Figure 3.8d**. By increasing the shell thickness, the templates of CdSe , $\text{CdSe}/6\text{CdS}$ and $\text{CdSe}/13\text{CdS}$ QDs exhibit a prolonged lifetime of ~ 19 , 29 and 43 ns, respectively. This extension of lifetime with increasing shell thickness in CdSe/CdS g-QDs indicates an efficient spatial separation of holes and electrons derived from the quasi-type II band structure in these g-QDs systems^{58,143}.

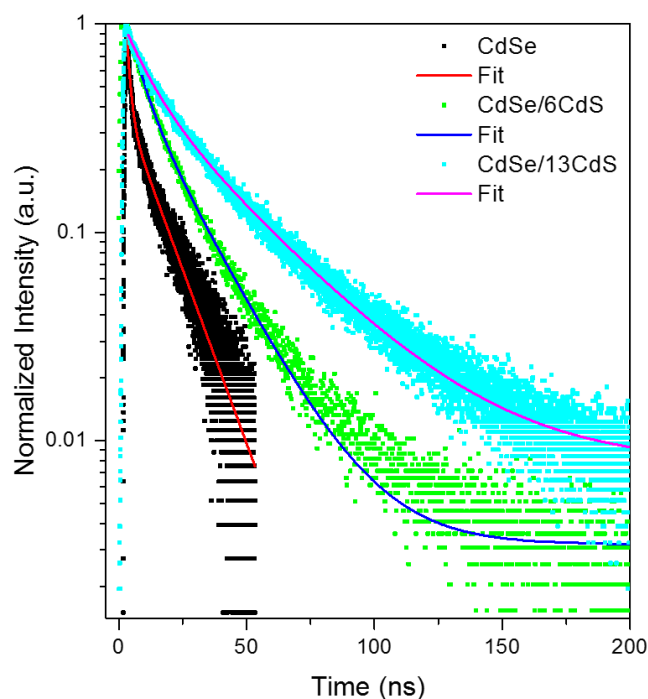


Figure 3.10 Transient PL spectra of CdSe, CdSe/6CdS and CdSe/13CdSg-QDs, showing fitted lifetime of ~19 ns, 29 ns and 43 ns, respectively.

After sequential cation exchange, the bare CISE QDs and the Zn-CISE/CIS g-QDs with different shell thickness were fitted by a tri-exponential or bi-exponential decay with standard deviation less than 10%, respectively. The fitting parameters and PLQY of CISE, Zn-CISE/6CIS and Zn-CISE/13CIS g-QDs were listed in **Table 3.4**.

Table 3.4 Optical parameters of CISE, Zn-CISE/6CdS and Zn-CISE/13CdS g-QDs including parameters of fitted lifetime and the measured PLQY.

Sample	PL peak (nm)	τ_1 (ns)	τ_2 (ns)	τ_3 (ns)	B1 (%)	B2 (%)	B3 (%)	τ_{average} (ns)	PLQY (%)
CISE	765	211	46	5	64.1	30.49	5.38	200±10	10±2%
Zn-CISE/6CdS	1075	236	23	--	82	17.94	----	230±5	2±0.1%
Zn-CISE/13CdS	1100	309	23	--	91	8.97	----	300±10	1±0.1%

In the tri-exponential lifetime fitting, τ_1 is associated with the donor-acceptor transition, τ_2 is allocated to surface states and τ_3 represents the recombination of initially populated core states. In the bi-exponential lifetime fitting, the longer lifetime of τ_1 and shorter lifetime of τ_2 are attributed to the donor-acceptor recombination of carriers and donor-acceptor recombination

The bare CISE QDs exhibit an average lifetime of 200 ± 10 ns. In contrast, the Zn-CISE/6CIS and Zn-CISE/13CIS g-QDs exhibit longer average lifetimes of 230 ± 5 ns and 300 ± 10 ns, respectively. The longer average lifetime with increasing shell thickness in Zn-CISE/CIS g-QDs may be attributed to the efficient decrease in spatial overlap between electron and hole wave functions, leading to leakage of the electrons from the core to the shell region, resulting in suppressed recombination and leading to a prolonged lifetime. In conclusion, both the red shift of the PL peak and increasing lifetime with thicker shell of QDs demonstrate the formation of quasi-type II band alignment of the core and shell in the Zn-CISE/CIS g-QDs after sequential cation exchange^{49, 143, 147, 148}.

3.2 Theoretical investigation of near-infrared, heavy metal-free colloidal “giant” core/shell quantum dots

3.2.1 Theoretical calculation method

To theoretically describe the quasi type-II characteristics and understand the prolonged lifetime of the CISE/CIS g-QDs, we solved the stationary Schrödinger equation for the 1S states of electron and hole in COMSOL (a commercial software for finite element simulation). We used the bulk values for the effective masses of electrons (m_e) and holes (m_h), namely, $m_e = 0.09m_0$ and $m_h = 0.73m_0$ for CuInSe₂, and $m_e = 0.16m_0$ and $m_h = 0.85m_0$ for CuInS₂, where m_0 is the electron mass at rest in vacuum^{152, 153}. The potentials for electrons and holes as a function of position were approximated as the lowest unoccupied molecular orbital and highest occupied molecular orbital levels, respectively, for the bulk materials. For CuInSe₂, these levels are -4.60 eV and -5.64 eV respectively; while for CuInS₂, these levels are -4.39 eV and -5.92 eV respectively^{154, 155}. The band gaps for CuInSe₂ and CuInS₂ were 1.04 eV and 1.53 eV, respectively^{154, 155}. The barriers between the CuInSe₂ and CuInS₂ regions were taken as 0.21 eV and 0.28 eV for the CB and VB. The value of -9.8 eV represents the ionization energy for the lowest-energy electronic values in the system, which is used to obtain the potential barrier between the holes and the environment. The exact value doesn't really matter much in the context of the model as it is far from the band edges. **Figure 3.11** shows the band diagrams.

The parameters are summarized in the **Table 3.5**.

Table 3.5. Physical parameters of bulk CISe and CIS.

	Material	E_v (eV)	E_c (eV)	E_g (eV)	m_e / m_0	m_h / m_0
Shell	CuInS ₂	-5.92	-4.39	1.53	0.16	0.85
Core	CuInSe ₂	-5.64	-4.60	1.04	0.09	0.73

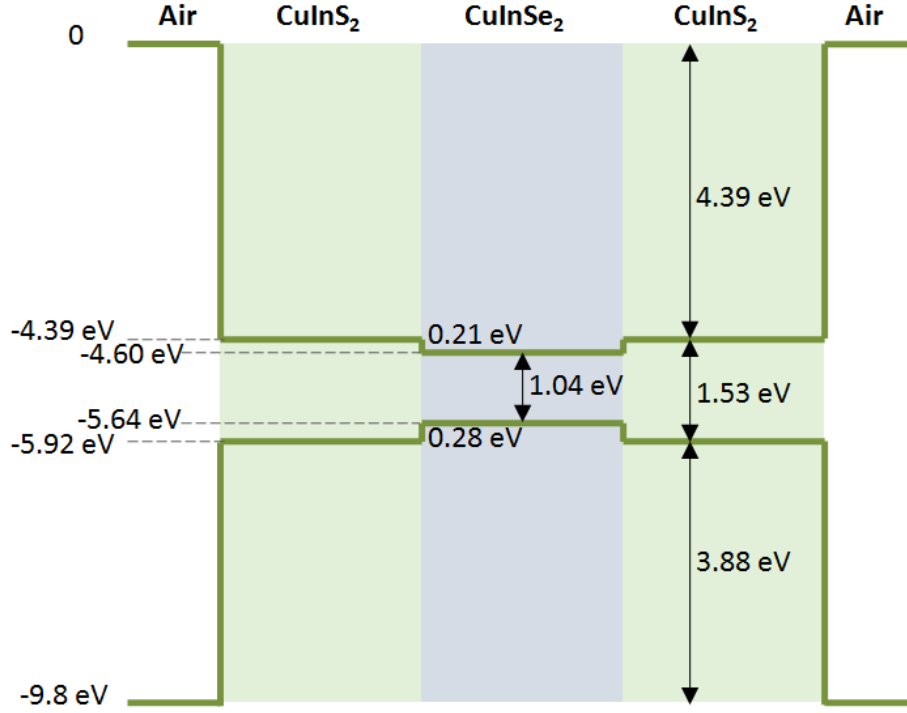


Figure 3.11 Band diagram of a CuInSe₂/CuInS₂ core/shell QD surrounded by air.

The interaction between electrons and holes was neglected in the calculations. The wave functions were computed from the effective-mass Schrödinger equation:

$$\vec{\nabla} \cdot \left(-\frac{\hbar^2}{2m^*(r)} \vec{\nabla} \psi \right) + V(r)\psi = E\psi \quad (3.1)$$

In solving this equation, the appropriate boundary conditions at the interfaces were applied.

Finally, the wave functions were normalized such that $\int |\psi_{\text{electron or hole}}|^2 dV = 1$.

The wave function of an impurity hole state (a general hole state in CuInSe/S QDs¹⁵⁶) is described by a Gaussian function:

$$\psi_{\text{hole}}(\mathbf{r}; \mathbf{r}_{\text{impurity}}) = A \exp\left(-\frac{(\mathbf{r} - \mathbf{r}_{\text{impurity}})^2}{2L_h^2}\right), \quad (\text{for impurity hole states}) \quad (3.2)$$

Here $\mathbf{r}_{\text{impurity}}$ is the position of impurity in the CISE core; the coefficient A is determined by $\int |\psi_{\text{hole}}|^2 dV = 1$; and the scale of hole L_h is far less than the QD radius (here we assume $L_h = 0.3$ nm). Considering the spherical symmetry of the wave function of 1S electrons, the squared overlap integral (OI) of Eq. (2) in the main text can be simplified as:

$$\text{OI}(h_{\text{shell}}) = N_{\text{impurity}} \cdot \frac{3}{R_{\text{core}}^3} \int_0^{R_{\text{core}}} \text{OI}_0(r_{\text{impurity}}) \cdot r_{\text{impurity}}^2 \cdot dr_{\text{impurity}}, \quad (3.3)$$

where r_{impurity} is the distance of the impurity site from the center of the core. In the experiment, the Cu and In atoms in the core are off-stoichiometry (Cu:In = 1:1.2). Then the numbers of Cu atoms and In atoms in the core can be estimated using the mass density and molar mass of CISE as $N_{\text{Cu}} = 176$ and $N_{\text{In}} = 212$. The number of In atoms that occupy the Cu sites is given by $N_{\text{impurity}} = N_{\text{In}_{\text{Cu}}} = 18$.

3.2.2 Wave function in CuInSe₂/CuInS₂ “giant” core/shell quantum dots

As shown in **Figure 3.12a**, the light emission process in the CISE/CIS g-QDs is attributed to either the recombination of the 1S electrons and the 1S holes or the recombination of the 1S electrons to the impurity holes in the core, or both¹⁵⁶. Our calculations show that the Eigen-energy of the 1S electron exceeds the energy barrier of the shell layer with thickness of 1–6 nm. As a consequence, electrons have a great probability of being found outside the CISE core, compared to a bare CISE QD. By increasing the thickness of the CIS shell, more electrons are likely to leak into the shell region. In contrast, the 1S VB holes are still well confined in the core for both a bare CISE QD and a CISE/CIS g-QD. And the probability profile of the 1S hole remains nearly unchanged with increasing shell layer thickness (from 1 to 6 nm). To qualitatively demonstrate the PL lifetime of the core/shell QDs, we calculated the squared overlap integral (OI) of the 1S electron and 1S hole as a function of shell thickness. The squared OI is given by:

$$\text{OI}(h_{\text{shell}}) = \frac{\left| \int \psi_{\text{electron}} \psi_{\text{hole}} dV \right|^2}{\int |\psi_{\text{electron}}|^2 dV \int |\psi_{\text{hole}}|^2 dV}, \quad (3.4)$$

for 1S electron and 1S hole, and

$$\text{OI}(h_{\text{shell}}) = N_{\text{impurity}} \cdot \frac{1}{V_{\text{core}}} \int_{\text{core}} \text{OI}_0(\mathbf{r}_{\text{impurity}}) dV_{\text{impurity}}, \quad (3.5)$$

with

$$\text{OI}_0(\mathbf{r}_{\text{impurity}}) = \frac{\left| \int \psi_{\text{electron}}(\mathbf{r}) \psi_{\text{hole}}(\mathbf{r}; \mathbf{r}_{\text{impurity}}) dV \right|^2}{\int |\psi_{\text{electron}}(\mathbf{r})|^2 dV \int |\psi_{\text{hole}}(\mathbf{r}; \mathbf{r}_{\text{impurity}})|^2 dV}, \quad (3.6)$$

for 1S electron and impurity hole. Here ψ_{electron} and ψ_{hole} are wave functions of 1S electron state and hole state, respectively, and $N_{\text{impurity}} = 18$ is the number of impurities in the CISE core. We assume a weak interaction between the impurity hole states. The lifetime of fluorescence emission should be proportional to the inverse of the squared overlap function. **Figure 3.12c** shows that the squared OI decreases with increasing shell layer thickness, proving that the lifetime should increase with increasing shell thickness. This trend is in qualitative agreement with the experimental measurements (PL and lifetime).

The as-prepared CISE/CIS g-QDs exhibit a broad absorption spectrum up to 1100 nm, PL spectrum in the second biological window of 1100-1400 nm and longer lifetime as high as ~300 ns compared to generic biomolecules with lifetime of around several ns, which makes them a great candidate for NIR deep-tissue imaging/sensors compared to toxic CdSe/CdS g-QDs as they are made of heavy metal-free elements, also the long PL lifetime of CISE/CIS g-QDs is favorable to obtain the fluorescence signals without background interference¹⁵⁷.

In addition, the quasi-type II nature of CISE/CIS g-QDs makes them superior candidates in solar technologies such as photovoltaics and hydrogen production as the electrons can efficiently transfer to the electron acceptors. The wide absorption spectrum (up to NIR region) of CISE/CIS g-QDs has a significant overlap with the solar spectrum, presenting great potential to boost the PCE in such g-QDs based devices.

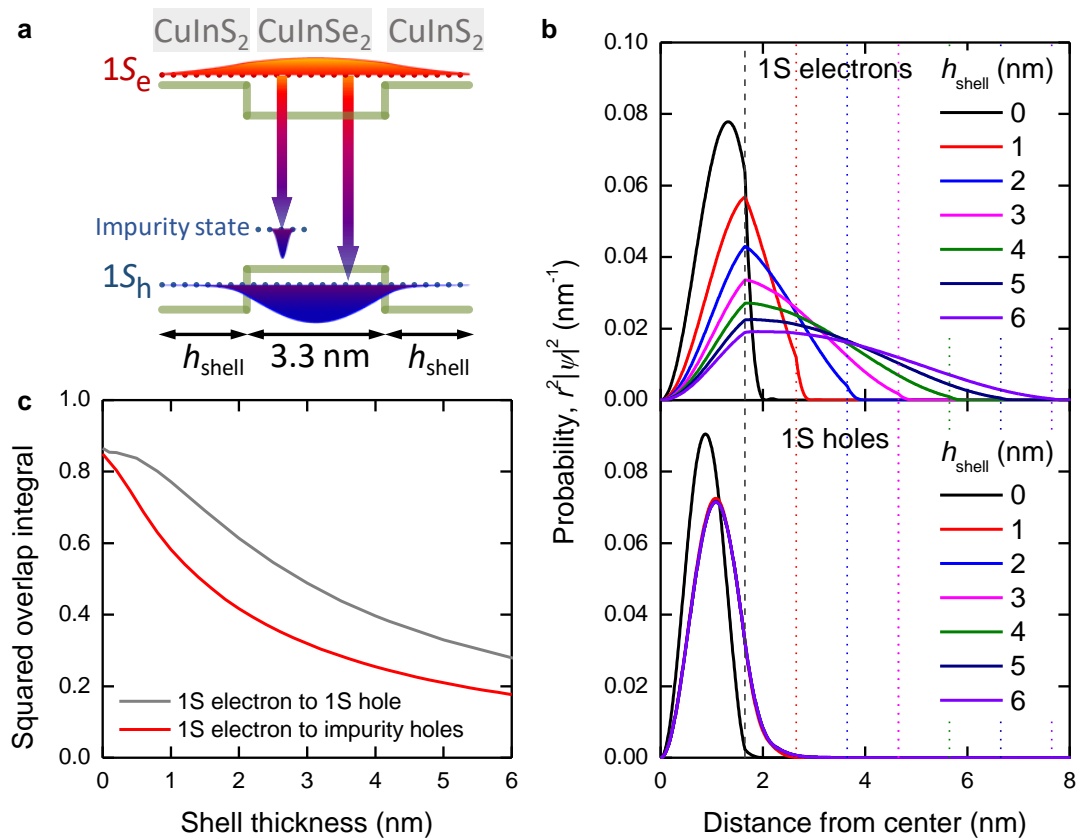


Figure 3.12 (a) Band structure of a CISE/CIS core/shell QD (3.3 nm-diameter core, 2 nm-thick shell) with energy levels and wave functions of 1S electron, 1S hole and impurity hole. (b) Normalized radial distribution functions for 1S electron and 1S hole of CISE/CIS core/shell QDs. The core diameter is 3.3 nm. The shell thickness varies from 0 (bare CISE QD) to 6 nm. Dashed vertical lines show the core/shell boundaries; dotted vertical lines show the shell/vacuum boundaries for each value of shell thickness. (c) Squared OI of the 1S electron state and hole states (1S hole and impurity hole) in CISE/CIS core/shell QDs as a function of shell layer thickness.

3.3 Fabrication and measurement of CuInSe₂/CuInS₂ “giant” core/shell quantum dots-based photoanode for solar-driven photoelectrochemical hydrogen production

3.3.1 Fabrication of CuInSe₂/CuInS₂ “giant” core/shell quantum dots-sensitized photoanode

TiO₂ films were first prepared: FTO glass substrates were cleaned ultrasonically for 15 min in Triton™ X-100, acetone, ethanol, respectively, followed by rinsing in DI water and drying in N₂ gaseous flow. The cleaned FTO glass substrates were further treated in a UV-ozone cleaner for 10 min to eliminate surface organic contamination. A blocking layer of TiO₂ was then deposited on FTO substrates by spin coating at 6000 r.p.m. for 30 s using the commercial

solution Ti-Nanoxide BL/SC. Subsequently, as-prepared TiO₂ films were annealed at 500 °C in an oven for 30 min and cooled down to room temperature. Titania paste containing a mixture of nanoparticles ~20 nm and 450 nm in diameter (18 NR-AO) was used and tape-casted on FTO substrates and kept in air for 12 min, to obtain a homogeneous distribution. The films were dried at 120 °C for 6 min. The same titania paste (18 NR-AO) was then deposited again on top of FTO substrates by using the tape-casting technique and following procedures of spreading and drying (as-casted TiO₂ films were kept in air for 12 min and dried at 120 °C for 6 min). The electrodes were finally sintered at 500 °C for 30 min in an oven and cooled down to achieve the TiO₂ films.

To fabricate QDs-sensitized photoanode, EPD was used to deposit QDs on TiO₂ films. A pair of TiO₂ FTO glasses were vertically immersed in QDs solution and the distance between them was adjusted at 1 cm. A direct current (DC) bias of 50 V was applied for 60 min. To remove the absorbed QDs from the surface of the TiO₂ film, the as-deposited TiO₂/QDs electrode was rinsed with toluene at half the deposition time and at the end of the EPD procedure. For ligand exchange, the sample was then immersed in a hexadecyltrimethylammonium bromide (CTAB) solution (10 mg/ml in methanol) for 60 s and washed with methanol. To obtain an improved crystallization of QDs, the TiO₂/QDs film was placed in a vacuum container and post-annealed at 180 °C for 40 min. Subsequently, the SILAR method was used to deposit a ZnS capping layer on as-prepared TiO₂/QDs electrodes to prevent photocorrosion. In a typical ZnS deposition cycle, the TiO₂/QDs electrode was immersed into a 0.1 M solution of Zn(Ac)₂ for 1 min and then into 0.1 M solution of Na₂S for 1 min. After each immersion, the electrode was rinsed with corresponding solvents of methanol and methanol/DI water (1:1 V/V), respectively, and then dried in N₂ flow. After the SILAR procedure, the surface (excluding the active area) of the photoanode was covered with epoxy resin to complete device fabrication.

3.3.2 Incident photo to current efficiency measurement and theoretical calculation of hydrogen generation rate

The Incident photon to current efficiency (IPCE) describes the ratio of photogenerated electrons collected by the electrodes over the number of incident monochromatic photons. To derive the IPCE values, we performed current–voltage measurements using different band-pass optical

filters. IPCE can be calculated by using the following equation:

$$\text{IPCE}\% = \frac{c \times h}{e} \frac{J(\text{A}/\text{cm}^2)}{\lambda(\text{nm}) \times P(\text{W}/\text{cm}^2)} \times 100 \quad (3.7)$$

Where J is the photocurrent density, P is the incident radiation intensity at a given wavelength, λ is the wavelength of the incident photon, c , h , and e are the speed of light, Planck's constant, and the elementary electric charge, respectively. To confirm the contribution of infrared photons to the photocurrent, we applied band-pass filters with wavelength center at 405 nm, 460 nm, 505 nm, 694 nm, 785 nm, 855 nm, 940 nm. For each filter, the incident radiation intensity at the position of the sample was measured by Newport power-meter.

The theoretical number of moles of hydrogen was obtained according to Faraday's law¹⁵⁸:

$$q = nF \quad (3.8)$$

With the definitions of electrolysis based on the following equations:

$$n = \frac{m}{m_e} \quad \text{and} \quad q = \int_{t_1}^{t_2} I dt \quad (3.9)$$

Where n is the number of equivalents, m is the mass of the substance liberated at an electrode in grams (g), m_e is the molar mass of the substance in grams per mol (g/mol), i.e. n equals to the number of moles. A common assumption on the current being constant over time, allow us to use the mathematical equivalent that can be simplified as⁹⁹:

$$n = \frac{1}{z} \frac{q}{F} = \frac{1}{z} \frac{I \times t}{F} \quad (3.10)$$

Where z is the number of transferred electrons per mole of water (i.e. $z=2$), q is the electric charge in coulombs (C), F is the Faraday constant (i.e. 96484.34 C/mole), I is the photocurrent in amperes (A) and t is time in seconds (s).

3.3.3 Photoelectrochemical performance of CuInSe₂/CuInS₂ “giant” core/shell quantum dots-sensitized photoanode

TEM image and corresponding EDS spectra of TiO₂/Zn-CISe/6CIS g-QDs heterostructure is shown in **Figure 3.13**, demonstrating that the QDs (denoted by white dashed circles) are homogeneously dispersed on the surface of TiO₂ nanoparticles without any noticeable aggregation.

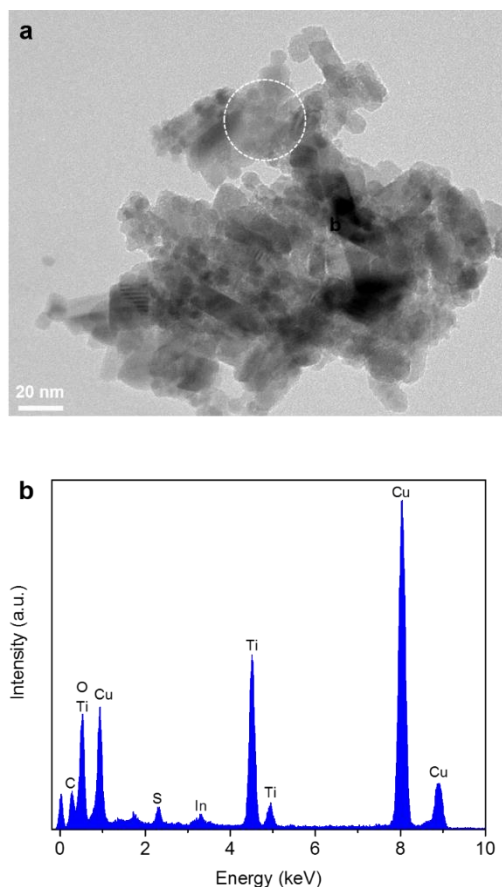


Figure 3.13 (a) TEM image of $\text{TiO}_2/\text{Zn-CISe}/6\text{CIS}$ g-QDs heterostructure with uniform distribution of QDs (white dash circle represents QDs on the surface of TiO_2). (b) EDS spectra of $\text{TiO}_2/\text{Zn-CISe}/6\text{CIS}$ g-QDs heterostructure. Elements of Zn and Se are not detected, due to their relatively small amount in the QDs.

Cross-section SEM imaging and corresponding EDS analysis of the Zn-CISe/6CIS g-QDs-sensitized photoelectrode are displayed in **Figure 3.14**. The thickness of the mesoporous TiO_2 film is estimated to be $\sim 20.5 \mu\text{m}$ (**Figure 3.14a**). EDS spectra (**Figure 3.14b**) and two-dimensional (2D) EDS mapping (**Figure 3.14c-i**) exhibit the presence of Cu, In, Se, S, Zn, Ti and O, consistent with the chemical composition in the Zn-CISe/6CIS g-QDs-sensitized photoanode. The element of In has overlap EDS signal with Sn, leading to the richer EDS signal of In at the surface. Similarly, due to the relatively low molar concentration of Se in the g-QDs, the EDS signal of Se is weaker in the TiO_2 film compared to other elements, such as In and Cu. The observed stronger Se signal in the substrate with respect to that in the TiO_2 film is due to the additional contribution from the O signal because of elemental Se overlapping with O (**Figure 3.14d**). The relative mass concentration of Zn-CISe/6CIS g-QDs with respect to TiO_2 is reported in **Figure 3.14b** (the content of Zn is much higher as we deposited 2 ZnS layer on

the QDs-based photoanode to protect photocorrosion), whereas semi-quantified QD loading amounts in the TiO₂ film are presented in the EDS line scan (**Figure 3.14j**, measured along the yellow line in **Figure 3.14a**). In parallel, cross-sectional SEM imaging and relevant EDS analysis of Zn-CISe/13CIS g-QDs-sensitized photoanode are reported in **Figure 3.15**. All the EDS analyses demonstrate the uniform dispersion of g-QDs in the TiO₂ film.

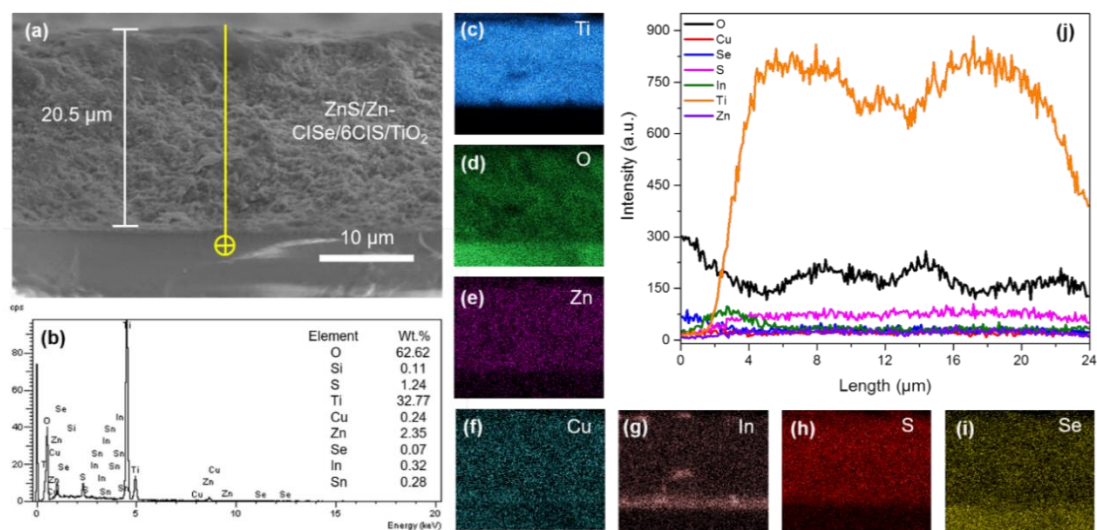


Figure 3.14 (a) Cross-sectional SEM image of Zn-CISe/6CIS g-QDs-sensitized photoelectrode and relevant (b) EDS spectra of all chemical composition with relative mass concentration, (c) EDS 2D mapping of all the elements including (c) Ti, (d) O, (e) Zn, (f) Cu, (g) In, (h) S and (i) Se, and (j) EDS line scan illustrating the semi-quantified variation of elements along the yellow line (highlighted in the SEM image).

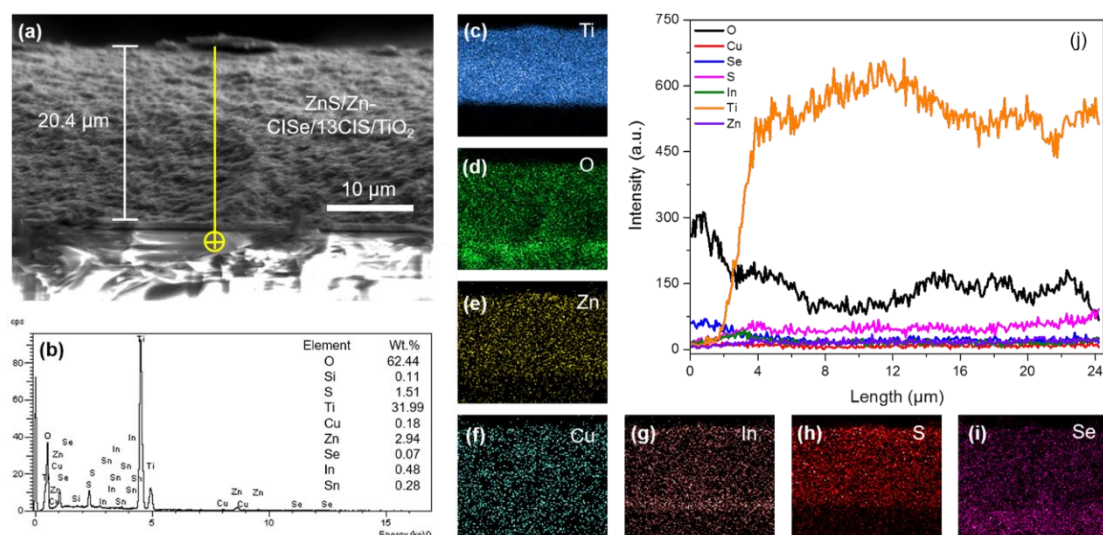


Figure 3.15 (a) Cross-sectional SEM image of Zn-CISe/13CIS g-QDs-sensitized photoanode and corresponding (b) EDS spectra. EDS mapping analysis of (c) Ti, (d) O, (e) Zn (f) Cu (g) In (h) S (i) Se and (j) EDS line scan illustrating the semi-quantified variation of elements along the yellow line (highlighted in SEM image).

The approximate band alignment and schematic diagram of Zn-CISe/CIS g-QDs-sensitized photoanode for PEC cells is illustrated in **Figure 3.16a**. The Zn-CISe/CIS g-QDs can form a favorable band alignment with TiO₂ for efficient charge dissociation of photogenerated carriers at the QDs/TiO₂ interface, where photoexcited holes oxidize the sacrificial agent (Na₂S and Na₂SO₃) in the electrolyte and the electrons are injected into TiO₂, collected by the FTO electrode and transferred to the Pt counter electrode for water reduction to produce hydrogen

18.

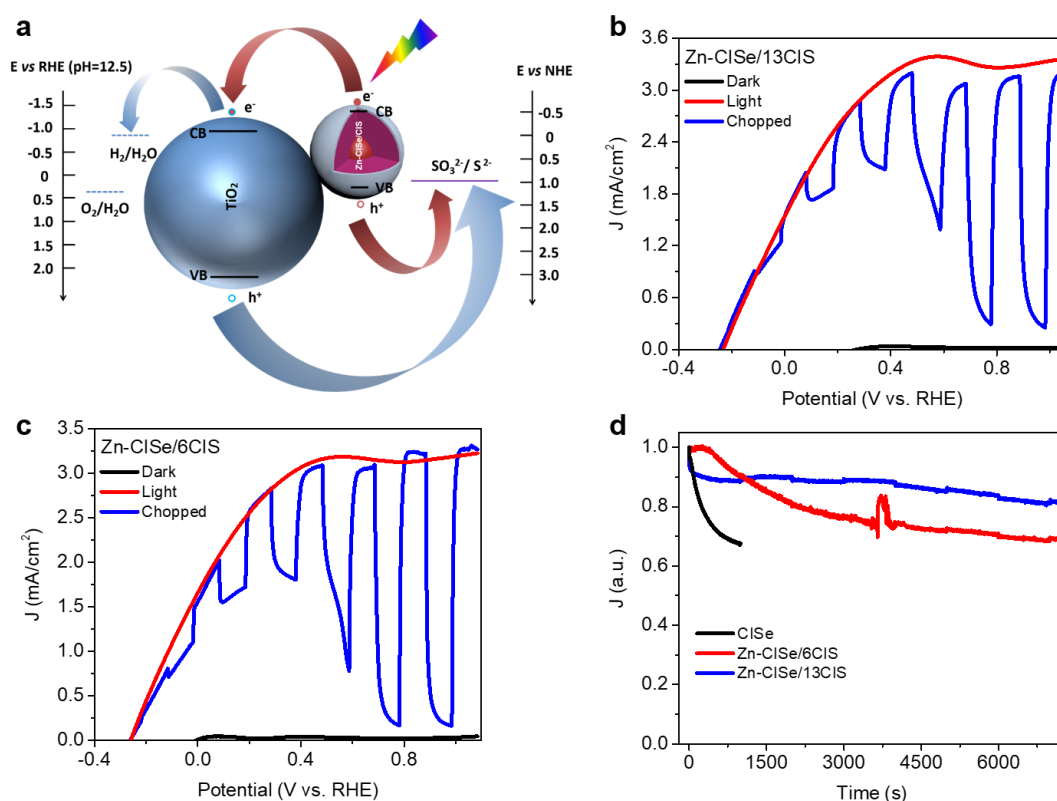


Figure 3.16 (a) Approximate band alignment and schematic diagram of Zn-CISe/CIS g-QDs-sensitized photoanodes. Photocurrent density-bias potential dependence (versus RHE) of (b) Zn-CISe/13CIS g-QDs and (c) Zn-CISe/6CIS g-QDs-sensitized photoanodes in the dark (black curve), under continuous (red curve) and chopped (blue curve) illumination (AM 1.5G, 100 mW/cm²). (d) Photocurrent density as a function of time (stability measurements) of TiO₂/CISe/ZnS (black curve), TiO₂/Zn-CISe/6CIS/ZnS (red curve) and TiO₂/Zn-CISe/13CIS/ZnS (blue curve) photoelectrodes at 0.8 V versus RHE under AM 1.5G irradiation (100 mW/cm²).

Figure 3.16b and c displays the photocurrent density as a function of applied potential for Zn-CISe/13CIS and Zn-CISe/6CIS g-QDs-sensitized photoanodes in the dark (black curve), under continuous (red curve) and chopped (blue curve) illumination (AM 1.5 G, 100 mW/cm², 30 cm from the sun simulator to PEC cell), which exhibits a saturated photocurrent density of ~3 and

3.1 mA/cm² obtained at ~0.8 V versus the RHE, respectively. For comparison, the CISE QDs-sensitized photoanode only shows a saturated photocurrent density of ~1.5 mA/cm² (**Figure 3.17**). The Zn-CISE/13CIS and Zn-CISE/6CIS g-QDs-sensitized photoanodes exhibit higher photocurrent density than bare CISE QDs-sensitized photoanode, which we attribute to both their enhanced light absorption and quasi-type II band alignment. The PEC cell based on the bare TiO₂ photoanode (**Figure 3.18**) exhibits a saturated photocurrent density of ~0.25 mA/cm², which is much lower compared to the QDs-sensitized photoanodes (~1.5, 3 and 3.1 mA/cm²), indicating the QDs loading in the TiO₂ mesoporous film is the dominant contribution to the enhancement of saturated photocurrent density.

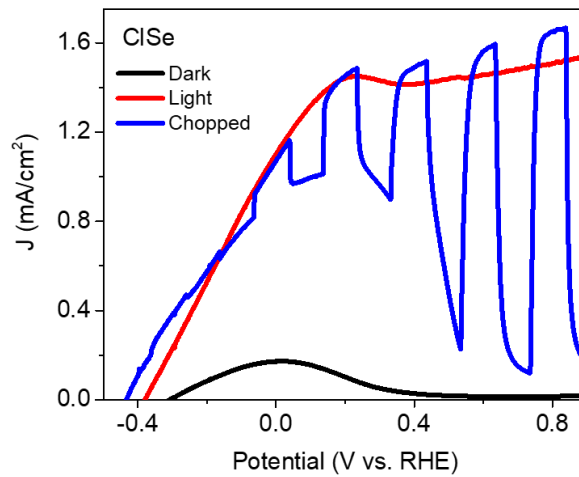


Figure 3.17 Photocurrent density versus bias potential (versus RHE) for TiO₂/CISE/ZnS photoanode in the dark (black curve), under continuous (red curve) and chopped (blue curve) illumination (AM 1.5 G, 100 mW/cm²).

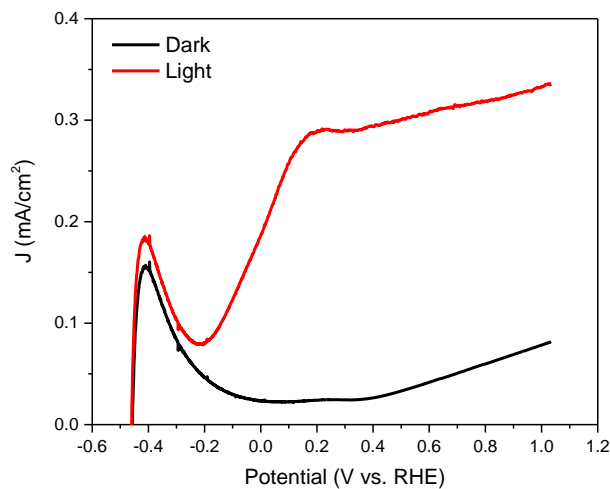


Figure 3.18 Current density versus bias potential (vs RHE) for FTO/TiO₂ photoanode with photocurrent density of ~0.25 mA/cm² under illumination of one sun (AM 1.5G, 100 mW/cm²).

The saturated photocurrent density of Zn-CISe/13CIS and Zn-CISe/6CIS g-QDs-sensitized photoanodes are higher than previous reports of green NIR QDs (CuInSeS, Ag₂S and CuInS₂ QDs with photocurrent density of ~0.3, 0.6 and 2 mA/cm², respectively) sensitized photoelectrodes for hydrogen generation^{118, 129, 139}. The incident photo to current efficiency (IPCE) was derived from current-voltage measurements (**Figure 3.19**). The results show the contribution of NIR photons, even largely decreased compare to the UV-visible photons, which are consistent with the broad UV-visible-NIR absorption of the Zn-CISe/CIS g-QDs, with contribution to IPCE originating from the UV-vis and NIR region, up to 1000 nm.

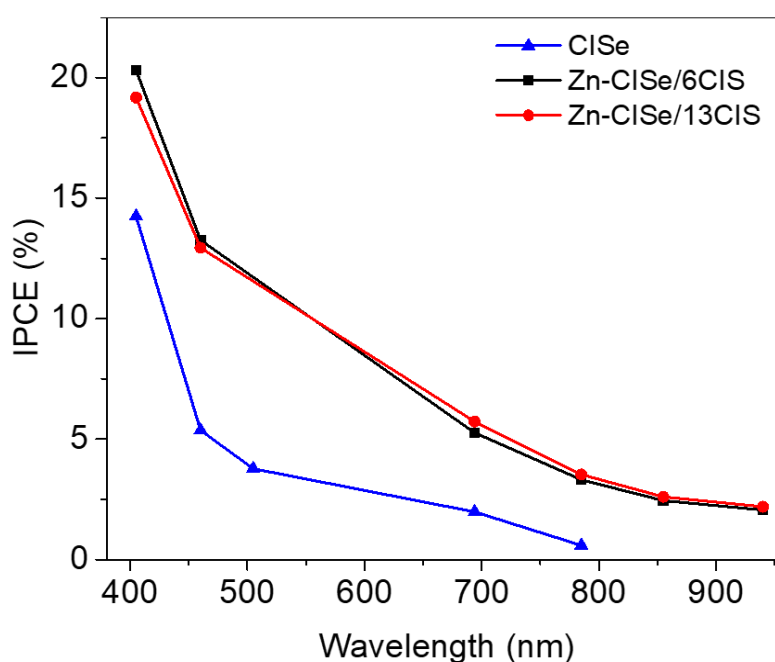


Figure 3.19 IPCE spectra of TiO₂/CISe/ZnS, TiO₂/Zn-CISe/6CIS and TiO₂/Zn-CISe/13CIS QDs-sensitized photoelectrodes at 0.8 V versus RHE.

We further measured the PEC performance of photoanodes sensitized by intermediate products of Cu₂Se, Cu₂Se/6Cu₂S and Cu₂Se/13Cu₂S QDs (**Figure 3.20**), showing saturated photocurrent of ~0.8, 0.85 and 0.55 mA/cm² respectively, which are much lower than the Zn-CISe/CIS g-QDs. While the PEC cells using CdSe, CdSe/6CdS and CdSe/13CdS QDs-sensitized photoanodes exhibit much higher photocurrent of ~4.5, 6 and 7 mA/cm² (**Figure 3.21**) than that of the Zn-CISe/CIS g-QDs. However, the highly toxic heavy metal of Cd hinders their potential applications due to environmental and health concerns.

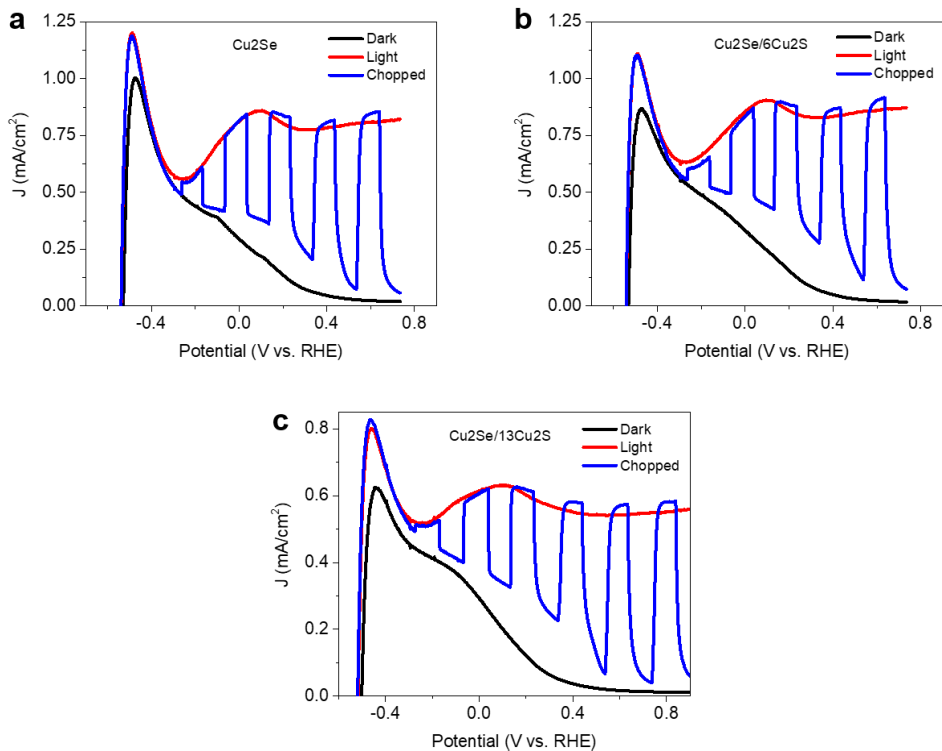


Figure 3.20 Photocurrent density versus bias potential (versus RHE) for (a) the TiO₂/Cu₂Se/ZnS, (b) TiO₂/Cu₂Se/6Cu₂S/ZnS and (c) TiO₂/Cu₂Se/13Cu₂S/ZnS photoanodes in the dark (black curve), under continuous (red curve) and chopped (blue curve) illumination (AM 1.5 G, 100 mW/cm²).

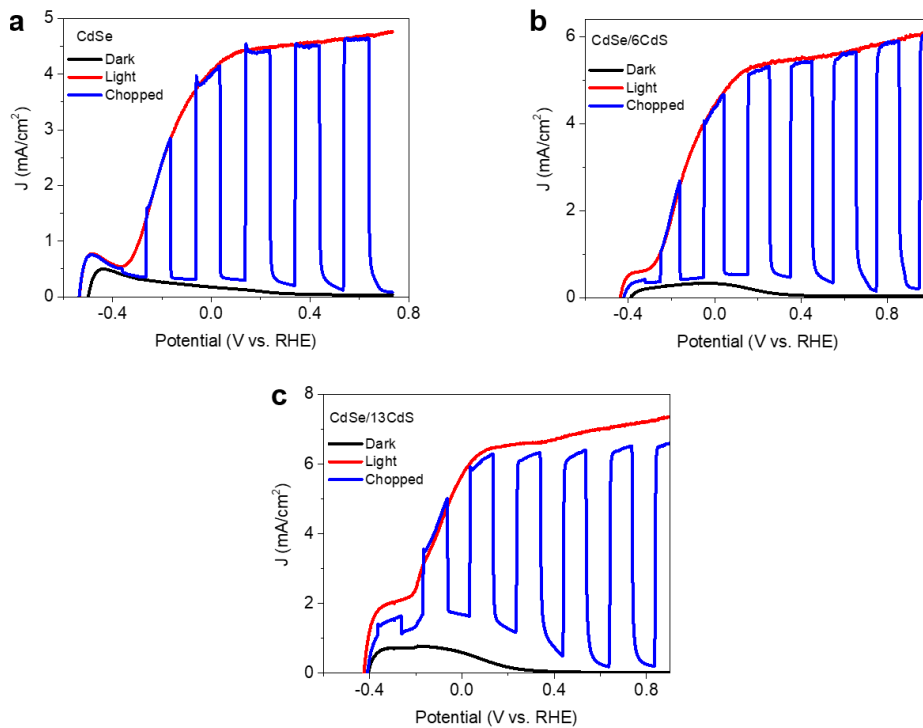


Figure 3.21 Photocurrent density versus bias potential (vs RHE) for (a) the TiO₂/CdSe/ZnS, (b) TiO₂/CdSe/6CdS/ZnS and (c) TiO₂/CdSe/13CdS/ZnS photoanodes in the dark (black curve), under continuous (red curve) and chopped (blue curve) under illumination of one sun (AM 1.5G, 100 mW/cm²).

Figure 3.16d displays the photocurrent density as a function of time for $\text{TiO}_2/\text{Zn-CISe}/\text{ZnS}$ (black curve), $\text{TiO}_2/\text{Zn-CISe}/6\text{CIS}/\text{ZnS}$ (red curve) and $\text{TiO}_2/\text{Zn-CISe}/13\text{CIS}/\text{ZnS}$ (blue curve) photoanodes measured at 0.8 V versus RHE under standard AM 1.5G solar illumination ($100 \text{ mW}/\text{cm}^2$). To better understand the percentage of decay trend, we divide the maximum photocurrent density of the photoanodes to make the curves decay from the value of 1. The bare CISe QDs based PEC cell shows a rapid decay of photocurrent density, $\sim 30\%$ drop from the initial photocurrent density only after $\sim 0.2 \text{ h}$ illumination, while the Zn-CISe/6CIS and Zn-CISe/13CIS g-QDs based PEC cells show only $\sim 31\%$ and $\sim 20\%$ drop from the initial photocurrent density even after 2h illumination. This improvement is due to the formation of a very thick CuInS_2 shell on the CuInSe_2 core for enhanced chemical- and photo- stability in this type of NIR, heavy metal-free g-QDs during the anode preparation by EPD and further cell operation in corrosive electrolyte (pH of 12.5~13). The photostability of the PEC system based on Zn-CISe/6CIS and Zn-CISe/13CIS QDs-sensitized photoanodes is comparable with the best reported photoanode made of QDs (for instance, $\sim 30\%$ drop after 2 h for TiO_2 nanowire/CdS/Co-Pi structures and 30% drop after 20 min for TiO_2 nanorod/CdS/NiO/CdSe structures due to the photocorrosion of QDs-sensitized electrode)^{140, 141}, indicating good stability in these PEC systems. H_2 evolution was further estimated based on the CdSe/CdS g-QDs in our previous work⁶⁷, which serves as a reference to calculate the H_2 evolution of PEC cells based on Zn-CISe/6CIS and Zn-CISe/13CIS g-QDs-sensitized photoanodes (**Figure 3.22**).

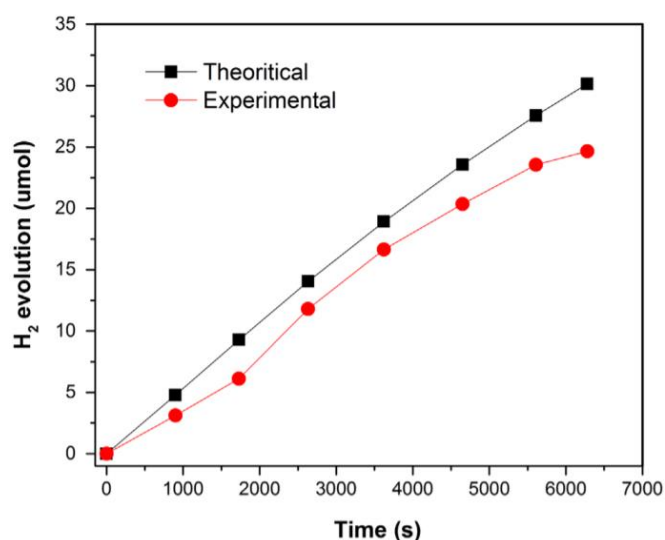


Figure 3.22 H_2 evolution of CdSe/CdS g-QDs, as a function of time under $100 \text{ mW}/\text{cm}^2$ illumination with AM 1.5 G filter. The evolution of H_2 exhibits a nearly linear increase over time⁶⁷.

This approach is quite reliable, because the only difference in our g-QDs based PEC system is the type of g-QDs, and all other components including electrolyte, counter electrode and reference electrode (Ag/AgCl) are the same. The evolution of H₂ shows a nearly linear increase over time and is in good agreement with the theoretical curve (**Figure 3.22**). We use the saturated photocurrent density (**Figure 3.16b** and **c**) and integrated the current density (**Figure 3.16d**), and the theoretical hydrogen generation rate of Zn-CISe/6CIS and Zn-CISe/13CIS g-QDs-sensitized photoanode is $\sim 24.3 \text{ mL}\cdot\text{cm}^{-2}\cdot\text{day}^{-1}$ and $\sim 26.5 \text{ mL}\cdot\text{cm}^{-2}\cdot\text{day}^{-1}$, respectively.

3.3 Summary

We demonstrated the synthesis of Zn-CISe/CIS g-QDs made of heavy metal-free elements using the sequential cation exchange approach. Morphology investigations confirmed the thick shell of CuInS₂ and WZ crystal structure of as-synthesized g-QDs. The spherical shape of CISe/CIS g-QDs can be accurately preserved and the shell thickness can be controlled by tuning the width of the CdSe/CdS g-QDs template. ICP-OES measurements demonstrate the nearly full exchange of heavy metal of Cd from an initial CdSe/CdS g-QDs template to a final product consisting of heavy metal-free Zn-CISe/CIS g-QDs. The optical properties of such g-QDs are characterized by tunable absorption, PL peak and lifetime in the NIR region by varying the shell thickness, demonstrating the quasi-type II band alignment and paving the way towards potential applications in QDs-based photovoltaic devices. The PEC performance of photoanodes sensitized with Zn-CISe/CIS g-QDs shows an outstanding saturated photocurrent density as high as $\sim 3.1 \text{ mA}/\text{cm}^2$. The stability of the as-fabricated QDs-sensitized photoanode is comparable to the best reported QD-based anodes^{123, 140, 141}.

CHAPTER 4 SYNTHESIS AND CHARACTERIZATION OF NEAR- INFRARED COLLOIDAL HETEROSTRUCTURED PYRAMIDAL “GIANT” CORE/SHELL QUANTUM DOTS FOR HIGH PERFORMANCE PHOTOELECTROCHEMICAL CELLS

In this section, NIR-emitting CISES/CdSeS/CdS heterostructured g-QDs with pyramidal-shape are prepared by using a facile two-step approach. The crystalline structure of CdSeS/CdS shell is demonstrated to be zinc blende (ZB) phase. The optical properties of these pyramidal-shaped g-QDs show a NIR emission (~830 nm) with high PLQY. The elongated PL lifetime with increasing shell thickness manifests the efficient spatial separation of electron/hole in these pyramidal-shaped heterostructured g-QDs, which is also proved by the theoretical calculations. QDSCs and QDs-based PEC devices fabricated by these pyramidal-shaped g-QDs exhibit outstanding performance as a result of their efficient spatial electron-hole separation/transport.

I conducted most of the experimental work, and the theoretical part was done by Dr. Xiang-Tian Kong. Dr. Haiguang Zhao assisted me a lot for the optical characterization, I wrote the draft of the manuscript.

4.1 Synthesis and characterization of near-infrared colloidal heterostructured pyramidal “giant” core/shell quantum dots

Tailoring the shape/chemical composition of heterostructured QDs (e.g. dot-in-rod and tetrapod structure) has been demonstrated as an effective method to control their charge carrier/exciton dynamics^{159, 160}. However, for optimization of these heterostructured QDs-based optoelectronic devices, it is still challenging to address some limitations of these heterostructures (e.g. stability). The g-QDs have shown outstanding photo-chemical/physical stability and optimized optical properties such as prolonged PL lifetime. Most of g-QDs possess spherical shape and are able to efficiently separate electrons and holes in all directions, while the electron-hole wave functions still have some overlap for fast recombination^{49, 57, 63, 65, 143, 147}. In recent years, non-spherical heterostructured QDs have shown efficient electron-hole separation, as exhibited by

their very long PL lifetime ¹⁵⁹, holding great potential for high performance photovoltaic applications .

4.1.1 Synthesis of near-infrared colloidal heterostructured pyramidal $\text{CuInSe}_x\text{S}_{2-x}/\text{CdSeS}/\text{CdS}$ “giant” core/shell quantum dots

To synthesize heterostructured pyramidal “giant” $\text{CuInSeS}/\text{CdSeS}/\text{CdS}$ QDs, pyramidal CuInSeS QDs were first synthesized by the method described elsewhere ⁵⁴. Afterwards, “giant” $\text{CuInSeS}/\text{CdSeS}/\text{CdS}$ core/shell QDs were synthesized via the modified approaches reported by Klimov’s group, which were normally employed in the synthesis of $\text{CuInS}_2/\text{Zn}(\text{Cd})\text{S}$ core/shell QDs ^{55, 94}. For growth of the shell on CuInSeS QDs, 1 mL of 0.2 M Cd-oleate prepared by dissolving the CdO in OA and ODE was first injected into the reaction solution ($\sim 1 \times 10^{-7}$ mol of CuInSeS QDs in 5 mL of ODE) at 160 °C, then a mixture of 0.2 M Cd-oleate (10 mL), S (2 mmol) powder dissolved in 2 mL of TOP (97%) and 8 mL of ODE is added dropwise into the reaction solution heated to 215 °C at the rate of 4 mL/h for 5 h.

During the injection of Cd/S precursors, i.e. the growth of g-QDs, for convenience, intermediate products formed at different growth stages were extracted and labeled as CdS#1 to CdS#9 according to the injection volumes of Cd and S precursors, as listed in **Table 4.1**.

Table 4.1 Detailed information for injection volumes of mixed Cd and S precursors and corresponding sample labels during shell growth of heterostructured $\text{CuInSeS}/\text{CdSeS}/\text{CdS}$ g-QDs.

Injection Volumes	0.5 mL	1.4 mL	2.5 mL	3.2 mL	4 mL	6 mL	10 mL	15 mL	20 mL
Sample Labels	CdS#1	CdS#2	CdS#3	CdS#4	CdS#5	CdS#6	CdS#7	CdS#8	CdS#9

CdS#6 g-QDs with optimized alloyed shell thickness were synthesized by introducing a CdSeS interfacial layer with additional Se precursor: 1 mL of 0.2 M Cd-oleate was first injected into the reaction solution ($\sim 1 \times 10^{-7}$ mol of CuInSeS QDs in 5 mL of ODE and 5 mL of OLA) at 160 °C, then a mixture of 0.2 M Cd-oleate (1.5 mL), 0.4 M Se in TOP (0.75 mL), and 0.4 M S in ODE (0.75 mL) is added dropwise into the reaction solution heated to 215 °C at the rate of 4 mL/h, followed by injection of a mixture of 0.2 M Cd-oleate (1.5 mL) and 0.2 M S in ODE (1.5 mL) under 215 °C with a rate of 4 mL/h.

4.1.2 Structure and optical properties

Figure 4.1a shows representative TEM images of initial CISES core QDs, which exhibit a typical pyramidal shape with average size of 5.5 ± 0.7 nm (the sizes of these QDs are defined as the height of the projected triangles⁵⁴ and summarized in **Figure 4.2**). The inset HRTEM image displays a lattice spacing of 0.328 nm that is well indexed to the (112) plane of alloyed CISES QDs with chalcopyrite phase^{149, 161}, which is consistent with XRD and SAED patterns (**Figure 4.3**) of as-synthesized CISES QDs.

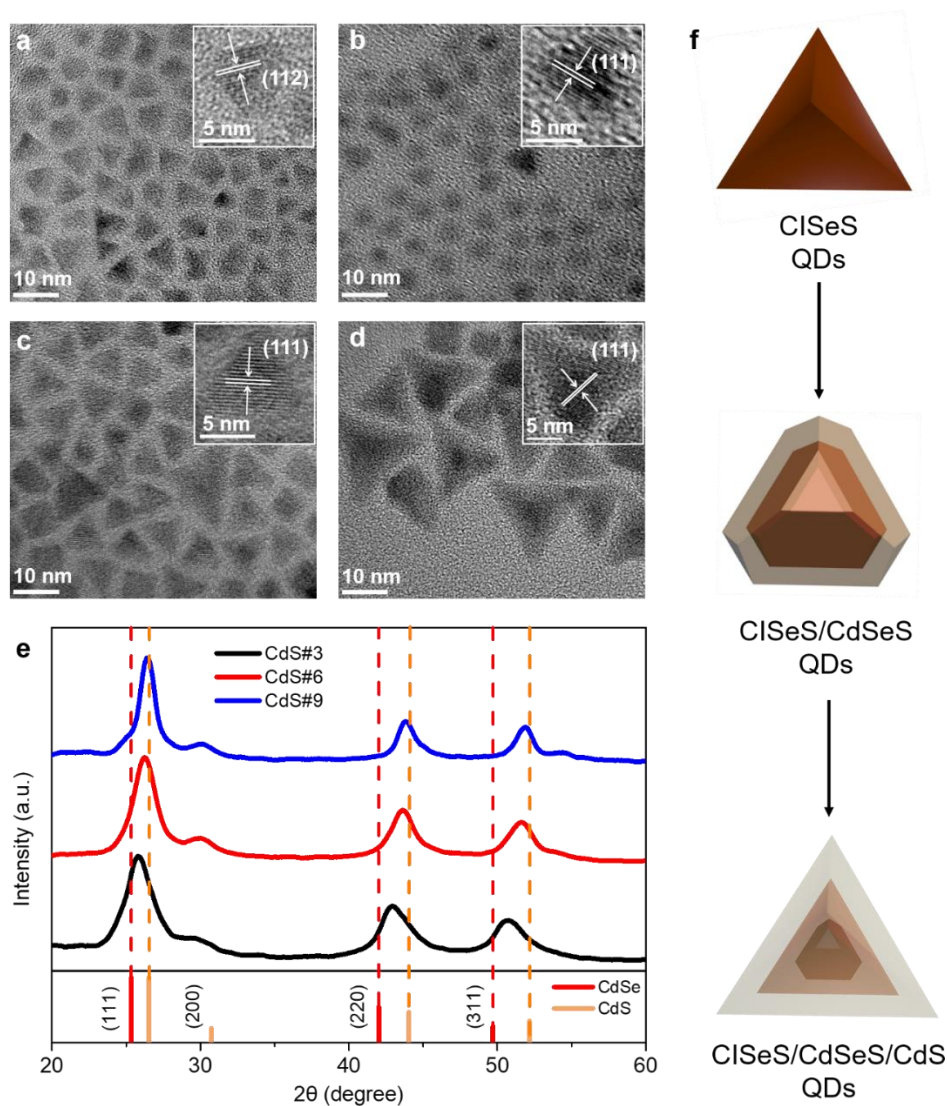


Figure 4.1 TEM images of (a) CISES with inset HRTEM images displaying (112) plane of chalcopyrite phase. TEM images of (b) CdS#3 and (c) CdS#6 QDs with inset HRTEM images exhibiting (111) plane of ZB phase CdSeS. (d) TEM images of CdS#9 QDs with inset HRTEM images showing (111) plane of ZB phase CdS. (e) XRD patterns of CdS#3, CdS#6 and CdS#9 QDs. (f) Schematic diagram of growth processes and structure of heterostructured CISES/CdSeS/CdS g-QDs.

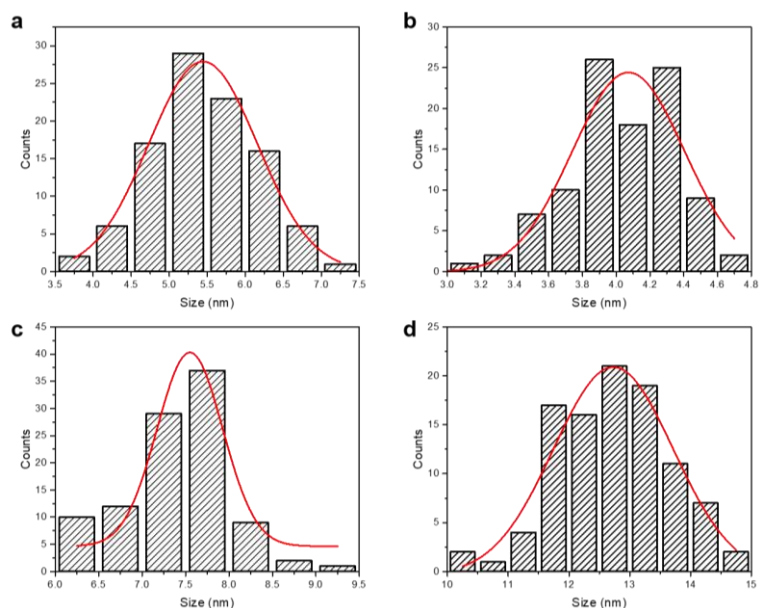


Figure 4.2 Size distribution of (a) CISeS, (b) CdS#3, (c) CdS#6 and (d) CdS#9 QDs, showing sizes of 5.5 ± 0.7 nm, 4.0 ± 0.3 nm, 7.4 ± 0.6 nm and 12.7 ± 0.9 nm, respectively. Sizes are measured as the height of projected triangles (distance from a vertex to the middle of the opposite side) in TEM images for at least 100 QDs.

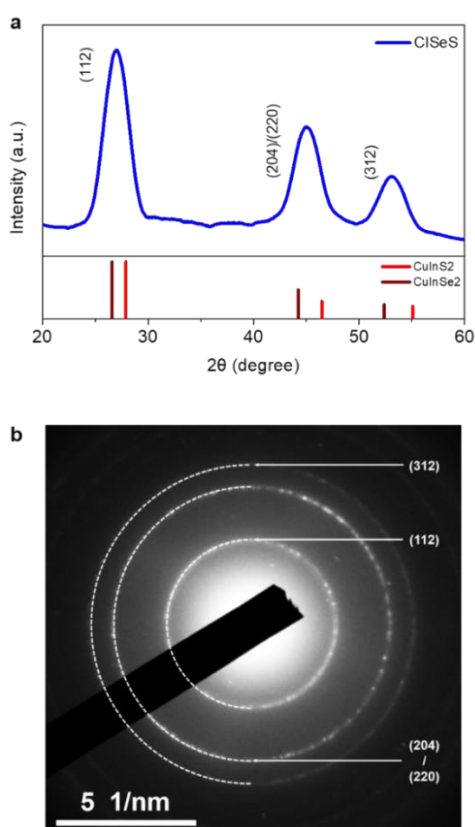


Figure 4.3 (a) XRD pattern of CISeS QDs films prepared by drying the dropped CISeS QDs solution on the top of silicon substrate. (b) SAED pattern of CISeS QDs. All of the diffraction peaks lie between (112), (204/220) and (312) facets of pure chalcopyrite CuInS_2 (JCPDS card no. 03-065-1572) and pure chalcopyrite CuInSe_2 (JCPDS card no. 00-040-1487), indicating the chalcopyrite phase and alloyed nature of as-prepared CISeS core QDs.

Compared with CISES QDs, TEM images of CdS#3 (with 2.5 mL of injected Cd/S precursors) QDs (**Figure 4.1b**) present a decreasing average size of 4.0 ± 0.3 nm and different shapes. The decreasing size of QDs is attributed to the cation exchange process following the injection of precursors at an early stage, which is consistent with previous work on similar QD systems (i.e. CuInS₂/CdS and CuInS₂/ZnS QDs)^{55, 94}. The cation exchange process in the synthesis of QDs usually leads to the formation of core/shell structures^{53, 92}. Unlike the pyramidal CISES QDs, the four corners of pyramids are not observed in CdS#3 sample (**Figure 4.1b** and **Figure 4.4**). We assume that these CdS#3 QDs possess a possibly quasi-octahedral shape that is formed by etching away the four corners of CISES pyramids during the cation exchange process^{55, 94}.

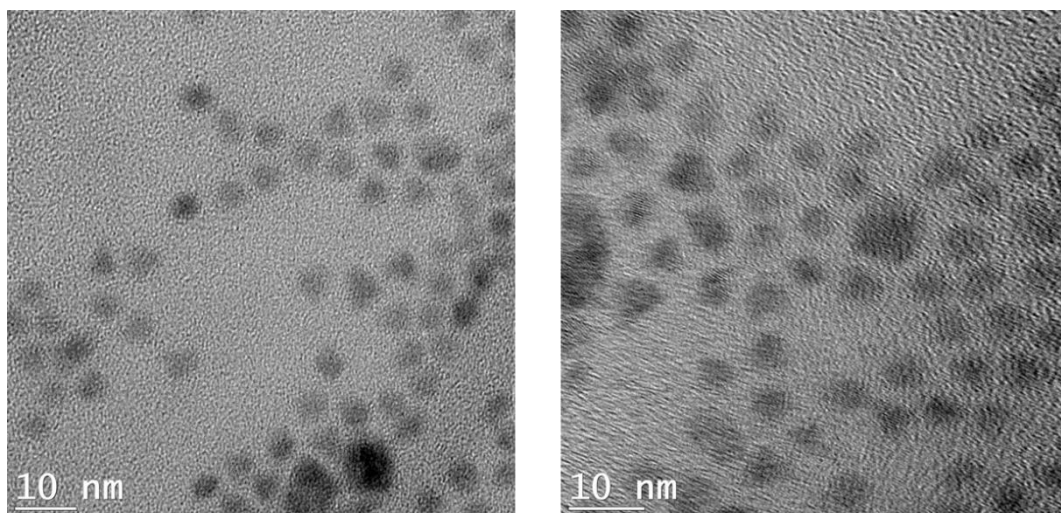


Figure 4.4 TEM of CdS#3 QDs, showing possible quasi-octahedral shape.

The HRTEM image of CdS#3 QDs (Inset image in **Figure 4.1b**) shows a lattice spacing of 0.343 nm, which lies between 0.335 nm [indexed to the (111) plane of ZB phase CdS] and 0.351 nm [indexed to the (111) plane of ZB phase CdSe] that is well indexed to the (111) plane of the alloyed ZB phase CdSeS. The diffraction peaks of CdS#3 QDs in the XRD pattern (**Figure 4.1e**) are found in between the diffraction peaks of pure ZB phase CdS and CdSe, indicating that CdSeS crystallizes in an alloyed ZB phase, which is consistent with its SAED patterns (**Figure 4.5a**).

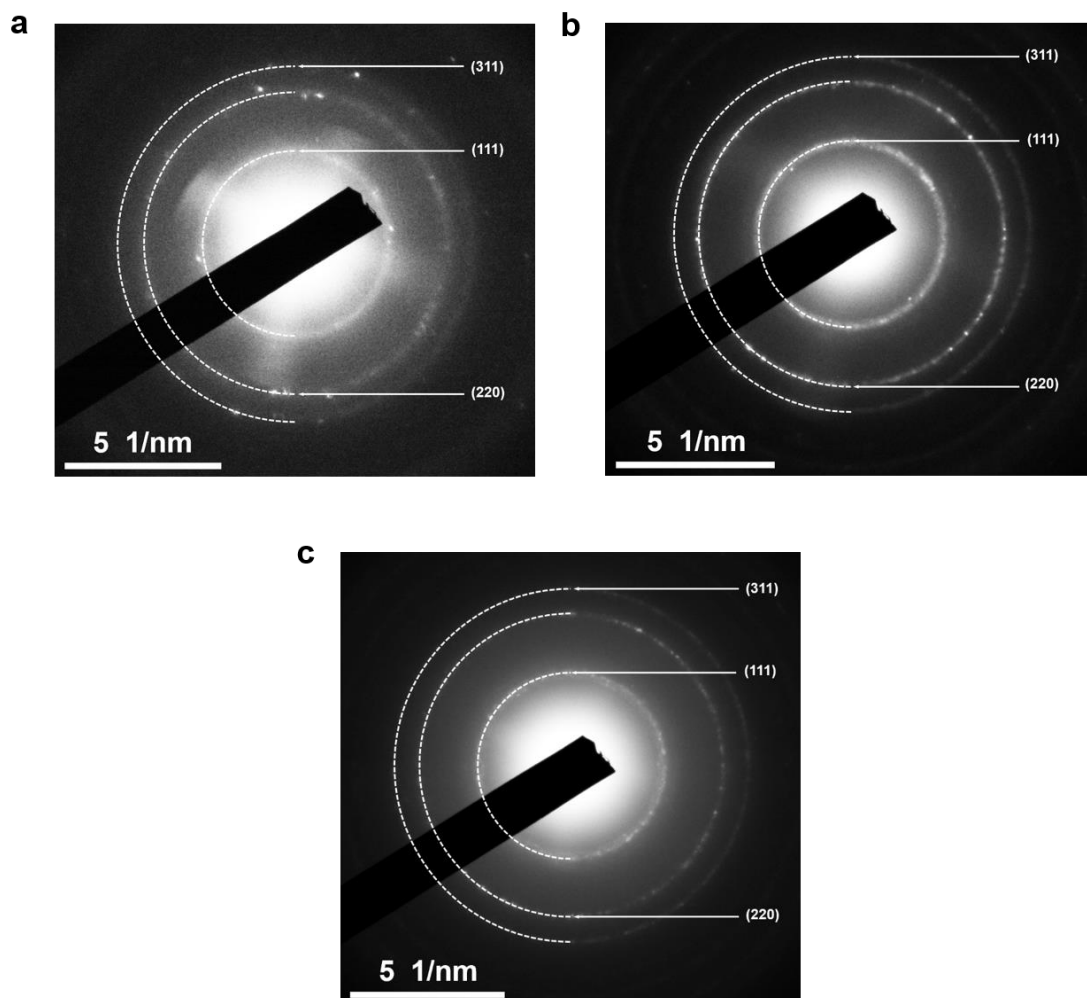


Figure 4.5 SAED patterns of (a) CdS#3, (b) CdS#6 and (c) CdS#9 QDs, which are consistent with the XRD patterns in Figure 4.1e.

There are no diffraction peaks of CISES core in the XRD patterns of CdS#3 QDs, which is attributed to the simultaneously decreasing size of the CISES core and the increasing CdSeS shell thickness during the cation exchange process. As a result, the signal of the XRD pattern is dominated by the CdSeS shell materials in CdS#3 QDs and the contribution from the CISES core is below the detection limit of XRD. These results show that the CdS#3 QDs are CISES/CdSeS core/shell QDs with ZB phase CdSeS shell. In particular, there was a core-etching effect at an early growth stage of g-QDs^{55, 94}: the pyramidal-shaped CISES core QDs were etched during the cation exchange process, resulting in CISES/CdSeS core/shell QDs with the quasi-octahedral shape.

Figure 4.1c displays TEM images of CdS#6 (with 6 mL of injected Cd/S precursors) QDs with an average size of 7.4 ± 0.6 nm and pyramidal shape. When increasing the injection volume of

Cd/S precursors, the CdS#3 QDs with quasi-octahedral shape was observed to grow at a faster rate at the four corners of the pyramids, leading to the larger size and restored pyramidal shape of CdS#6 QDs. This conclusion can also be drawn from the TEM images (**Figure 4.6c** and **d**) of QDs at growth stages between CdS#3 and CdS#6 QDs.

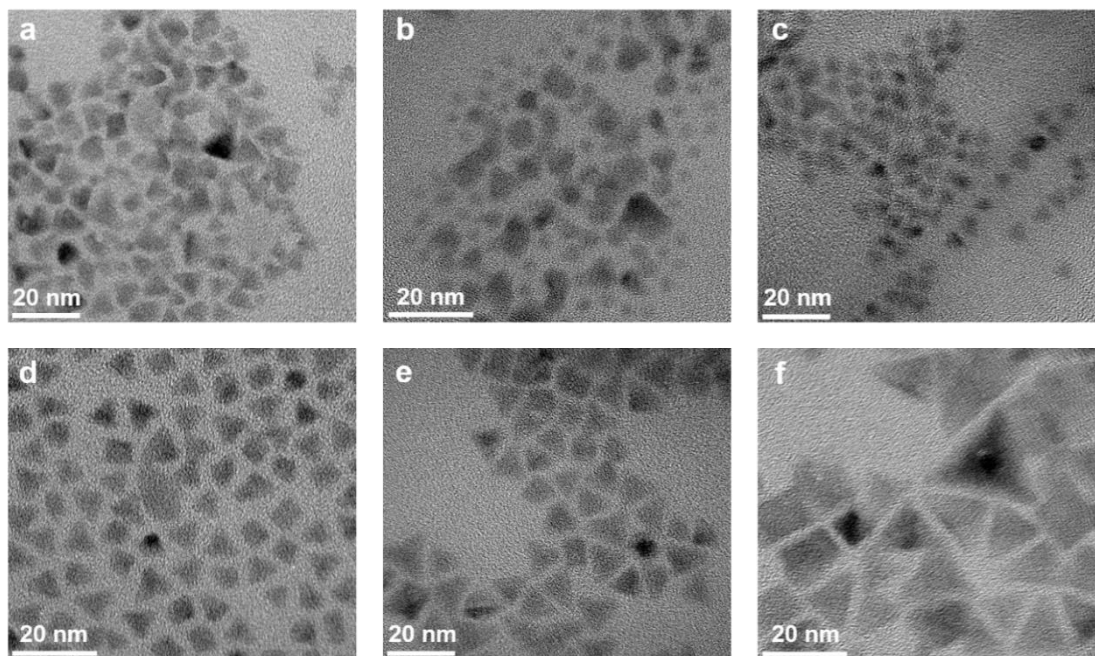


Figure 4.6 Representative TEM images of (a) CdS#1, (b) CdS#2, (c) CdS#4, (d) CdS#5, (e) CdS#7 and (f) CdS#8 QDs.

The HRTEM image (Inset image in **Figure 4.1c**), XRD (**Figure 4.1e**) and SAED (**Figure 4.5b**) patterns of CdS#6 QDs demonstrated that their shell materials consisted of alloyed ZB phase CdSeS. Nonetheless, the lattice spacing and diffraction peaks are very close to those of the pure ZB phase CdS, indicating a higher S/Se ratio in the CdS#6 QDs as compared with CdS#3 QDs. The higher S/Se ratio in CdS#6 QDs is attributed to the fact that the composition of Se is constant (from CISES QDs) during the entire reaction while the injection of S precursor leads to a decreasing ratio of Se and S in the resulting g-QDs. TEM images of CdS#9 (with 20 mL of injected Cd/S precursors) QDs are shown in **Figure 4.1d**, exhibiting heterostructured g-QDs with pyramidal shape and average size of 12.7 ± 0.9 nm. The HRTEM image (Inset image in **Figure 4.1d**), XRD (**Figure 4.1e**) and SAED (**Figure 4.5c**) patterns are well indexed to the ZB phase CdS, demonstrating the formation of the outer CdS shell in the subsequent growth stages of CdS#9 CdS. Moreover, the HRTEM image of CdS#9 g-QDs (**Figure 4.7**) clearly exhibits two (111) facets of the CdS shell, and the as-measured angle (observed from [110] direction)

of the projected triangle is 70.5° . This value is consistent with the three dimensional geometry of the pyramids, demonstrating that the CdS#9 QDs possess a pyramidal shape.

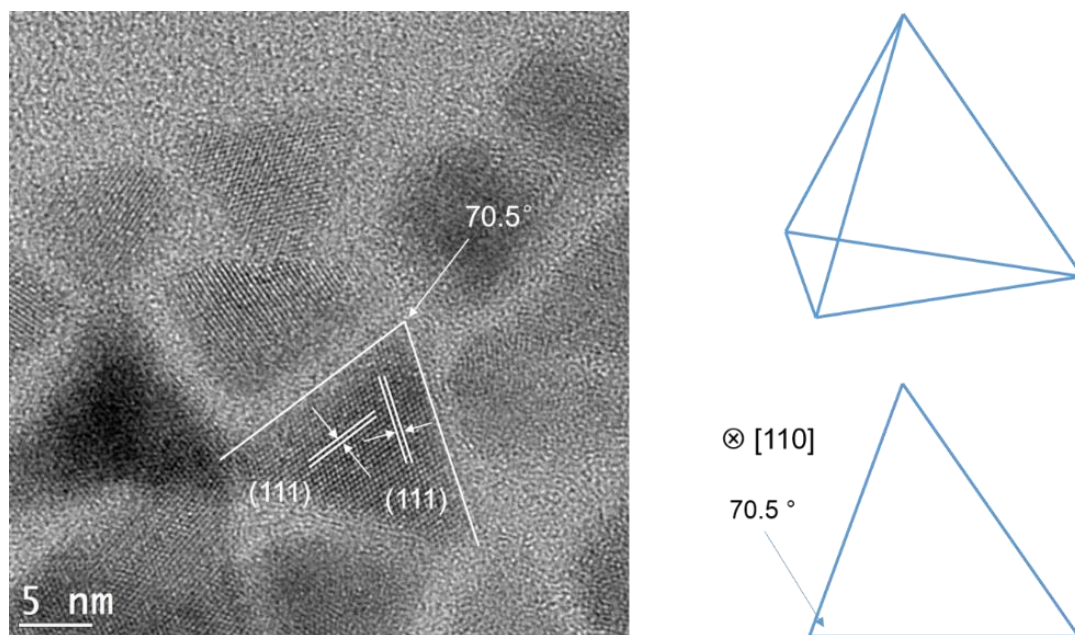


Figure 4.7 HRTEM image of CdS#9 g-QDs, showing two (111) facets and the angle of 70.5 degree observed from [110] direction, which is consistent with the three-dimensional pyramid's geometry.

TEM images and the corresponding size distribution of other growth stages of g-QDs are shown in **Figure 4.6** and **Figure 4.8**. Based on these results, we briefly summarize the growth dynamics of this type of heterostructured g-QDs, as illustrated in **Figure 4.1f**: the initial CISES core QDs with pyramidal shape were first etched so as to decrease the size and obtain a quasi-octahedral shape.

This is caused by an early cation exchange process (i.e. a common phenomenon in the growth of core/shell CuInSe(S)/Cd(Zn)S QDs^{55, 94}), which leads to the formation of CISES/CdSeS core/shell QDs with ZB phase CdSeS. The subsequent growth of the shell results in CISES/CdSeS core/shell g-QDs with higher S/Se ratio and increasing size of QDs, and the morphology of the QDs is restored to a pyramidal shape. With continued growth of QDs, an outer CdS shell with ZB phase is then formed on CISES/CdSeS core/shell g-QDs and leads to the growth completion of heterostructured pyramidal-shaped CISES/CdSeS/CdS g-QDs.

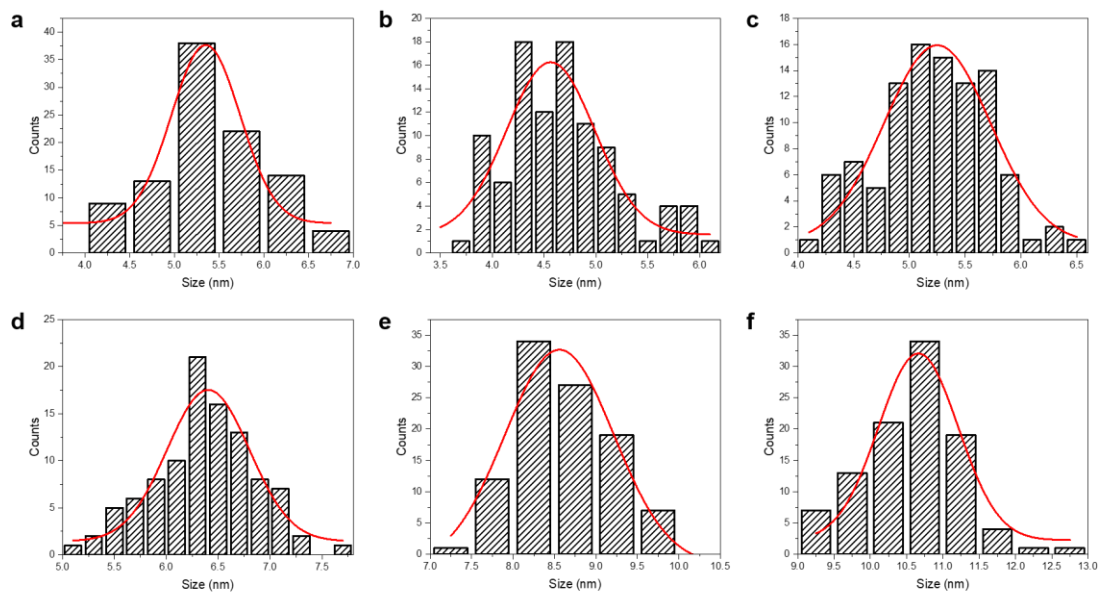


Figure 4.8 Size distribution of (a) CdS#1, (b) CdS#2, (c) CdS#4, (d) CdS#5, (e) CdS#7 and (f) CdS#8 QDs. Sizes were measured as the height of projected triangles (distance from a vertex to the middle of the opposite side) in TEM images for at least 100 QDs.

The pyramidal heterostructured CISES/CdSeS/CdS g-QDs were successfully synthesized by using pyramidal-shaped CISES QDs as initial core materials. The crystal structure of their shell materials could be easily controlled and was demonstrated to be ZB phase CdSeS and CdS. Usually, the CdS shell have a WZ phase or mixed WZ and ZB phase, due to the high reaction temperature (240 to 300 °C)^{49, 64, 83, 147}. In our case, due to the alloyed interfacial CdSeS layer that has the ZB crystalline structure, the subsequent growth of CdS (at 215 °C) conveniently crystallizes in the ZB phase. Generally, g-QDs such as CdSe/CdS and PbSe/CdSe/CdSe with ZB phase shell materials possess less structural defects as compared to their WZ counterparts, leading to superior optical properties such as high PLQY and suppressed photoblinking^{61, 162, 163}, which are promising candidates for optoelectronic devices, for instance, high performance QDs-based LEDs¹⁶⁴.

Figure 4.9a-c displayed the optical properties of heterostructured CISES/CdSeS/CdS g-QDs dispersed in solution. **Figure 4.9a** shows the absorption spectra of QDs at various growth stages. The initial CISES QDs exhibit a typical absorption spectrum covering UV-visible-NIR region without apparent excitonic peaks⁵⁴. In contrast, with subsequent growth of the shell, the core/shell QDs exhibit a strong absorption feature in the UV-visible region, which is consistent

with the typical absorption spectra of shell materials (i.e. CdSeS or CdS)¹⁶⁵.

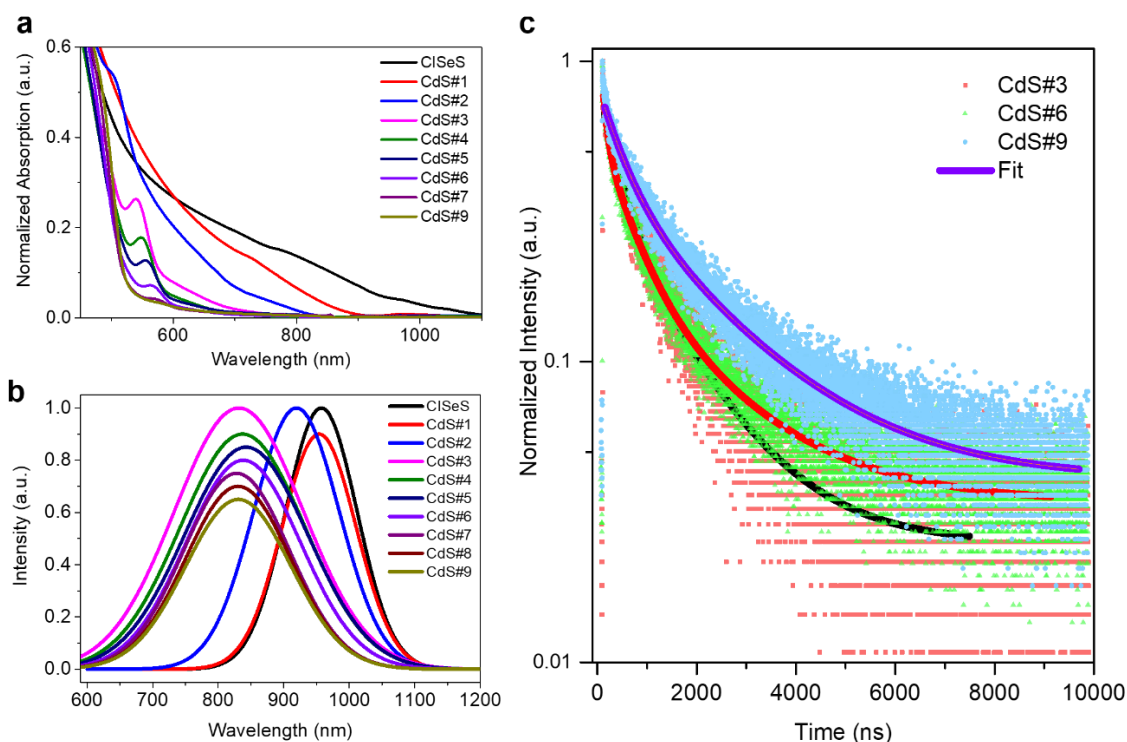


Figure 4.9 (a) UV-Vis absorption and (b) PL spectra of heterostructured CISES/CdSeS/CdS g-QDs at different growth stages in toluene. (c) PL lifetime of CdS#3, CdS#6 and CdS#9 g-QDs in toluene.

There is a quantum-confined feature in the absorption spectra of the QDs, which is expressed by the absorption peaks from absorption spectra of CdS#3 to CdS#6 QDs. The absorption peak positions of QDs are listed in **Table 4.2**. We attribute these absorption peaks to the CISES/CdSeS core/shell QDs as there is a red shift and broadening of the peaks from CdS#3 (~541 nm) to CdS#6 (~567 nm) QDs with the gradual growth of the shell, and the peaks finally diminish in CdS#9 g-QDs.

Table 4.2 Absorption peak positions of heterostructured CISES/CdSeS/CdS QDs (CdS#2 to CdS#7).

Sample Labels	CdS#2	CdS#3	CdS#4	CdS#5	CdS#6	CdS#7
Absorption Peak (nm)	506	541	548	556	568	576

All these results are consistent with the quantum-confined effect of increasing sizes of QDs. The redshift and broadening of the absorption peaks is also consistent with the formation of CISES/alloyed CdSeS core/shell QDs, as confirmed by the XRD (**Figure 4.1e**) and SAED

patterns (**Figure 4.5a and b**) of CdS#3 and CdS#6 QDs. The absorption spectrum of the final CdS#9 QDs exhibits no obvious absorption peak, since their absorption is dominated by the thick CdS shell.

PL spectra of CISES/CdSeS/CdS g-QDs at different growth stages in solution are also shown in **Figure 4.9b** and the detailed PL peak positions are listed in **Table 4.3**. All the QDs exhibit PL emission in the NIR region (over 700 nm), indicating that the origin of PL emission in these QDs originates from the core materials of CISES, which exhibits typical emission in the 800 to 1000 nm range ⁵⁴. It is noted that the PL peaks are relatively broad, which has been illustrated by Klimov's group that the PL from CISES QDs generally originates from radiative recombination of the delocalized electrons and localized holes (located at the Cu-correlated defects), leading to the random positioning of the emitting center in the QD with large variation of PL peak positions for consequent PL broadening ⁹⁴. Moreover, the large size distribution of as-synthesized CISES/CdSeS/CdS g-QDs may contribute to the PL broadening as well ¹⁶⁶.

We observe a continuous blue shift of PL peaks from CISES to CdS#3 QDs, which is attributed to the decreasing size of the QDs caused by the core-etching effect in the early growth stages ^{55, 94}. This is also consistent with the decreasing size from CISES QDs to CdS#3 QDs observed in TEM images (**Figure 4.1a, b and Figure 4.6**).

Table 4.3 PL peak positions of CISES core QDs and corresponding core/shell QDs (CdS#1 to CdS#9).

Sample Labels	CISES	CdS#1	CdS#2	CdS#3	CdS#4	CdS#5	CdS#6	CdS#7	CdS#8	CdS#9
PL Peak (nm)	~957	~954	~919	~830	~837	~842	~838	~830	~830	~830

In contrast, a red shift of PL peaks is displayed in the PL spectra of CdS#3 to CdS#5 (with 4 mL of injected Cd/S precursors). We infer that there is electron delocalization corresponding to the increasing thickness of CdSeS shell ^{49, 144}. After growing the outer thick CdS shell, the PL peaks of CdS#7 (with 10 mL of injected Cd/S precursors) to CdS#9 QDs further blue shifted to ~830 nm that is identical to the CdS#3 QDs.

We attribute this blue shift to the outmost CdS shell that possesses wider band gap than alloyed

CdSeS. The wider band gap is favorable to confine the electrons and results in less possibility of electrons delocalization. We further estimated the band gap of all the QDs based on the Tauc plot (**Figure 4.10**) of the QD's absorption spectra (This method is quite reliable while may still show some uncertainties ^{167, 168}), and then used the band gap and PL peaks to determine the Stokes shift of the QDs, as listed in **Table 4.4**.

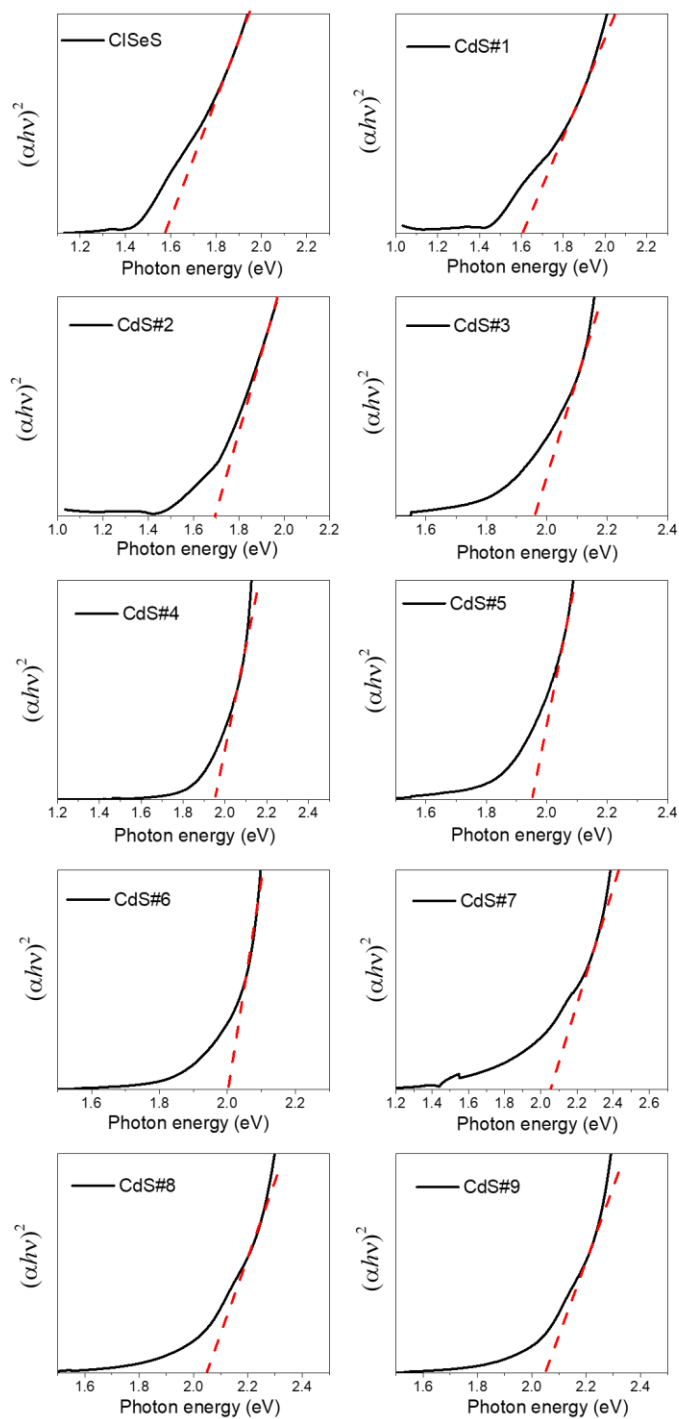


Figure 4.10 Tauc plot derived from absorption spectra of all QDs.

Table 4.4 Stokes shift of CISES QDs to CdS#9 g-QDs.

Sample	E_g (eV)	Abs peak(nm)	PL peak(nm)	Stokes Shift (nm)
CISES	1.58	784	957	173
CdS#1	1.60	774	954	180
CdS#2	1.70	729	919	190
CdS#3	1.95	635	830	195
CdS#4	1.95	635	837	202
CdS#5	1.95	635	842	207
CdS#6	2.00	620	838	218
CdS#7	2.05	604	830	226
CdS#8	2.05	604	830	226
CdS#9	2.05	604	830	226

With the growth of the shell, the Stokes shift gradually increases from ~173 nm (CISES QDs) to ~226 nm (CdS#7 QDs) and then remains constant for CdS#8 and CdS#9 QDs. The enhanced Stokes shift of g-QDs with the increase of shell thickness is likely due to the strong delocalization of electrons into the shell region, which is consistent with other g-QDs systems^{59, 66}.

The PLQY of QDs was measured and shown in **Figure 4.11** and **Table 4.5**. The PLQY of core/shell QDs is much higher than that of the initial CISES QDs, which have a very low PLQY of ~0.1%. For the PLQY of core/shell QDs, there is an increasing trend from CdS#1 (with 0.5 mL of injected Cd/S precursors) to CdS#6 QDs (maximal PLQY of ~17%), and further growth of thicker shells leads to the decrease of PLQY from CdS#7 to CdS#9 QDs. The increasing PLQY with growth stages from CdS#1 to CdS#6 QDs is ascribed to the effective surface defects/traps passivation by inorganic shell growth, and the maximum PLQY of ~17% was obtained from CdS#6 QDs, since most of the nonradiative recombination sites were passivated at this optimized growth stage⁴⁹.

Generally, the PLQY is determined by both the radiative decay rate and non-radiative decay rate¹⁶⁹. From CdS#1 to CdS#6 QDs, the radiative decay rate decreases due to the electron delocalization and may cause the PLQY to decrease. Simultaneously, the formation of the inorganic shell can effectively passivate the surface defects/traps of QDs, leading to largely reduced number of surface recombination centers. This surface passivation results in lower non-radiative decay rate, which is the dominant process from CdS#1 to CdS#6 QDs and leads to

enhanced PLQY. This maximal PLQY is also comparable to that of the recently reported PbSe/CdSe/CdSe g-QDs (~18%)⁶¹. For other CISES QDs, they generally show PLQY around 5% to 10%^{55, 170}, which is less than our champion samples (17%). On the other hand, in the g-QDs system, the formation of a very thick shell can create defects/dislocations etc. at the interface or within the shell, which act as recombination centers and thus lead to the decreasing PLQY^{49, 50}. In our case, as the thickness of the CdS shell increases, the strain due to the lattice mismatch between CdSeS and CdS could result in the formation of defects/dislocations at the interface of CdSeS/CdS shell or within the CdS shell, which could serve as nonradiative recombination centers, causing the reduced PLQY^{49, 50}.

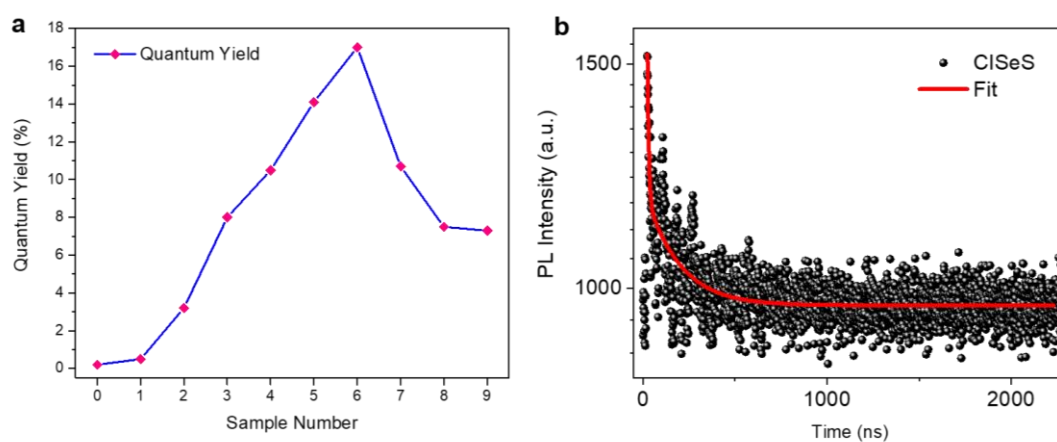


Figure 4.11 (a) PLQY of CISES QDs (sample No. 0) and corresponding core/shell QDs (CdS#1 to CdS#9 QDs). (b) Transient PL spectrum of CISES QDs with fitted average lifetime of $\sim 165 \pm 4$ ns.

Table 4.5 PLQY of bare CISES QDs and relevant core/shell QDs (CdS#1 to CdS#9).

Sample Labels	CISES	CdS#1	CdS#2	CdS#3	CdS#4	CdS#5	CdS#6	CdS#7	CdS#8	CdS#9
QY (%)	0.1	0.5	3.2	8	10.5	14.1	17	10.7	7.5	7.3

Figure 4.9c displays the transient PL decay of CdS#3, CdS#6 and CdS#9 g-QDs, a triexponential decay is used to fit these curves, showing fitted average lifetimes of 1.28 μ s, 1.69 μ s and 1.94 μ s, respectively. Herein, τ_1 is assigned to the donor-acceptor transition, τ_2 is associated with the surface states and τ_3 is the recombination of initially populated core states^{86, 150}.

Compared to CISES core QDs with fitted average lifetime of ~ 0.165 μ s, there is an obvious

prolonged lifetime for heterostructured CISES/CdSeS/CdS g-QDs with increasing shell thickness (PL lifetime of CdS#2, CdS#4, CdS#5 and CdS#8 QDs were shown in **Figure 4.12**), as summarized in **Table 4.6**.

Table 4.6. Average lifetime of the CISES core QDs and corresponding core/shell QDs (CdS#2 to CdS#6, CdS#8 and CdS#9).

Sample Labels	CISES	CdS#2	CdS#3	CdS#4	CdS#5	CdS#6	CdS#8	CdS#9
Lifetime(τ_{measure})	165±4 ns	1.01 μs	1.28 μs	1.46 μs	1.53 μs	1.69 μs	1.91 μs	1.94 μs

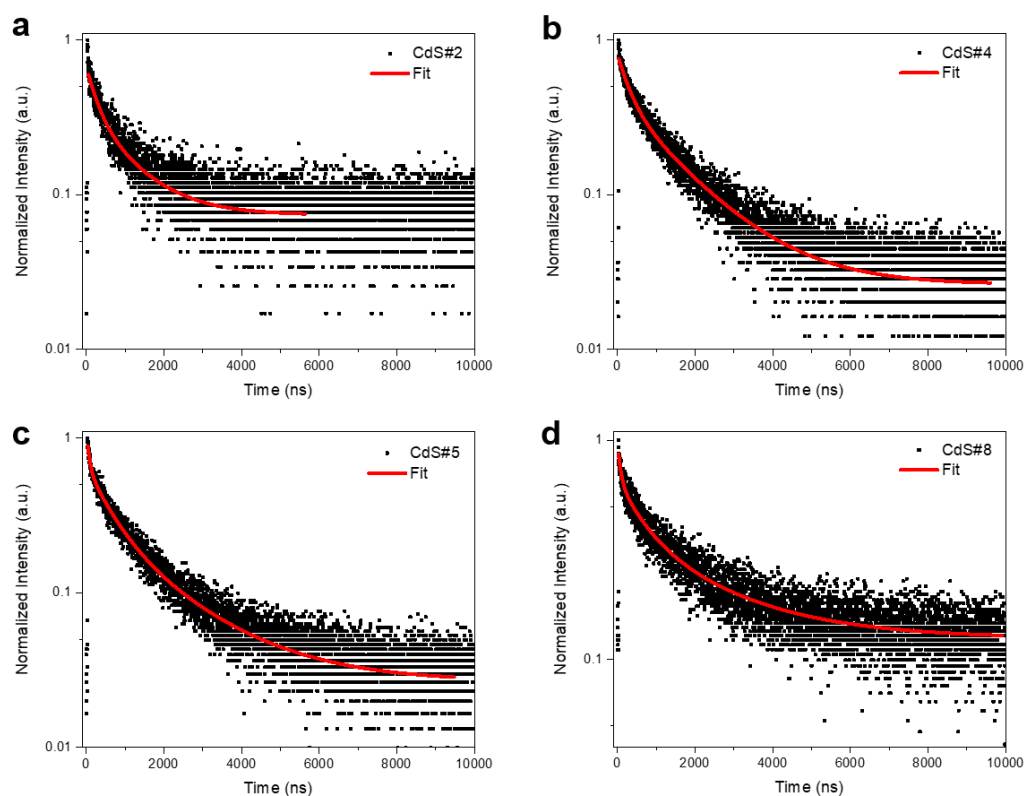


Figure 4.12 PL decay curves of (a) CdS#2, (b) CdS#4, (c) CdS#5 and (d) CdS#8 QDs, displaying fitted average lifetime of ~1.01 μs , 1.46 μs , 1.53 μs and 1.91 μs , respectively.

The prolonged lifetime with increasing shell thickness of as-synthesized g-QDs is consistent with previous work on g-QDs systems, which attributed this phenomenon to the delocalization of electrons in the shell region, while the holes are still confined in the core region^{49, 144}. In our case, we also suggested that the hole is still confined to the CISES core while the electron is delocalized over the entire shell region, leading to a largely reduced electron-hole overlap and prolonged lifetime. The large difference (more than one order of magnitude) of average lifetime before and after shell growth is attributed to the designed pyramidal geometry for more efficient

spatial separation of electrons and holes in as-synthesized g-QDs than conventional spherical shaped g-QDs^{159,171}. As the lifetime of g-QDs can be directly correlated with their electron/hole wavefunctions, we compared our pyramidal-shaped g-QDs with other spherical giant core/shell QDs, as summarized in **Table 4.7**. As-synthesized pyramidal-shaped CISES/CdSeS/CdS g-QDs exhibit a very long lifetime of $\sim 2 \mu\text{s}$. This value is much higher than the corresponding value found for spherical CdSe/CdS g-QDs (PL lifetime: $\sim 40 \text{ ns}$), spherical CISE/CIS g-QDs (PL lifetime: $\sim 300 \text{ ns}$) and spherical PbS/CdS g-QDs (PL lifetime: $\sim 1 \mu\text{s}$)^{63,68,145}. All these results demonstrate the pyramidal g-QDs may have particular optical properties compared to spherical g-QDs.

Table 4.7 PL lifetime of spherical g-QDs with respect to as-synthesized pyramidal-shaped g-QDs.

QDs type	PL lifetime (ns)	Reference
Spherical CdSe/CdS	~ 40	68
Spherical CuInSe ₂ /CuInS ₂	~ 300	63
Spherical PbS/CdS	~ 1000	145
Pyramidal-shaped CISES/CdSeS/CdS	~ 2000	This work

4.2 Theoretical study of near-infrared colloidal heterostructured pyramidal “giant” core/shell quantum dots

4.2.1 Theoretical calculation method

A commercial software of COMSOL is employed to solve the stationary Schrödinger equation for the 1S electrons and holes in pyramidal CISES/CdSeS/CdS g-QDs. The electron and hole-potentials as a function of position were approximated as the lowest unoccupied molecular orbital and the highest occupied molecular orbital levels of their bulk materials. The bulk values for the effective masses of electrons and holes were used. We neglect the interaction between electrons and holes for simulations. The wave functions were computed from the effective-mass Schrödinger equation. The appropriate boundary conditions at the interfaces were used to solve this equation and the wave functions were normalized as below: $\int |\psi|^2 dV = 1$. The wave function of an impurity hole state can be expressed by the equation:

$$\psi_{\text{hole}}(\mathbf{r}; \mathbf{r}_{\text{impurity}}) = A \exp\left(-\frac{(\mathbf{r} - \mathbf{r}_{\text{impurity}})^2}{2L_h^2}\right) \quad (4.1)$$

In this equation, $\mathbf{r}_{\text{impurity}}$ represents the position of the impurity in the CISEs core; the coefficient A can be derived from the equation: $\int |\psi_{\text{hole}}|^2 dV = 1$; We set the scale of hole L_h to be 0.3 nm (L_h is generally much less than QD size). From the experimental data, the molar ratio of Cu:In in CISEs is 1:1.2. Based on this point, the molar mass and mass density of CISEs are employed to calculate the numbers of Cu atoms and In atoms.

4.2.2 Wave function in pyramidal $\text{CuInSe}_x\text{S}_{2-x}/\text{CdSeS}/\text{CdS}$ “giant” core/shell quantum dots

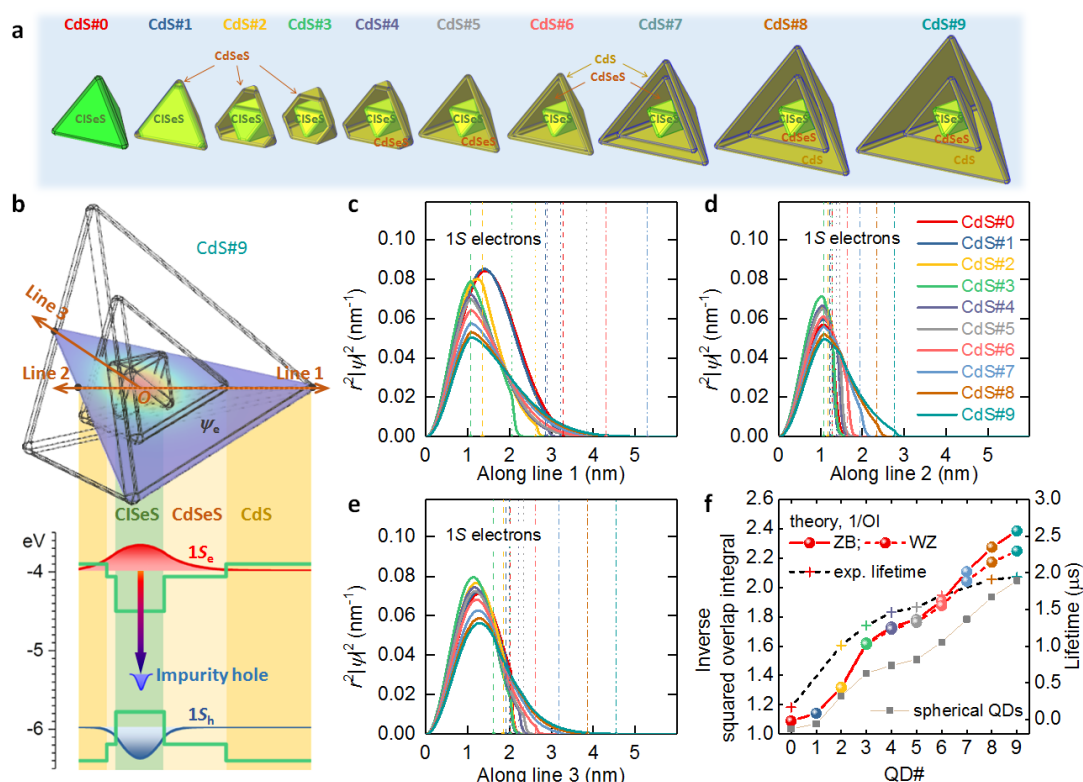


Figure 4.13 Theoretical modeling of the CISEs/CdSeS/CdS g-QDs. (a) Geometrical models of the series of g-QDs (CdS#0-9). Each edge of each component of the QDs is rounded by a radius of 0.3 nm. (b) Electronic band structure with energy levels and wave functions of 1S electrons, impurity holes and 1S holes in a g-QD (CdS#9). (c)-(e) Normalized radial distribution function of 1S electrons in the series of g-QDs along Line 1, Line 2 and Line 3, respectively. The Lines 1-3 are vectors pointing from the origin to the vertex, face center and edge center of the tetrahedron QD, respectively, as demonstrated in (b). The vertical lines show the positions of the surfaces of CISEs (dashed), CdSeS (dotted) and CdS (dash-dotted) of each g-QD. (f) Inverse squared OI of the 1S electrons and impurity holes in the series of g-QDs with two different crystal structures, ZB and WZ, for the CdSeS shell and CdS shell. The inverse squared overlap of pyramidal QDs is much higher than that of the spherical QDs (ZB). The experimental lifetime is plotted for comparison (right axis).

We estimated the shape and size of each component in g-QDs at different growth stages according to the growth dynamics of the series of g-QDs. In our models (Figure 4.13a), we

further assume that (1) the etching process of the CISeS core size stopped when the injection volume of the mixed Cd and S precursors exceeded 2.5 mL (as for the cases of CdS#3 to 9 QDs), (2) the growth process of the CdSeS shell stopped when the injection volume became greater than 4 mL and (3) the outermost CdS shell was grown only if the injection volume was greater than 4 mL (as for the cases of CdS#5 to 9 QDs). (4) The interfacial strain in core/shell structure is ignored in this model.

The wave functions of the 1S electrons were calculated by solving the stationary Schrödinger equation with the bulk band alignment (**Figure 4.13b** and **Figure 4.14** for more details). The details of the geometrical and physical parameters are listed in **Table 4.8** and **4.9**, respectively.

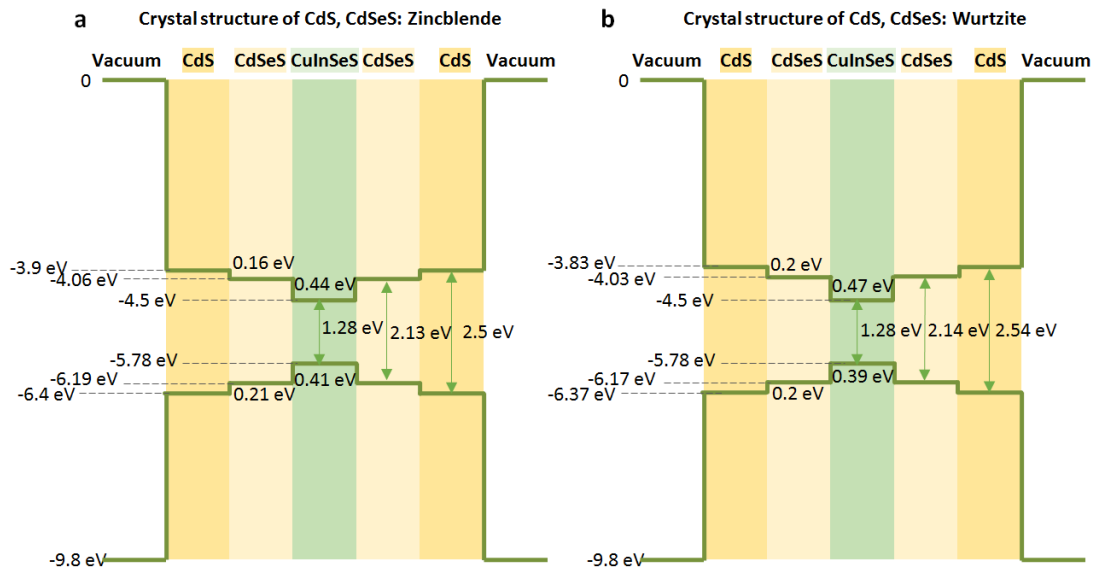


Figure 4.14 Band structure for the CISeS/CdSeS/CdS heterostructure. (a) The crystal structure of the shells (CdSeS and CdS) is ZB phase, which applies to the samples in the experiments. (b) The crystal structure of the shells (CdSeS and CdS) is WZ phase, which are used for comparison purpose in theoretical models.

Table 4.8 Physical parameters used in modeling.

	E_v (eV)	E_c (eV)	E_g (eV)	m_c / m_0	m_{hh} / m_0
CISeS	-5.78	-4.50	1.28	0.13	0.79
CdSeS (ZB)	-6.19	-4.06	2.13	0.17	0.57
CdS (ZB)	-6.4	-3.9	2.5	0.21	0.68
CdSeS (WZ)	-6.17	-4.03	2.14	0.17	0.57
CdS (WZ)	-6.37	-3.83	2.54	0.21	0.68
CdSe	-5.97	-4.22	1.75	0.13	0.45
Vacuum	-9.8	0	--		1

Table 4.8 Geometrical parameters used in modeling.

Sample name	CdS#0	CdS#1	CdS#2	CdS#3	CdS#4	CdS#5	CdS#6	CdS#7	CdS#8	CdS#9
Size (nm)	5.5	5.4	4.7	4.0	5.2	6.4	7.2	8.8	10.7	12.7
Overall shape	Tetra		Octahedron				Tetrahedron			
CISeS size (nm)	5.5	4.9	3.0	2.5	2.5	2.5	2.5	2.5	2.5	2.5
CdSeS size (nm)	--	0.5	1.7	1.5	2.7	3.9	3.9	3.9	3.9	3.9
CdS size (nm)	--	--	--	--	--	0.0	0.8	2.4	4.3	6.3

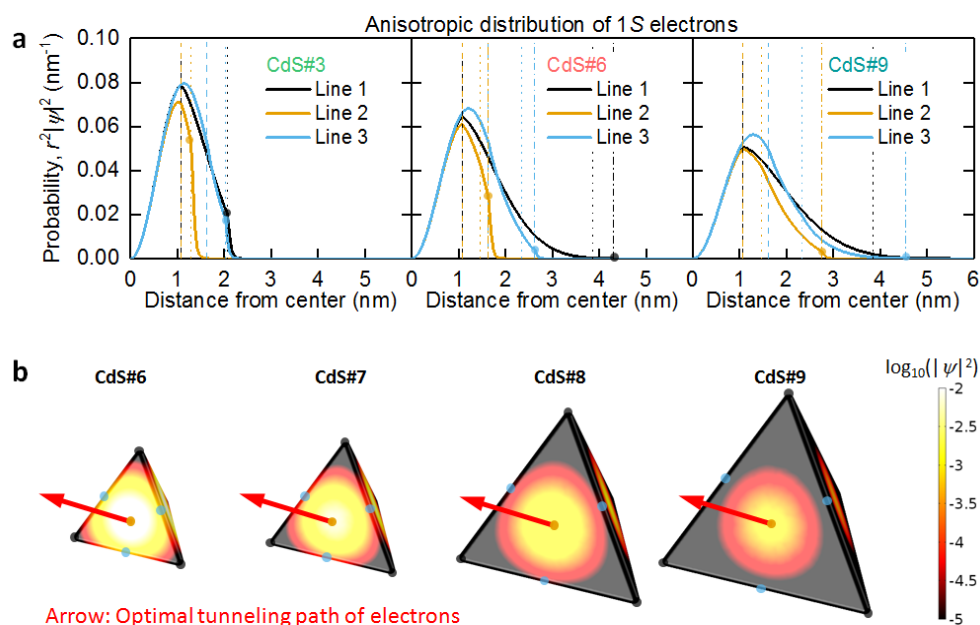


Figure 4.15 (a) Radial distributions of 1S electrons in the g-QDs (CdS#3, CdS#6, CdS#9) along three different directions. The Lines 1-3 are vectors pointing from the origin to the vertex, face center and edge center of the tetrahedron QD, respectively, as demonstrated in Figure 1b of the main text. **(b)** Maps of wave functions, $\log_{10}(|\psi|^2)$, at the QD surfaces for the g-QDs with two shells, CdS#6-9. The optical tunneling path of 1S electrons in the QDs is shown by the red arrow, which is along Line 2.

Our calculations show that the Eigen energies of the 1S electrons exceed the CdSeS energy barrier for the CdS#1-9 QDs. Thus, the electrons have a higher probability of being found in the shell layers than holes. The radial probability distributions of the 1S electrons along three different lines are shown in **Figure 4.13c-e**. The delocalization effect of the 1S electrons

becomes prominent for QDs with thick CdS shell layers, e.g., CdS#6 to 9 QDs. Moreover, the wave functions of 1S electrons in the g-QDs are spatially anisotropic because of the non-spherical shapes of the QDs, yielding the direction-dependent localization degree of the 1S electrons (**Figure 4.15a**).

Unlike isotropic spherical QDs, the electron wave functions spread considerably out of the CISES core along Line 1 (from the origin to the vertex of the tetrahedron-shaped QDs); whereas the electrons are better confined in the direction of Line 2 (from the origin to the face center of the QDs). Along Line 3 (from the origin to the edge center), the electron wave functions have slightly better confinement than those along Line 1. In contrast, the holes wave functions are almost confined in the core region (**Figure 4.16**), indicating the quasi-type II band structure of as-synthesized g-QDs.

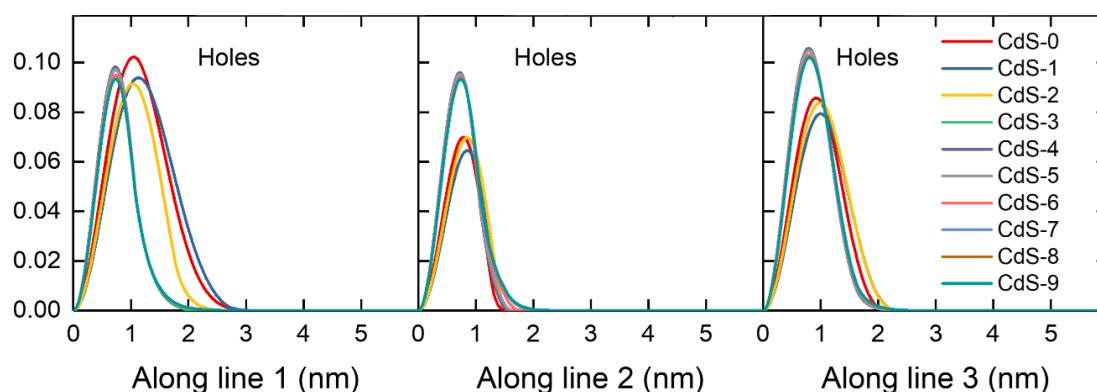


Figure 4.16 Normalized radial distribution function of holes in the series of g-QDs along Line 1, Line 2 and Line 3, respectively. The Lines 1-3 are vectors pointing from the origin to the vertex, face center and edge center of the tetrahedron QD, respectively.

As a consequence of the geometrical anisotropy and asymmetric electron-hole distribution, Line 2 is the most efficient path for electron tunneling from the CISES core to the QD surface (**Figure 4.15b**). The electrons tunneling to the QD surface can be used in many optoelectronic applications such as PEC cells and QDSCs^{34, 68, 145}, where the tunneling rate depends on both the probability density of the electrons at the QD's surface and the lifetime of the photoexcited electrons.

To qualitatively evaluate the lifetime of the photoexcited carriers in the g-QDs, we calculated the squared OI of the photoexcited carriers in the series of g-QDs, CISES to CdS#9 QDs. Upon

photoexcitation, the 1S holes nonradiatively moved from the VB to the impurity in the core¹⁵⁶. The luminescence of the g-QDs is attributed to the radiative recombination of the CB 1S electrons with the impurity holes¹⁵⁶. The squared OI between 1S electrons and impurity holes can be written as

$$OI = N_{\text{impurity}} \frac{1}{V_{\text{core}}} \int_{\text{core}} OI_0(\mathbf{r}_{\text{impurity}}) dV_{\text{impurity}} \quad (4.2)$$

with

$$OI_0(\mathbf{r}_{\text{impurity}}) = \frac{\left| \int \psi_{\text{electron}}(\mathbf{r}) \psi_{\text{hole}}(\mathbf{r}; \mathbf{r}_{\text{impurity}}) dV \right|^2}{\int |\psi_{\text{electron}}(\mathbf{r})|^2 dV \int |\psi_{\text{hole}}(\mathbf{r}; \mathbf{r}_{\text{impurity}})|^2 dV} \quad (4.3)$$

Here ψ_{electron} and ψ_{hole} are wave functions of the 1S electron state and impurity hole state, respectively, and N_{impurity} is the number of impurities in the CISES core (see section 4.2.1 for description of impurity holes). The PL lifetime should be proportional to the inverse squared OI. **Figure 4.13f** shows that the inverse squared OI continuously increases from core CISES QDs to core/shell CdS#9 g-QDs. This trend qualitatively agrees with the measured lifetime, indicating that the prolonged lifetime in the experiments resulted from the reduced overlap between 1S electrons and impurity holes. To show the beneficial role of the geometrical anisotropy, we compare the lifetime of pyramidal QDs with that of spherical QDs. The gray square dots in **Figure 4.13f** show the calculated lifetime of spherical QDs. The spherical QDs have similar configurations of the shells to the corresponding pyramidal QDs (see **Table 4.10** for geometrical parameters).

The length of the most efficient path of electron tunneling for each spherical QD is set as the same as the corresponding pyramidal QD. As shown, the inverse square OI of pyramidal QDs is greater than that of the spherical QDs for the two series of QDs, indicating that anisotropic shapes of QDs can prolong the lifetime of the electrons in them. Moreover, we show that g-QDs with the ZB crystal structure of CdSeS and CdS have longer lifetime than those with WZ crystal structure of the shell layers, confirming that the ZB phase of CdSeS and CdS in our experiments played a beneficial role in creating the good optical properties (long PL lifetime

with high PLQY). These simulation results indicate the quasi-type II band structure of these g-QDs, which is consistent with the experimental data.

Table 4.10 Geometry parameters of spherical QDs calculated in Figure 4.13f.

CdS #	0	1	2	3	4	5	6	7	8	9
Core radius	1.91	1.82	1.49	1.26	1.26	1.26	1.26	1.26	1.26	1.26
CdSeS shell thickness	-	0.035 16	0.105 47	0.210 93	0.316 4	0.386 71	0.386 71	0.386 71	0.386 71	0.386 71
CdS shell thickness	-	-	-	-	-	-	0.175 79	0.492 19	0.878 91	1.300 79

Core radius = Effective radius of CISES (nm); CdSeS shell thickness = Thickness along best tunneling path of CdSeS (nm); CdS shell thickness = Thickness along best tunneling path of CdS (nm).

4.3 Fabrication and measurement of pyramidal $\text{CuInSe}_x\text{S}_{2-x}/\text{CdSeS}/\text{CdS}$ “giant” core/shell quantum dots-based optoelectronic devices

4.3.1 Fabrication of pyramidal $\text{CuInSe}_x\text{S}_{2-x}/\text{CdSeS}/\text{CdS}$ “giant” core/shell quantum dots-sensitized photoanode and solar cells

To fabricate the QDs-sensitized photoelectrode, colloidal QDs in toluene were deposited into double layer TiO_2 mesoporous films (prepared by doctor-blading technique⁶⁷) by using EPD approach¹⁹. An applied bias of 50 V was added on the two electrodes for 30 min. Subsequently, the as-deposited QDs-sensitized electrodes were rinsed with toluene to remove the unbound QDs on the surface of the TiO_2 film. The positions of two QDs-sensitized electrodes were then exchanged and an applied bias of 75 V was added for another 90 min.

These electrodes were then dipped into a CTAB solution (10 mg/ml in methanol) for 1 min and rinsed with methanol for 1 min; these procedures were repeated twice. Next, two-layer of ZnS is deposited on QDs-sensitized photoanodes by using the SILAR method so as to avoid photocorrosion. Finally, an insulating glue was employed to cover the photoanode’s surface excluding the active area (with size of $\sim 0.15 \text{ cm}^2$) to finalize device fabrication.

For fabrication of QDSCs, the as-prepared anode was further coated with silica (the anode was

immersed in 0.01 M tetraethylorthosilicate/ethanolic solution for 2 h at 35 °C). The electrolyte was prepared by mixing polysulfide in H₂O/methanol (1/1, v/v) (1 M Na₂S, 1 M S, and 0.1 M NaOH). The Cu₂S counter electrode was deposited by soaking the brass in hydrochloric acid (HCl, 30%) at 70 °C for 10 min.

Then, as-treated brasses were dipped in a polysulfide electrolyte (2 M S, 2 M Na₂S and 0.2 M NaOH) solution for 10 min to produce Cu₂S. In the end, QDSCs were constructed by sandwiching the Cu₂S counter electrode and the QDs-modified photoanode via using a plastic spacer (thickness of ~25 μm).

4.3.2 Device performance of pyramidal CuInSe_xS_{2-x}/CdSeS/CdS “giant” core/shell quantum dots-sensitized photoanode and solar cells

We used heterostructured pyramidal-shaped CISES/CdSeS/CdS g-QDs to fabricate a photoanode for PEC hydrogen production. Before fabricating QDs-based optoelectronic devices, we further optimized the shell thickness of an interfacial CdSeS layer of CdS#6 g-QDs (the optimized synthesis process is described in SI and the optical characterization is shown in **Figure 4.17**).

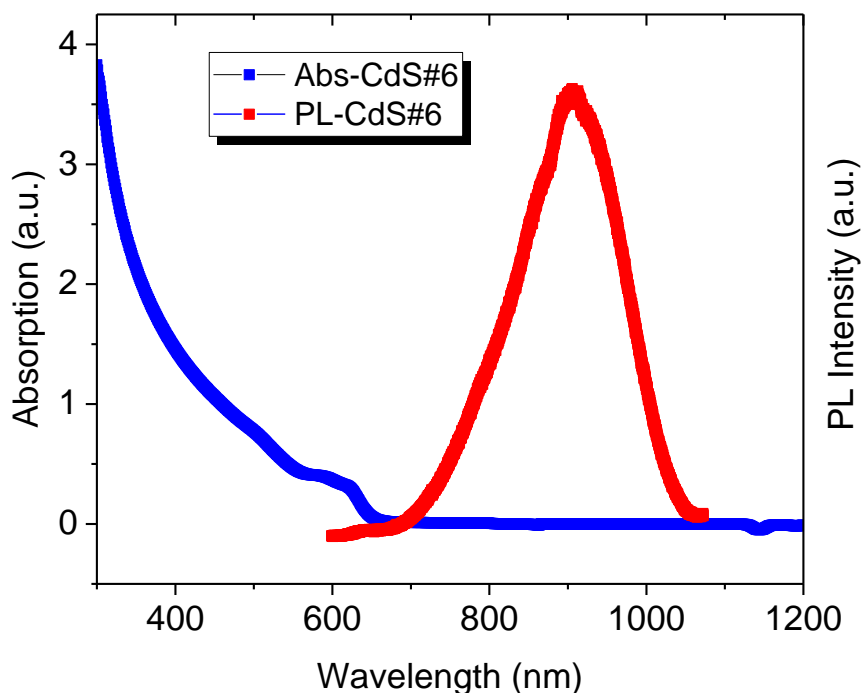


Figure 4.17 UV-visible absorption and PL spectra of optimized CdS#6 g-QDs for fabrication of PEC and solar cells.

A TEM image and relevant EDS spectra of TiO₂/CdS#6 g-QDs/ZnS heterostructure are shown in **Figure 4.18**, indicating that g-QDs (denoted by white dashed circles) are uniformly dispersed in the TiO₂ films.

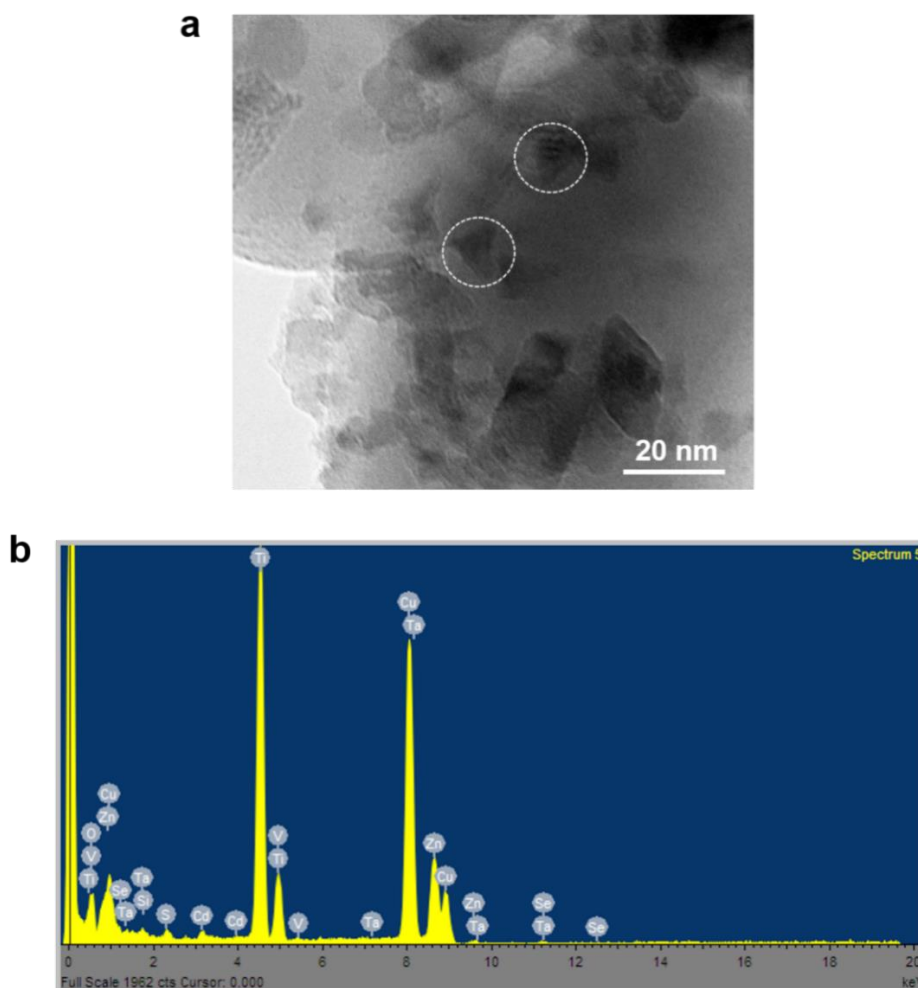


Figure 4.18 (a) TEM image of CdS#6 g-QDs-sensitized photoelectrode with homogeneous distribution of QDs (white dashed circle indicates the QDs on the surface of TiO₂ nanoparticles). (b) EDS spectra of CdS#6 g-QDs-sensitized photoelectrode.

To further verify this conclusion, cross-sectional SEM imaging and relevant EDS measurements (**Figure 4.19**) of the CdS#6 g-QDs-sensitized photoelectrode were carried out. The mesoporous TiO₂ films show an approximate thickness of ~20.1 μm (**Figure 4.19a**). The relative mass concentration of CdS#6 g-QDs/TiO₂ heterostructure is reported in **Figure 4.19b**, confirming the existence of the main chemical composition (Cd, Se, S, Si, Ti and O) in the CdS#6 g-QDs-sensitized photoanode.

The element of Cu and In in CISES core QDs are not detected due to the relatively large volume

of CdSeS/CdS shell materials in these g-QDs, while the elements of Cd, S and Se are main elements in the g-QDs and show very homogeneous distribution in the 2D EDS mapping (Figure 4.19c-e) imaging.

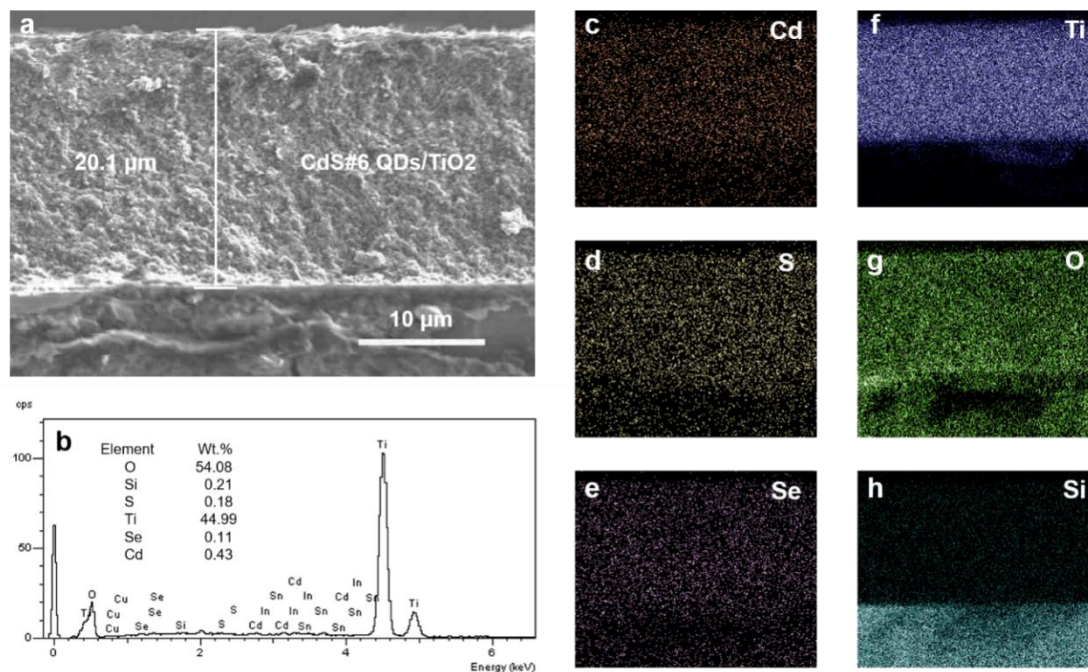


Figure 4.19 (a) Cross-sectional SEM image of CdS#6 g-QDs-sensitized photoanode and corresponding (b) EDS spectra. EDS mapping analysis of (c) Cd, (d) S, (e) Se, (f) Ti, (g) O and (h) Si.

Figure 4.20a shows the scheme and predictable band alignment of pyramidal-shaped CISeS/CdS/CdS g-QDs-sensitized photoanode. The CISeS/CdS/CdS g-QDs form a staggered band alignment with TiO₂ that allows for efficient charge separation, in which situation the photogenerated electrons are injected into TiO₂ and move to the counter electrode (Pt) to conduct water reduction and enable hydrogen generation^{123, 158}.

The hole scavengers (i.e. Na₂S and Na₂SO₃) in the electrolyte are consumed by photogenerated holes. A typical three-electrode electrochemical cell was employed to estimate the PEC performance of these g-QDs-sensitized photoanodes. Before PEC measurements, an extra inorganic ZnS capping layer is deposited on the QDs-sensitized photoanode by SILAR method to avoid photocorrosion of the electrodes. The PEC measurements are all conducted under standard one sun illumination (AM 1.5 G, 100 mW/cm²).

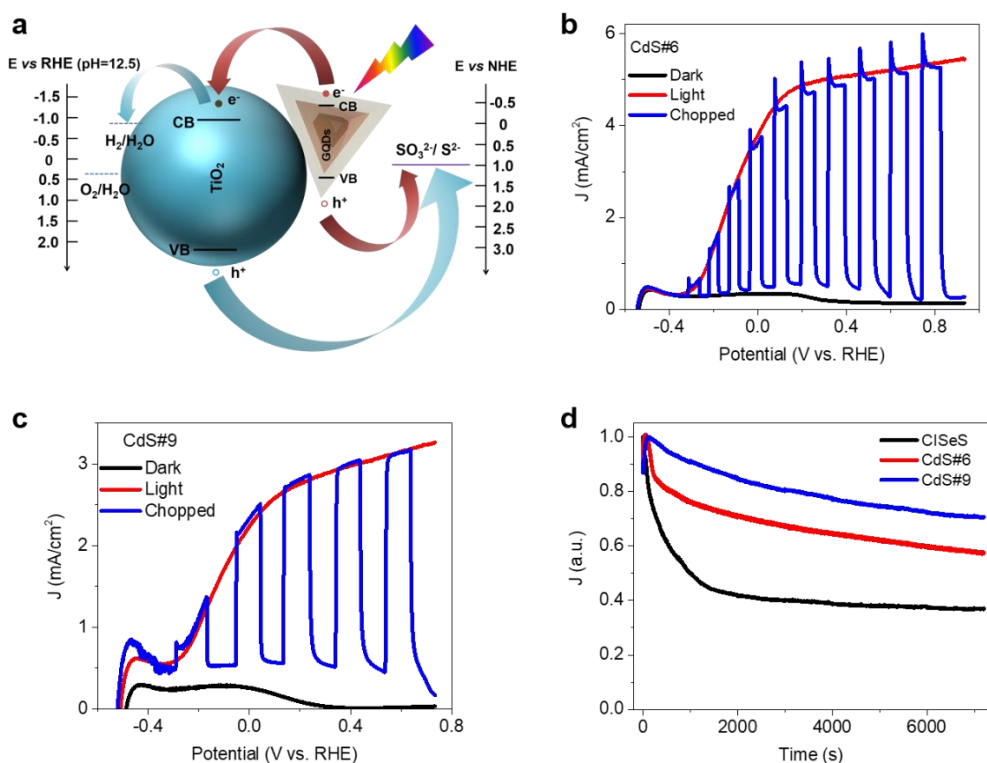


Figure 4.20 (a) Scheme and predictable band alignment and of heterostructured CISES/CdSeS/CdS g-QDs-based photoelectrodes. Linear sweep voltammetry of (b) TiO₂/CdS#6 g-QDs/ZnS and (c) TiO₂/CdS#9 g-QDs/ZnS systems in the dark and under AM 1.5 G irradiation at 100 mW/cm². (d) Normalized steady state current density-time (J-t) curves of CISES QDs (black curve), CdS#6 g-QDs and CdS#9 g-QDs-decorated photoanodes at 0.6 V versus RHE under standard one sun illumination.

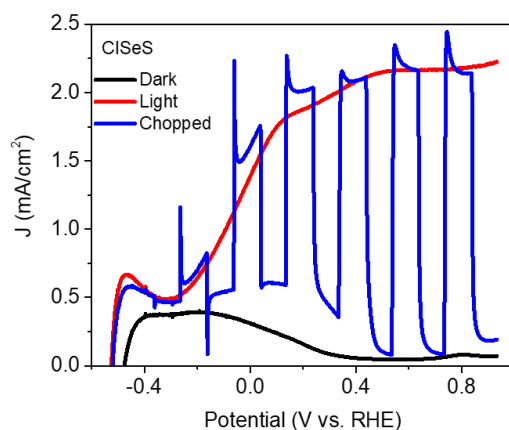


Figure 4.21 Linear sweep voltammetry of TiO₂/CISES/ZnS photoanode in the dark (black curve), under continuous (red curve) and chopped (blue curve) under standard one sun illumination (AM 1.5 G, 100 mW/cm²).

As shown in **Figure 4.20b** and **c**, the CdS#6 and CdS#9 g-QDs-sensitized photoanodes yield a saturated photocurrent density of ~ 5.5 and ~ 3 mA/cm² at ~ 0.6 V versus the RHE. The

performance of our g-QDs based PEC cells is comparable to PbS/CdS g-QDs based PEC system¹⁴⁵. In contrast, the bare CISES QDs-sensitized photoanode shows a lower saturated photocurrent density of $\sim 2.1 \text{ mA/cm}^2$ (**Figure 4.21**).

Although the CdS#6 and CdS#9 g-QDs possess less light absorption in visible-NIR region than bare CISES QDs, the prolonged lifetime for efficient electron-hole separation and largely enhanced PLQY for suppressed surface charge carrier recombination are very favorable in general PEC systems⁹⁹, leading to higher saturated photocurrent density in CdS#6 and CdS#9 g-QDs-sensitized photoanodes than the CISES QDs-sensitized photoanode.

Steady state current density-time ($J-t$) curves of CISES QDs (black curve), CdS#6 g-QDs and CdS#9 g-QDs-modified photoanodes measured at 0.6 V versus RHE is exhibited in **Figure 4.20d**. The curves are normalized by dividing the maximum photocurrent density (decay from the value of 1), allowing us to visualize the decay trend. The photocurrent density of TiO₂/bare CISES QDs/ZnS-based PEC cell exhibit a rapid decay of photocurrent density, maintaining only 40% of its initial value after 2 h illumination.

In contrast, the CdS#6 and CdS#9 g-QDs based PEC cells present a lower percentage decay, maintaining $\sim 60\%$ and $\sim 70\%$ of its initial value after 2h illumination. This enhanced stability of g-QDs based PEC cells is ascribed to the construction of CdSeS/CdS thick shell on the CISES core QDs for improved photo- and chemical- stability, which is comparable with the best reported CdS QDs-based PEC systems^{99, 140, 141, 172-174}, demonstrating the long-term stability of these pyramidal g-QDs based PEC system.

In addition, CdS#6 g-QDs were used as light harvesters to fabricate QDSCs. As shown in **Figure 4.22**, the preliminary device based on CdS#6 g-QDs shows promising performance (PCE = 1.5 %, $J_{sc} = 5 \text{ mA cm}^{-2}$, $V_{oc} = 0.527 \text{ V}$ and FF = 57%) under one-sun simulated sunlight (AM 1.5G, 100 mW cm^{-2}), suggesting the versatility of CISES/CdSeS/CdS g-QDs for applications in optoelectronic devices.

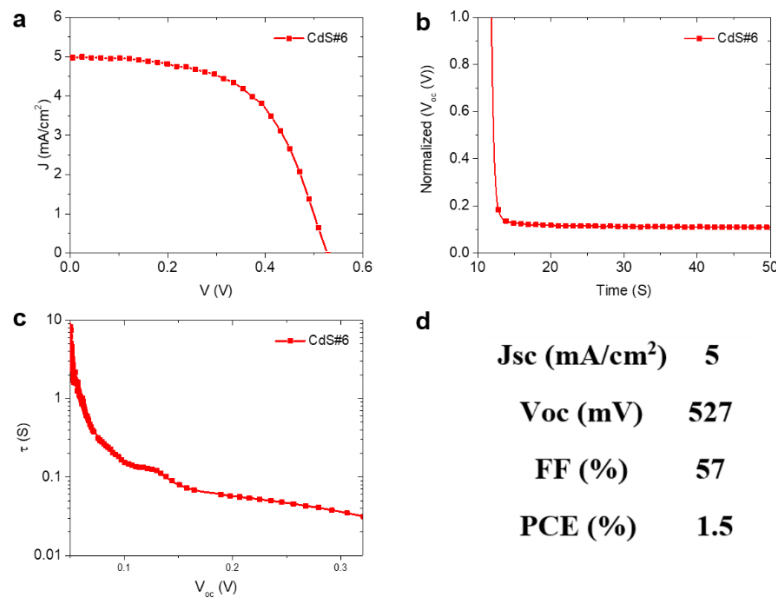


Figure 4.22 (a) Current density versus voltage curve of CdS#6 g-QDs based solar cells under one sun irradiation (AM 1.5 G, 100 mW cm^{-2}). (b) Open circuit voltage (V_{oc}) decay as the function of time. (c) Electron lifetime (τ) as a function of V_{oc} calculated from V_{oc} decay measurements. (d) Photovoltaic parameters calculated from I–V measurements of QDSCs based on CdS#6 g-QDs as light harvesters.

4.4 Summary

In summary, we synthesized heterostructured CISES/CdSeS/CdS g-QDs with pyramidal-shape and NIR emission via using a facile two-step approach. The morphology and crystal structure characterizations demonstrated the growth dynamics of as-synthesized heterostructured g-QDs with shell materials of ZB phase CdSeS and CdS. The shell thickness of as-synthesized g-QDs can be tuned by varying the injection volume of precursors. The as-obtained g-QDs have high PLQY, long lifetime and NIR active absorption and emission spectra. In addition, the prolonged PL lifetime with increasing shell thickness indicates the reduced spatial electron-hole overlap benefiting from core/shell/shell pyramidal structure and their quasi-type II band structure. This conclusion of quasi-type II band structure in these g-QDs is consistent with simulation results, showing their potential applications in QDs-based optoelectronic devices. The PEC cells and QDSCs based on heterostructured CISES/CdSeS/CdS g-QDs exhibits excellent optoelectronic performance in terms of efficient charge carrier separation and transfer in such pyramidal-shaped g-QDs.

CHAPTER 5 CONCLUSIONS AND PERSPECTIVES

5.1 Conclusions

In Chapter 3, we fabricated a high efficiency and stable QDs-based PEC cells for hydrogen generation, in which the photosensitizers are NIR, heavy metal-free core/shell QDs. We first synthesized a new type of NIR, environmentally friendly core/shell CISES/ZnS QDs by using a cation exchange method. EPD is then used to deposit these NIR, “green” core/shell QDs in the mesoporous TiO₂ film to form the TiO₂/Zn-CISES heterostructure. TEM images show that both the CISES QDs and CISES/ZnS (Zn-CISES) core/shell QDs have a pyramidal shape and analogous sizes, indicating that the as-grown ZnS shell is very thin (~0.1 nm). The morphology of TiO₂/Zn-CISES heterostructure shows the intimate contact of QDs on TiO₂ nanoparticles, which is beneficial to accelerate the electron transfer between QDs and TiO₂. The optical characterizations of core/shell Zn-CISES QDs exhibit a typical NIR absorption and PL spectra. The core/shell Zn-CISES QDs show enhanced PL intensity and prolonged lifetime with respect to bare CISES QDs, demonstrating that the ZnS shell is effective to passivate the surface defects/traps of CISES QDs. The EDS mapping of TiO₂/Zn-CISES heterostructure proves that these NIR, heavy metal-free Zn-CISES core/shell QDs were uniformly distributed in the TiO₂ mesoporous film. Moreover, the VB position of Zn-CISES QDs is studied by UPS and used to precisely determine the band alignment of QDs/TiO₂ anode, showing favorable alignment for efficient separation and transfer of photogenerated electron-hole pairs. The NIR, heavy metal-free Zn-CISES core/shell QDs-sensitized photoanodes were used to fabricate solar-driven PEC devices. Upon exposure to standard one sun illumination (AM 1.5G, 100 mW/cm²), the CISES QDs-based PEC cell exhibited a saturated photocurrent density of ~ 2.57 mA/cm², while the Zn-CISES core/shell QDs-based PEC cell shows a higher saturated photocurrent density of ~5.3 mA/cm², indicating that the ZnS shell can effectively passivate the surface defects/traps of CISES QDs for reduced charge recombination, thereby improving the performance of QDs-sensitized PEC cell. Moreover, the Zn-CISES core/shell QDs-based PEC cell shows better device stability than the bare CISES QDs-based PEC device, indicating that the NIR, “green” Zn-CISES QDs are promising to achieve high efficiency and robust PEC cells for hydrogen

generation. However, such core/shell QDs still present limitation of the composition and structure of the shell, which can be further tuned, for instance, by Zn alloying to further increase the driving force for electron injection from QDs into TiO₂ and improve the performance of PEC cells.

In Chapter 4, we developed a novel environment-friendly Zn-treated CISE/CIS g-QDs by using sequential cation exchange method. As-synthesized g-QDs possess a thick CuInS₂ shell with WZ structure, and this sequential cation exchange technique does not significantly change the morphology and structure of initial CdSe/CdS g-QDs template. This indicates that the shell thickness of as-synthesized Zn-CISE/CIS g-QDs can be tuned by controlling the shell thickness of the g-QDs template. The optical properties of as-prepared g-QDs show tunable NIR absorption and PL spectra with various shell thicknesses. It is found that the PL lifetime can be prolonged by increasing the thickness of Zn-CISE/CIS g-QDs, demonstrating that this type of NIR and heavy metal-free g-QDs possess a "quasi-type II" band structure, in which the electron can delocalize to the shell region with increasing shell thickness while holes are still confined within the core region. By choosing appropriate physical parameters, we calculated the wave functions of the electrons and holes as a function of shell thickness in as-synthesized NIR, "green" g-QDs. The spatial distribution of electron-hole wave shows that the electrons gradually delocalize into the shell region with increasing shell thickness, while the holes are still confined within the core region, which is an indicative of "quasi-type II" band structure and consistent with the optical measurements. As a proof of concept, these NIR, heavy metal-free g-QDs were used as photosensitizers for fabrication of PEC cells for hydrogen production. As-fabricated QDs-based PEC cell exhibits a saturated photocurrent density of ~3 mA/cm² with good device stability under standard one sun illumination (AM 1.5G, 100 mW/cm²). These results indicate that these NIR heavy metal-free g-QDs are very promising components of future optoelectronic technologies. The limitations of these g-QDs is the hole accumulation induced by the "quasi-type II" band structure, which can be optimized by introducing the CuInSeS alloyed shell for gradient band energy level to accelerate the hole transfer.

In Chapter 5, we synthesized pyramidal-shaped CISES/CdSeS/CdS g-QDs through a facile two-step approach. As synthesized pyramidal-shaped g-QDs possess a thick CdSeS/CdS shell with

ZB phase. The optical properties of these g-QDs exhibit NIR PL emission (emission peak at ~830 nm), high PLQY (~17%), and very long PL lifetime (in the magnitude of μs). The PL lifetime is prolonged with the increasing shell thickness of as-synthesized NIR, pyramidal-shaped g-QDs, demonstrating their "quasi-type II" band structure for efficiently spatial electron-hole separation. According to the morphology and optical properties of the pyramidal-shaped g-QDs at different growth stages, we choose appropriate physical parameters and solve the Schrödinger equation to simulate the electron-hole wave functions in these g-QDs, which exhibit a direction-dependent electron-hole wave function distribution. With the increasing shell thickness, the electrons can delocalize into the shell region while the holes are almost confined within the core region, confirming "quasi-type II" band structure. Due to the efficient electron-hole separation in such g-QDs, these g-QDs were used to fabricate QDs-based PEC cell, showing saturated photocurrent density up to $\sim 5.5 \text{ mA/cm}^2$ and outstanding device stability under standard one sun irradiation. These results imply that pyramidal-shaped g-QDs can effectively improve the electron-hole separation and can be used to fabricate high performance and stable optoelectronic devices, while the major limitation for their practical applications is still the heavy metal (Cd) in these g-QDs, the next step may focus on investigating heavy metal-free shell materials in these non-spherical g-QDs.

5.2 Perspectives

Although we synthesized a variety of NIR core/shell QDs and studied the morphology/composition, optical properties and their application in solar-driven PEC hydrogen production, there are still several issues to be optimized for further improvements. Future developments of these NIR core/shell QDs can focus on the following aspects:

(i) In addition to the NIR, environmentally friendly CuInSe(S) and its core/shell structured QDs we reported, more other types of heavy metal-free QDs such as AgInS₂, AgInTe₂ and Ag₂S/ZnS etc. with absorption and/or PL spectrum covering the UV-visible-NIR region are promising candidates for solar energy applications, which may be employed to fabricate QDs-sensitized photoelectrodes for high-efficiency solar-driven PEC hydrogen production. Moreover, the composition and structure of the shell in these core/shell QDs can be tuned in order to further

optimize the optoelectronic properties of these NIR core/shell QDs, for example, Zn alloyed CISES QDs exhibit a higher CB edge, leading to larger driving force for electron injection from QDs into TiO₂ compared to bare CISES QDs, thereby improving the performance and stability of corresponding QDs-based optoelectronic devices.

(ii) Improving the optoelectronic properties of NIR, environmentally friendly Zn-CISE/CIS g-QDs by tuning their shell thickness and composition, for instance, introducing the alloyed CuInSeS layer between the CISE and CIS layer to enhance the hole transfer rate of the QDs, thus optimizing the performance of these NIR environment-friendly g-QDs-based optoelectronic devices. Another promising direction is to use these QDs for the biomedical applications, such as biosensors and bioimaging, etc.

(iii) Synthesizing NIR, heavy metal-free and non-spherical g-QDs, such as pyramid SnSe/SnSe_xS_{1-x}/SnS g-QDs with well-controlled crystal structure, ultralong PL lifetime for highly efficient electron-hole separation and transport. In addition, it is also possible to further enhance the light absorption by tuning the shell composition of these non-spherical g-QDs, such as using AgInS(Se) shell to expand its absorption spectrum to the NIR region.

(iv) Tuning the core sizes instead of the shell thickness in these g-QDs to comprehensively investigate their corresponding optoelectronic properties. Optimize the PEC measurement such as using gas chromatography (GC) to measure the authentic volume of generated hydrogen from QDs-based PEC cells.

(v) Changing the current corrosive electrolyte (i.e. Na₂S/Na₂SO₃) to be neutral solution (e.g. Na₂SO₄) and measure relevant performance of QDs-based PEC cells. Applying the CISES/ZnS, Zn-CISE/CIS and CISES/CdSeS/CdS core/shell QDs in other optoelectronic devices such as photodetectors, LEDs and LSCs etc.

BIBLIOGRAPHY

1. Carey, G. H.; Abdelhady, A. L.; Ning, Z. J.; Thon, S. M.; Bakr, O. M.; Sargent, E. H. *Chemical Reviews* 2015, 115, 23, 12732-12763.
2. Lesnyak, V.; Gaponik, N.; Eychmuller, A. *Chemical Society Reviews* 2013, 42, 7, 2905-2929.
3. Litvin, A. P.; Martynenko, I. V.; Purcell-Milton, F.; Baranov, A. V.; Fedorov, A. V.; Gun'ko, Y. K. *Journal of Materials Chemistry A* 2017, 5, 26, 13252-13275.
4. Zhao, H.; Rosei, F. *Chem* 2017, 3, 2, 229-258.
5. Wang, Y.; Hu, A. *Journal of Materials Chemistry C* 2014, 2, 34, 6921-6939.
6. Alivisatos, A. P. *Science* 1996, 271, 5251, 933-937.
7. Kagan, C. R.; Lifshitz, E.; Sargent, E. H.; Talapin, D. V. *Science* 2016, 353, 6302.
8. Holmes, M. A.; Townsend, T. K.; Osterloh, F. E. *Chemical Communications* 2012, 48, 3, 371-373.
9. Takagahara, T.; Takeda, K. *Physical Review B* 1992, 46, 23, 15578-15581.
10. Smith, A. M.; Nie, S. *Accounts of Chemical Research* 2010, 43, 2, 190-200.
11. Zhang, J.; Gao, J.; Church, C. P.; Miller, E. M.; Luther, J. M.; Klimov, V. I.; Beard, M. C. *Nano Letters* 2014, 14, 10, 6010-6015.
12. Razgoniaeva, N.; Moroz, P.; Yang, M.; Budkina, D. S.; Eckard, H.; Augspurger, M.; Khon, D.; Tarnovsky, A. N.; Zamkov, M. *Journal of the American Chemical Society* 2017, 139, 23, 7815-7822.
13. Reiss, P.; Carriere, M.; Lincheneau, C.; Vaure, L.; Tamang, S. *Chemical Reviews* 2016, 116, 18, 10731-10819.
14. Nozik, A. J.; Beard, M. C.; Luther, J. M.; Law, M.; Ellingson, R. J.; Johnson, J. C. *Chemical Reviews* 2010, 110, 11, 6873-6890.
15. Moreels, I.; Lambert, K.; Smeets, D.; De Muynck, D.; Nollet, T.; Martins, J. C.; Vanhaecke, F.; Vantomme, A.; Delerue, C.; Allan, G.; Hens, Z. *ACS Nano* 2009, 3, 10, 3023-3030.
16. Ghosh Chaudhuri, R.; Paria, S. *Chemical Reviews* 2012, 112, 4, 2373-2433.
17. Wehrenberg, B. L.; Wang, C. J.; Guyot-Sionnest, P. *Journal of Physical Chemistry B* 2002, 106, 41, 10634-10640.
18. Pattantyus-Abraham, A. G.; Kramer, I. J.; Barkhouse, A. R.; Wang, X. H.; Konstantatos, G.; Debnath, R.; Levina, L.; Raabe, I.; Nazeeruddin, M. K.; Gratzel, M.; Sargent, E. H. *ACS Nano* 2010, 4, 6, 3374-3380.
19. Jin, L.; AlOtaibi, B.; Benetti, D.; Li, S.; Zhao, H.; Mi, Z.; Vomiero, A.; Rosei, F. *Advanced Science* 2016, 3, 3, 1500345.
20. Kwak, J.; Bae, W. K.; Lee, D.; Park, I.; Lim, J.; Park, M.; Cho, H.; Woo, H.; Yoon, D. Y.; Char, K.; Lee, S.; Lee, C. *Nano Letters* 2012, 12, 5, 2362-2366.
21. Meinardi, F.; McDaniel, H.; Carulli, F.; Colombo, A.; Velizhanin, K. A.; Makarov, N. S.; Simonutti, R.; Klimov, V. I.; Brovelli, S. *Nature Nanotechnology* 2015, 10, 10, 878-885.
22. Murray, C. B.; Norris, D. J.; Bawendi, M. G. *Journal of the American Chemical Society* 1993, 115, 19, 8706-8715.
23. Murray, C. B.; Kagan, C. R.; Bawendi, M. G. *Annual Review of Materials Science* 2000, 30, 545-610.
24. Talapin, D. V.; Rogach, A. L.; Kornowski, A.; Haase, M.; Weller, H. *Nano Letters* 2001, 1,

- 4, 207-211.
25. Li, J. J.; Wang, Y. A.; Guo, W.; Keay, J. C.; Mishima, T. D.; Johnson, M. B.; Peng, X. *Journal of the American Chemical Society* 2003, 125, 41, 12567-12575.
26. de Mello Donega, C.; Liljeroth, P.; Vanmaekelbergh, D. *Small* 2005, 1, 12, 1152-1162.
27. Park, J.; Joo, J.; Kwon, S. G.; Jang, Y.; Hyeon, T. *Angewandte Chemie International Edition* 2007, 46, 25, 4630-4660.
28. Chan, S.; Liu, M.; Latham, K.; Haruta, M.; Kurata, H.; Teranishi, T.; Tachibana, Y. *Journal of Materials Chemistry C* 2017, 5, 8, 2182-2187.
29. Tang, J.; Hinds, S.; Kelley, S. O.; Sargent, E. H. *Chemistry of Materials* 2008, 20, 22, 6906-6910.
30. van Embden, J.; Chesman, A. S. R.; Jasieniak, J. J. *Chemistry of Materials* 2015, 27, 7, 2246-2285.
31. de Mello Donega, C. *Chemical Society Reviews* 2011, 40, 3, 1512-1546.
32. Swafford, L. A.; Weigand, L. A.; Bowers, M. J., 2nd; McBride, J. R.; Rapaport, J. L.; Watt, T. L.; Dixit, S. K.; Feldman, L. C.; Rosenthal, S. J. *Journal of the American Chemical Society* 2006, 128, 37, 12299-12306.
33. Kwon, S. G.; Piao, Y.; Park, J.; Angappane, S.; Jo, Y.; Hwang, N.-M.; Park, J.-G.; Hyeon, T. *Journal of the American Chemical Society* 2007, 129, 41, 12571-12584.
34. Zhao, H.; Fan, Z.; Liang, H.; Selopal, G. S.; Gonfa, B. A.; Jin, L.; Soudi, A.; Cui, D.; Enrichi, F.; Natile, M. M.; Concina, I.; Ma, D.; Govorov, A. O.; Rosei, F.; Vomiero, A. *Nanoscale* 2014, 6, 12, 7004-7011.
35. Zhao, H.; Chaker, M.; Ma, D. *Journal of Materials Chemistry* 2011, 21, 43, 17483-17491.
36. Zhao, H.; Chaker, M.; Wu, N.; Ma, D. *Journal of Materials Chemistry* 2011, 21, 24, 8898-8904.
37. Zhao, H.; Liang, H.; Vidal, F.; Rosei, F.; Vomiero, A.; Ma, D. *Journal of Physical Chemistry C* 2014, 118, 35, 20585-20593.
38. Reiss, P.; Protiere, M.; Li, L. *Small* 2009, 5, 2, 154-168.
39. Etgar, L.; Yanover, D.; Čapek, R. K.; Vaxenburg, R.; Xue, Z.; Liu, B.; Nazeeruddin, M. K.; Lifshitz, E.; Grätzel, M. *Advanced Functional Materials* 2013, 23, 21, 2736-2741.
40. Ning, Z.; Tian, H.; Yuan, C.; Fu, Y.; Qin, H.; Sun, L.; Agren, H. *Chemical Communications* 2011, 47, 5, 1536-1538.
41. Zhao, H.; Jin, L.; Zhou, Y.; Bandar, A.; Fan, Z.; Govorov, A. O.; Mi, Z.; Sun, S.; Rosei, F.; Vomiero, A. *Nanotechnology* 2016, 27, 49, 495405.
42. De Geyter, B.; Justo, Y.; Moreels, I.; Lambert, K.; Smet, P. F.; Van Thourhout, D.; Houtepen, A. J.; Grodzinska, D.; de Mello Donega, C.; Meijerink, A.; Vanmaekelbergh, D.; Hens, Z. *ACS Nano* 2011, 5, 1, 58-66.
43. Girma, W. M.; Fahmi, M. Z.; Permadi, A.; Abate, M. A.; Chang, J.-Y. *Journal of Materials Chemistry B* 2017, 5, 31, 6193-6216.
44. Park, J.; Dvoracek, C.; Lee, K. H.; Galloway, J. F.; Bhang, H.-e. C.; Pomper, M. G.; Searson, P. C. *Small* 2011, 7, 22, 3148-3152.
45. Kim, S.; Fisher, B.; Eisler, H. J.; Bawendi, M. *Journal of the American Chemical Society* 2003, 125, 38, 11466-11467.
46. Dennis, A. M.; Mangum, B. D.; Piryatinski, A.; Park, Y. S.; Hannah, D. C.; Casson, J. L.; Williams, D. J.; Schaller, R. D.; Htoon, H.; Hollingsworth, J. A. *Nano Letters* 2012, 12, 11,

5545-5551.

47. Wu, K.; Liang, G.; Kong, D.; Chen, J.; Chen, Z.; Shan, X.; McBride, J. R.; Lian, T. *Chemical Science* 2016, 7, 2, 1238-1244.
48. Wu, K.; Song, N.; Liu, Z.; Zhu, H.; Rodriguez-Cordoba, W.; Lian, T. *Journal of Physical Chemistry A* 2013, 117, 32, 7561-7570.
49. Chen, Y.; Vela, J.; Htoon, H.; Casson, J. L.; Werder, D. J.; Bussian, D. A.; Klimov, V. I.; Hollingsworth, J. A. *Journal of the American Chemical Society* 2008, 130, 15, 5026-5027.
50. Dabbousi, B. O.; Rodriguez-Viejo, J.; Mikulec, F. V.; Heine, J. R.; Mattoussi, H.; Ober, R.; Jensen, K. F.; Bawendi, M. G. *Journal of Physical Chemistry B* 1997, 101, 46, 9463-9475.
51. Xu, S.; Ziegler, J.; Nann, T. *Journal of Materials Chemistry* 2008, 18, 23, 2653-2656.
52. Zhong, H.; Scholes, G. D. *Journal of the American Chemical Society* 2009, 131, 26, 9170-9171.
53. Lambert, K.; Geyter, B. D.; Moreels, I.; Hens, Z. *Chemistry of Materials* 2009, 21, 5, 778-780.
54. McDaniel, H.; Kopolov, A. Y.; Draguta, S.; Makarov, N. S.; Pietryga, J. M.; Klimov, V. I. *Journal of Physical Chemistry C* 2014, 118, 30, 16987-16994.
55. Li, L. A.; Pandey, A.; Werder, D. J.; Khanal, B. P.; Pietryga, J. M.; Klimov, V. I. *Journal of the American Chemical Society* 2011, 133, 5, 1176-1179.
56. Nasilowski, M.; Nienhaus, L.; Bertram, S. N.; Bawendi, M. G. *Chemical Communications* 2017, 53, 5, 869-872.
57. Navarro-Pardo, F.; Zhao, H. G.; Wang, Z. M. M.; Rosei, F. *Accounts of Chemical Research* 2018, 51, 3, 609-618.
58. Garcia-Santamaria, F.; Chen, Y.; Vela, J.; Schaller, R. D.; Hollingsworth, J. A.; Klimov, V. I. *Nano Letters* 2009, 9, 10, 3482-3488.
59. Kundu, J.; Ghosh, Y.; Dennis, A. M.; Htoon, H.; Hollingsworth, J. A. *Nano Letters* 2012, 12, 6, 3031-3037.
60. Brovelli, S.; Schaller, R. D.; Crooker, S. A.; Garcia-Santamaria, F.; Chen, Y.; Viswanatha, R.; Hollingsworth, J. A.; Htoon, H.; Klimov, V. I. *Nature Communications* 2011, 2, 280.
61. Hanson, C. J.; Hartmann, N. F.; Singh, A.; Ma, X.; DeBenedetti, W. J. I.; Casson, J. L.; Grey, J. K.; Chabal, Y. J.; Malko, A. V.; Sykora, M.; Piryatinski, A.; Htoon, H.; Hollingsworth, J. A. *Journal of the American Chemical Society* 2017, 139, 32, 11081-11088.
62. Lim, J.; Jeong, B. G.; Park, M.; Kim, J. K.; Pietryga, J. M.; Park, Y. S.; Klimov, V. I.; Lee, C.; Lee, D. C.; Bae, W. K. *Advanced Materials* 2014, 26, 47, 8034-8040.
63. Tong, X.; Kong, X.-T.; Zhou, Y.; Navarro-Pardo, F.; Selopal, G. S.; Sun, S.; Govorov, A. O.; Zhao, H.; Wang, Z. M.; Rosei, F. *Advanced Energy Materials* 2018, 8, 2, 1701432.
64. Bae, W. K.; Padilha, L. A.; Park, Y. S.; McDaniel, H.; Robel, I.; Pietryga, J. M.; Klimov, V. I. *ACS Nano* 2013, 7, 4, 3411-3419.
65. Zhao, H.; Benetti, D.; Jin, L.; Zhou, Y.; Rosei, F.; Vomiero, A. *Small* 2016, 12, 38, 5354-5365.
66. Meinardi, F.; Colombo, A.; Velizhanin, K. A.; Simonutti, R.; Lorenzon, M.; Beverina, L.; Viswanatha, R.; Klimov, V. I.; Brovelli, S. *Nature Photonics* 2014, 8, 5, 392-399.
67. Adhikari, R.; Jin, L.; Navarro-Pardo, F.; Benetti, D.; AlOtaibi, B.; Vanka, S.; Zhao, H.; Mi, Z.; Vomiero, A.; Rosei, F. *Nano Energy* 2016, 27, 265-274.
68. Selopal, G. S.; Zhao, H.; Tong, X.; Benetti, D.; Navarro-Pardo, F.; Zhou, Y.; Barba, D.;

- Vidal, F.; Wang, Z. M.; Rosei, F. *Advanced Functional Materials* 2017, 27, 30, 1701468.
69. Tsoi, K. M.; Dai, Q.; Alman, B. A.; Chan, W. C. *Accounts of Chemical Research* 2013, 46, 3, 662-671.
70. Jaishankar, M.; Tseten, T.; Anbalagan, N.; Mathew, B. B.; Beeregowda, K. N. *Interdisciplinary Toxicology* 2014, 7, 2, 60-72.
71. Bolisetty, S.; Peydayesh, M.; Mezzenga, R. *Chemical Society Reviews* 2019, 48, 2, 463-487.
72. Kim, H. S.; Kim, Y. J.; Seo, Y. R. *Journal of Cancer Prevention* 2015, 20, 4, 232-240.
73. Turner, A. *Science of the Total Environment* 2019, 657, 1409-1418.
74. Haney, J., Jr. *Regulatory Toxicology and Pharmacology* 2016, 77, 175-83.
75. Chen, C.; Xun, P.; Nishijo, M.; He, K. *Journal of Exposure Science and Environmental Epidemiology* 2016, 26, 5, 437-444.
76. Huff, J.; Lunn, R. M.; Waalkes, M. P.; Tomatis, L.; Infante, P. F. *International Journal of Occupational and Environmental Health* 2007, 13, 2, 202-212.
77. Komarek, M.; Ettler, V.; Chrastny, V.; Mihaljevic, M. *Environment International* 2008, 34, 4, 562-577.
78. Grandjean, P. *The Lancet* 2010, 376, 9744, 855-856.
79. Araki, S.; Sato, H.; Yokoyama, K.; Murata, K. *American Journal of Industrial Medicine* 2000, 37, 2, 193-204.
80. Barregard, L.; Fabricius-Lagging, E.; Lundh, T.; Molne, J.; Wallin, M.; Olausson, M.; Modigh, C.; Sallsten, G. *Environmental Research* 2010, 110, 1, 47-54.
81. Steenland, K.; Boffetta, P. *American Journal of Industrial Medicine* 2000, 38, 3, 295-299.
82. Rehman, K.; Fatima, F.; Waheed, I.; Akash, M. S. H. *Journal of Cellular Biochemistry* 2018, 119, 1, 157-184.
83. Coropceanu, I.; Bawendi, M. G. *Nano Letters* 2014, 14, 7, 4097-4101.
84. Yu, W. W.; Qu, L.; Guo, W.; Peng, X. *Chemistry of Materials* 2003, 15, 14, 2854-2860.
85. Lifshitz, E.; Brumer, M.; Kigel, A.; Sashchiuk, A.; Bashouti, M.; Sirota, M.; Galun, E.; Burshtein, Z.; Le Quang, A. Q.; Ledoux-Rak, I.; Zyss, J. *Journal of Physical Chemistry B* 2006, 110, 50, 25356-25365.
86. Leach, A. D.; Macdonald, J. E. *Journal of Physical Chemistry Letters* 2016, 7, 3, 572-583.
87. Sandroni, M.; Wegner, K. D.; Aldakov, D.; Reiss, P. *ACS Energy Letters* 2017, 2, 5, 1076-1088.
88. Zhang, Y.; Hong, G.; Zhang, Y.; Chen, G.; Li, F.; Dai, H.; Wang, Q. *ACS Nano* 2012, 6, 5, 3695-3702.
89. Cao, Q.; Cheng, Y.-F.; Bi, H.; Zhao, X.; Yuan, K.; Liu, Q.; Li, Q.; Wang, M.; Che, R. *Journal of Materials Chemistry A* 2015, 3, 40, 20051-20055.
90. Pichaandi, J.; van Veggel, F. C. J. M. *Coordination Chemistry Reviews* 2014, 263, 138-150.
91. Hamanaka, Y.; Ogawa, T.; Tsuzuki, M.; Kuzuya, T. *Journal of Physical Chemistry C* 2011, 115, 5, 1786-1792.
92. Park, J.; Kim, S.-W. *Journal of Materials Chemistry* 2011, 21, 11, 3745-3750.
93. Kameyama, T.; Takahashi, T.; Machida, T.; Kamiya, Y.; Yamamoto, T.; Kuwabata, S.; Torimoto, T. *Journal of Physical Chemistry C* 2015, 119, 44, 24740-24749.
94. Zang, H.; Li, H.; Makarov, N. S.; Velizhanin, K. A.; Wu, K.; Park, Y. S.; Klimov, V. I. *Nano Letters* 2017, 17, 3, 1787-1795.
95. Tong, X.; Kong, X.-T.; Wang, C.; Zhou, Y.; Navarro-Pardo, F.; Barba, D.; Ma, D.; Sun, S.;

- Govorov, A. O.; Zhao, H.; Wang, Z. M.; Rosei, F. *Advanced Science* 2018, 5, 8, 1800656.
96. Pan, Z.; Mora-Sero, I.; Shen, Q.; Zhang, H.; Li, Y.; Zhao, K.; Wang, J.; Zhong, X.; Bisquert, J. *Journal of the American Chemical Society* 2014, 136, 25, 9203-9210.
97. McDaniel, H.; Fuke, N.; Makarov, N. S.; Pietryga, J. M.; Klimov, V. I. *Nature Communications* 2013, 4, 2887.
98. Walter, M. G.; Warren, E. L.; McKone, J. R.; Boettcher, S. W.; Mi, Q.; Santori, E. A.; Lewis, N. S. *Chemical Reviews* 2010, 110, 11, 6446-6473.
99. Gratzel, M. *Nature* 2001, 414, 6861, 338-344.
100. Wang, G.; Wang, H.; Ling, Y.; Tang, Y.; Yang, X.; Fitzmorris, R. C.; Wang, C.; Zhang, J. Z.; Li, Y. *Nano Letters* 2011, 11, 7, 3026-3033.
101. Wang, G.; Yang, X.; Qian, F.; Zhang, J. Z.; Li, Y. *Nano Letters* 2010, 10, 3, 1088-1092.
102. Yang, X. Y.; Wolcott, A.; Wang, G. M.; Sobo, A.; Fitzmorris, R. C.; Qian, F.; Zhang, J. Z.; Li, Y. *Nano Letters* 2009, 9, 6, 2331-2336.
103. Chen, X.; Shen, S.; Guo, L.; Mao, S. S. *Chemical Reviews* 2010, 110, 11, 6503-6570.
104. Kudo, A.; Miseki, Y. *Chemical Society Reviews* 2009, 38, 1, 253-278.
105. Sahai, S.; Ikram, A.; Rai, S.; Shrivastav, R.; Dass, S.; Satsangi, V. R. *Renewable & Sustainable Energy Reviews* 2017, 68, 19-27.
106. Kandi, D.; Martha, S.; Parida, K. M. *International Journal of Hydrogen Energy* 2017, 42, 15, 9467-9481.
107. Li, T.-L.; Lee, Y.-L.; Teng, H. *Journal of Materials Chemistry* 2011, 21, 13, 5089-5098.
108. Ruberu, T. P. A.; Dong, Y.; Das, A.; Eisenberg, R. *ACS Catalysis* 2015, 5, 4, 2255-2259.
109. Beard, M. C. *Journal of Physical Chemistry Letters* 2011, 2, 11, 1282-1288.
110. Yan, Y.; Crisp, R. W.; Gu, J.; Chernomordik, B. D.; Pach, G. F.; Marshall, A. R.; Turner, J. A.; Beard, M. C. *Nature Energy* 2017, 2, 5, 17052.
111. Cheng, C.; Karuturi, S. K.; Liu, L.; Liu, J.; Li, H.; Su, L. T.; Tok, A. I. Y.; Fan, H. J. *Small* 2012, 8, 1, 37-42.
112. Sun, W. T.; Yu, Y.; Pan, H. Y.; Gao, X. F.; Chen, Q.; Peng, L. M. *Journal of the American Ceramic Society* 2008, 130, 4, 1124-1125.
113. Xie, Z.; Liu, X.; Wang, W.; Wang, X.; Liu, C.; Xie, Q.; Li, Z.; Zhang, Z. *Nano Energy* 2015, 11, 400-408.
114. Hensel, J.; Wang, G. M.; Li, Y.; Zhang, J. Z. *Nano Letters* 2010, 10, 2, 478-483.
115. Gao, X.-F.; Li, H.-B.; Sun, W.-T.; Chen, Q.; Tang, F.-Q.; Peng, L.-M. *Journal of Physical Chemistry C* 2009, 113, 18, 7531-7535.
116. Jin-nouchi, Y.; Hattori, T.; Sumida, Y.; Fujishima, M.; Tada, H. *ChemPhysChem* 2010, 11, 17, 3592-3595.
117. Trevisan, R.; Rodenas, P.; Gonzalez-Pedro, V.; Sima, C.; Sanchez, R. S.; Barea, E. M.; Mora-Sero, I.; Fabregat-Santiago, F.; Gimenez, S. *Journal of Physical Chemistry Letters* 2013, 4, 1, 141-146.
118. Wu, L.; Chen, S.-Y.; Fan, F.-J.; Zhuang, T.-T.; Dai, C.-M.; Yu, S.-H. *Journal of the American Chemical Society* 2016, 138, 17, 5576-5584.
119. Li, T.-L.; Teng, H. *Journal of Materials Chemistry* 2010, 20, 18, 3656-3664.
120. Sheng, P.; Li, W.; Tong, X.; Wang, X.; Cai, Q. *Journal of Materials Chemistry A* 2014, 2, 44, 18974-18987.
121. Wang, K.; Tong, X.; Zhou, Y.; Zhang, H.; Navarro-Pardo, F.; Selopal, G. S.; Liu, G.; Tang,

- J.; Wang, Y.; Sun, S.; Ma, D.; Wang, Zhiming M.; Vidal, F.; Zhao, H.; Sun, X.; Rosei, F. *Journal of Materials Chemistry A* 2019, 7, 23, 14079-14088.
122. Sheng, W.; Sun, B.; Shi, T.; Tan, X.; Peng, Z.; Liao, G. *ACS Nano* 2014, 8, 7, 7163-7169.
123. Rodenas, P.; Song, T.; Sudhagar, P.; Marzari, G.; Han, H.; Badia-Bou, L.; Gimenez, S.; Fabregat-Santiago, F.; Mora-Sero, I.; Bisquert, J.; Paik, U.; Kang, Y. S. *Advanced Energy Materials* 2013, 3, 2, 176-182.
124. Zhang, Z.; Li, X.; Gao, C.; Teng, F.; Wang, Y.; Chen, L.; Han, W.; Zhang, Z.; Xie, E. *Journal of Materials Chemistry A* 2015, 3, 24, 12769-12776.
125. Chen, H.; Chao, P.; Han, D.; Wang, H.; Miao, J.; Zhong, H.; Meng, H.; He, F. *ACS Applied Materials & Interfaces* 2017, 9, 8, 7362-7367.
126. Bergren, M. R.; Makarov, N. S.; Ramasamy, K.; Jackson, A.; Guglielmetti, R.; McDaniel, H. *ACS Energy Letters* 2018, 3, 3, 520-525.
127. Fuhr, A. S.; Yun, H. J.; Makarov, N. S.; Li, H.; McDaniel, H.; Klimov, V. I. *ACS Photonics* 2017, 4, 10, 2425-2435.
128. Sun, J.; Zhao, J.; Masumoto, Y. *Applied Physics Letters* 2013, 102, 5, 053119.
129. Li, T. L.; Teng, H. *Journal of Materials Chemistry* 2010, 20, 18, 3656-3664.
130. Jin, L.; Zhao, H.; Ma, D.; Vomiero, A.; Rosei, F. *Journal of Materials Chemistry A* 2015, 3, 2, 847-856.
131. Hines, D. A.; Forrest, R. P.; Corcelli, S. A.; Kamat, P. V. *Journal of Physical Chemistry B* 2015, 119, 24, 7439-7446.
132. Wang, Z.; Wen, X. D.; Hoffmann, R.; Son, J. S.; Li, R.; Fang, C. C.; Smilgies, D. M.; Hyeon, T. *Proceedings of the National Academy of Sciences of the United States of America* 2010, 107, 40, 17119-17124.
133. McDaniel, H.; Fuke, N.; Pietryga, J. M.; Klimov, V. I. *Journal of Physical Chemistry Letters* 2013, 4, 3, 355-361.
134. Brown, P. R.; Kim, D.; Lunt, R. R.; Zhao, N.; Bawendi, M. G.; Grossman, J. C.; Bulovic, V. *ACS Nano* 2014, 8, 6, 5863-5872.
135. Basu, K.; Benetti, D.; Zhao, H.; Jin, L.; Vetrone, F.; Vomiero, A.; Rosei, F. *Scientific Reports* 2016, 6, 23312.
136. Tang, J.; Kemp, K. W.; Hoogland, S.; Jeong, K. S.; Liu, H.; Levina, L.; Furukawa, M.; Wang, X.; Debnath, R.; Cha, D.; Chou, K. W.; Fischer, A.; Amassian, A.; Asbury, J. B.; Sargent, E. H. *Nature Materials* 2011, 10, 10, 765-771.
137. Ip, A. H.; Thon, S. M.; Hoogland, S.; Voznyy, O.; Zhitomirsky, D.; Debnath, R.; Levina, L.; Rollny, L. R.; Carey, G. H.; Fischer, A.; Kemp, K. W.; Kramer, I. J.; Ning, Z.; Labelle, A. J.; Chou, K. W.; Amassian, A.; Sargent, E. H. *Nature Nanotechnology* 2012, 7, 9, 577-582.
138. Li, W.; Sheng, P.; Feng, H.; Yin, X.; Zhu, X.; Yang, X.; Cai, Q. *ACS Applied Materials & Interfaces* 2014, 6, 15, 12353-12362.
139. Yu, X.; Liu, J.; Genc, A.; Ibanez, M.; Luo, Z.; Shavel, A.; Arbiol, J.; Zhang, G.; Zhang, Y.; Cabot, A. *Langmuir* 2015, 31, 38, 10555-10561.
140. Yang, H. B.; Miao, J.; Hung, S.-F.; Huo, F.; Chen, H. M.; Liu, B. *ACS Nano* 2014, 8, 10, 10403-10413.
141. Ai, G.; Li, H.; Liu, S.; Mo, R.; Zhong, J. *Advanced Functional Materials* 2015, 25, 35, 5706-5713.
142. Sukhovatkin, V.; Hinds, S.; Brzozowski, L.; Sargent, E. H. *Science* 2009, 324, 5934, 1542-

- 1544.
143. Pal, B. N.; Ghosh, Y.; Brovelli, S.; Laocharoensuk, R.; Klimov, V. I.; Hollingsworth, J. A.; Htoon, H. *Nano Letters* 2012, 12, 1, 331-336.
144. Acharya, K. P.; Nguyen, H. M.; Paulite, M.; Piryatinski, A.; Zhang, J.; Casson, J. L.; Xu, H.; Htoon, H.; Hollingsworth, J. A. *Journal of the American Chemical Society* 2015, 137, 11, 3755-3758.
145. Jin, L.; Sirigu, G.; Tong, X.; Camellini, A.; Parisini, A.; Nicotra, G.; Spinella, C.; Zhao, H.; Sun, S.; Morandi, V.; Zavelani-Rossi, M.; Rosei, F.; Vomiero, A. *Nano Energy* 2016, 30, 531-541.
146. van der Stam, W.; Bladt, E.; Rabouw, F. T.; Bals, S.; Donega Cde, M. *ACS Nano* 2015, 9, 11, 11430-11438.
147. Ghosh, Y.; Mangum, B. D.; Casson, J. L.; Williams, D. J.; Htoon, H.; Hollingsworth, J. A. *Journal of the American Chemical Society* 2012, 134, 23, 9634-9643.
148. Park, Y. S.; Bae, W. K.; Pietryga, J. M.; Klimov, V. I. *ACS Nano* 2014, 8, 7, 7288-7296.
149. Tong, X.; Zhou, Y.; Jin, L.; Basu, K.; Adhikari, R.; Selopal, G. S.; Tong, X.; Zhao, H.; Sun, S.; Vomiero, A.; Wang, Z. M.; Rosei, F. *Nano Energy* 2017, 31, 441-449.
150. Berends, A. C.; Mangnus, M. J. J.; Xia, C.; Rabouw, F. T.; de Mello Donega, C. *Journal of Physical Chemistry Letters* 2019, 10, 7, 1600-1616.
151. Qi, K.; Wang, Y.; Wang, R.; Wu, D.; Li, G.-D. *Journal of Materials Chemistry C* 2016, 4, 9, 1895-1899.
152. Shabaev, A.; Mehl, M. J.; Efros, A. L. *Physical Review B* 2015, 92, 3, 035431.
153. Neumann, H. *Solar Cells* 1986, 16, 317-333.
154. Chen, S.; Gong, X. G.; Walsh, A.; Wei, S.-H. *Applied Physics Letters* 2009, 94, 4, 041903.
155. Wei, S.-H.; Zunger, A. *Journal of Applied Physics* 1995, 78, 6, 3846.
156. Knowles, K. E.; Nelson, H. D.; Kilburn, T. B.; Gamelin, D. R. *Journal of the American Chemical Society* 2015, 137, 40, 13138-13147.
157. Wu, X.; Liu, H.; Liu, J.; Haley, K. N.; Treadway, J. A.; Larson, J. P.; Ge, N.; Peale, F.; Bruchez, M. P. *Nature Biotechnology* 2003, 21, 1, 41-46.
158. Osterloh, F. E. *Chemical Society Reviews* 2013, 42, 6, 2294-2320.
159. Lee, D. C.; Robel, I.; Pietryga, J. M.; Klimov, V. I. *Journal of the American Chemical Society* 2010, 132, 29, 9960-9962.
160. Wu, K.; Hill, L. J.; Chen, J.; McBride, J. R.; Pavlopoulos, N. G.; Richey, N. E.; Pyun, J.; Lian, T. *ACS Nano* 2015, 9, 4, 4591-4599.
161. Panthani, M. G.; Khan, T. A.; Reid, D. K.; Hellebusch, D. J.; Rasch, M. R.; Maynard, J. A.; Korgel, B. A. *Nano Letters* 2013, 13, 9, 4294-4298.
162. Nan, W.; Niu, Y.; Qin, H.; Cui, F.; Yang, Y.; Lai, R.; Lin, W.; Peng, X. *Journal of the American Chemical Society* 2012, 134, 48, 19685-19693.
163. Qin, H.; Niu, Y.; Meng, R.; Lin, X.; Lai, R.; Fang, W.; Peng, X. *Journal of the American Chemical Society* 2014, 136, 1, 179-187.
164. Dai, X.; Zhang, Z.; Jin, Y.; Niu, Y.; Cao, H.; Liang, X.; Chen, L.; Wang, J.; Peng, X. *Nature* 2014, 515, 7525, 96-99.
165. Ouyang, J.; Vincent, M.; Kingston, D.; Descours, P.; Boivineau, T.; Zaman, M. B.; Wu, X.; Yu, K. *Journal of Physical Chemistry C* 2009, 113, 13, 5193-5200.
166. Pietryga, J. M.; Park, Y. S.; Lim, J.; Fidler, A. F.; Bae, W. K.; Brovelli, S.; Klimov, V. I.

- Chemical Reviews* 2016, 116, 18, 10513-10622.
167. Coulter, J. B.; Birnie, D. P. *physica status solidi (b)* 2018, 255, 3.
168. Tauc, J.; Grigorovici, R.; Vancu, A. *physica status solidi (b)* 1966, 15, 2, 627-637.
169. Bronstein, N. D.; Li, L.; Xu, L.; Yao, Y.; Ferry, V. E.; Alivisatos, A. P.; Nuzzo, R. G. *ACS Nano* 2014, 8, 1, 44-53.
170. Xie, R. G.; Rutherford, M.; Peng, X. G. *Journal of the American Chemical Society* 2009, 131, 15, 5691-5697.
171. Pak, C.; Woo, J. Y.; Lee, K.; Kim, W. D.; Yoo, Y.; Lee, D. C. *Journal of Physical Chemistry C* 2012, 116, 48, 25407-25414.
172. Korala, L.; Wang, Z.; Liu, Y.; Maldonado, S.; Brock, S. L. *ACS Nano* 2013, 7, 2, 1215-1223.
173. Cao, S.; Yan, X.; Kang, Z.; Liang, Q.; Liao, X.; Zhang, Y. *Nano Energy* 2016, 24, 25-31.
174. Zhang, Z.; Gao, C.; Wu, Z.; Han, W.; Wang, Y.; Fu, W.; Li, X.; Xie, E. *Nano Energy* 2016, 19, 318-327.

RÉSUMÉ

L' introduction

Les nanocristaux semi-conducteurs colloïdaux, souvent nous utiliserons le terme « quantum dots » (QD's) colloïdaux, ont attiré de nombreux intérêts de chercheurs au cours des dernières décennies ¹⁻⁶. Les QD's colloïdales sont des cristaux semi-conducteurs nanométriques (inférieur à ~ 20 nm de diamètre) couché de molécules tensioactives (ligands) et dispersés en solution, montrant des niveaux d'énergie discrets entre ceux de la molécule et ceux des semi-conducteurs en masse ^{6,7}. De façon générale, le semi-conducteur en masse a une énergie de bande interdite (E_g), lorsque le semi-conducteur absorbe un photon avec une énergie supérieure à E_g , les électrons dans la bande de valence peuvent être excités à la bande de conduction et laisser un trou dans la bande de valence, qui on parlera alors de cette paire d'électrons-trous comme « exciton ». La taille de l'exciton est définie par le rayon de Bohr (R_B) des matériaux semi-conducteurs. Une fois que la taille d'un semi-conducteur est comparable ou inférieure à R_B , les porteurs de charge deviennent spatialement confinés, il en résulte que le effet de « confinement quantique » qui conduit aux propriétés optoélectroniques dépendant de la taille des QD's ⁸⁻¹⁰.

Cet effet de confinement quantique unique des QD's permet la conception et la synthèse de QD's avec une taille, une forme et une composition chimique contrôlables pour obtenir un contrôle précis des propriétés optoélectroniques ^{1, 13, 14}. Au cours des dernières décennies, une variété de QD's colloïdales de haute qualité avec une large absorption de lumière, une émission de PL dépendant de la taille, un rendement quantique photoluminescent élevé (PLQY) et une bonne stabilité chimique / photo ont été obtenues en utilisant divers types de techniques ¹⁵⁻¹⁷. En raison de ces excellentes propriétés optoélectroniques, les QD's ont été largement utilisés comme blocs de construction dans les technologies solaires, y compris les diodes électroluminescentes (LED), les concentrateurs solaires luminescents (LSC), les cellules solaires QD's-sensibilisées (QDSC), et le photoélectrochimie (PEC) génération d'hydrogène *etc.*, fournissant une plate-forme puissante pour le développement de nombreuses classes de dispositifs optoélectroniques ^{7, 18-21}.

Des méthodes de décomposition thermique rentables et de haute qualité sont couramment utilisées pour synthétiser des QD's colloïdales de taille et de forme contrôlables^{23, 29-31}. Dans ces méthodes, la séparation des étapes de nucléation et de croissance peut être réalisée par une technique d'injection à haute température ou de la méthode de mise en température. La méthode d'injection à haute température se réfère à l'approche qui injecte rapidement les précurseurs dans un ballon à haute température avec des solvants réactionnels. La température pour injecter le précurseur est un facteur clé qui détermine la décomposition des précurseurs. Après l'injection de précurseurs, la sursaturation des précurseurs conduit à la nucléation des QD's. En raison de cela, les précurseurs sont injectés à basse température, la température globale de la réaction est abaissée et l'étape de nucléation est terminée. Avec la consommation des monomères précurseurs dans le processus de nucléation, la sursaturation diminuée induit alors la croissance subséquente des QD's^{26, 32}. Tandis que dans la méthode de mise en température, ces deux étapes sont réalisées en chauffant régulièrement le mélange des précurseurs et des ligands organiques. Avec l'apport continu d'énergie thermique externe, les précurseurs peuvent atteindre la sursaturation nécessaire et la nucléation uniforme initiale et la croissance des QD's³³.

Les QD's nus couchés de ligands organiques sont très sensibles à leur environnement chimique de surface et présentent typiquement des états de pièges liés à la surface, qui servent de centre de recombinaison non radiative pour les porteurs de charge photoexcités, réduisant ainsi la PLQY et la stabilité à long terme³⁵⁻³⁷. La formation de la structure cœur-coquille s'est révélée être une approche efficace pour améliorer la passivation de surface des QD's. Dans ces systèmes cœur-coquille, la coquille inorganique robuste peut protéger les QD's du cœur et supprimer la création de défauts/pièges de surface pour améliorer la PLQY et la stabilité^{16, 38}. De Plus, il est possible de moduler la structure de bande des QD's coeur-coquille pour améliorer la séparation et le transfert des porteurs de photoexcitée porteurs de charge (électrons-trous) en choisissant de manière appropriée les matériaux de cœur et de coquille, ce qui est prometteur pour diverses applications photovoltaïques telles que QDSC et PEC cellules QD's basées^{19, 39-41}.

Un cas particulier dans les différents types de QD's coeur-coquille est le coeur-coquille QD's « géant » (g-QD's), qui possède une coquille très épaisse (de 1,5 nm à dizaines de nm) et un

coeur avec un comportement de confinement quantique⁵⁷. Les g-QD's présentaient une stabilité chimique et photo exceptionnelle par rapport aux QD's nus et aux QD's à coeur-coquille mince, ceci étant attribué à la coquille épaisse qui isolait efficacement le matériau de base de la chimie de surface et de l'environnement ambiant chimique de QD's^{49, 58, 59}. Dans les systèmes des g-QD's, en adaptant de manière appropriée les structures de bande électroniques et les compositions chimiques, les électrons peuvent être délocalisés dans la région de la coquille alors que les trous sont encore confinés dans la région centrale. La délocalisation efficace des électrons dans la région de la coquille entraîne une durée de vie des excitons significativement prolongée et la formation d'un alignement de bande quasi ou complet type II dans les g-QD's^{57, 60}. Les g-QD's montrent généralement une stabilité photo et chimique supérieure, et leurs propriétés optoélectroniques accordables se traduisent par un grand Stokes-shift, une absorption efficace de la lumière et une séparation/transfert de charge favorables aux techniques solaires^{63, 66-68}.

Au cours des dernières décennies, les recherches sur les QD's colloïdales sont principalement axées sur l'amélioration de leurs propriétés optoélectroniques telles que le PLQY et la stabilité^{4, 6, 13, 38}. Par exemple, la synthèse de QD's à base de Cd du groupe II-VI (CdS, CdSe, CdTe, *etc.*) avec un PLQY élevé et leurs divers dispositifs optoélectroniques à base de QD's à haute performance ont été rapportés^{22, 83}. Ces QD's à base de Cd possèdent principalement une absorption et un spectre PL dans le visible, puisque la bande interdite de ces matériaux est comprise entre 1,7 eV et 3,5 eV⁸⁴. En outre, il existe d'autres QD's tels que InP, PbSe, PbS, Ag₂S, Ag₂Se, CuInS₂ et CuInSe₂ QD's montrant l'émission de PL dans la région proche infrarouge allant de *ca.* 700 nm à 5000 nm. Comparés aux QD's visibles, ces QD's proche infrarouge (NIR) présentent les avantages suivants: (1) Malgré l'émission de NIR PL, ces QD's montrent également une absorption de lumière NIR, ce qui est favorable pour améliorer l'efficacité des dispositifs photovoltaïques tels que les cellules solaires; (2) L'émission NIR des QD's peut être accordée à la longueur d'onde (~ 1500 à 1600 nm) pour la communication optique; (3) Ces points quantiques NIR avec une émission proche infrarouge de plus de 700 nm montrent des applications biomédicales potentielles telles que l'imagerie biomédicale; (4) Avec un PLQY élevé, ces NIR QD's peuvent être utilisés pour les NIR LED⁸⁵⁻⁸⁹;

Tenant ces avantages, les QD's NIR ont été largement utilisés pour réaliser des dispositifs optoélectroniques en haute performance tels que les QDSCs, les photodétecteurs, les LED et les cellules PEC, *etc.*^{19, 39, 90}. Cependant, il existe encore plusieurs limites dans ces QD's NIR. Par exemple, les QD's NIR tels que le PbSe, le PbS et le PbTe qui contiennent du métal lourd hautement toxique de Pb, ce qui peut causer une pollution environnementale très grave et nuire à la santé humaine. Ces métaux lourds de QD's dans les dispositifs optoélectroniques correspondants entravent davantage leur commercialisation future. Par conséquent, il est important d'étudier la synthèse de NIR, les QD's respectueux de l'environnement et leurs applications dans les dispositifs optoélectroniques et biomédicaux. Au cours des dernières années, NIR, QD's respectueux de l'environnement tels que AgInS₂, CuInS₂, CuInSe₂ et CISES QD's ont attiré beaucoup d'attention et sont largement étudiés pour les dispositifs optoélectroniques et biomédicaux^{13, 91}. Néanmoins, ces QD's verts NIR sont très sensibles à l'environnement ambiant en raison de leurs compositions multiniveaux, qui sont susceptibles d'induire les états de défauts de surface / pièges. Ces défauts de surface agissent comme des centres de recombinaison non radiatifs et se traduisent par une très faible PLQY et une stabilité chimique/photostatique⁹²⁻⁹⁴. Dans cette perspective, la construction d'une structure cœur-coquille est une approche efficace pour améliorer les propriétés optoélectroniques et la stabilité de ces QD's.

La cellule PEC à énergie solaire est un système photovoltaïque capable de capter l'énergie solaire pour séparer l'eau et produire l'énergie hydrogène⁹⁸. Au cours des dernières années, l'utilisation de QD colloïdales pour sensibiliser les matériaux semi-conducteurs a été démontrée comme une méthode efficace pour améliorer la performance des cellules PEC^{105, 106}. Plus précisément, des QD à base de Cd (*e.g.* CdS, CdSe, CdTe *etc.*) ont été utilisés pour sensibiliser les semi-conducteurs à large bande interdite (TiO₂, ZnO, *etc.*) avec différentes morphologies (par exemple nanotubes, nanofils, *etc.*) pour améliorer les performances PEC.^{19, 67, 107, 108}. Cette amélioration est attribuée aux propriétés suivantes des QD's: (1) Bande interdite réglable en fonction de la taille pour correspondre au spectre solaire et obtenir une absorption efficace de la lumière; (2) L'effet de confinement quantique pour un grand coefficient d'absorption optique; (3) Grand moment dipolaire intrinsèque pour la séparation efficace des porteurs de charge

photoexcités; (4) L'effet de génération d'excitons multiples pour un grand nombre de porteurs photogénérés^{109, 110}. Par conséquent, les matériaux semi-conducteurs modifiés QD's sont capables de faciliter la séparation, le transport et la génération de porteurs de charge, améliorant ainsi les performances de la cellule PEC.

Objectifs de recherche de la these

Cette thèse se compose de trois parties avec trois objectifs pertinents:

Partie I: Diodes colloïdales NIR sans métaux lourds pour une production d'hydrogène PEC efficace

Avec les développements rapides des techniques synthétiques des QD's colloïdales et leurs applications dans les dispositifs optoélectroniques tels que les dispositifs PEC à base de QD's et QDSC's, les QD's NIR tels que PbS, PbSe et leurs structures cœur/coquille sont devenus des nanomatériaux attractifs pour les dispositifs optoélectroniques. Leur absorption de lumière NIR qui correspond au spectre solaire. Cependant, la plupart des QD's NIR contiennent des éléments toxiques tels que Pb et Cd. Bien que ces dispositifs optoélectroniques à base de QD's NIR aient montré d'excellentes performances, les éléments toxiques dans les processus de synthèse QD's et de fabrication de dispositifs sont nocifs pour la santé humaine et l'environnement, entravant ainsi la commercialisation et l'application pratique des dispositifs optoélectroniques QD's.

Par conséquent, les objectifs de la partie I sont:

1. Investigation de la synthèse, de la morphologie et des propriétés optiques des CIS QD's/CS/ZnS exemptes de métaux lourds.
2. Étudier la morphologie, la distribution des éléments et l'alignement de la bande de la photoanode à base de QD's basée sur CISes/ZnS écologique/NIR.
3. Comparaison des performances PEC et de la stabilité des dispositifs CEP CISes et CISes/ZnS à base de QD's de cœur-coquille et analyse de la fonction du coquille ZnS sur les CISes QD's.

Dans la partie I, nous rapportons la fabrication d'un dispositif PEC à l'aide de NIR colloïdal CISes QD's sensibilisés la couche TiO₂ mésoporeux comme photoanode. Illustré sur la Figure R1a, les CISes QD's présentent une forme triangulaire projetée dans les images TEM,

suggérant une forme pyramidale avec une taille moyenne de 5,64 nm ($\pm 0,77$ nm), où la taille est définie comme la hauteur des triangles projetés. Nous avons utilisé une approche d'échange de cations pour former une coquille protectrice inorganique mince de ZnS sur les CISEs QD's. Parallèlement, pour la comparaison, nous avons également synthétisé des CISEs QD's couché par CdS via une approche d'échange de cations. Les CISEs QD's/ZnS et CISEs/CdS ont montré une structure pyramidale et une distribution de taille similaires, ce qui indique que le traitement de surface Zn et Cd ne modifie pas la taille/structure globale.

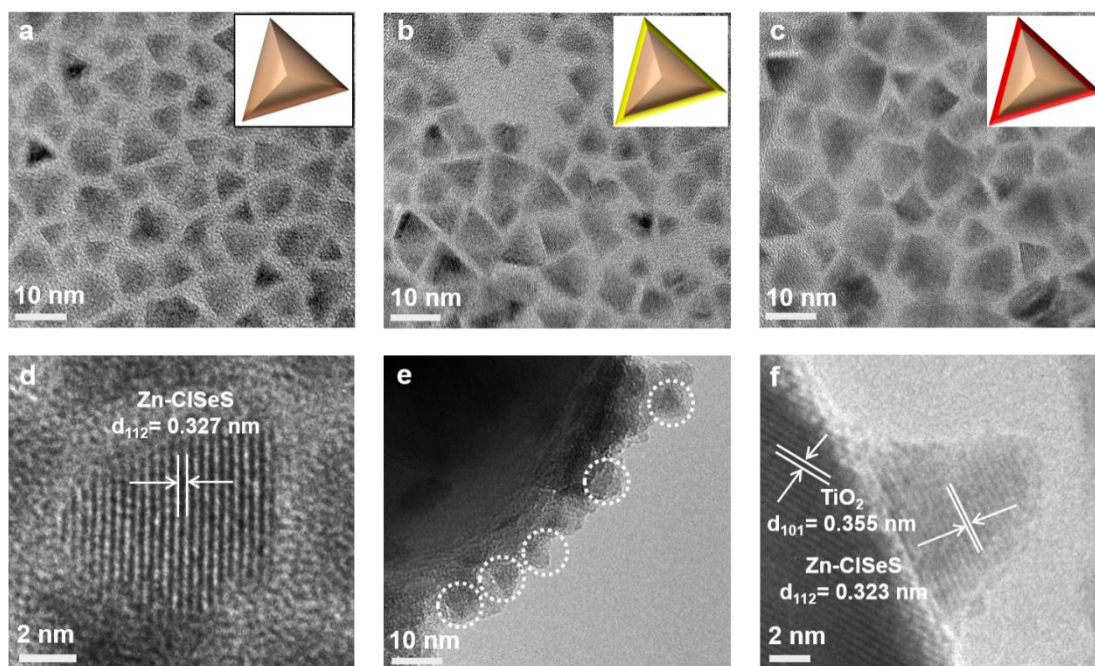


Figure R1. Images TEM de (a) CISEs QD's; (b) Cd-CISEs QD's (c) Zn-CISEs présentant une structure pyramidale analogue et des tailles presque identiques. Les images en encart de (a), (b) et (c) affichent des diagrammes schématiques des structures CISEs, Cd-CISEs et Zn-CISEs QD's, respectivement. (d) Image HRTEM de Zn-CISEs QD's individuel avec un espacement réticulaire de 0,327 nm. (e) Image TEM de hétérostructure TiO₂/Zn-CISEs avec une dispersion uniforme Zn-CISEs QD's (un cercle en pointillés blancs présente une seule QD's sur la surface de TiO₂). (f) Image HRTEM de TiO₂ / hétérostructure simple Zn-CISEs QD's (Image de grossissement supérieur du cercle blanche en (e)).

Un image de microscopie électronique à transmission à haute résolution (HRTEM) d'un seul Zn-CISEs QD's est présentée sur la figure R1(d). L'espacement mesuré du réseau de 0,327 nm se situe entre 0,319 nm (indexé sur le plan (112) du CuInS₂ pur) et 0,335 nm (indexé au plan (112) du CuInSe₂ pur) qui est cohérent avec le plan (112) du CISEs QD's, allié démontrant la nature de l'alliage de CISEs. Les QD ont été déposés dans un film de TiO₂ mésoporeux par dépôt électrophorétique (EPD) pour obtenir un contact intime entre les QD's et les

nanoparticules de TiO_2 (Figure R1e et f). Par la suite, deux couches de ZnS préparées par un procédé successif d'adsorption et de réaction de la couche ionique (SILAR) ont été recouvertes sur l'anode $\text{TiO}_2/\text{CISeS}$ pour empêcher la photocorrosion.

Comme montré sur la Figure R2, le système PEC fabriqué basé sur la photoanode $\text{TiO}_2/\text{CISeS}/\text{ZnS}$ présentait une densité de photocourant saturée de $\sim 2,57 \text{ mA/cm}^2$ sous une irradiation solaire standard de 1,5 G AM (100 mW/cm^2). Pour supprimer les pièges de surface des QD's CISeS nus, une coquille ultramince de ZnS a été cultivée sur des QD's CISeS de cœur par échange de cations à trois températures de réaction (50, 100 et 150 °C). Il a été démontré que les QD's CISeS avec traitement Zn à 100 °C présentaient des propriétés optiques optimales en termes d'intensité de photoluminescence (PL) et de durée de la vie prolongée, résultant en une forte réduction des défauts/pièges de surface. La cellule PEC optimisée utilisant ces CISeS / ZnS cœur-coquille QD's (avec traitement Zn à 100 °C, dénommé ZD-CISeS QD's) a montré une recombinaison de charge réduite, conduisant à une stabilité largement améliorée et une densité de photocourant saturée atteignant environ $4,3 \text{ mA/cm}^2$ comparé aux CISeS QD's nus. C'est la plus haute densité de photocourant rapportée jusqu'à ce jour pour un dispositif PEC à base de QD's colloïdales NIR sans métal lourd pour la production d'hydrogène. De plus, la photoanode à base de Zn-CISeS QD's présente également une très bonne stabilité (figure R2d). Après 9h d'illumination, la cellule PEC basée sur la photoanode Zn-CISeS QD's montre seulement une densité de $\sim 23\%$ de la densité photoélectrique initiale, qui est environ 3 fois inférieure à celle de la photoanode CISeS QD's sensibilisée ($\sim 62\%$ 2h) en raison de la présence d'une mince couche de ZnS. Il n'y a pas de changement de couleur notable de la zone active pour l'anode à base de Zn-CISeS avant et après un test PEC de 9h (encadré sur la figure R2d), ne montrant aucun changement morphologique significatif de photoanode à base de Zn-CISeS QD's et démontrant une bonne stabilité du anode pendant la mesure qui est compatible avec une perte de densité de courant inférieure.

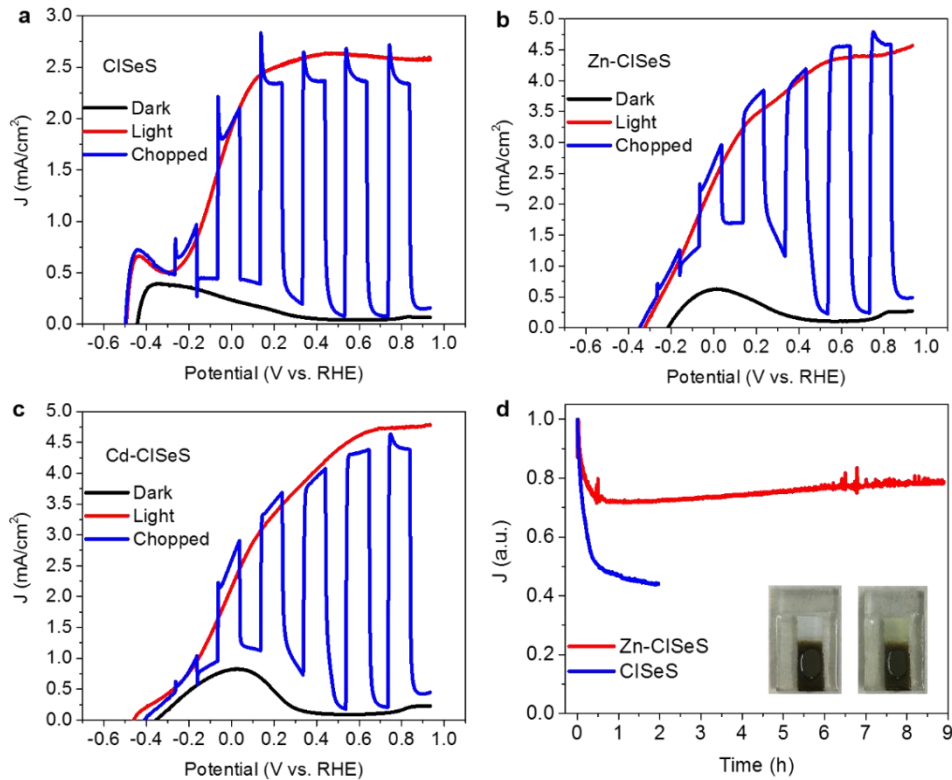


Figure R2. La dépendance densité-potential du courant des photoanodes sur TiO₂/Cd-CdSeS/ZnS, (b) TiO₂/Zn-CdSeS/ZnS et (c) TiO₂/Cd-CdSeS/ZnS dans l'obscurité (en noire), continu (en rouge) et coupé (en bleue) (d) Mesures de stabilité (densité de photocourant en fonction du temps) de TiO₂/Cd-CdSeS/ZnS et TiO₂/Zn-CdSeS/ZnS Photoanodes à 0.6 V versus RHE sous illumination AM 1.5G (100 mW/cm²) et images optiques de photoanode TiO₂ / Zn-CdSeS / ZnS avant (gauche) et après (droite) mesure de stabilité (9h, AM 1.5G, 100 mW/cm²).

La publication pertinente est:

Xin Tong, Yufeng Zhou, Lei Jin, Kaustubh Basu, Rajesh Adhikari, Gurpreet Singh Selopal, Xin Tong, Haiguang Zhao, Shuhui Sun, Alberto Vomiero, Zhiming M. Wang, and Federico Rosei. *Nano Energy*, 2017, 31, 441-449.

Partie II: Synthèse et application de NIR, g-QD's respectueux de l'environnement

Ces dernières années, les g-QD's ont été largement étudiés et ont montré des propriétés optoélectroniques et une stabilité exceptionnelles, qui sont des candidats idéaux pour les nanodispositifs. Les propriétés optiques (*e.g.* Stokes-shift) et la structure de bande des g-QD's sont réalisables pour syntoniser et satisfaire les exigences de divers dispositifs optoélectroniques tels que les LSCs, les LEDs, les QDSCs et les cellules PEC. Cependant, la

plupart des g-QD's actuels contiennent des métaux lourds tels que le Cd qui sont nocifs pour la santé humaine et l'environnement naturel. La caractéristique toxique de ces g-QD's n'est pas favorable à leur commercialisation et à leurs applications réelles en future. De plus, la majorité des g-QD's possèdent une absorption optique visible et une émission de PL, ce qui entrave leurs applications optoélectroniques et biomédicales dans la région NIR.

Par conséquent, les objectifs de la partie II sont les suivants:

1. Synthétiser des NIR g-QD's CISE/CIS sans métaux lourds, avec une épaisseur de coquille différente et étudier leur morphologie et leur structure cristalline.
2. Étudier les propriétés optiques des g-QD's CISE/CIS non-synthétisés non-synthétisés, incluant les spectres d'absorption et de PL, ainsi que la durée de vie du PL.
3. Choisir des paramètres physiques appropriés et des modèles théoriques pour calculer les fonctions d'onde électron-trou dans ces g-QD's CISE/CIS respectueux de l'environnement.
4. La mesure de la performance et de la stabilité de ces cellules PEC basées sur g-QD's et l'analyse de l'influence de l'épaisseur de la coquille sur les performances du dispositif.

Dans la partie II, nous avons suivi une procédure similaire pour synthétiser des NIR g-QD's de cœur-coquille sans métaux lourds, (CISE/CIS g-QD's) par une approche d'échange de cations séquentielle utilisant CdSe/CdS-QD's comme modèles initiaux. La morphologie des g-QD's de CISE/CIS tels que synthétisés confirme la formation d'une coquille épaisse de CuInS_2 sur les QD's de CuInSe_2 . Contrairement à la forme irrégulière des QD's CuInS (Se) typiques synthétisés directement, nous avons contrôlé avec précision la forme sphérique par la méthode d'échange de cations. Diffraction par diffraction d'électrons (SAED) et diffraction des rayons X sur poudre (XRD) indiquent que la structure cristalline des g-QD's synthétisés est la phase WZ, qui est dominée par le matériau de l'enveloppe (*i.e.* CuInS_2). Les mesures par spectrométrie d'émission optique de plasma couplé par induction (ICP-OES) indiquent l'échange complet du métal lourd du Cd de la matrice initiale CdSe/CdS g-QD's aux g-QD's CISE/CIS exempts de métaux lourds avec une épaisseur jusqu'à 5 nm.

La Figure R3 présente les propriétés optiques et les spectres d'absorption et de PL accordables de QD's dans la région NIR (jusqu'à ~ 1100 nm). La durée de vie PL des g-QD's avec diverses épaisseurs de coquille a été mesurée par spectroscopie de fluorescence transitoire et prolongée

avec des coquilles plus épaisses, démontrant l'alignement de la bande quasi-type II dans les g-QD's synthétisés, ce qui est cohérent avec les résultats de simulation.

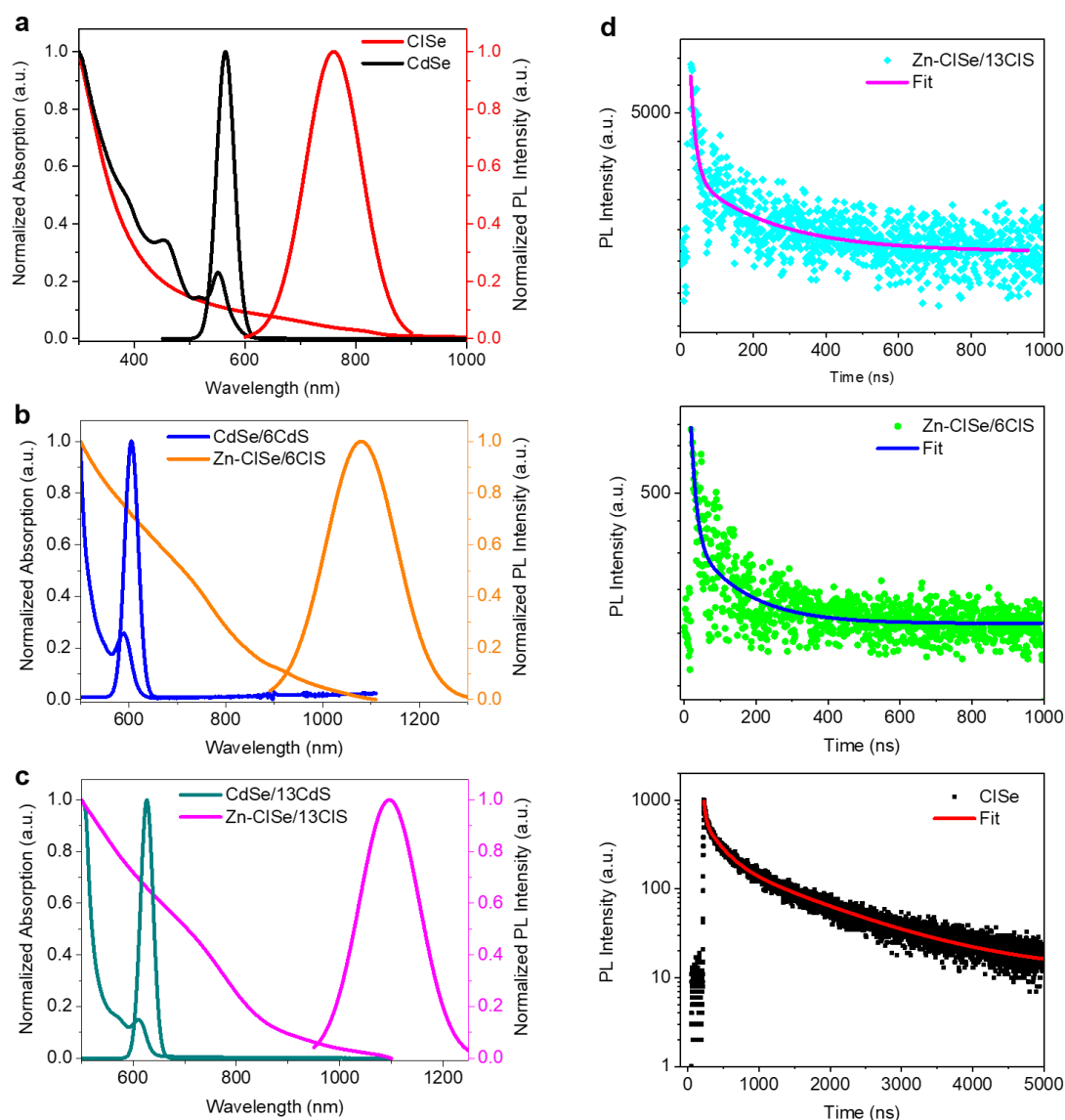


Figure R3. L'absorption et les spectres PL de (a) CISE, (b) Zn-CISE/6CIS et (c) Zn-CISE/13CIS g-QD's dans le toluène avant et après échange cationique séquentiel. (d) Spectres PL transitoires des Zn-CISE/CIS g-QD's dans le toluène.

Comme la preuve de concept, nous avons fabriqué des photoanodes basées sur ces g-QD's sans métaux lourds et NIR pour la production d'hydrogène PEC. Les g-QD's CISE/CIS après traitement de surface Zn (Zn-CISE/CIS) ont été déposés dans un film de TiO_2 par dépôt électrophorétique (EPD). Comme le montre la Figure R4, les photoanodes telles que Zn-CISE/6CIS et Zn-CISE/13CIS g-QD's comme sensibilisateurs présentent une densité de photocourant saturée aussi élevée que $\sim 3,1 \text{ mA/cm}^2$ et $\sim 3 \text{ mA/cm}^2$ avec de très bonnes stabilité,

comparable aux meilleurs dispositifs PEC basés sur les QD's. Ces résultats indiquent que les g-QD's Zn-CiSe/CIS exempts de métaux lourds sont des matériaux prometteurs pour diverses applications d'énergie solaire rentables et respectueuses de l'environnement, telles que la génération d'hydrogène PEC.

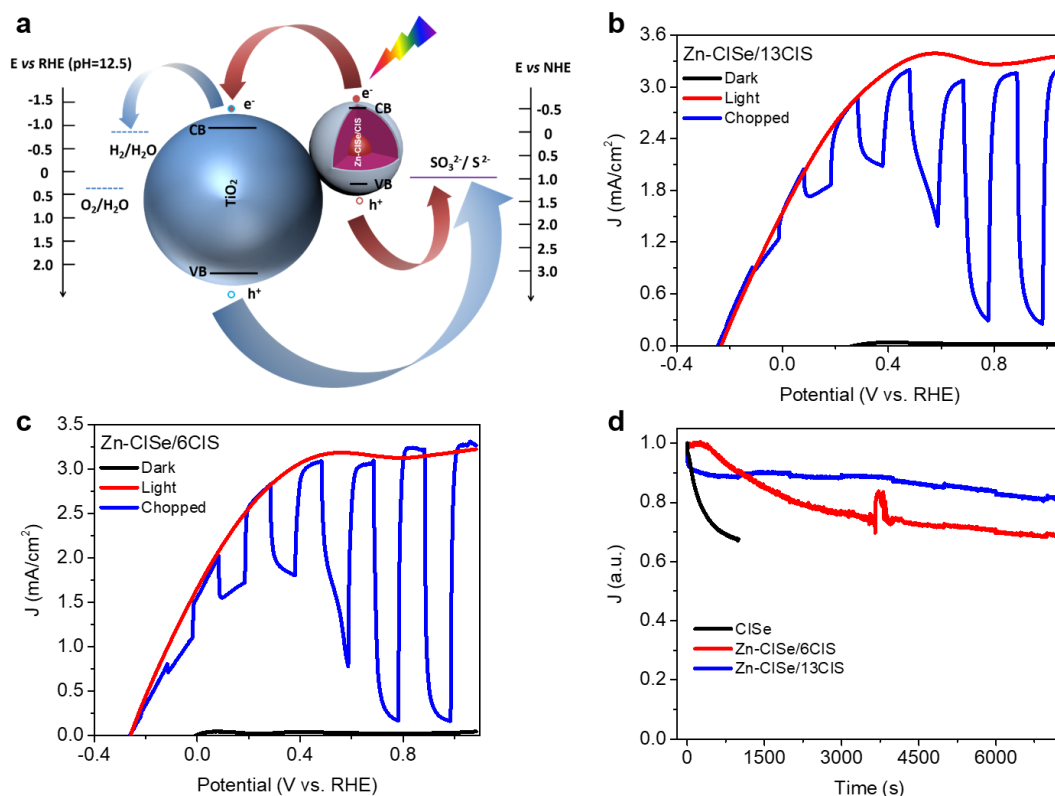


Figure R4. (a) Alignement approximatif des bandes et schémas des photoanodes sensibilisées au Zn-CiSe/CIS g-QD's. Dépendance du potentiel de polarisation photocourant (par rapport à RHE) des Zn-CiSe/13CIS g-QD's et (c) des photoanodes sensibilisées Zn-CiSe/6CIS g-QD's dans l'obscurité (en noire), sous une courbe continue (en rouge) et l'éclairage haché (en bleue) (AM 1,5G, 100 mW/cm²). (d) Densité photocourant en fonction du temps (mesures de stabilité) de TiO₂/CISE/ZnS (en noire), TiO₂/Zn-CiSe/6CIS/ZnS (en rouge) et TiO₂/Zn-CiSe/13CIS/ZnS (en bleue) photoélectrodes à 0,8 V par rapport à RHE sous irradiation AM 1,5G (100 mW/cm²).

La publication pertinente est:

Xin Tong, Xiang-Tian Kong, Yufeng Zhou, Fabiola Navarro-Pardo, Gurpreet Singh Selopal, Shuhui Sun, Alexander O. Govorov, Haiguang Zhao, Zhiming M. Wang, and Federico Rosei. *Advanced Energy Materials*, 2018, 8, 2, 1701432.

Partie III: Propriétés optoélectroniques dans les g-QD's émettant dans le proche infrarouge et

de forme pyramidale

Il a été démontré que les QD's non sphériques hétérostructurées présentent d'excellentes propriétés optoélectroniques telles qu'une durée de vie ultra-longue, favorable aux dispositifs photovoltaïques. Néanmoins, ces QD's non sphériques hétérostructurées ont encore plusieurs limitations dont la stabilité. Les g-QD's avec une coquille épaisse ont présenté une stabilité photo/chimique supérieure et sont considérés comme des éléments de construction prometteurs pour les technologies solaires. Puisque la plupart des g-QD's sont sphériques, il est intéressant de synthétiser des g-QD's non-sphériques et d'étudier leurs propriétés optoélectroniques. De plus, comme la plupart des g-QD's sont optiquement actifs dans la région ultraviolette visible, l'extension de l'émission optique des g-QD's dans la région NIR devrait constituer une orientation de recherche prometteuse dans ce domaine.

Par conséquent, les objectifs de la partie III sont les suivants:

1. Préparation de g-QD's CISES/CdSeS/CdS hétérostructurés de forme pyramidale.
2. Étude des propriétés optoélectroniques des g-QD's pyramidaux tels que préparés.
3. Utilisation de modèles théoriques appropriés pour simuler les fonctions spatiales d'onde électron-trou dans de telles g-QD's pyramidales.
4. Fabrication et mesure de cellules PEC et de QDSC à base de g-QD's de forme pyramidale.

Dans la partie III, nous décrivons la synthèse des g-QD's hétérogènes hétérogènes CISES/CdSeS/CdS avec une forme pyramidale et une émission NIR en utilisant une méthode facile en deux étapes. Comme le montre la figure R5, les images obtenues par microscopie électronique en transmission (TEM) confirment la forme pyramidale avec une grande taille (jusqu'à environ 13 nm) et la dynamique de croissance des g-QD's synthétisés. Des diagrammes de diffraction d'électrons dans une zone sélectionnée (SAED) et de XRD démontrent que les matériaux de coquille de la couche de CdSeS/CdS cristallisent dans la structure de zinceblende (ZB).

Les propriétés optiques (Figure R6) montrent un décalage vers le rouge des pics excitoniques dans les spectres d'absorption de ce type de g-QD's, ce qui indique la croissance subséquente des coquille de CdSeS et CdS alliées sur les QD's du cœur CISES. Les spectres PL des g-QD's montrent une émission NIR (~ 830 nm) et un décalage bleu des pics PL dans ces g-QD's montre

la diminution de la taille des QD's, qui est induite par l'effet de gravure du noyau. Cet effet est causé par un processus d'échange de cations dans les premiers stades de croissance, ce qui est également compatible avec les images TEM. La durée de vie PL prolongée avec une épaisseur de coquille croissante indique la structure de bande quasi-type II pour une séparation spatiale efficace des électrons et des trous dans de telles g-QD's hétérostructurées de forme pyramidale, conformément aux calculs théoriques.

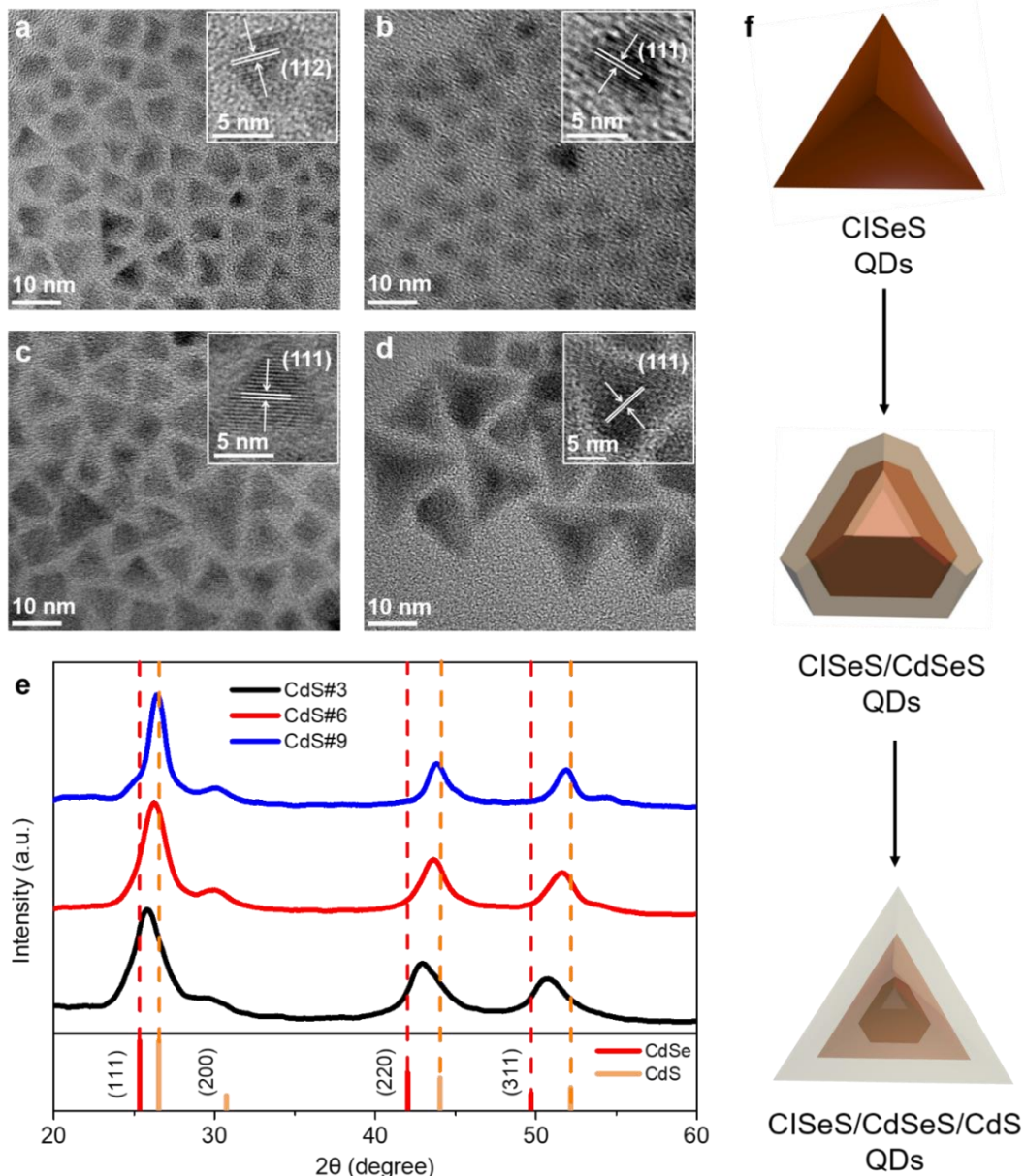


Figure R5. Images TEM (a) CISeS avec des images HRTEM incrustées montrant le plan (112) de la phase chalcopyrite. Images TEM de (b) CdS#3 et (c) CdS#6 QD's avec des images HRTEM insérées présentant le plan (111) de la phase ZB CdSeS. (d) des images TEM de QD's CdS#9 avec des images HRTEM incrustées montrant le plan (111) de la phase ZB CdS. (e) Diffractogrammes des QD's CdS#3, CdS#6 et CdS#9. (f) Schéma des croissances et de la structure des g-QD's CISeS/CdSeS/CdS hétérostructurés.

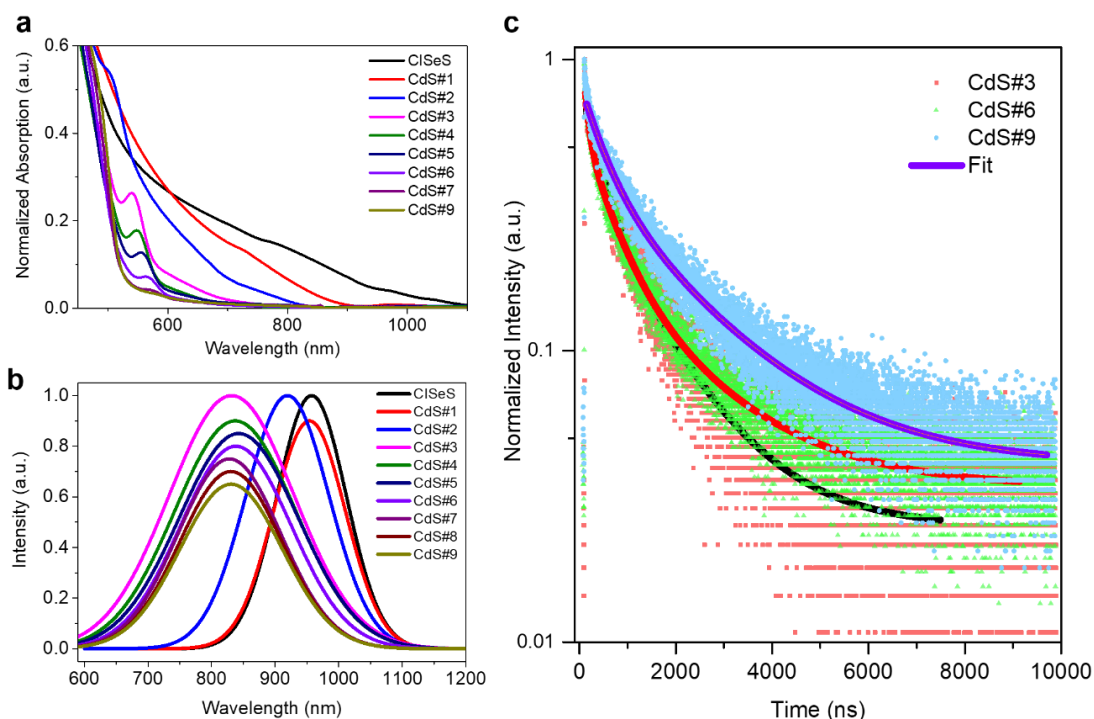


Figure R6. L'absorption UV-Vis et les spectres PL de g-QD's hétérostructurés CISES/CdSeS/CdS à différents stades de croissance dans le toluène. (c) les durées de vie PL des g-QD's CdS#3, CdS#6 et CdS#9 dans le toluène.

Ces g-QD's ont ensuite été utilisés comme cueilleuses légères pour fabriquer des QDSC et des photoanodes sensibilisées aux QD's pour la production d'hydrogène PEC. Comme le montre la Figure R7, la photoanode sensibilisée QD's telle que fabriquée présente une densité de photocourant saturée aussi élevée que $\sim 5,5 \text{ mA/cm}^2$ avec une très bonne stabilité, comparable aux meilleurs systèmes PEC basés sur les QD's. De plus, les QDSC basés sur ces g-QD's présentent également de bonnes performances. Ces résultats suggèrent que les g-QD's hétérostructurés et hétérostructurés CISES/CdSeS/CdS sont des matériaux prometteurs pour toutes sortes de technologies photovoltaïques à haut rendement, à faible coût et durables, y compris la production d'hydrogène à base de PEC solaire.

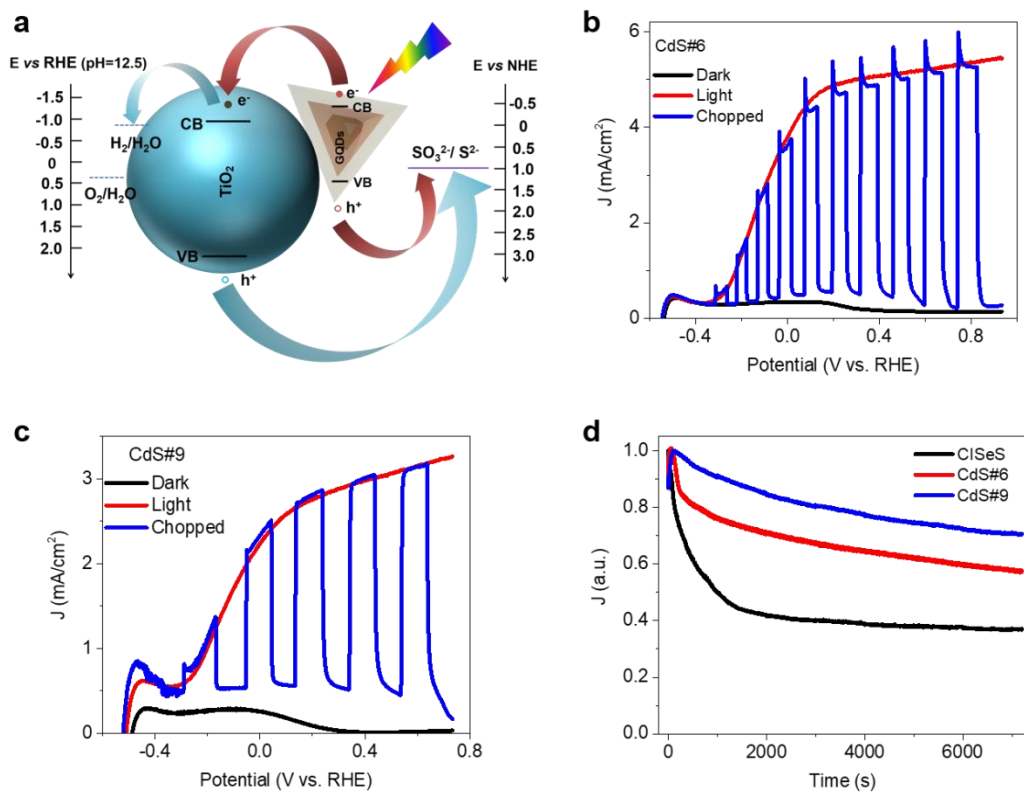


Figure R7. (a) Le schéma avec alignement de bande prévisible et de photoélectrodes à base de g-QD's CISES/CdSeS/CdS hétérostructurées. Voltammétrie à balayage linéaire de (b) les systèmes $\text{TiO}_2 / \text{CdS}\#6$ g-QD's/ZnS et (c) $\text{TiO}_2/\text{CdS}\#9$ g-QD's/ZnS dans l'obscurité et sous irradiation AM 1,5 G à 100 mW/cm². (d) Les courbes normalisées de densité de courant à l'état stationnaire (J -t) de CISES QD's (en noire), CdS#6 g-QD's et CdS#9 g-QD's-photoanodes décorées à 0,6 V par rapport à RHE sous un éclairage solaire standard.

La publication pertinente est:

Xin Tong, Xiang-Tian Kong, Chao Wang, Yufeng Zhou, Fabiola Navarro-Pardo, David Barba, Dongling Ma, Shuhui Sun, Alexander O. Govorov, Haiguang Zhao, Zhiming M. Wang, and Federico Rosei. *Advanced Science*, 2018, 5, 8, 1800656